# A computational study of the domain states for magnetite

Tom M. Wright

A thesis submitted in fulfilment of the requirements
for the degree of Doctor of Philosophy
to the
University of Edinburgh
1995

# Abstract

A three-dimensional micromagnetic model is described which predicts the equilibrium magnetization states of magnetite, one of the most common natural magnetic minerals. Solutions are presented for cubic, octahedral and irregularly shaped grains and their stability to external magnetic fields studied. Two aspects of the model make it more powerful than previous models. Firstly, a Fourier transform algorithm has been developed which reduces the number of calculations from $\mathcal{O}(N^2)$ to $\mathcal{O}(N \log N)$, where $N$ is the number of elementary magnetization vectors. Secondly, the model is implemented on a parallel computer which reduces the computation time by a factor of approximately $1/(4N_p)$, where $N_p = 16000$ is the number of processors.

Cubic and octahedral grains smaller than $d = 0.07\mu$m, where $d$ is the width of grain, occupy uniform magnetization states. However Néel's relaxation theory predicts that these single-domain (SD) states are only stable to thermal fluctuations in grains larger than $d \simeq 0.045\mu$m. Therefore SD states are only stable over a narrow size range suggesting that a significant percentage of remanence in magnetic minerals resides in grains larger than $0.07\mu$m.

Between $0.07\mu$m and $0.1\mu$m grains can occupy either flower states or vortex states. The magnetization in flower states is mostly uniform but with some deflection at the corners of the grain. Vortex states are characterized by a circular magnetization pattern which rotates around a line running through the centre of the grain. For cubic grains, vortex states are lower energy states than SD states for all grain sizes. However for octahedral grains, vortex states are energetically favourable only in grains larger than $0.11\mu$m. Hysteresis simulations show that vortex states can predict remanences which are 1/4 of those predicted by SD theory and coercivities which are 2/3. These results are important in showing how a gradual transition in the bulk magnetic properties of magnetite, from SD states to multi-domain states can occur.

Flower states are unstable in grains larger than $0.1\mu$m and grains between $0.2\mu$m and $1\mu$m can occupy one of several different vortex states, each one of which is a separate local energy minimum state. The model predicts that the high values of saturation remanence and coercivity measured experimentally in grains in this size range are due to grains occupying high energy vortex states with an associated high magnetic moment. There is a gradual transition from

vortex states in grains below 1$\mu$m to multi-domain states in grains larger than 1$\mu$m. During this transition vortices become localized features which can nucleate domain walls.

Domain states in cubic grains smaller than 4$\mu$m are characterised by separate surface and interior domains. In the interior of the grain the magnetocrystalline anisotropy controls the magnetization to align along the easy $\langle 111 \rangle$ directions. At the surface of the grain the magnetostatic energy controls the magnetization to align parallel to the surface in order to reduce the number of magnetic surface charges. The magnetocrystalline anisotropy then aligns these surface domains in the $\langle 110 \rangle$ directions. The direction of the magnetization in octahedral grains is controlled by a shape anisotropy which aligns domains in the intermediate $\langle 110 \rangle$ directions throughout the grain.

Simulations of Bitter patterns on the modelled domain structures suggest that any experimentally observed Bitter patterns on magnetite grains smaller than $d \approx 4\mu$m will not be related to either the surface or interior domain structures. The magnetocrystalline anisotopy controls the magnetization in iron to align in the $\langle 100 \rangle$ directions throughout the grain and because of this cubic grains of iron occupy lamellar two-dimensional domain states. Furthermore, simulated Bitter patterns of 1$\mu$m cubic grains of iron image the domains walls clearly and thus represent the magnetization state of the whole grain.

# Acknowledgments

My thanks go to Dr. Wyn Williams for assisting me throughout this project and to Klaus Ramstock for initial discussions concerning the FFT technique. My thanks also to Dr. Randy Enkin, Karl Fabian, Dr. Franz Heider, Dr. Les Thomson and James King for general discussions. I would like to thank the Edinburgh Parallel Computing Centre (EPCC), Shane Voss and Ian Chisholm for computing support and the secretarial staff at the Geology and Geophysics department for their assistance. I would also like to thank my parents for their support. This project was funded by the Natural Environment Research Council.

# Contents

# Appendices

# List of symbols

## Mathematical symbols

| | |
|---|---|
| $C_e$ | Exchange constant |
| $d$ | Edge length of cubic crystal |
| $d_0$ | Critical grain size separating uniform and non-uniform states |
| $d_w$ | Width of a domain wall |
| $\mathbf{d}$ | Search direction |
| $E^e$ | Exchange energy |
| $E^a$ | Anisotropy energy |
| $E^d$ | Magnetostatic energy |
| $E^h$ | External field energy |
| $E^s$ | Magnetostrictive energy |
| $E^{el}$ | Elastic energy |
| $\mathbf{g}$ | Gradient |
| $H$ | Magnetic induction (mT), the strength of a magnetic field is $\mu_0 H$. |
| $H_c$ | Coercivity |
| $K_1$ | First order magnetocrystalline anisotropy constant |
| $M_{rs}$ | Saturation remanent magnetization |
| $M_s$ | Saturation magnetization |
| $M_x$ | component of the magnetization in the $x$ direction |
| $M_{tot}$ | Total moment, $M_{tot} = (M_x^2 + M_y^2 + M_z^2)^{1/2}/M_s$ |
| $\mathbf{m}$ | $\alpha\mathbf{i} + \beta\mathbf{j} + \gamma\mathbf{k}$ |
| $n$ | Number of sub-cubes to a grain edge |
| | (but also used in chapters 2 & 3 to represent the outward normal direction) |
| $N$ | Total number of sub-cubes, for cubic grains $N = n^3$ |
| $\mathbf{n}$ | Normal direction to a charged plate. |
| $s_{ij}$ | stress tensor |
| $U_{ij}$ | Strain tensor |
| $\mathbf{x}$ | A set of variables |
| $W$ | Interaction co-efficient between two charged plates |
| $\Delta$ | Edge length of sub-cube |
| $\chi_0$ | Initial susceptibility |
| $\gamma_0$ | Gyromagnetic ratio |
| $\lambda$ | Damping co-efficient |
| $\lambda_{100}, \lambda_{111}$ | Magnetostrictive constants |

| | |
|---|---|
| $\theta$ | Azimuthal angle |
| $\phi$ | Co-latitudinal angle |
| $\alpha, \beta, \gamma$ | Cartesian components of the magnetization |
| $\sigma$ | Amount of surface charge, $\sigma = \mathbf{M} \cdot \mathbf{n}$ |

## Abbreviations

| | |
|---|---|
| $1d$ | One-dimensional |
| $2d$ | Two-dimensional |
| $3d$ | Three-dimensional |
| 2D | Two-domain |
| 3D | Three domain |
| AEM | Absolute energy minimum |
| AF | Alternating field |
| CG | Conjugate gradient |
| CM | Connection machine |
| CRM | Chemical remanent magnetization |
| FFT | Fast Fourier transform |
| GA | Genetic algorithm |
| LEM | Local energy minimum |
| MD | Multi-domain |
| NRM | Natural remanent magnetization |
| $\mathcal{O}$ | Order of magnitude |
| PSD | Pseudo-single-domain |
| SA | Simulated annealing |
| SD | Single-domain |
| TRM | Thermo-remanent magnetization |
| VTRM | Thermoviscous remanent magnetization |

## Crystallographic notation

| | |
|---|---|
| (111) | Direction of the outward normal to a plane |
| {111} | The set of planes; $(111)$,$(\bar{1}11)\ldots(\bar{1}\bar{1}\bar{1})$ |
| [111] | Vector direction |
| $\langle 111 \rangle$ | The set of vector directions; $[111]$,$[\bar{1}11]\ldots[\bar{1}\bar{1}\bar{1}]$ |

## Physical Constants

| | |
|---|---|
| $\mu_0$ | Permeability of free space, $\mu_0 = 4\pi \times 10^{-7} H\mathrm{m}^{-1}$ |
| $k_b$ | Boltzmann's constant, $k_b = 1.38 \times 10^{-23}\mathrm{JK}^{-1}$ |

# List of Figures

# Chapter 1. Introduction

The most effective recorders of the intensity and direction of the geomagnetic field are magnetic minerals which occupy single-domain (SD) magnetization states. These SD states are dominated by the exchange coupling which forces neighbouring atomic moments to align parallel to each other resulting in the maximum magnetic moment. However the size range over which grains occupying SD states are able to maintain a recording over geological timescales is very narrow. Thermal activation destroys the remanence carrying capabilities of grains smaller than the superparamagnetic threshold size ($d_s$) and grains larger than the critical size ($d_0$) occupy non-uniform magnetization states. These non-uniform states are dominated by the long-range magnetostatic energy which favours non-coherent magnetization states with flux closure. Stacey (1963) referred to non-uniform magnetization states which occur in grains slightly larger than $d_0$ as pseudo-single-domain (PSD) states. Although the total magnetic moment of any non-uniform state is necessarily less than that of a SD state, PSD states with high moments have been postulated. In addition PSD states are still thought to be stable enough to successfully record the geomagnetic field over geological periods.

For magnetite, the most common natural magnetic mineral the size range over which SD states are stable is between $d_s \simeq 0.045\mu$m and $d_0 \simeq 0.07\mu$m. However Stacey (1963) found that the grain size distributions of optically visible magnetite in igneous rocks generally peaks at approximately $1\mu$m and because of this concluded that the predominant carriers of remanence were PSD grains. It is therefore important to understand the parameters which control the stability of magnetic remanence in these PSD grains in order to reliably interpret recordings of the geomagnetic field by magnetic minerals. This chapter introduces palaeomagnetism, rock magnetism, micromagnetism, describes the aims of the project and presents a thesis plan.

## 1.1 Palaeomagnetism

Palaeomagnetism is based on recovering the intensity and direction of an ancient geomagnetic field and was first utilized in reconstructing the movements of continental plates. Despite the obvious similarity of the coastlines of South America and Africa, the continental drift hypothesis postulated by Wegener (1922) was mostly ignored by North American geologists for 40 years, although less so by European geologists such as Holmes (1928). The development of palaeomagnetism played a key role in producing experimental data which would confirm the continental drift hypothesis. Assuming the Earth's magnetic field has remained essentially dipolar and that the geomagnetic field has been axially aligned when averaged over tens of thousands of years the palaeolatitude at which a particular sample cooled through its Curie temperature can be obtained from the direction of fossil magnetizations. By mapping out apparent polar wander (APW) paths, defined as a series of palaeolatitudes for rocks of different ages it became evident that the continents had moved large distances. In addition different continents showed different APW paths implying that relative movement between continents had occurred. Although palaeomagnetism essentially confirmed the continental drift hypothesis and in particular vindicated the palaeolatitudes which Wegener deduced on palaeoclimatic grounds, continental drift had still been largely unaccepted until 1960. This was largely because no plausible mechanisms had been proposed which did not involve deep rooted continents 'sailing' though oceanic crust.

Continental drift became plausible only after Dietz (1961) proposed the sea floor spreading hypothesis to explain how ocean basins form and evolve. This hypothesis was originally conceived by Hess who postulated that continents rafted passively and drifted in response to the growth of ocean basins. It was the interpretation of the magnetic stripes measured over the Atlantic ocean as recording reversals in the geomagnetic field, firstly by L.W. Morley[1] and later by Vine and Mathews (1963) which confirmed the sea-floor spreading hypothesis. The most compelling evidence for continental drift came when Vine (1966) correlated oceanic reversal stripes with similar sequences from relatively stationary Icelandic basalts and calculated the rate at which the Atlantic has been spreading. These spreading rates were later verified beautifully by Maxwell *et al* (1970)

[1]Rejected by *Nature* in Feb. 1963 and *J. Geoph. Res.* in April 1963 and finally published by W. Glen (1982)

from palaeontological dating results of sediment cores from the ocean drilling project. Despite the success of plate tectonics in unifying many aspects of geology, certain fundamental concepts such as the mechanism for driving the plates remain ambiguous.

In a broader sense palaeomagnetism has contributed to our understanding of a wide variety of processes. For example, the correlation between oxygen isotope records and susceptibility measurements has meant that magnetic measurements on lake sediments has become a rapid new technique for studying recent climate changes (Kukla *et al* 1988, Williams 1994). Other applications include magnetostratigraphy, aeromagnetic mapping of ore bodies, monitoring industrial pollution (Thompson and Oldfield 1986) and archeological investigations (Clark 1990).

## 1.2 Rock magnetism

A main reason for the wide spread sceptism of APW paths which were derived during the 1950s was due to an incomplete understanding of how magnetic minerals record the Earth's weak magnetic field over geological time scales. For example it was proposed that removing a sample from an outcrop by drilling demagnetized it in a similar way to when a steel bar becomes demagnetized from hammering (Creer pers. comm.). Additionally, the discovery of natural self-reversal properties in the Haruna dacite in Japan by Nagata *et al* (1951) suggested that all reversal sequences in rock layers may be due to the self-reversal of a grain's magnetization with time and not to reversals in the geomagnetic field, although it later became clear that self-reversal was an exotic phenomenon (Stacey and Banerjee 1974). Rock magnetism developed in order to provide a physical understanding of the magnetic memory of rocks and as the subject has developed there has been a greater symbiosis between rock magnetism, palaeomagnetism and geology. The remainder of this section reviews some of the concepts and assumptions in rock magnetism.

As the constituent magnetic minerals in an igneous melt cool through the Curie temperature they acquire a thermoremanent magnetization (TRM). Palaeomagnetism assumes that the direction of the acquired TRM is in the direction of the geomagnetic field at the time of cooling. After crystallization magnetic minerals commonly acquire a secondary magnetization component, due to either a thermo-viscous remanent magnetization (VTRM) defined as a thermal

activation of pre-existing magnetite, (Kent 1985) or a chemical remanent magnetization (CRM). CRMs occurring naturally in palaeomagnetic samples have been attributed to either the development of new magnetite (McCabe *et al* 1983) or to the oxidation of magnetite to haematite (Kent and Miller 1987).

Palaeomagnetists traditionally use techniques such as alternating field (AF) demagnetizing or thermal cleaning in order to distinguish between the secondary and primary components and to determine the direction of the primary magnetization. From a palaeomagnetic point of view it is essential to be able to identify secondary remagnetizations correctly. Van der Voo (1989) showed that many poles once considered reliable are now recognized as recording secondary magnetizations. For example early studies by Irving *et al* (1963) were unable to fit palaeomagnetic poles from Australia with the reconstruction of the supercontinent Gondwanaland due to a failure to remove stubborn overprints (Robertson 1979). Figure 1.1 shows examples of some thermal demagnetization plots from Australian samples showing both primary and secondary components. The secondary components are removed only after heating to a relatively high temperature of 400°C. These secondary components are thought to be caused by

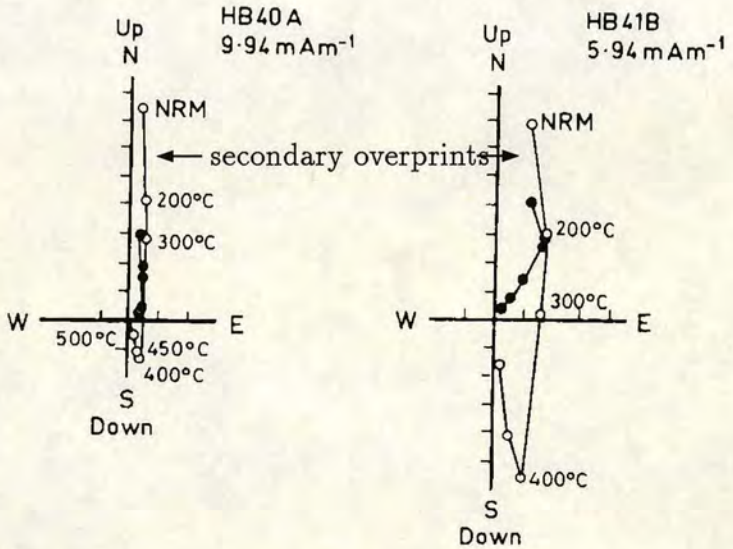


**Figure 1.1.** Orthogonal projections of thermal demagnetization vectors from two samples from South Australia following the method outlined by Zijderveld (1967). Solid and open symbols refer to the horizontal and vertical plane respectively. The plots were obtained by heating up the samples to 500°C and both samples show a persistent random overprint that is removed after heating to 400°C (Schmidt and Embleton 1981).

the heating of rocks which was associated with the opening of the Tasman sea 82 m.y. ago. Many other Australian samples show overprints which are thought to be due to hot spots under the continental plate.

Néel's (1949) theory describes TRM acquisition in terms of a SD model and is able to quantitatively predict temperatures needed to remove a secondary component. However these predicted temperatures are consistently between 100°C and 150°C lower than those required experimentally (Kent 1985, Pullaiah *et al* 1975). Néel's SD model has been rigorously proven (Moon and Merrill 1988) and the discrepancy is thought to arise because a significant percentage of TRM remanence resides in PSD grains which occupy non-uniform magnetization states.

A major aim of rock magnetism is to extend Néel's SD model to a model based on general non-uniform states. Such a model would need to predict the temperature at which samples need to be heated in order to remove any secondary components.

Given that a secondary overprint can be attributed solely to thermo-viscous processes, in addition to recording the direction and intensity of an ancient geomagnetic field multi-component palaeomagnetic samples also record thermal histories. In order to recover these thermal histories a non-SD theory of TRM acquisition would be useful so that palaeomagnetic samples can be used along with geologic information to deduce constraints on the temperature and duration of tectonic processes (Elmore and McCabe 1991). Together with geological evidence this would produce new tools in which we could determine how long and at what temperature particular samples have been heated to in the past and in turn provide constraints on tectonic processes.

To summarize: a non-SD theory of TRM acquisition would be useful as –

- A reliability test; Given geological constraints on the age, (e.g K-Ar dating) and the temperature of a thermal event (e.g. associated coalification, mineral alteration or palaeontological data) a theory would predict at what temperature a sample needs to be heated in order to remove any secondary components.

- An interpretive tool; To decide on the origin of any remagnetizations present, either a VTRM or a CRM and to provide constraints on the temperature and duration of such events.

## 1.3 Micromagnetism

The rapid development in data storage technology has led to a corresponding interest in understanding the associated magnetization processes. The commercial importance of fine magnetic grains also extends to the pharmaceutical industry, e.g. dyes and cell separation techniques that use $3\mu$m para-magnetic spheres. One of the aims of computational micromagnetics is to predict the magnetic domain states which ferromagnetic grains may occupy, either as equilibrium or transient states, both of which will in general be non-uniform magnetization configurations. By studying the domain states which grains occupy and the effect of interactions between grains, the recording industry aims to optimize the recording capabilities of thin films. Rock magnetism has a different emphasis to the recording industry in that micromagnetics is used more as an interpretive rather than an engineering tool. For example it is important to determine whether thermal cleaning completely removes any secondary overprints. More generally rock magnetism aims to define and justify the assumptions used in research fields such as palaeomagnetism and environmental magnetism.

Micromagnetic modelling is important because parameters such as the stability of non-uniform magnetization states to either thermal fluctuations or external fields can only be predicted using a computational approach. A computational approach is also necessary due to the difficulty in determining magnetic states directly from experimental observations. The resolution of colloid techniques such as the Bitter pattern method are limited in theory by the wavelength of light and in practise domains have only been observed on grains larger than $10\mu$m. However the important size range in understanding the PSD behaviour of magnetite, the most common natural magnetic mineral is between $0.1\mu$m to $5\mu$m. More fundamentally the interpretation of experimentally obtained domain patterns is strongly dependent on current theories of magnetization processes. For example, does the two-dimensional Bitter pattern shown in figure 1.2 image a surface magnetization or a two-dimensional lamellar domain state which extends through the grain?

A magnetization state is described by the spatial distribution of electron spins within a grain. Micromagnetic theory aims to predict these magnetization states by using aspects of classical electrodynamics and some theories of condensed

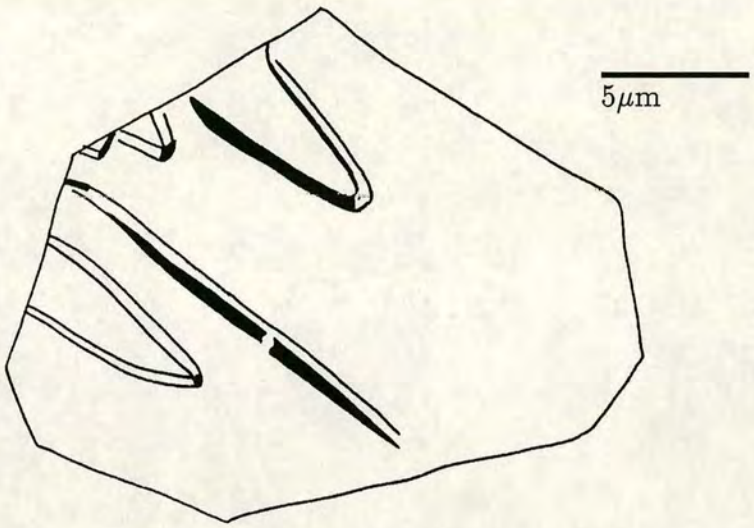


**Figure 1.2.** Sketch of a room temperature Bitter pattern from a 30$\mu$m polished laboratory grown magnetite grain. The shaded areas represent regions of relatively high colloid density and are interpreted as locating domain walls (Heider 1988).

matter physics. However, quantum mechanics - even though it provides the fundamental magnetic unit, i.e. the electronic spin, is not generally considered explicitly. Instead the magnetic sample is usually described by a set of macroscopic variables such as the direction cosines of the magnetization within the sample and each variable is taken to represent an average of many electron spins.

## 1.4 Thesis objectives

Before the acquisition of a TRM by non-uniform domain states can be modelled the simpler problem of modelling PSD states under isothermal conditions first needs to be addressed. The aim of this study is to increase the resolution of previous micromagnetic models by improving the efficiency of the algorithm and by implementing the algorithm on a parallel computer. Results will be presented which predict the transition from SD states to non-uniform PSD states to multi-domain states. The origin of PSD remanences and their stability to externally applied magnetic fields will also be predicted. In addition it is important to determine the extent to which analytic SD theory can be applied to magnetite and if possible to suggest simplified models for PSD states.

## 1.5 Thesis plan

Chapter 2 introduces the main concepts in domain theory, reviews previous theories for PSD domain states and illustrates the need for a computational micromagnetic approach. Chapter 3 reviews previous micromagnetic models and chapter 4 describes the model used in this thesis. Chapter 5 presents results which show how the magnetization evolves with grain size and simulates Bitter patterns by calculating the stray field above the surface of the grain. To test if the magnetization states for cubic grains apply generally to magnetite, chapter 6 presents results for elongated, octahedral and irregularly shaped grains. Figure 1.3 shows how saturation remanence ($M_{rs}$) and coercivity ($H_c$) values are obtained from experimental hysteresis curves. The accuracy of the model will be tested in chapter 7 by comparing predicted values of $M_{rs}$ and $H_c$ with experimental values. Assuming that the predicted values agree with the experimental values the magnetization states will be used to determine the mechanisms for PSD remanences and stability. Chapter 8 compares results from the model with previous models and discusses the relationship between simulated Bitter patterns and experimental domain observations.

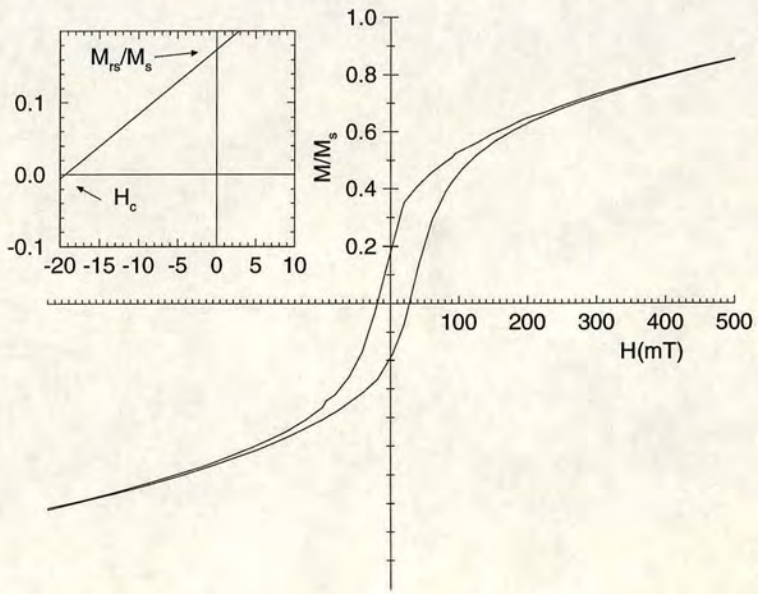


**Figure 1.3.** Hysteresis curve obtained from a natural soil sample, an enlarged section of the hysteresis curve shows the saturation remanence ($M_{rs}/M_s$) and the coercivity ($H_c$). $M_{rs}$ and $H_c$ indicate the strength and the stability of the signal respectively.

# Chapter 2. Domain states of fine grained magnetite

## 2.1 Introduction

This chapter describes the magnetization states for fine magnetite grains at different grain sizes, reviews previous models for PSD behaviour and compares predictions for PSD behaviour by some of these models with experimental measurements. Magnetite is the commonest single natural magnetic mineral, occurring as a primary or secondary mineral in continental and oceanic igneous, sedimentary and metamorphic rocks. The spontaneous magnetization in magnetite arises due to the net difference between the anti-parallel magnetizations $M_A$ and $M_B$ in the tetrahedrally coordinated A-sites and octahedrally coordinated B sites of the magnetite lattice. This results in a spontaneous ferrimagnetism, which for the purposes of this study magnetite will be considered as a ferromagnet. Kittel (1949) predicted a discontinuity in the magnetic properties as the grain size increases from SD to multi-domain (MD) grains which has never been observed experimentally for magnetite, either in values of saturation remanence or coercive force (Kneller and Luborsky 1963) or in TRM values (Parry 1965). PSD grains were postulated by Stacey (1963) as having properties which are intermediate between SD and MD magnetite grains. Magnetite has been classed into the following categories.

- Grains smaller than the superparamagnetic threshold, $d_s$ occupy SD states but as the energy barrier to domain reversal at room temperature is smaller than $k_b$T (the energy of thermal fluctuations) they are unable to record the geomagnetic field. Appendix A describes how Néel's SD theory can be used to calculate $d_s$, for a relaxation time of $\tau_s$ =10s, $d_s = 0.045\mu$m.

- Grains in the size range, $0.045 \lesssim d \leq d_0$ occupy SD states, the value for the critical size $d_0$ will be reviewed in chapter 3 and for cubic grains is usually given as $d_0 \simeq 0.07\mu$m. Values for the coercivity and saturation remanence of SD grains can be calculated analytically. If an array of SD grains is saturated by an external field and the field then removed, the direction of the magnetizations will be uniformly distributed over a hemisphere. An integration of the magnetization over the hemisphere gives $M_{rs}/M_s = 1/2$. The

coercivity can be calculated by considering the maximum torque required for a SD grain to reverse direction and using the material parameters for magnetite gives values of $H_c = 34.7$mT (Stacey and Banerjee 1974).

- Experimental hysteresis curves measured on PSD grains between $0.07 \lesssim d \lesssim 1\mu$m show values for $M_{rs}/M_s$ and $H_c$ which are a significant fraction of those measured in SD grains. PSD grains are thought to be common in natural magnetite samples, not only because of the narrow size range for SD grains but also because plots of $M_{rs}$ as a function of $H_c$ have consistently shown that most natural samples lie between the extremes of high $M_{rs}$ and $H_c$ values characterised by SD grains and low $M_{rs}$ and $H_c$ values characterised by MD grains (Day *et al* 1977). The PSD effect is also seen in TRM acquisition, TRM intensity decreases gradually over many decades of grain size and there is no sudden drop in TRM intensity which would mark a SD to MD transition (Dunlop 1990).

- Grains larger than $20\mu$m exhibit soft multi-domain characteristics with low values for $M_{rs}$ and $H_c$.

## 2.2 Psuedo-single-domain models

Stacey (1963) originally proposed that the high magnetic moments of PSD states is due to domain walls being pinned away from their equilibrium positions by dislocations and imperfections. Figure 2.1a shows a sketch of a domain wall being pinned away from a central equilibrium position resulting in an imbalance in the size of the domain and a net magnetic moment.

Stacey and Banerjee (1974) proposed that PSD grains contain small regions which behave like SD grains embedded in a soft MD matrix. These SD like moments have been attributed to closure domains (figure 2.1b) and Verhoogen (1959) proposed that screw dislocations could produce stress regions in which the magnetization acts as a SD grain. The objection to the models shown in figures 2.1a,b is that the SD moments are unable to rotate independently of the surrounding MD matrix.

Yu and Morrish (1955) considered the exchange energy of a circular spin configuration in ellipsoid grains, the magnetocrystalline energy was neglected and in an ellipsoid grain the circular spin configuration produces no surface magnetic charges and thus no magnetostatic energy. However the curling mode has

until recently been considered inappropriate for magnetite which usually crystallizes in cubic or octahedral forms. Figure 2.1c shows that in general, surface magnetic charges will occur at the edges of the grain resulting in a high magnetostatic energy. Simple analytic calculations by Butler and Banerjee (1975) showed that these free poles would make the curling mode energetically unfavourable for magnetite. However less constrained calculations may reduce the magnetostatic energy by rotating the magnetization to align along the cube edges at the expense of the exchange energy. In addition the transition from a SD state to a curling mode (with no net magnetic moment) has not been considered consistent with the development of PSD behaviour.

For these reasons early models assumed a SD to a two-domain (2D) transition instead of a SD to a curling mode. Domain wall moments, referred to as 'psarks' have been favoured as a source for PSD remanence as they have a net moment of $(2/\pi)M_s$ which is a significant fraction of $M_s$, the moment of an individual SD grain (Dunlop 1977). In addition, unlike the models shown in figures 2.1a and 2.1b, domain wall moments can exhibit true SD behaviour by rotating independently of each of the adjacent domains.

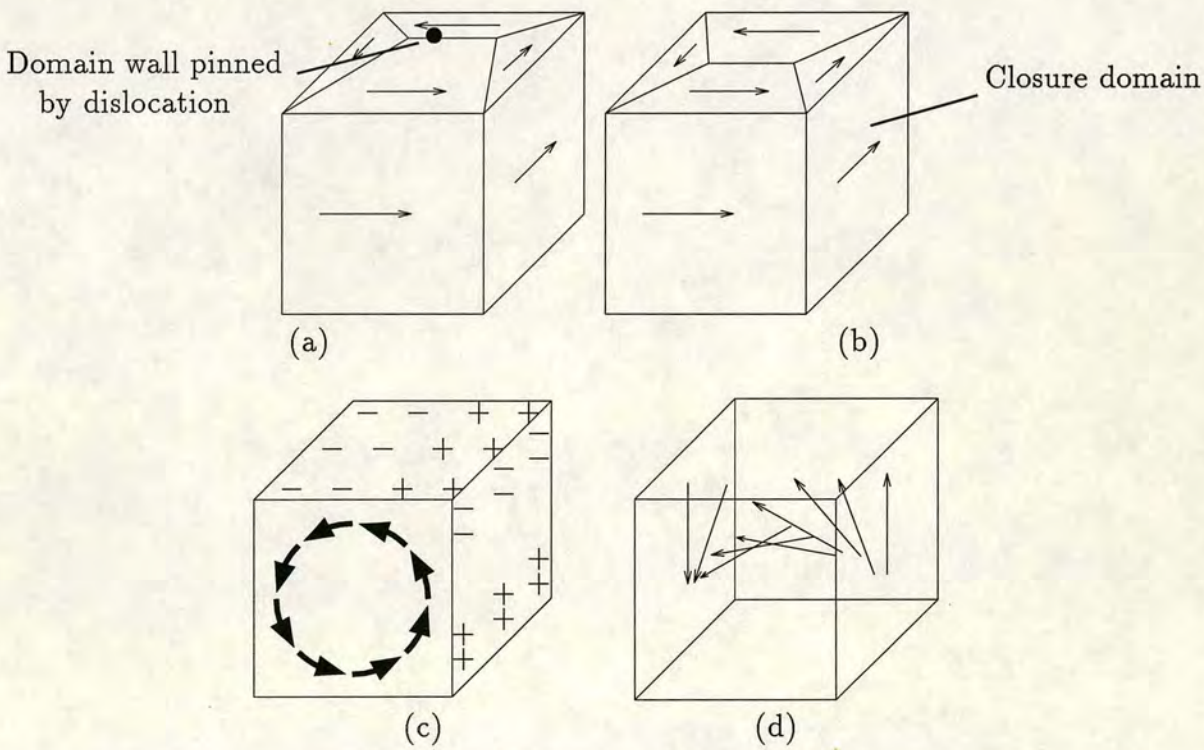


**Figure 2.1.** Sketch of four proposed models for PSD remanence, (a) Barkhausen discreteness, (b) closure domains which act as a small SD grain, (c) a curling mode and (d) domain wall moment.

The objection to the 'psark' model is that only grains occupying a 2D state with a single domain wall would be able to contribute to PSD remanences. The domain walls in grains containing three or more domains would rotate in opposite directions in order to reduce their mutual energy. This cancels out the moment of each domain wall resulting in a large reduction in the total moment of the domain state. Calculations by Butler and Banerjee (1975) have put the size at which a 3 domain state becomes more energetically favourable than a 2D state at $\approx 0.25\mu$m. This then leaves the anomalously high remanences in PSD grains between $0.25\mu$m and $5\mu$m still unaccounted for.

Moon and Merrill (1985) suggested a mechanism which they called transdomain TRM acquisition to explain the high stability of PSD sized grains. As a MD grain can occupy several equilibrium states (corresponding to different numbers of domains) there is therefore an activation energy for a grain to change from one equilibrium state to another by nucleating or denucleating a domain wall. Assuming that the activation energy associated with domain wall nucleation is smaller than that associated with domain wall movement then TRM acquisition would be controlled by this transdomain process. Although this is a possible model Moon and Merrill (1985) were unable to make predictions of the dependence of coercivity and saturation remanence with grain size.

A possible explanation for PSD remanences for grains above the the critical size, $d_0$ could be due to grains trapped in high energy SD states. Halgedahl and Fuller (1980) observed that some grains as large as $10\mu$m showed no Bitter patterns and interpreted these grains as as being in so-called metastable SD states. They then developed a theory of PSD stability based on the idea that a certain fraction of grains will occupy these metastable SD states. The probability that a grain whose equilibrium number of domain walls is $\lambda$ actually containing $w$ domain walls is assumed to follow a Poisson distribution,

$$P(w) = \lambda^w e^{-\lambda}/w! \tag{2.1}$$

and by using simple Kittel domain theory the dependence of $M_{rs}$ on $d$ becomes,

$$M_{rs}/M_s = 1.36\exp[-(d/d_0)^{1/2}] \quad . \tag{2.2}$$

This metastable SD model depends on large grains being able to occupy SD states. It is difficult to envisage how grains as large as $10\mu$m could occupy SD states, imperfections such as sharp grain edges would increase the demagnetizing

field locally making it less likely for the SD state to exist in large grains.

## 2.3 Magnetites suitable for testing PSD models

The advantage of using synthetically grown grains to test theories for PSD remanences is that the grain size can be controlled and contamination by small SD grains minimized. In addition they are thought to have a small number of crystalline imperfections and corresponding low internal stress fields compared to samples obtained by crushing and sieving natural grains. Results from previous models and the present model will be compared with grains grown using the hydrothermal method and those precipitated from solution.

The hydrothermal method uses magnetite as a seed material which is then recrystallized under temperature and pressure. The grains show octahedral, rhombic, dodecahedral and cubic form and the size of the grains obtained are an exponential function of the recrystallization temperature, ranging from 3$\mu$m at 350°C to 130$\mu$m at 800°C (J. King, pers. comm.). Heider (1988) concluded that the internal stress fields in hydrothermal grains are low and are similar to naturally occurring grains. He compared dislocation densities by counting etch pits produced by HCL on hydrothermal grains and on a natural 5mm octahedron grain that had crystallized in a schist. The dislocation densities were measured as $2.9 \pm 1.7 \times 10^{10}\mathrm{m}^2$ and $1.0 \pm 0.8 \times 10^{10}\mathrm{m}^2$ for the hydrothermal and natural crystals respectively. This implies that the synthetically grown grains have similar low internal stress fields to uncrushed natural grains.

Precipitated grains were produced by T. Takadak of Kyoto University and described by Dunlop (1973). Colloidal $Fe(OH)_2$ grains were precipitated from an aqueous solution of $FeSO_4$ and magnetite produced by oxidizing with air bubbled through the suspension. The grain size was controlled by varying the temperature and the initial concentration of $Fe^{2+}$ ions.

Figure 2.2 lists the grain sizes for grains grown using the hydrothermal method and by precipitation. Although the grain size distributions are narrower than any grains previously grown the standard deviations about the mean size are still between 30% and 40%.

| Hydrothermal | | Precipitation | |
|---|---|---|---|
| $d(\mu m)$ | $\pm \sigma(\mu m)$ | $d(\mu m)$ | $\pm \sigma(\mu m)$ |
| 0.8 | $\pm$ 0.31 | 0.037 | $\pm$ 0.015 |
| 4.6 | $\pm$ 1.9 | 0.076 | $\pm$ 0.25 |
| 11.7 | $\pm$ 3.4 | 0.1 | $\pm$ 0.03 |
| 37 | $\pm$ 5 | 0.22 | $\pm$ 0.04 |
| 51 | $\pm$ 16 | | |
| 112 | $\pm$ 34 | | |
| 306 | $\pm$ 81 | | |

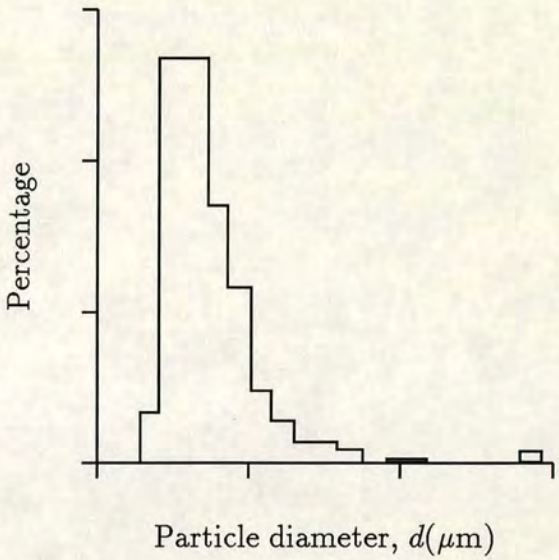


**Figure 2.2.** Grain size ($d$) and standard deviation ($\sigma$) for hydrothermal and precipitated grains, obtained from scanning electron microscope images. The grain size distribution is shown for the 0.8$\mu$m hydrothermal sample and was obtained by Heider (1988) from measurements of 327 grains from several micrographs.

## 2.4 Tests of previous PSD models

In principle these models have distinct temperature and field responses although experimental tests have proved inconclusive. Figure 2.3 shows a plot of experimentally measured values of $M_{rs}/M_s$ and PSD grains are usually defined as being between approximately 0.08$\mu$m and 1.0$\mu$m where $M_{rs}/M_s$ is between 0.1 and 0.06. Figure 2.3 also shows that neither the 'psark' model nor the metastable SD model agree with experimental measurements of $M_{rs}$. Dunlop (1986) concluded that room temperature measurements of $M_{rs}$ and $H_c$ were unable to determine the validity of any of the proposed PSD models. These results, together with the theoretical objections for each of the PSD models demonstrate the need for a computational approach to modelling PSD states.

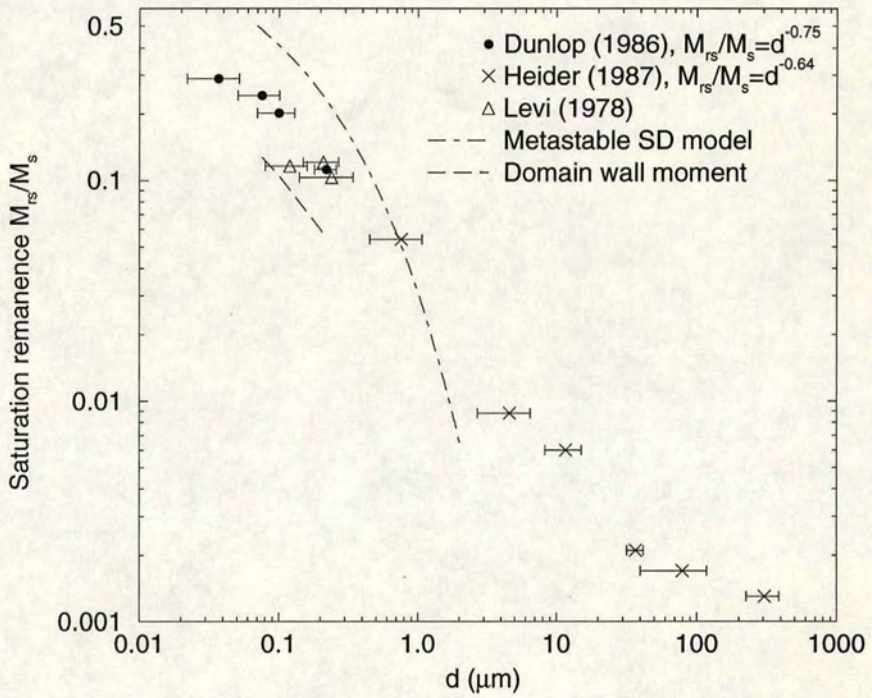


**Figure 2.3.** Variation of saturation remanence ($M_{rs}/M_s$) as a function of grain size for a domain wall model and a metastable SD model compared to experimental data from laboratory grown magnetite. The exponents for the experimental results are quoted from the original papers.

# Chapter 3. Micromagnetic modelling

## 3.1 Introduction

A magnetic structure is defined by the spatial distribution of electron spins throughout the grain and the magnetization states will be assumed to be equilibrium states. Section 3.2 briefly describes the free energy formulations, section 3.3 derives the condition for equilibrium and section 3.4 reviews some important aspects of previous micromagnetic models. Section 3.5 reviews optimization techniques and section 3.6 reviews previous micromagnetic solutions for magnetite.

## 3.2 Free magnetic energy

The total free energy, $E^{total}$, is usually written as,

$$E^{total} = E^e + E^a + E^d + E^h \tag{3.1}$$

where $E^e$ is the exchange energy, $E^a$ is the magnetocrystalline anisotropy, $E^d$ is the magnetostatic interaction energy and $E^h$ is the interaction of the grain with an externally applied field. In general there will be other terms such as a surface anisotropy term and a magnetoelastic energy which is discussed in section 3.7. Each of these energy terms is a volume integral given by,

$$\begin{aligned} E^e &= \tfrac{1}{2}\int C_e[(\nabla\alpha)^2 + (\nabla\beta)^2 + (\nabla\gamma)^2]d\tau, \quad E^a = \int \omega_a d\tau, \\ E^d &= \tfrac{1}{2}\int \mathbf{M}\cdot\mathbf{H}'d\tau, \qquad\qquad E^h = -\int \mathbf{M}\cdot\mathbf{H}_0 d\tau \end{aligned} \tag{3.2}$$

where $C_e = 2A$ where A is the exchange constant, $\alpha$, $\beta$ and $\gamma$ are the direction cosines of the magnetization $\mathbf{M}_s$ with respect to the $\langle 100\rangle$ crystal basis vectors, $w_a$ is the magnetocrystalline anisotropy energy density, $\mathbf{H}'$ is the self-demagnetizing field, $\mathbf{H}_o$ is the external field, $\tau$ denotes the volume of the body and $S$ its surface. The magnetocrystalline energy is an expansion of the crystalline anisotropy density satisfying the symmetry of the underlying crystal lattice. It is a phenomalogical term given by,

$$w_a = K_1(\alpha^2\beta^2 + \beta^2\gamma^2 + \alpha^2\gamma^2) + K_2(\alpha^2\beta^2\gamma^2) \tag{3.3}$$

The magnetocrystalline anisotropy controls the magnetization to align in certain preferential directions. These directions are referred to as easy axes and are shown in figure 3.1.

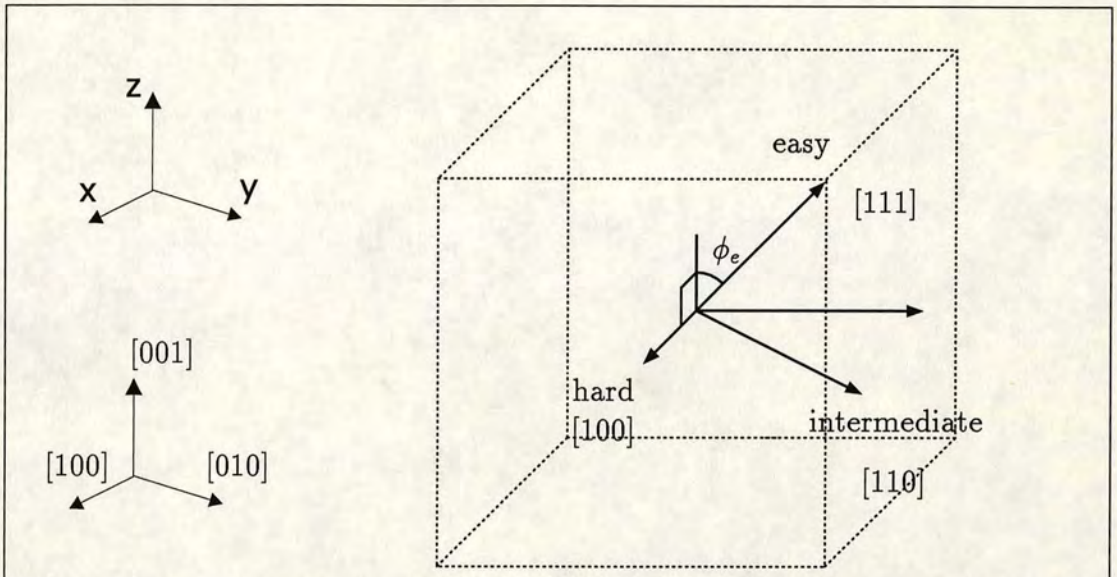


**Figure 3.1.** Diagram showing the relationship between the crystallographic axes and the $x, y, z$ directions and the easy and hard magnetocrystalline axes for magnetite.

## 3.3 Condition for equilibrium

The calculus of variations is used to minimize the definite integrals in equation 3.2. To derive the equilibrium condition it is necessary to retain only terms of first degree in the small variation $\delta\mathbf{M} = M_s\delta\mathbf{m} = M_s\delta(\alpha\mathbf{i} + \beta\mathbf{j} + \gamma\mathbf{k})$. The resulting variation of $E^{total}$ is,

$$\delta E^{total} = \int \Big\{ C_e[(\nabla\alpha)\cdot\delta(\nabla\alpha) + (\nabla\beta)\cdot\delta(\nabla\beta) + (\nabla\gamma)\cdot\delta(\nabla\gamma)] + \frac{\partial\omega_a}{\partial\mathbf{m}}\cdot\delta\mathbf{m} - \frac{1}{2}(\mathbf{M}\cdot\delta\mathbf{H}' + \mathbf{H}'\cdot\delta\mathbf{M}) - \mathbf{H}_0\cdot\delta\mathbf{M}\Big\}\mathrm{d}\tau \tag{3.4}$$

Using Green's theorem,

$$C_e\int(\nabla\alpha)\cdot\nabla\delta\alpha\mathrm{d}\tau = C_e\int\frac{\partial\alpha}{\partial n}\delta\alpha\mathrm{d}S - C_e\int(\nabla^2\alpha)\delta\alpha\mathrm{d}\tau \tag{3.5}$$

where $n$ is the outward normal to the surface and

$$-\frac{1}{2}\int(\mathbf{M}\cdot\delta\mathbf{H}'+\mathbf{H}'\cdot\delta\mathbf{M})\mathrm{d}\tau=-\int\mathbf{H}'\cdot\delta\mathbf{M}\mathrm{d}\tau \tag{3.6}$$

equation 3.4 becomes,

$$\delta E^{total}=\int[-C_e\nabla^2\mathbf{m}+\frac{\partial\omega_a}{\partial\mathbf{m}}-M_s\mathbf{H}]\cdot\delta\mathbf{m}\mathrm{d}\tau+\int C_e\frac{\partial\mathbf{m}}{\partial n}\mathrm{d}S \tag{3.7}$$

where $\mathbf{H}=\mathbf{H}_0+\mathbf{H}'$. Equation 3.7 is of the form,

$$\delta E^{total}=-\int\mathbf{H}_{eff}\cdot\delta\mathbf{m}\mathrm{d}\tau-\int\mathbf{H_s}\cdot\delta\mathbf{m}\mathrm{d}S \tag{3.8}$$

where the effective field $\mathbf{H}_{eff}$ is defined as

$$\mathbf{H}_{eff}=-\frac{\partial E^{\,total}}{\partial\mathbf{M}} \quad . \tag{3.9}$$

Setting $\delta\mathbf{m}=\delta\theta\times\mathbf{m}$, where $\delta\theta$ is a small vector rotation, equation 3.8 becomes,

$$\delta E^{total}=-\int\mathbf{m}\times\mathbf{H}_{eff}\cdot\delta\theta\mathrm{d}\tau-\int\mathbf{m}\times\mathbf{H_s}\cdot\delta\theta\mathrm{d}S \tag{3.10}$$

The expression $\mathbf{M}\times\mathbf{H}_{eff}$ yields the torque on the magnetization at each point in the grain. For equilibrium, $\delta E^{total}=0$ for arbitrary $\delta\theta$, i.e. $\mathbf{m}\times\mathbf{H}_{eff}=0$ at each point of $\tau$ and $\mathbf{m}\times\mathbf{H_s}=0$ at each point on the surface $S$.

The resulting equations are commonly referred to as Brown's equations,

$$\mathbf{m}\times\mathbf{H}_{eff}=\mathbf{m}\times[C_e\bigtriangledown^2\mathbf{m}-\frac{\partial w_a}{\partial\mathbf{m}}+M_s\mathbf{H}]=0\text{ in }\tau \tag{3.11}$$

$$\mathbf{m}\times C_e\frac{\partial\mathbf{m}}{\partial n}=0\text{ on }S \quad . \tag{3.12}$$

Differentiating the constraint $\mathbf{m}^2=1$ gives,

$$\mathbf{m}\cdot\frac{\partial\mathbf{m}}{\partial n}=0 \tag{3.13}$$

and equations 3.12 and 3.13 can both be true only if,

$$\frac{\partial\mathbf{m}}{\partial n}=0\text{ on }S \tag{3.14}$$

giving the boundary condition for $\mathbf{m}$ on $S$.

## 3.4 Previous micromagnetic models

The first calculations by Landau and Lifshitz (1935) considered a domain wall in an infinitely large system which is controlled solely by the anisotropy and exchange energy. However, in order to ignore the magnetostatic interaction the model had to assume an infinitely long grain which would make domains impossible (Brown 1978). Kittel (1949) formulated analytic expressions for domain sizes but these are only valid for a large number of domains in an infinite medium.

One-dimensional ($1d$) models by Amar (1957,1958a,b) constrained the magnetization to rectangular uniform antiparallel domains and modelled domain walls as rectangular blocks uniformly magnetized at $\pm 90°$ to these domains. Figure 3.2a shows an Amar model in which the only variable to be minimized is the width of the domain wall $d_w$.

The first micromagnetic models were $1d$ models developed by Brown and LaBonte (1965) who used the discretization scheme shown in figure 3.2b. These $1d$ models were extended to the two-dimensional ($2d$) models shown in figure 3.2c by La Bonte (1969), Hubert (1968) and Fredkin and Koehler (1987). Three-dimensional ($3d$) micromagnetic models using the scheme shown in figure 3.2d were developed independently by Schabes and Bertram (1988) and Williams and Dunlop (1989)

A general feature of previous micromagnetic models is that they have been implemented on serial computers. Each energy term is calculated by sequentially summing over each magnetization variable. Recent developments in parallel computers have enabled large increases in the power of scientific models and many aspects of micromagnetism are readily mapped onto parallel computer architectures. For example, the anisotropy and external field energy are local terms which only depend on the direction of magnetization at a particular lattice-site. Thus calculating the anisotropy energy involves assigning the cartesian components of the magnetization to each processor and multiplying each component simultaneously as in equation 3.3.

The magnetostatic energy calculation ($E^d$) is the most computationally expensive calculation as each magnetization vector interacts with every other vector. This makes the problem a so-called $N-$body problem requiring $\mathcal{O}(N^2)$ calculations, where $N$ is the total number of sub-cubes. Ideally each processor in a parallel computer would be connected to every other processor. However in practice, parallel computers such as Thinking Machine's Connection Machine CM-200

are constructed so that each processor connects to only a few other processors. This means that $E^d$ cannot be directly converted from a serial sum over each element onto a parallel computer.

$N-$body problems are ubiquitous in scientific problems and a technique often used is a fast Fourier transform (FFT) method. This method reduces the number of calculations from $\mathcal{O}(N^2)$ to $\mathcal{O}(N \log N)$ and also allows $E^d$ to be implemented on a parallel computer. This technique was first applied by Giles *et al* (1990) who calculated $E^d$ by using a two-dimensional FFT routine with periodic boundary conditions. A similar method was developed by Yuan and Bertram (1992) on low resolution two-dimensional magnetic systems with non-periodic or non-magnetic boundary conditions. The major component of this thesis is the implementation of a general $3d$ FFT algorithm with non-periodic boundary conditions on the CM-200 parallel computer.

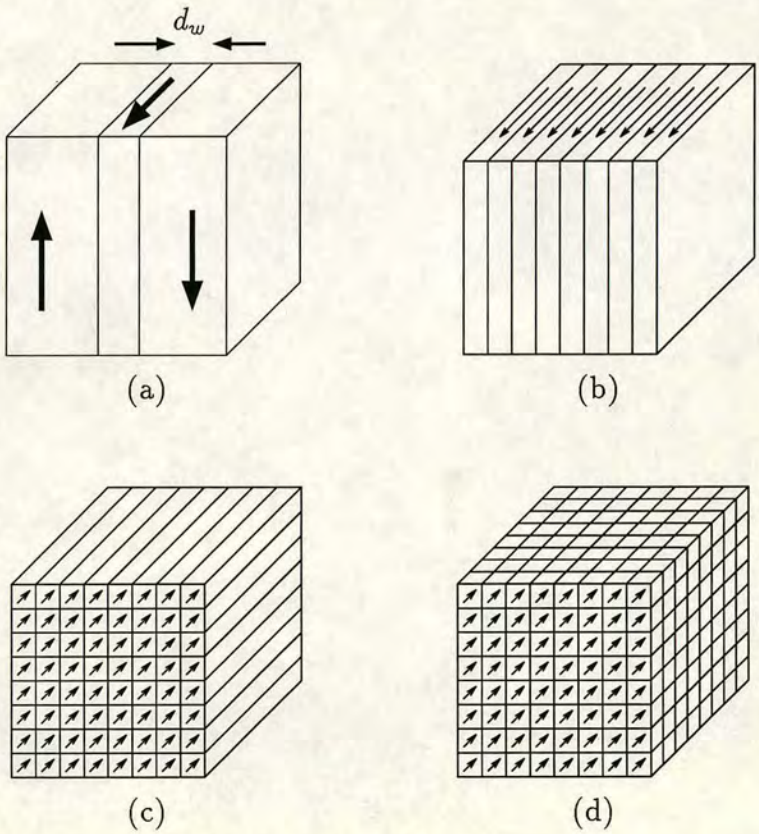


**Figure 3.2.** (a) Constrained model by Amar (1958*a*), (b) $1d$ model of a cubic grain used by Brown an LaBonte (1965), the vectors are constrained to rotate in the plane of each plate, (c) $2d$ model used by LaBonte (1965), (d) $3d$ model by Schabes and Bertram (1988). The resolution of the model is described by the number of sub-cubes to a grain edge.

## 3.5 Optimization techniques

Optimization techniques may be classed into two categories, either those which attempt to search for an absolute energy minimum (AEM) state or those which are restricted to searching for a local energy minimum (LEM) state. Before deciding on a particular optimization procedure there is always first a 'meta-optimization problem', i.e. it is necessary to decide which technique is best suited to the particular function and the computational facilities available.

Both simulated annealing (SA) and genetic algorithms (GAs) are methods which attempt to search for AEM states using analogies with natural optimization procedures. Kirkpatrick *et al* (1983) introduced the concept of simulated annealing by using an analogy with the way liquids freeze and crystallize or the way metals cool and anneal. At high temperatures the molecules of a liquid move freely with respect to one another and if the liquid cools slowly the atoms are able to line up and form a completely ordered pure crystal. If a liquid is cooled quickly or quenched it does not reach this state but rather ends up in a polycrystalline or amorphous state with a higher energy. Thomson *et al* (1994) developed a SA algorithm to calculate AEM magnetization states for grains between $0.01\mu$m and $0.2\mu$m and found similar states to those calculated by Williams and Dunlop (1989) who used a LEM search technique. Due to the extensive search space SA minimization methods are notoriously slow, calculations on a serial machine using a $5 \times 5 \times 5$ model typically took 36 times longer to find an equilibrium state than calculations using LEM search techniques. This means that SA is limited to finding equilibrium states in low resolution models. Attempts have been made to parallelize SA algorithms (Boissin and Lutton 1993), however the decrease in computation time would not have enabled the resolution of the model to be increased sufficiently over previous $3d$ models.

Rather than perturbing a single model, GAs work on a population of models and mimic evolution by natural selection to find a single optimum model (Holland 1992). For example, Sambridge and Drijkoningen (1992) successfully applied genetic algorithms to geophysical inversion problems although Ingber and Rosen (1992) found that a modified version of simulated annealing was superior to standard genetic algorithms on a suite of standard test problems. Implementing SA and GAs on parallel computer architectures is a new field and the implicit parallelism of GAs may result in fast global minimizations on large scale parallel computers (Stender *et al* 1994).

Global optimization techniques are robust and attempt to find a global energy minimum at the expense of a high computation cost. Methods which search for LEM states converge to an equilibrium state much faster than SA or GAs at the expense of a restricted search space. Enkin and Dunlop (1987) used a modified Newton method which requires calculating the second derivative of the energy function. This method is only possible on low resolution models as the second derivative requires storage of $\mathcal{O}(N^2)$ variables. Steepest descent methods are commonly used in micromagnetic calculations. The gradient (which is equal to the effective field, $\mathbf{H}_{eff}$) is calculated at each sub-cube and the magnetization vectors rotated by some amount in the direction of steepest descent (Schabes and Bertram 1988). This is repeated iteratively at each sub-cube until some convergence factor is reached.

In general heading downhill in the steepest direction at each iteration is inefficient and the conjugate gradient (CG) technique uses a more sophisticated method for determining the search directions. This method was implemented by Williams (1989,1993) and is likely to be important in high resolution models with a larger number of variables.

## 3.6 Review of micromagnetic results for magnetite

One-dimensional micromagnetic calculations have concentrated on Amar type models because the curling mode shown in figure 2.1c has until recently been considered inappropriate for magnetite with crystal faces. Stacey (1963) repeated the calculations of Kittel (1949) for magnetite by assuming that the width of the domain wall was negligible in comparison to the grain size. This calculation was refined by Butler and Banerjee (1975) using the Amar model. Shcherbakov (1978) and Moskowitz and Banerjee (1979) extended the Amar model by calculating the energies and equilibrium size ranges for 2D and 3D grains. Argyle and Dunlop (1984) refined these calculations by subdividing the domain wall into two equal parts. Table 3.2 summarizes predictions by these models for the size at which the 2D state becomes a lower energy state than the SD state ($d_0$). The main conclusion from the Amar models is that the size at which the 2D state becomes energetically favourable is close to the superparamagnetic threshold size ($d_s$) suggesting that only a small proportion of grains will occupy a stable SD state.

The first unconstrained micromagnetic results for magnetite were calculated

| | | |
|---|---|---|
| Butler and Banerjee (1975) | Amar model | $d_0 = 0.076\mu$m |
| Moskowitz and Banerjee (1979) | Amar model | $d_0 = 0.08\mu$m |
| Argyle and Dunlop (1984) | Amar model | $d = 0.06\mu$m |
| Moon and Merrill (1985) | $1d$ micromagnetic model | $d_0 = 0.08\mu$m |
| Heider and Williams (1988) | $1d$ micromagnetic model | $d_0 = 0.12\mu$m |
| Williams and Dunlop (1989) | $3d$ micromagnetic model | $d_0 = 0.05\mu$m |

**Table 3.2.** Summary of various calculations for $d_0$

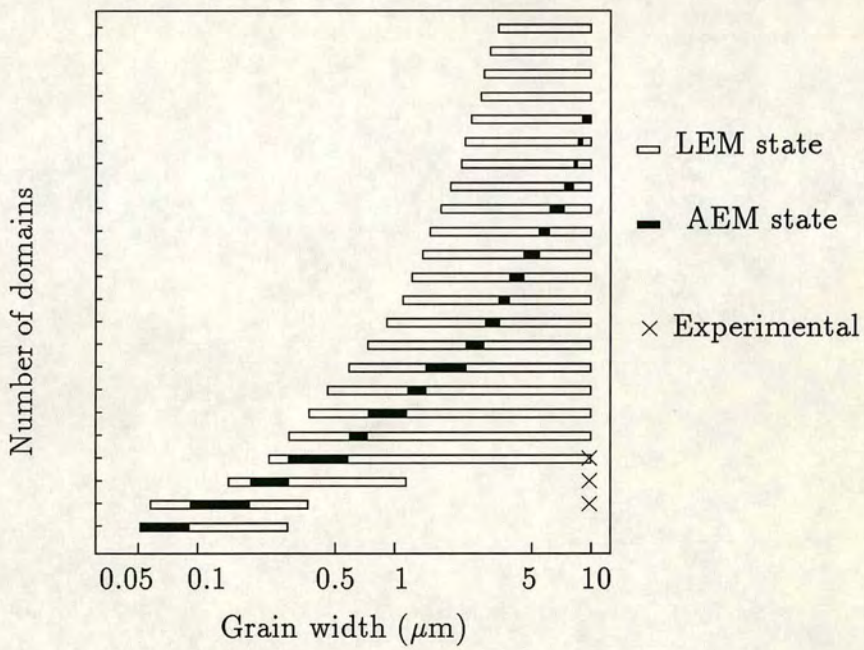


**Figure 3.3.** Theoretical stable size range for various one-dimensional unconstrained LEM states for cubic magnetite. Grains can occupy more than one equilibrium state for all grains larger than $0.06\mu$m (from Moon and Merrill 1985). The experimental results ($\times$) are domain observations from Heider (1988).

by Moon and Merrill (1984,1985) using a $1d$ micromagnetic model similar to thatused by Brown and LaBonte (1965). A steepest descent method was employed to find equilibrium states and these consisted of well defined domains and domain walls. Although domains and domain walls were not imposed as in the Amar models, the $1d$ nature meant that they were necessarily a result. An important result was that the model predicted grains could occupy an AEM state and several higher energy LEM states as shown in figure 3.3. The model contradicted experimental Bitter pattern observations as it predicted a $10\mu$m grain could occupy several LEM states, ranging from a 4 domain state to a 20 domain state, far more than the 2 or 3 domains typically observed. This discrepancy is a long standing problem which occurs in both Amar and Kittel models for magnetite and titanomagnetite (Moskowitz and Halgedahl 1987).

Enkin and Dunlop (1987) developed a more sophisticated $1d$ model by using a modified Newton minimization method to calculate equilibrium states. Figure 3.4 shows their results for the dependence of the energy with grain size for a SD state and a 2D state. The results for the 2D state were obtained by sequentially using the result from the minimization procedure at one grain size as an initial guess at a larger grain size. The critical grain size, $d_0$ is defined as the point at which the 2D state is a lower energy state than the SD state. Energy diagrams such as figure 3.4 are useful in determining which states are available at a particular grain

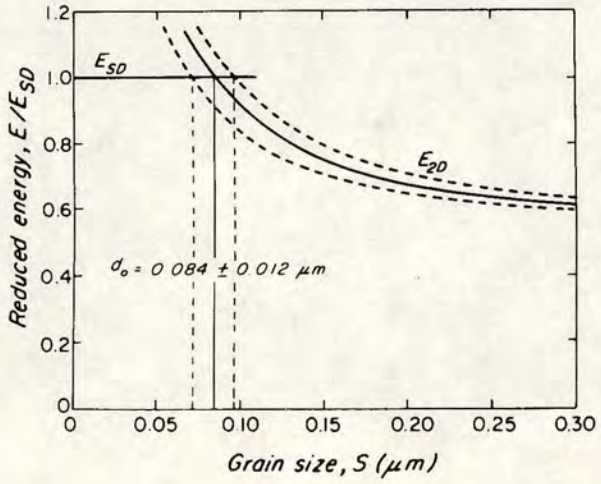


**Figure 3.4.** Energy of two-domain structures in cubes as a function of grain size using $1d$ unconstrained models (Enkin and Dunlop 1987). The solid line was produced using the best estimate of the exchange constant, the dashed lines use plus or minus the uncertainty given by Moskowitz and Banerjee (1979).

size, although for these $1d$ results the concept of a critical size relies on assuming that grains are always in their lowest energy state. The value of $d_0$ calculated by Enkin and Dunlop (1987) was determined with an erroneous factor of 0.5 in the exchange constant and, using the corrected value, Heider and Williams (1988) recalculated $d_0$ as $0.12\mu$m.

Two-dimensional models by Xu *et al* (1994) have predicted magnetization states which consist of domains and associated closure domains. Figure 3.5 shows that the equilibrium solution for a $1\mu$m grain consists of three well defined domains. Although these $2d$ models reconciled the discrepancy between the number of domains observed and calculated theoretically, $2d$ results should be regarded as provisional until confirmed by $3d$ results with a similar resolution of $50 \times 50 \times 50$.

Three-dimensional calculations using steepest descent methods (Schabes and Bertram 1988), CG methods (Williams and Dunlop 1989) and SA algorithms (Thomson 1993) have each predicted magnetization states such as those shown in figure 3.6. The state shown in figure 3.6a is essentially a SD state but with significant deflection of the magnetization at the grain's corners. This state is normally referred to as a flower state and an important factor that will be studied in this thesis is whether the deflection at the corners affects the accuracy of analytic SD theories.

Instead of a transition from a SD to a two-domain state predicted by both Amar models and $1d$ micromagnetic models, $3d$ models have predicted a transition from a flower state to the state shown in figure 3.6b. This state, referred to as a vortex state is essentially a 2 dimensional structure in which the magnetization curls round a central line which runs parallel to a grain edge. Results using the CG method have agreed with SA calculations by showing that vortex states are the lowest energy states for grains smaller than $0.5\mu$m.

Williams (1989,1990) predicted that the magnetocrystalline anisotropy does not align the magnetization along the easy $\langle 111 \rangle$ directions in grains smaller than $1\mu$m. This may either be a real effect in small grains or a limitation of $3d$ models with a low resolution. In addition the magnetic surface charges shown in figure 2.1c also arise in the vortex state shown in figure 3.6b. This also suggests that the vortex state may be constrained by the low resolution of the model.

These $3d$ models have confirmed that several stable LEM states are available to magnetite grains of a particular size and that the existence of LEM states which were predicted by $1d$ models are not artifacts of using a low dimension. The existence of LEM states are important as Enkin and Williams (1994) showed

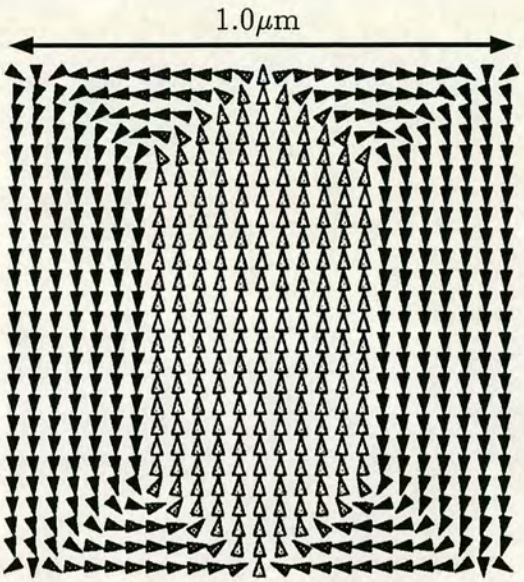


**Figure 3.5.** Magnetization state for a 1$\mu$m grain using the 2$d$ model shown in figure 3.2c. The vectors have been interpolated down from a resolution of $50 \times 50$ to $25 \times 25$ sub-cubes for clarity.

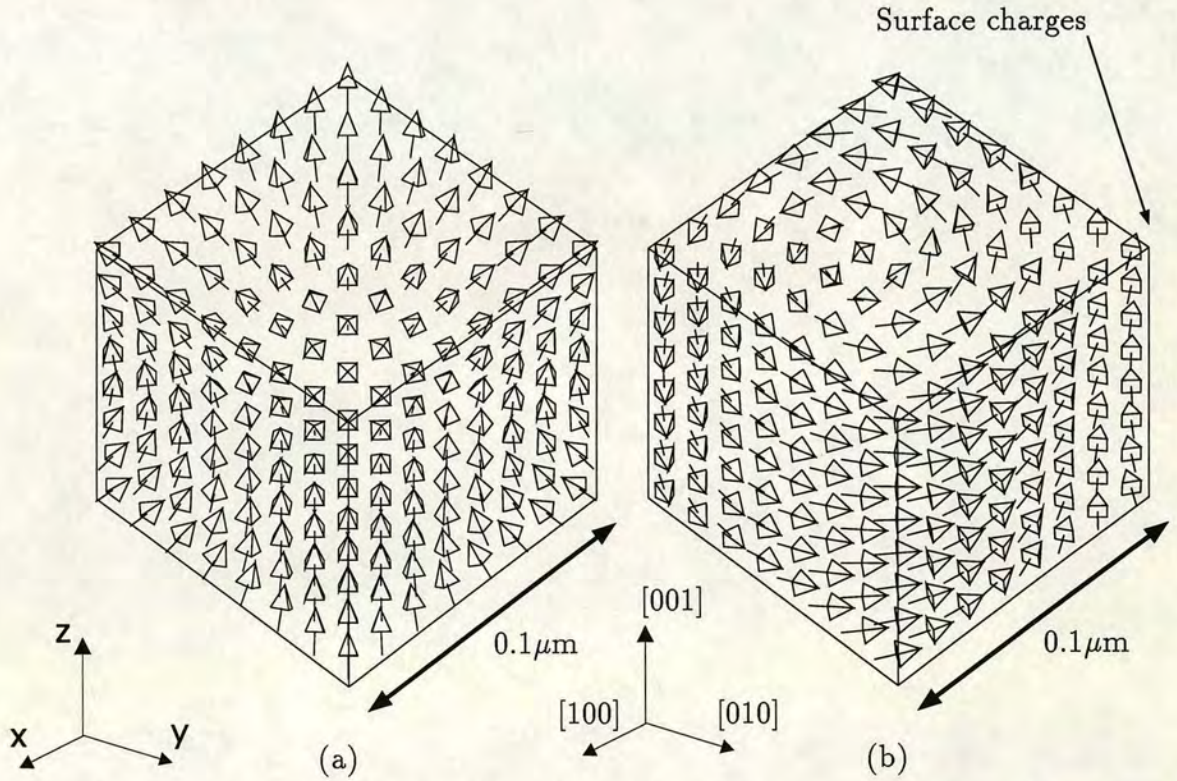


**Figure 3.6.** Magnetization states for a 3$d$ model using a resolution of $8 \times 8 \times 8$ sub-cubes, (a) flower state (b) vortex state.

that a flower state can reverse direction by forming an intermediate vortex state. Furthermore the stability of a particular LEM state, such as the flower state to perturbations by thermal fluctuations is directly related to the energy barrier between the flower state and the vortex state. If the energy barrier is greater than $61k_b$T then the LEM state will be stable over geological time scales. The calculations of energy barriers between LEM states is beyond the scope of the thesis and the stability of PSD grains will be determined qualitatively by simulating hysteresis curves.

If magnetite grains do occupy vortex states and are not an artifact of low resolution models then the transition from vortex states in small grains to the lamellar domains shown in figure 1.2 needs to be understood. One possibility is that the lamellar domains seen in Bitter patterns are only surface effects which possibly shield an interior vortex structure. Alternatively vortex states and lamellar domains may both be possible states but at larger grain sizes, vortex states become high energy states which are rarely occupied.

A guide to the resolution required to model PSD grains in the size range $0.5\mu\text{m} < d < 5\mu\text{m}$ can be obtained by considering the width of a domain wall. Domain walls have a typical width of approximately $0.1\mu$m in magnetite (Stacey and Banerjee 1974) and arbitrarily assigning a minimum of 3 spins to a wall requires a sub-cube edge length of $\Delta \simeq 0.03\mu$m. For example, to predict the domain states of a $1\mu$m grain a resolution of 30 sub-cubes to a side would be required.

## 3.7 Magnetoelastic effect

Incorporating full magnetoelastic interactions in which the magnetization interacts with the crystal lattice and vice versa is extremely difficult and models to date have either ignored this effect or approximated the interactions by a linear stress effect. A linear stress effect is just an extra phenomalogical energy term equivalent to an additional anisotropy energy $E^s$,

$$\begin{aligned} E^s &= -\frac{3}{2}\lambda_{100}\int(\alpha^2U_{11}+\beta^2U_{22}+\gamma^2U_{33})dV \\ &\quad -3\lambda_{111}\int(\alpha\beta U_{12}+\beta\gamma U_{23}+\gamma\alpha U_{31})dV \end{aligned} \tag{3.15}$$

where $U_{ij}$ are the components of the strain tensor, $\alpha$,$\beta$,$\gamma$ are the cartesian magnetization components and $\lambda_{111}$,$\lambda_{100}$ are the magnetostriction constants.

A full nonlinear stress interaction arises when the strain tensor $U_{ij}$ becomes a variable dependent on the magnetization, and which needs to be solved at each iteration of the magnetization minimization routine. This involves incorporating the purely elastic term $E^{el}$,

$$\begin{aligned} E^{el} &= \frac{1}{2}\int [C_{11}(U_{11}^2 + U_{22}^2 + U_{33}^2) + C_{44}(U_{12}^2 + U_{23}^2 + U_{13}^2) \\ &\quad + C_{44}(U_{11}U_{22} + U_{22}U_{33} + U_{11}U_{13})]dV \end{aligned} \tag{3.16}$$

where $C_{12}, C_{11}, C_{44}$ are the elastic constants and using the condition for mechanical equilibrium, and the stress tensor $s_{ij}$

$$\sum_j \frac{\partial s_{ij}}{\partial x} = 0, \quad s_{ij} = \frac{\partial E}{\partial U_{ij}}, \qquad E = E^s + E^{el} \quad . \tag{3.17}$$

Using a linear dependence for $U_{ij}$ with the displacements $u_1$,$u_2$,$u_3$,

$$U_{11} = \frac{\partial u_1}{\partial x}, \quad U_{12} = \frac{1}{2}\left(\frac{\partial u_1}{\partial y} + \frac{\partial u_2}{\partial x}\right) \tag{3.18}$$

then produces a set of $3d$ non-linear second order partial differential equations (PDEs) to be solved for $U_{ij}$. Due to their complexity, there is no computational algorithm to solve these PDEs to date and in addition Brown (1969) also reasoned that even a linear definition for $U_{ij}$ is a severe and unrealistic approximation.

Xu and Merrill (1992) took the extreme view that the coercivity of PSD grains is controlled primarily by the magnetoelastic effect and modelled the effect of a stress due to a dislocation on a domain wall using equation 3.15. In addition to the difficulty in solving the PDEs mentioned previously, the present study concentrates on developing a high resolution model which ignores magnetoelastic effects. Firstly, because early $3d$ micromagnetic models imply that these classical domain walls are unlikely to exist in palaeomagnetically important small grains ($d < 0.5\mu$m) which are dominated by vortex states. Secondly, experimental comparisons between stressed and unstressed grains have been confined to relatively large grains ($d > 3\mu$m) and thus there is no experimental evidence for magnetostrictive control in palaeomagnetically important small grains ($d < 1\mu$m). Furthermore the magnitude of $E^s$ and $E^{el}$ for a stress field near a a screw dislocation (the maximum stress field in a crystal) showed that $E^s$ and $E^{el}$ are of an order of magnitude less than $E^a$,$E^e$ or $E^d$. This suggests that stress effects are only important in relatively large (and thus palaeomagnetically less important)

grains containing clusters of dislocations. As the model used in this study ignores the magnetoelastic effect, micromagnetic calculations will be compared with the synthetically grown grains described in chapter 2 and not with crushed and sieved natural samples which may contain a high dislocation density.

## 3.8 Summary

Previous $3d$ calculations have predicted a transition from a flower state to a vortex state instead of a SD to a 2D transition predicted by $1d$ models. It is important to increase the resolution of previous models to ensure that vortex states are not a result of using a low resolution. Increasing the resolution will also enable grains larger than $0.5\mu$m to be modelled. The main features of the micromagnetic model described in this study are;

- An increase in the resolution by using a FFT algorithm to calculate the magnetostatic energy and implementing the model on the parallel Connection Machine CM-200 computer.
- The conjugate gradient technique is implemented to calculate equilibrium magnetization states.
- The model considers the exchange, magnetocrystalline, magnetostatic and external field energy terms.
- The magnetoelastic effect will be ignored due to the importance of increasing the resolution of the model and also because of the complexity of the partial differential equations.

# Chapter 4. Description of the Model

## 4.1 Introduction

This chapter describes how the energy functions are discretized and how the magnetostatic energy is calculated using the FFT algorithm. As well as modeling cubic grains the high resolution cubic system will be used as a starting point from which to 'sculpt out' grains of arbitrary shape, e.g. octahedral or irregularly shaped grains.

The algorithm was implemented on a 16000 processor TMC Connection Machine CM-200 data parallel computer which associates a few data-elements with each processor (Hillis 1985). In this study a data-element corresponds to the azimuthal and co-latitude of each elementary vector, as shown in figure 4.1b. In addition to a decrease in computation time gained by calculating the anisotropy and exchange energy in parallel there are efficient parallel FFT routines available. Using a parallel architecture enables the computation time to be reduced further, from $\mathcal{O}(N \log N)$ for a conventional serial FFT algorithm to $\mathcal{O}([N/N_p] \log N)$ on the CM-200, where $N_p$ is the number of processors available. Appendix B describes some aspects of the CM-Fortran code and compares timings and accuracy of the present model with previous models.

The geometry of the $3d$ cubic model is described first and sections 4.3 and 4.4 describes the discretization of the energy and gradient terms. Section 4.5 describes the conjugate gradient routine, Section 4.6 describes how non-cubic grains can be modelled and section 4.7 gives the material parameters for magnetite. Sections 4.8 and 4.9 describe how Bitter patterns and hysteresis curves can be modelled.

## 4.2 Geometry of model

Figure 4.1 shows the cubic system used, the edge length of the grain is denoted by $d$ and the cube subdivided into $N = n^3$ sub-cubes of edge length $\Delta$ ($\Delta = d/n$). In the centre of each sub-cube is an elementary magnetic vector $\mathbf{M}_l$ of constant magnitude $M_s$ whose direction represents the average direction of all the atomic magnetic vectors within that sub-cube. For each energy term except for the exchange energy the position of the sub-cube in the $3d$ coordinate system will be

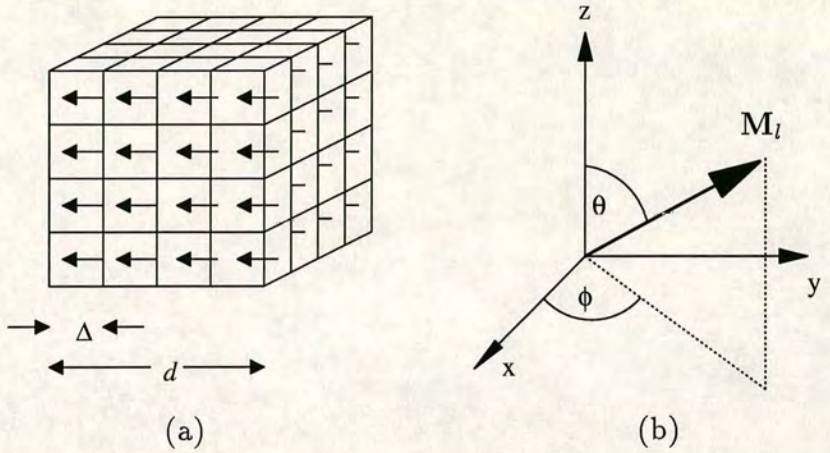


**Figure 4.1.** (a) A cubic crystal of edge length $d$ is modelled by subdividing a cube into $N = n^3$ sub-cubes each of edge length $\Delta$. In the above diagram $n = 4$. (b) Each elementary magnetization vector is defined by the azimuthal angle ($\phi$) and the co-latitudinal angle ($\theta$).

abbreviated from $ijk$ to the single subscript $l$. The direction of $\mathbf{M}_l$ varies with the azimuth ($\phi$) and the colatitude ($\theta$) and has direction cosines $(\alpha, \beta, \gamma)$ given by,

$$\mathbf{m}_l = \frac{\mathbf{M}_l}{M_s} = \begin{pmatrix} \alpha_l \\ \beta_l \\ \gamma_l \end{pmatrix} = \begin{pmatrix} \cos(\phi_l)\sin(\theta_l) \\ \sin(\phi_l)\sin(\theta_l) \\ \cos(\theta_l) \end{pmatrix} . \tag{4.1}$$

## 4.3 Discretization of energy terms

For each energy term integration over the volume of the grain is approximated by a sum over the sub-cubes in which a continuous function $f(\theta, \phi)$ is replaced by a discrete function $f_l$,

$$E = \int\int\int f(\theta, \phi) dx\, dy\, dz \approx \sum_l f_l \tau \quad , \tag{4.2}$$

where $\tau = \Delta^3$ is the volume of each sub-cube and the sum is over each of the 3 dimensions.

### Exchange energy

Using the approximation that the angle between atomic spins is small, Brown (1978) obtained the following expression for the exchange energy $E^e$,

$$E^e = \frac{C_e}{2}\int(\nabla \mathbf{m})^2 dV \approx \frac{C_e}{2}\sum_{i,j,k}(\nabla \mathbf{m}_{ijk})^2\Delta^3. \tag{4.3}$$

A first order approximation would be to assume that the magnetization varies linearly between sub-cubes. Using $\mathbf{m}\cdot\mathbf{m} = 1$,

$$(\nabla \mathbf{m}_{ijk})^2 = \frac{(\mathbf{m}_{(i+1)jk} - \mathbf{m}_{ijk})^2}{\Delta^2} = \frac{2}{\Delta^2}\left(1 - \mathbf{m}_{ijk}\cdot\mathbf{m}_{(i+1)jk}\right) \tag{4.4}$$

giving

$$E^e = \Delta C_e \sum_{i=1}^{n}\sum_{j=1}^{n}\sum_{k=1}^{n} 1 - \mathbf{m}_{ijk}\cdot\mathbf{m}_{(i+1)jk}, \tag{4.5}$$

plus similar expressions for the $j$ and $k$ directions. A more accurate approximation would be to start from equation 4.3 and use Green's formula,

$$\begin{aligned} E^e &= \frac{C_e}{2}\int(\nabla \mathbf{m})^2 dV = -\frac{C_e}{2}\int \mathbf{m}\cdot\nabla^2\mathbf{m} dV + \int \nabla\mathbf{m}\frac{\partial \nabla\mathbf{m}}{\partial n} dS \\ &\approx -\frac{C_e}{2}\Delta^3\sum_{i,j,k}\mathbf{m}_{ijk}\cdot\nabla^2\mathbf{m}_{ijk} \end{aligned} \tag{4.6}$$

A 5 point difference scheme in one dimension is given by,

$$\frac{\partial^2 f}{\partial x^2} = \frac{1}{12}\frac{-f_{i-2} + 16f_{i-1} - 30f_i + 16f_{i+1} - f_{i+2}}{\Delta^2} \quad , \tag{4.7}$$

so in three dimensions equation 4.6 becomes

$$E^e = -\frac{C_e\Delta}{2}\sum_{i=1}^{n}\sum_{j=1}^{n}\sum_{k=1}^{n}\mathbf{m}_{ijk}\cdot\nabla^2\mathbf{m}_{ijk}, \tag{4.8}$$

where $\nabla^2$ is the 5 point difference (equation 4.7) extended to three dimensions.

To ensure that the boundary condition, $\partial\mathbf{m}/\partial n = 0$ is satisfied, (in this case $n$ is the outward normal to the grain boundary) the magnetization needs to be reflected at the boundary. Figure 4.2 shows that for a $1d$ system using the five point exchange formulation the vectors need to be copied from the two sub-cubes nearest the surface. This is purely a mathematical device and does not imply that any type of periodic boundary conditions have been imposed.

The two formulations were compared using the $1d$ domain wall shown in figure 4.2. The vectors are described by the co-latitude ($\theta$) with the azimuthal angle ($\phi$) kept equal to zero. The spins on the outer edges are $\pi/2$ radians apart and the intermediate spins are described by a balance between an exchange energy term and a uniaxial anisotropy energy (Chikazumi and Charap 1964),

$$\theta = 2\tan^{-1}(10^x) \tag{4.9}$$

Figure 4.3a shows the dependence of $\theta$ with $x$ and figure 4.3b shows how the exchange energy depends on the resolution. Both formulations converge to the same value and the 5 point formulation converges at a lower resolution and is thus more accurate.

Figure 4.4 shows how the exchange energy depends on the angle between two spins (i.e. figure 4.2 with a resolution of $n = 2$), the spin at $x = 0$ is kept fixed and the neighbouring spin varied from $\theta = 0°$ to $\theta = 360°$. The five point formulation results in higher values of $E^e$ for all angles of $\theta$. Although the same value of the exchange constant was used for both formulations, the 5 point formulation effectively produces a stiffer exchange interaction between the spins. This means that the 5 point formulation is less likely to to produce magnetization states in which neighbouring spins have large angles between them. One aim of this study is to determine whether the more accurate 5 point formulation affects the vortex states in any way. For example, at the centre of a vortex, neighbouring spins are separated by large angles and a stiffer exchange may penalize this.

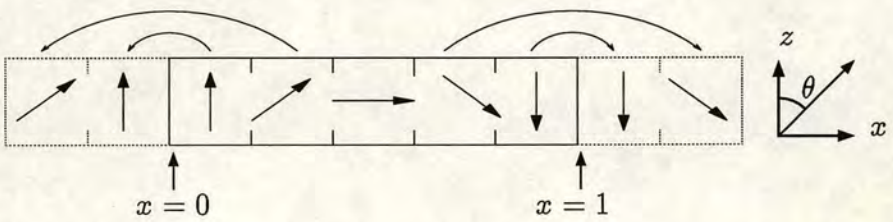


**Figure 4.2.** A one-dimensional system with $n = 5$ showing how the boundary conditions are satisfied for the five point exchange formulation. A similar scheme is used for the linear exchange formulation but only the sub-cube nearest the boundary is reflected.

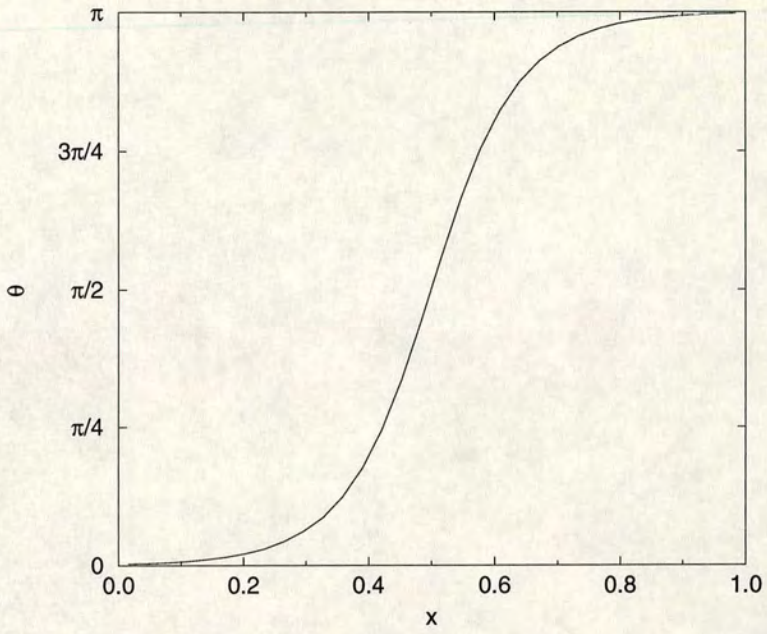


(a) Variation of $\theta$ with $x$

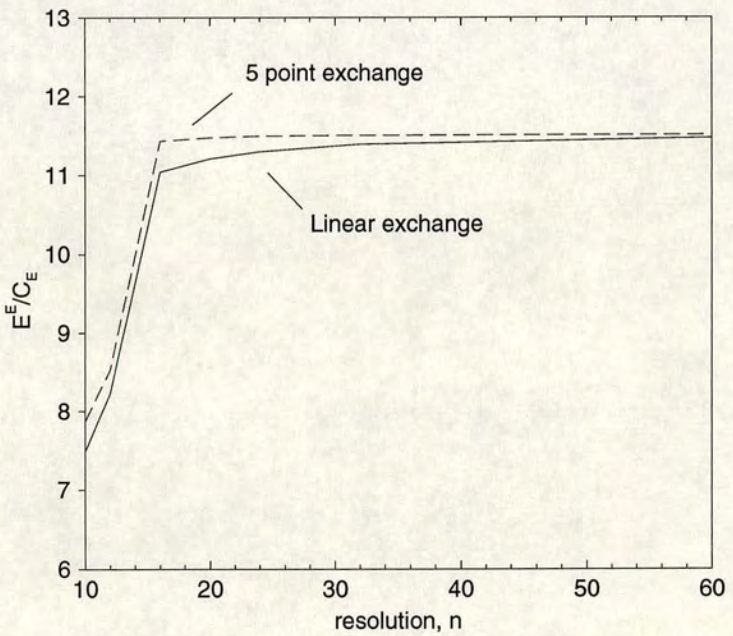


(b)

**Figure 4.3.** (a) Variation of the test function through the grain and (b) the dependence of the exchange energy with resolution $n$, ' ——— ' linear formulation, '- - - -' 5 point formulation.

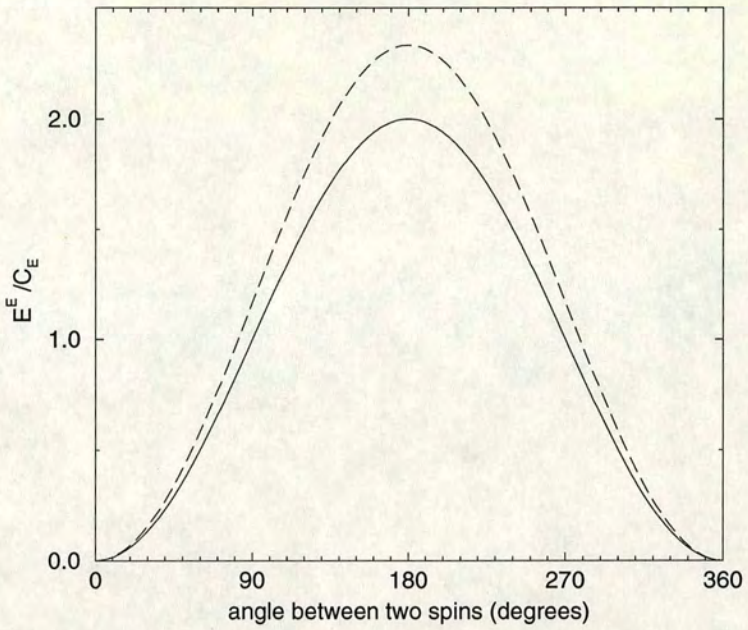


(a)

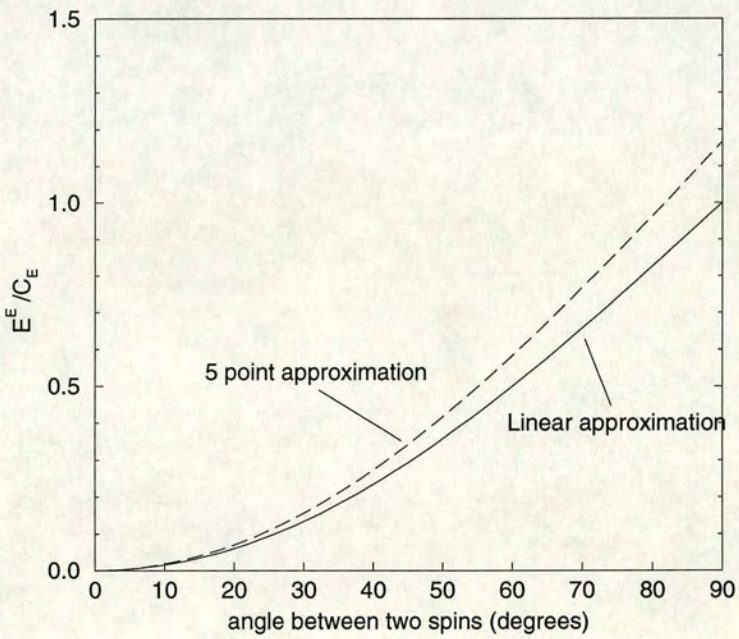


(b)

**Figure 4.4.** Dependence of the exchange energy $E^e$ on the angle $\theta$ between two spins, figure (b) is a magnified section of (a); ' ——— ' linear formulation, '- - - -' 5 point formulation.

### Anisotropy energy

The cubic anisotropy is approximated by using the first anisotropy constant, $K_1$ and is a local term independent of the resolution. Equation 3.3 can be transformed to give,

$$E^a = \frac{K_1}{2} \sum_l (1 - (\mathbf{m}_l)^4) \Delta^3 \quad . \tag{4.10}$$

For magnetite and nickel $K_1$ is negative, resulting in the energy contour shown in figure 4.5. The easy $\langle 111 \rangle$ and intermediate $\langle 110 \rangle$ directions are low energy directions whereas the hard $\langle 100 \rangle$ directions are high energy directions. The convention used in this study will be that $E^a = 0$ for a SD state aligned along one of the $\langle 100 \rangle$ hard directions and $E^a < 0$ for a SD state aligned in one of the $\langle 111 \rangle$ or $\langle 110 \rangle$ easy directions.

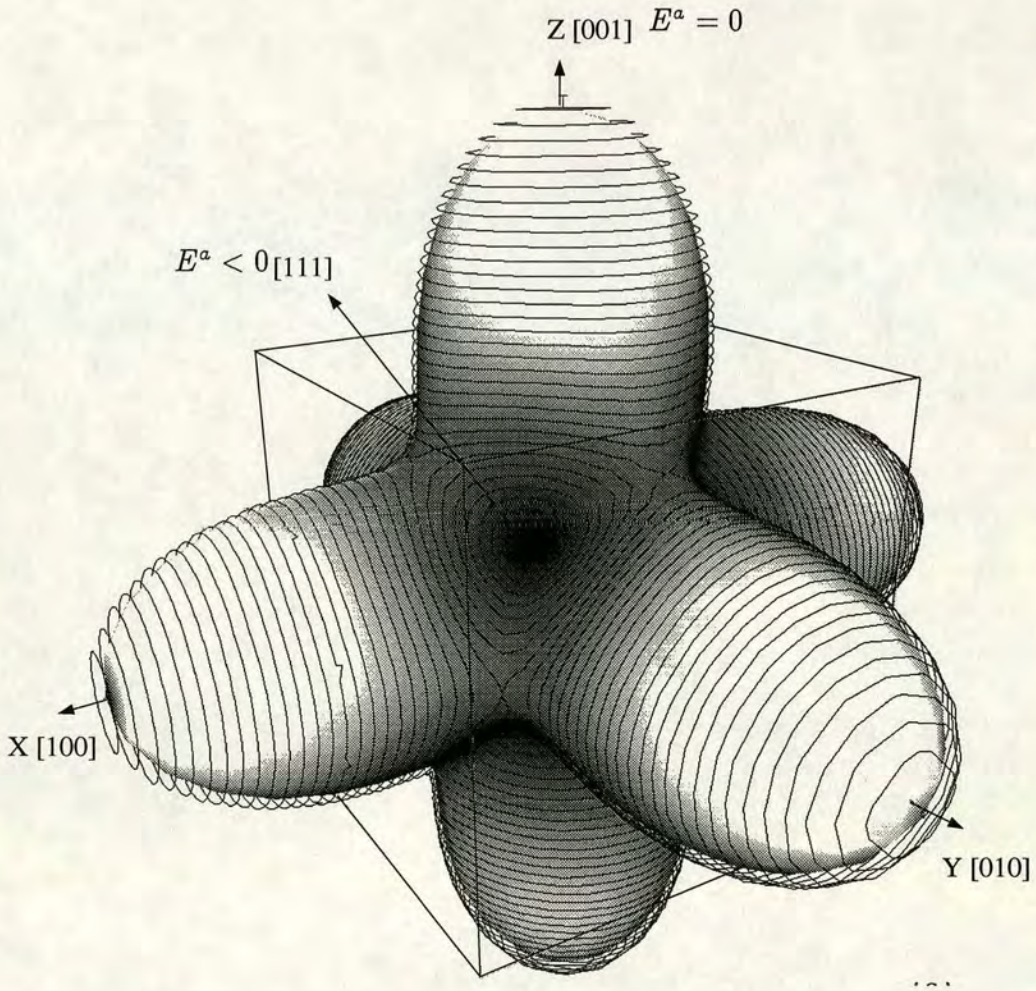


**Figure 4.5.** Three-dimensional contour plot of the magnetocrystalline energy for magnetite. The light and dark regions represent low and high values of $E^a$ respectively. The hard $\langle 100 \rangle$ axes are high energy regions and the easy $\langle 110 \rangle$ and $\langle 111 \rangle$ are low energy regions (Williams and Dunlop 1995).

### External field energy

Applying an external field $\mathbf{H}$ to the model with magnitude $H$ (mT) and direction $\theta_H$ and $\phi_H$ gives as an expression for $E^h$,

$$E^h = -\sum_l M_s \mathbf{H} \cdot \mathbf{m}_l \Delta^3. \tag{4.11}$$

### Magnetostatic Energy

This section describes how the FFT technique can be extended to calculate the magnetostatic energy for three-dimensional systems. Using Maxwell's equations for the field, $\mathbf{H}'$ due to all the elementary magnetic vectors,

$$\nabla \times \mathbf{H}' = \frac{4\pi}{c}\mathbf{J} \quad , \tag{4.12}$$

and assuming that the current density, $\mathbf{J}$ equals zero we can define a scalar potential $\Phi$ such that $\mathbf{H}' = -\nabla\Phi$. For a ferromagnet with volume $V_2$ and surface $S_2$, the potential at a point $\mathbf{r}_1$ due to a magnetostatic charge at $\mathbf{r}_2$ can be calculated from Green's function (Jackson 1975),

$$\Phi(\mathbf{r}_1) = -\frac{1}{4\pi}\int_V \frac{\nabla \cdot \mathbf{M}(\mathbf{r}_2)}{|\mathbf{r}_1 - \mathbf{r}_2|} dV_2 + \frac{1}{4\pi}\oint_S \frac{\mathbf{M}(\mathbf{r}_2) \cdot \mathbf{n}_2}{|\mathbf{r}_1 - \mathbf{r}_2|} dS_2 \quad , \tag{4.13}$$

The model described in this study assumes that the magnetization within each sub-cube is of constant direction and magnitude ($\nabla \cdot \mathbf{M} = 0$). Equation 4.13 then reduces to solely the second term and the calculation becomes a sum over charged plates. Two methods for splitting a cubic system into charged plates have previously been used: (a) Berkov *et al* (1993) used an algorithm in which the the fundamental unit is a charged plate and the calculation is a sum over each charged plate; (b) Williams and Dunlop (1989) considered the fundamental unit to be a pair of charged plates and the calculation is a sum over each sub-cube. I implemented both schemes using a conventional $N^2$ serial algorithm and found them to be identical in terms of the accuracy and number of calculations required (the difference in $E^d$ between the two schemes was less than $10^{-7}\%$). The second method in which the sub-cube is the fundamental unit was used as the FFT algorithm is easier to implement, this is described in appendix D. Furthermore, using the sub-cube as the fundamental unit means that it is easy to modify the distance between each sub-cube from zero to some arbitrary distance. This would be useful for future projects in which each sub-cube represents a complete

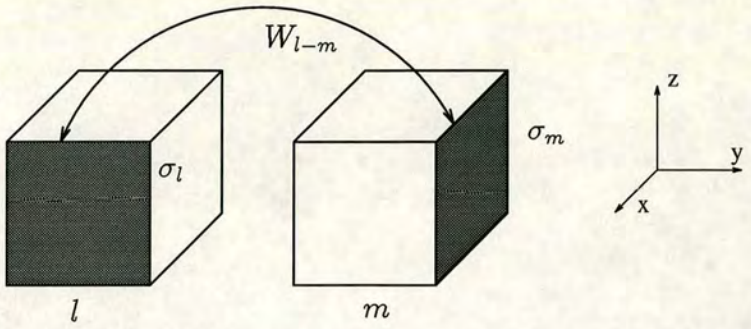


**Figure 4.6.** Magnetostatic interaction between two orthogonal plates.

SD grain and the interactions between SD grains either as in thin films or a $3d$ assemblage could be studied.

Using the divergence theorem, $\int_V \nabla \cdot \mathbf{F} dV = \int_S \mathbf{F} \cdot \mathbf{n} dS$ and denoting $\sigma_l$ as the charge density on plate $l$, $\sigma = \mathbf{m} \cdot \mathbf{n}$, $\sigma \in \{\alpha,\beta,\gamma\}$, the energy per unit volume between the two plates shown in figure 4.6 becomes,

$$\begin{aligned} E^d_{lm} &= -\mu_0 \int \mathbf{M}(\mathbf{r}_l) \cdot \mathbf{H}' dV = \mu_0 \int \mathbf{M}(\mathbf{r}_l) \cdot \nabla \Phi dV \\ &= \mu_0 \int \left[\nabla \cdot (\Phi \mathbf{M}(\mathbf{r}_l)) - \Phi \nabla \cdot \mathbf{M}(\mathbf{r}_l)\right] dV = \mu_0 M_s \int_{S_l} \sigma_l \Phi dS_l \quad .(4.14) \end{aligned}$$

The potential, $\Phi$ at $l$ due to the plate at position $m$ is given by the first term in equation 4.13 so $E^d_{lm}$ becomes,

$$E^d_{lm} = \frac{\mu_0 M_s^2}{4\pi} \int_{S_l} \int_{S_m} \frac{\sigma_l \sigma_m}{|\mathbf{r}_l - \mathbf{r}_m|} dS_l dS_m = \frac{\mu_0 M_s^2}{4\pi} W_{l-m} \sigma_m \sigma_l \qquad (4.15)$$

where $W_{l-m}$ is a coefficient with dimension $\Delta^3$ and is calculated using the method of Rhodes and Rowland (1954). For example, for the two orthogonal plates shown in figure 4.6, with $(y_l, z_l)$ and $(x_m, z_m)$ the set of points inside the charged plates $\sigma_l$ and $\sigma_m$ respectively, then $W_{l-m}$ is given by,

$$W_{l-m} = \int_0^\Delta \int_0^\Delta \int_0^\Delta \int_0^\Delta \frac{1}{r} dy_l dz_l dx_m dz_m \quad , \qquad (4.16)$$

where $r$ is the distance between $(y_l, z_l)$ and $(x_m, z_m)$. Appendix C describes the evaluation of the integral in equation 4.16.

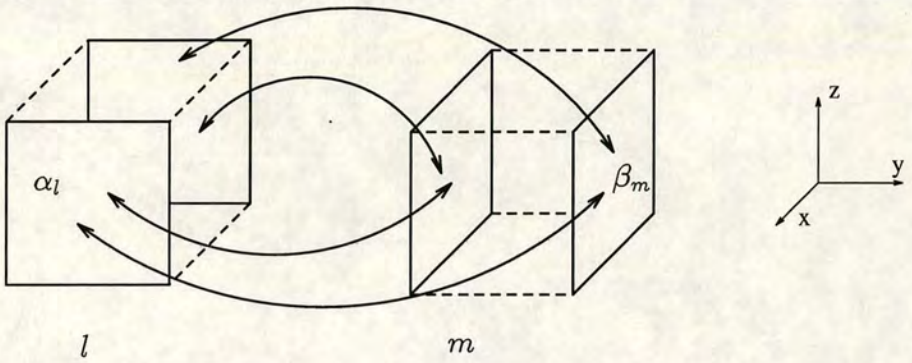


**Figure 4.7.** The four interactions required for each configuration of charged plates. $W^{\alpha\beta}$ is the sum of each of the four interactions shown.

Figure 4.7 shows the 4 interactions which make up $W^{\alpha\beta}$. The energy between the $\alpha$ plates at cube $l$ and the $\beta$ plates at cube $m$ for the whole system is given by,

$$E^d = \frac{\mu_0 M_s^2}{8\pi} \sum_l \sum_m W_{l-m}^{\alpha\beta} \alpha_l \beta_m \quad . \tag{4.17}$$

All summations are assumed to be from 1 to $n$ in each of the 3 dimensions. A factor of a half has been introduced in order to cancel the effect of counting combinations of plates twice during the full double summation. In addition, the reverse situation to that shown in figure 4.7 has to be considered, i.e. the interaction between the $\beta$ plates at cube $l$ and the $\alpha$ plates at cube $m$,

$$E_{\alpha\beta}^d = \frac{\mu_0 M_s^2}{8\pi} \sum_l \sum_m W_{l-m}^{\alpha\beta} \alpha_l \beta_m + W_{l-m}^{\beta\alpha} \beta_l \alpha_m \quad . \tag{4.18}$$

There is an also an additional constant value for each sub-cube given by $(2/3)\pi\mu_0 M_s^2 \Delta^3$ (Rhodes and Rowland 1954). The full magnetostatic energy is given by the following expression,

$$E^d = \frac{\Delta^3}{8\pi} \mu_0 M_S^2 \sum_l \sum_m (\mathbf{m}_m \mathbf{W}) \cdot \mathbf{m}_l \tag{4.19}$$

where the demagnetizing tensor is defined as,

$$\mathbf{W} = \begin{bmatrix} W^{\alpha\alpha} & W^{\alpha\beta} & W^{\alpha\gamma} \\ W^{\beta\alpha} & W^{\beta\beta} & W^{\beta\gamma} \\ W^{\gamma\alpha} & W^{\gamma\beta} & W^{\gamma\gamma} \end{bmatrix} \qquad \begin{aligned} W^{\beta\alpha} &= W^{\alpha\beta} \\ W^{\gamma\alpha} &= W^{\alpha\gamma} \\ W^{\gamma\beta} &= W^{\beta\gamma} \end{aligned} \quad . \tag{4.20}$$

### Fast Fourier transform method

Equation 4.17 requires $O(N^2)$ calculations but by rewriting in terms of a convolution, and calculating in frequency space the number of calculations can be reduced to $O(N \log N)$. The energy between the surface charges $\sigma_l$ and $\sigma_m$ is given by,

$$E^d = \frac{\mu_0}{8\pi} \sum_l \sum_m W_{l-m} \sigma_l \sigma_m \tag{4.21}$$

For clarityi the superscript $\alpha\beta$ has been omitted from $W$. Using the standard equation for a convolution,

$$(W * \sigma)_l = \sum_m W_{l-m} \sigma_m \quad , \tag{4.22}$$

equation 4.17 can be written as

$$E^d = \frac{\mu_0}{8\pi} \sum_l \sigma_l (W * \sigma)_l \quad . \tag{4.23}$$

The first and obvious method to calculate the above convolution would be to use the convolution theorem,

$$(W * \sigma)_l = \mathcal{F}^{-1} \left( \tilde{W}_k \tilde{\sigma}_k \right), \tag{4.24}$$

where $\tilde{W}_k$ and $\tilde{\sigma}_k$ are the $3d$ Fourier transforms* of $W$ and $\sigma$. $E^d$ can then be obtained by multiplying the result from $\mathcal{F}^{-1} \left( \tilde{W}_k \tilde{\sigma}_k \right)$ by $\sigma_l$ in real space as in equation 4.23. But the inverse FFT can be eliminated by multiplying all three arrays in frequency space (see appendix D for a complete derivation),

$$E^d = \frac{\mu_0}{8\pi N} \sum_k \tilde{\sigma}_k \tilde{\sigma}_{-k} \tilde{W}_k \quad , \tag{4.25}$$

where $\tilde{\sigma}_{-k}$ represents the complex conjugate of $\tilde{\sigma}_k$. The expression for the complete magnetostatic energy calculated in frequency space is given by,

$$E^d = \frac{\mu_0 \Delta^3 M_s^2}{4\pi N} \sum_k (\tilde{\mathbf{m}}_k \tilde{\mathbf{W}}_k) \cdot \tilde{\mathbf{m}}_{-k} \quad , \tag{4.26}$$

*$k$ now denotes the position in $3d$ frequency space as opposed to the third dimension in normal space.

where $\tilde{\mathbf{W}}_k$ is the tensor,

$$\tilde{\mathbf{W}}_k = \begin{bmatrix} \frac{1}{2}\tilde{W}^{\alpha\alpha} & \frac{1}{2}\tilde{W}^{\alpha\beta} & \frac{1}{2}\tilde{W}^{\alpha\gamma} \\ \frac{1}{2}\tilde{W}^{\beta\alpha} & \frac{1}{2}\tilde{W}^{\beta\beta} & \frac{1}{2}\tilde{W}^{\beta\gamma} \\ \frac{1}{2}\tilde{W}^{\alpha\gamma} & \frac{1}{2}\tilde{W}^{\gamma\beta} & \frac{1}{2}\tilde{W}^{\gamma\gamma} \end{bmatrix} \quad . \tag{4.27}$$

As $W^{\alpha\beta} = W^{\beta\alpha}$ and $\tilde{W}$ is real, the number of calculations can be reduced by writing

$$\frac{1}{2}\sum_k \tilde{\alpha}_k\tilde{\beta}_{-k}\tilde{W}^{\alpha\beta} + \frac{1}{2}\sum_k \tilde{\beta}_k\tilde{\alpha}_{-k}\tilde{W}^{\beta\alpha} = \sum_k \tilde{\alpha}_k\tilde{\beta}_{-k}\tilde{W}^{\alpha\beta} \quad , \tag{4.28}$$

and the modified tensor $\mathbf{W}_k$ now becomes,

$$\tilde{\mathbf{W}}_k = \begin{bmatrix} \frac{1}{2}\tilde{W}^{\alpha\alpha} & \tilde{W}^{\alpha\beta} & \tilde{W}^{\alpha\gamma} \\ 0 & \frac{1}{2}\tilde{W}^{\beta\beta} & \tilde{W}^{\beta\gamma} \\ 0 & 0 & \frac{1}{2}\tilde{W}^{\gamma\gamma} \end{bmatrix} \quad . \tag{4.29}$$

### Implementing non-periodic Boundaries

The convolution theorem assumes that the surface charges ($\sigma$) are periodic in each of the 3 directions whereas real magnetite grains have a finite size with non-magnetic or free-air boundaries. Figure 4.8 shows how the interaction array ($W$) and the charges ($\sigma$) have to be arranged for a 1 dimensional system with $N = 8$ in order to satisfy non-periodic boundary conditions. For both $W$ and $\sigma$, arrays have to be allocated so that the dimension of the array in each direction is twice as large as the resolution of the model. For example, a $3d$ model with a resolution of $32 \times 32 \times 32$ sub-cubes requires arrays of size $64 \times 64 \times 64$ to be allocated. The additional values of the charges $\sigma$ are set to zero in order to model free air boundary conditions (Press *et al* 1986). The additional values of the array $W$ between $i = -1$ and $i = -N$ represent the interactions when the sub-cube $m$, (shown in figure 4.7) is to the left of sub-cube $l$. A similar method is implemented in the two other dimensions for the $3d$ model.

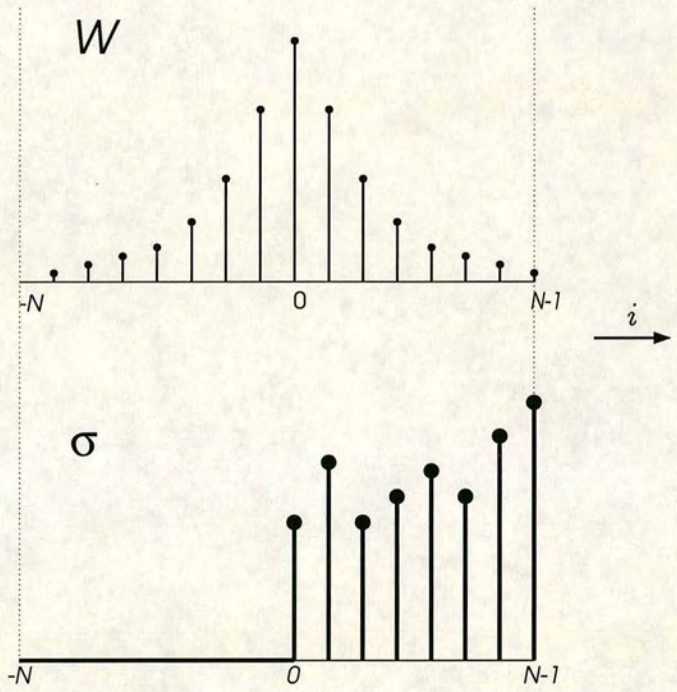


**Figure 4.8.** Arrangement of the interaction coefficients ($W$) and the array of charges ($\sigma$) for a one-dimensional model with $N = 8$. In this example $W$ is an even function, $W$ at $i = 0$ represents the self-energy of the sub-cube, $W$ at $i = -N$ is equal to zero.

## 4.4 Discretization of gradient terms

As the Cartesian direction cosines $\alpha$, $\beta$ and $\gamma$ have been calculated, it would be useful to use them in order to calculate the gradient. However, differentiating along the Cartesian basis vectors directly would make the problem a constrained one (it would be necessary to ensure $\mathbf{m} \cdot \mathbf{m} = 1$ at each iteration). As such it is preferable to use the chain rule to calculate the gradients along the polar basis vectors,

$$\frac{\partial E}{\partial \theta_l} = \frac{\partial E}{\partial \mathbf{m}_l} \cdot \frac{\partial \mathbf{m}_l}{\partial \theta_l} \qquad \frac{\partial E}{\partial \phi_l} = \frac{\partial E}{\partial \mathbf{m}_l} \cdot \frac{\partial \mathbf{m}_l}{\partial \phi_l} \quad . \tag{4.30}$$

### Anisotropy and external field gradients

The anisotropy and external field gradients are local terms given by,

$$\frac{\partial E^a}{\partial \theta_l} = -2K_1\Delta^3 \frac{\partial \mathbf{m}_l}{\partial \theta_l} \cdot (\mathbf{m}_l)^3 \qquad \frac{\partial E^h}{\partial \theta_l} = -\Delta^3 M_s \frac{\partial \mathbf{m}_l}{\partial \theta_l} \cdot \mathbf{H} \tag{4.31}$$

### Exchange gradients

Considering the linear exchange formulation, the gradient at a sub-cube $l$ is given by,

$$\frac{\partial E^e}{\partial \mathbf{m}_l} = -C_e\Delta \sum_i \left( \frac{\partial \mathbf{m}_i}{\partial \mathbf{m}_l} \cdot \mathbf{m}_{i+1} + \frac{\partial \mathbf{m}_{i+1}}{\partial \mathbf{m}_l} \cdot \mathbf{m}_i \right) \tag{4.32}$$

and as $\mathbf{m}_i$ is solely a function of $\theta_i$ and $\phi_i$ (equation 4.1),

$$\frac{\partial \mathbf{m}_i}{\partial \mathbf{m}_l} = \begin{cases} 1 & i = l \\ 0 & i \neq l \end{cases} \qquad \frac{\partial \mathbf{m}_{i+1}}{\partial \mathbf{m}_l} = \begin{cases} 1 & i+1 = l \\ 0 & i+1 \neq l \end{cases} \quad . \tag{4.33}$$

Eliminating $i$ by substituting $i = l$ for the first term in equation 4.32 and $i+1 = l$ for the second term gives,

$$\frac{\partial E^e}{\partial \theta_l} = -C_e\Delta \frac{\partial \mathbf{m}_l}{\partial \theta_l} \cdot (\mathbf{m}_{l+1} + \mathbf{m}_{l-1}) \tag{4.34}$$

and a similar expression for $\partial E^e / \partial \phi_l$.

Using equation 4.8 the gradient for the for the 5 point formulation is

$$\frac{\partial E^e}{\partial \mathbf{m}_l} = -\Delta \frac{C_e}{2} \sum_i \left( \frac{\partial \mathbf{m}_i}{\partial \mathbf{m}_l} \cdot \nabla^2 \mathbf{m}_i + \mathbf{m}_i \cdot \frac{\partial (\nabla^2 \mathbf{m}_i)}{\partial \mathbf{m}_l} \right) \tag{4.35}$$

$$\nabla^2 \mathbf{m}_i = \frac{-\mathbf{m}_{i-2} + 16\mathbf{m}_{i-1} + 30\mathbf{m}_i + 16\mathbf{m}_{i+1} - \mathbf{m}_{i+2}}{12} \tag{4.36}$$

$$\frac{\partial(\nabla^2 \mathbf{m}_i)}{\partial \mathbf{m}_l} = \frac{1}{12} \times \begin{cases} 30 & i = l \\ 16 & i+1 = l \\ 16 & i-1 = l \\ -1 & i+2 = l \\ -1 & i-2 = l \\ 0 & \text{otherwise} \end{cases} \tag{4.37}$$

so

$$\mathbf{m}_i \cdot \frac{\partial(\nabla^2 \mathbf{m}_i)}{\partial \mathbf{m}_l} = \frac{-\mathbf{m}_{l+2} + 16\mathbf{m}_{l+1} + 30\mathbf{m}_l + 16\mathbf{m}_{l-1} - \mathbf{m}_{l-2}}{12} = \nabla^2 \mathbf{m}_l \tag{4.38}$$

The first term in equation 4.35 reduces to $\nabla^2 \mathbf{m}_l$ and as the 5 point difference formula is symmetric, the second term also reduces to $\nabla^2 \mathbf{m}_l$, giving

$$\frac{\partial E^e}{\partial \theta_l} = -\Delta C_e \frac{\partial \mathbf{m}_l}{\partial \theta_l} \cdot \left(\nabla^2 \mathbf{m}_l\right) \quad , \tag{4.39}$$

and similarly for $\partial E^e / \partial \phi_l$.

### Magnetostatic gradients

Starting from equation 4.18 and considering just the interaction between the $\alpha$ and $\beta$ plates, the energy between the sub-cube at $l$ and all the other sub-cubes is,

$$E_l^d = \sum_m W_{l-m}^{\alpha\beta} \alpha_l \beta_m + \sum_m W_{l-m}^{\beta\alpha} \alpha_m \beta_l \tag{4.40}$$

$$\begin{aligned} \frac{\partial E_l^d}{\partial \theta_l} &= \sum_i \sum_m W_{l-m}^{\alpha\beta} \left( \frac{\partial \alpha_l}{\partial \theta_i} \frac{\partial \theta_i}{\partial \theta_l} \beta_m + \frac{\partial \beta_m}{\partial \theta_i} \frac{\partial \theta_i}{\partial \theta_l} \alpha_l \right) \\ &\quad + \sum_i \sum_m W_{l-m}^{\beta\alpha} \left( \frac{\partial \alpha_m}{\partial \theta_i} \frac{\partial \theta_i}{\partial \theta_l} \beta_l + \frac{\partial \beta_l}{\partial \theta_i} \frac{\partial \theta_i}{\partial \theta_l} \alpha_m \right) \end{aligned} \tag{4.41}$$

The condition for $i$ is simply,

$$\frac{\partial \theta_i}{\partial \theta_l} = \begin{cases} 1 & i = l \\ 0 & i \neq l \end{cases} \quad , \tag{4.42}$$

giving

$$\frac{\partial E_l^d}{\partial \theta_l} = \sum_m W_{l-m}^{\alpha\beta}\left(\frac{\partial \alpha_l}{\partial \theta_l}\beta_m + \frac{\partial \beta_m}{\partial \theta_l}\alpha_l\right) + \sum_m W_{l-m}^{\beta\alpha}\left(\frac{\partial \alpha_m}{\partial \theta_l}\beta_l + \frac{\partial \beta_l}{\partial \theta_l}\alpha_m\right) \tag{4.43}$$

and as $W^{\alpha\beta} = W^{\beta\alpha}$ and $\partial\beta_m/\partial\theta_l = \partial\alpha_m/\partial\theta_l = 0$,

$$\frac{\partial E_l^d}{\partial \theta_l} = \sum_m W_{l-m}^{\alpha\beta}\left(\alpha_l'\beta_m + \beta_l'\alpha_m\right), \tag{4.44}$$

where $\alpha'$ denotes the derivative $\partial\alpha_m/\partial\theta_l$.

The rest of this section will describe how the FFT technique can be applied to calculate the magnetostatic gradient using the minimum number of FFT calculations. The first term in equation 4.44 can be written as a convolution,

$$\alpha_l'\left(\sum_m W_{l-m}^{\alpha\beta}\beta_m\right) = \alpha_l'\left(W^{\alpha\beta} * \beta\right)_l = \alpha_l'\mathcal{F}^{-1}\left(\tilde{W}_k^{\alpha\beta}\tilde{\beta}_k\right)_l \quad . \tag{4.45}$$

and similarly for the second term,

$$\beta_l'\left(\sum_m W_{l-m}^{\alpha\beta}\alpha_m\right) = \beta_l'\left(W^{\alpha\beta} * \alpha\right)_l = \beta_l'\mathcal{F}^{-1}\left(\tilde{W}_k^{\alpha\beta}\tilde{\alpha}_k\right)_l \tag{4.46}$$

In order to calculate the gradients for each combination of plates it is necessary to use the property that Fourier transforms are linear,

$$\frac{\partial E_l^d}{\partial \theta_l} = \alpha_l'\mathcal{F}^{-1}(\xi_1) + \beta_l'\mathcal{F}^{-1}(\xi_2) + \gamma_l'\mathcal{F}^{-1}(\xi_3) \quad , \tag{4.47}$$

where the dummy variables $\xi_1$, $\xi_2$ and $\xi_3$ are given by,

$$\begin{aligned} \xi_1 &= \tilde{W}^{\alpha\beta}\tilde{\beta} + \tilde{W}^{\alpha\gamma}\tilde{\gamma} + \tilde{W}^{\alpha\alpha}\tilde{\alpha} \qquad \xi_2 = \tilde{W}^{\alpha\beta}\tilde{\alpha} + \tilde{W}^{\beta\gamma}\tilde{\gamma} + \tilde{W}^{\beta\beta}\tilde{\beta} \\ \xi_3 &= \tilde{W}^{\alpha\gamma}\tilde{\alpha} + \tilde{W}^{\beta\gamma}\tilde{\beta} + \tilde{W}^{\gamma\gamma}\tilde{\gamma} \quad . \end{aligned} \tag{4.48}$$

But as $\tilde{W}$ is real the number of inverse FFT routines required can be reduced from three to two by calculating $\mathcal{F}^{-1}[\xi_1 + i\xi_2]$,

$$\mathcal{F}^{-1}(\xi_1) = \Re(\mathcal{F}^{-1}[\xi_1 + i\xi_2]) \qquad \mathcal{F}^{-1}(\xi_2) = \Im(\mathcal{F}^{-1}[\xi_1 + i\xi_2]) \quad , \tag{4.49}$$

where $\Re$ and $\Im$ represent the real and imaginary components of a complex number. Thus to calculate the full gradient, three FFT calculations for $\alpha$,$\beta$ and $\gamma$ are required and two inverse transforms, $\mathcal{F}^{-1}[\xi_1 + i\xi_2]$ and $\mathcal{F}^{-1}(\xi_3)$.

### Test of the gradients

It is important to check that the gradients are calculated correctly. At each sub-cube the gradient was calculated using the expressions described in section 4.4. The gradient was also calculated numerically using

$$g_{numeric} = [E(\theta + \delta\theta, \phi) - E(\theta, \phi)]/\delta\theta] \tag{4.50}$$

where $\delta\theta$ is a small angle. Table 4.1 shows the largest difference between gradients calculated using the above formulations ($g_{analytic}$) and those calculated numerically ($g_{numeric}$). All the gradients are of the same order of magnitude as $\delta\theta$. Each difference has been normalized by the analytic value, i.e.$(g_{analytic} - g_{numeric})/g_{analytic})$.

| $E^h$ | $E^a$ | $E^e$ (linear approx.) | $E^e$ (5 point) | $E^d$ (FFT) |
|---|---|---|---|---|
| $6.246 \times 10^{-3}$ | $6.069 \times 10^{-2}$ | $1.8825 \times 10^{-2}$ | $5.948 \times 10^{-2}$ | $6.721 \times 10^{-3}$ |

**Table 4.1.** List of the maximum error in the gradient for each energy term. The magnetization state is a a vortex state of resolution $n = 4$. $\delta\theta = 0.01$radians.

## 4.5 Conjugate gradient method of minimization

For a full introduction to the conjugate gradient technique, see Press *et al* (1986); the basic routine will be described first and then the more sophisticated implementation used in this study. Let $\mathbf{x}$ be a vector of variables, in our case $\mathbf{x} = (\phi_1, \theta_1, \ldots, \phi_{N/2}, \theta_{N/2})$. Solely for this section $N$ will be redefined from the number of sub-cubes to the number of variables, so that $N = 2n^3$. $f(\mathbf{x})$ is the function to be minimized, $(f(\mathbf{x}) = E^{total} = E^e + E^d + E^a + E^h)$, and $\mathbf{g}(\mathbf{x})$ is the analytic gradient vector,

$$\mathbf{g}(\mathbf{x}) = \nabla f(\mathbf{x}) = \frac{\partial f}{\partial u_{\phi_1}} + \frac{\partial f}{\partial u_{\theta_1}} + \ldots + \frac{\partial f}{\partial u_{\phi_N/2}} + \frac{\partial f}{\partial u_{\theta_N/2}} \quad , \tag{4.51}$$

where the basis vectors $\mathbf{u}$ are defined by the set $\mathbf{u} = (u_{\phi_1}, u_{\theta_1}, \ldots, u_{\phi_{N/2}}, u_{\theta_{N/2}})$. The conjugate gradient method uses an iterative procedure to find a sequence $\mathbf{x}_i, \mathbf{x}_{i+1}, \ldots \mathbf{x}_{min}$, by minimizing along successive directions $\mathbf{d}_i$,$\mathbf{d}_{i+1}$,... using the vector $\mathbf{g}_i = \mathbf{g}(\mathbf{x}_i)$. The goal is to find a set of directions $\mathbf{d}_i$ that will reach a minimum in as few steps as possible. It is easy to see that apart from trivial quadratic functions, minimizing along either the basis vectors or along successive

steepest descent directions is inefficient. For any general function we want to minimize along a line such that we do not spoil the minimization along previous line searches. To find the conditions for a set of these directions $f(\mathbf{x})$ can be approximated by a Taylor series expansion.

$$\begin{aligned} f(\mathbf{x}) &= f(\mathbf{x}) + \sum_i \frac{\partial f}{\partial x_i} + \frac{1}{2}\sum_{ij} \frac{\partial^2 f}{\partial x_i \partial x_j} x_i x_j + \dots \\ &\approx c - \mathbf{b}\cdot\mathbf{x} + \frac{1}{2}\mathbf{x}\cdot\mathbf{A}\cdot\mathbf{x} \end{aligned} \tag{4.52}$$

where

$$c \equiv f(\mathbf{x}) \qquad \mathbf{b} \equiv -\nabla f\,|_{\mathbf{x}} \qquad \mathbf{A}_{ij} \equiv \left.\frac{\partial^2 f}{\partial x_i \partial x_j}\right|_{\mathbf{x}} \tag{4.53}$$

After minimizing in the direction $\mathbf{d}_i$ a new direction $\mathbf{d}_{i+1}$ is required so the minimization along the previous direction $\mathbf{d}_i$ is not spoilt. This condition is just that the change in the gradient stays perpendicular to $\mathbf{d}_i$,

$$0 = \mathbf{d}_i \cdot \delta(\nabla f) \quad . \tag{4.54}$$

The change in the gradient along a direction $\delta\mathbf{x}$ is given by,

$$\delta(\nabla f) = \mathbf{A}\cdot(\delta\mathbf{x}). \tag{4.55}$$

This gives the requirement for conjugacy that along some direction, $\mathbf{d}_{i+1} = \delta\mathbf{x}$

$$\mathbf{d}_i \cdot \mathbf{A} \cdot \mathbf{d}_{i+1} = 0 \quad . \tag{4.56}$$

A two-dimensional quadratic function shown in figure 4.9 illustrates the idea of finding conjugate directions. Starting at an initial point minimize along the direction of the basis vectors $\mathbf{d}_0 = (u_1, 0)$ and then $\mathbf{d}_1 = (0, u_2)$, find a new search direction that's conjugate to $\mathbf{d}_1$ by calculating $\mathbf{d}_2 = \mathbf{x}_2 - \mathbf{x}_0$. Minimize along $\mathbf{d}_2$ to get $\mathbf{x}_3$. Put $\mathbf{d}_0 = (0, u_2)$, $\mathbf{d}_1$ is equal to the the previous $\mathbf{d}_2$ and $\mathbf{d}_3 = \mathbf{x}_5 - \mathbf{x}_3$. And minimize along $\mathbf{d}_3$ to find $\mathbf{x}_{min}$. It can be proved that $\mathbf{d}_1$ and $\mathbf{d}_2$ satisfies equation 4.56 and for quadratic functions this scheme will find a minimum in $N(N+1)$ line minimizations. The number of line minimizations will increase for functions that are not quadratic.

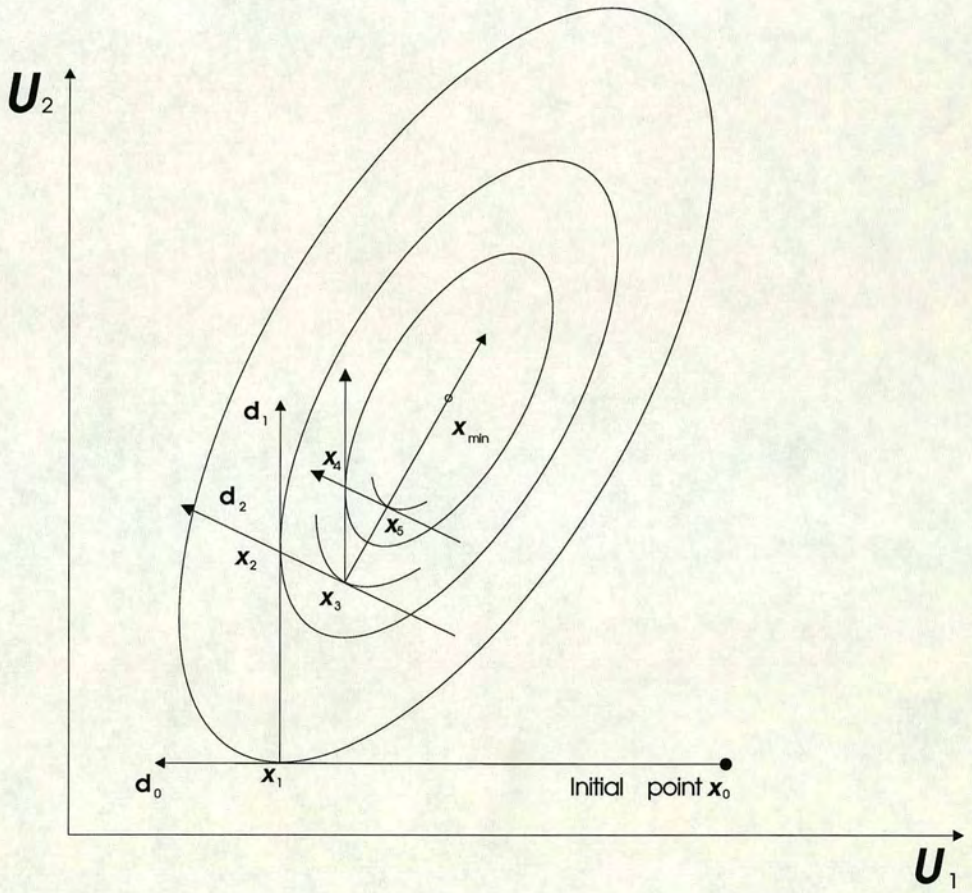


**Figure 4.9.** Schematic diagram of how the conjugate gradient method finds $x_{min}$, the minimum of a two-dimensional quadratic function.

The full implementation is taken from Powell (1977) who introduced the concept of restarting the minimization if the search along a set of directions becomes inefficient. This introduces a new counter $t$ which is reset every time a restart is required and two extra storage arrays $\mathbf{d}_t$ and $\mathbf{g}_t$. These are initially set to $\mathbf{d}_t = \mathbf{g}_t = -\nabla f(\mathbf{x}_0)$. The full algorithm is described by the following steps;

Step 1. Select $\mathbf{x}_0$, set $i = 0$ and set $\mathbf{g}_0 = \mathbf{d}_0 = -\nabla f(\mathbf{x}_0)$.

Step 2. Move a distance $\lambda$ along $\mathbf{d}_i$ such that $f(\mathbf{x} + \lambda \mathbf{d}_i)$ is at a minimum.

Step 3. Set $\mathbf{x}_{i+1} = \mathbf{x}_i + \lambda \mathbf{d}_i$ and $\mathbf{g}_{i+1} = \mathbf{g}(\mathbf{x}_{i+1})$

Step 4. If $\mathbf{g}(\mathbf{x}_{i+1}) = 0$ then a minimum is found and stop. If not choose a new search direction given by,

$$\mathbf{d}_{i+1} = -\mathbf{g}_{i+1} + \beta_i \mathbf{d}_i + \gamma_i \mathbf{d}_t, \tag{4.57}$$

$$\beta_i = \frac{(\mathbf{g}_{i+1} - \mathbf{g}_i) \cdot \mathbf{g}_{i+1}}{\mathbf{d}_i (\mathbf{g}_{i+1} - \mathbf{g}_i)} \qquad \gamma_i = \frac{\mathbf{g}_{i+1} \cdot (\mathbf{g}_{t+1} - \mathbf{g}_t)}{\mathbf{d}_t \cdot (\mathbf{g}_{t+1} - \mathbf{g}_t)} \tag{4.58}$$

Step 5. Check if a restart is need. If restarting set $t = i$, $\mathbf{d}_t = \mathbf{d}_i$, $\mathbf{g}_t = \mathbf{g}_i$ and goto step 1. If not restarting, goto step 2.

There are three conditions for restarting,

- If the gradients $\mathbf{g}_{i+1}$ and $\mathbf{g}_i$ lose their orthogonality it becomes inefficient to carry on searching. This condition is given by,

$$\mathbf{g}_{i+1} \cdot \mathbf{g}_i \geq 0.2(\mathbf{g}_{i+1} \cdot \mathbf{g}_{i+1}) \quad . \tag{4.59}$$

- After $N$ successive conjugate line searches the directions 'fold up' on each other, i.e. $\mathbf{d}_{t+1} = \mathbf{d}_{t+N+1}$. A restart is necessary if $(i + 1 - t) \geq N$.

- If the new search direction is not sufficiently down hill enough, i.e if

$$\mathbf{d}_i \cdot \mathbf{g}_{i+1} < 0.2\mathbf{d}_i \cdot \mathbf{g}_i \tag{4.60}$$

In the same way that searching along successive steepest descent directions is inefficient it is also inefficient to restart along the steepest direction. The direction used for restarting is given by equation 4.57 but with $\gamma_i$ set to zero.

## 4.6 Modelling non-cubic grain shapes

Non-cubic grains may be modelled using one or a combination of two methods: (a) by modifying the number of sub-cubes on a side in order to model general parallelepiped rectangular grains; or (b) modeling any arbitrary shaped grain by masking off sub-cubes which are not part of the grain. Sub-cubes which are not part of the grain are forced to have $\mathbf{M} = 0$ by setting $\alpha$,$\beta$ and $\gamma$ to zero at each iteration of the conjugate gradient routine. This involves calculating a single array whose value is 1 inside the grain and zero outside the grain and multiplying $\alpha$,$\beta$ and $\gamma$ by this array at each iteration. This means that the non-magnetic sub-cubes do not contribute to the total energy and if the gradients are also set to zero outside the grain, the CG routine will not attempt to modify these magnetizations.

Thomson (1993) calculated the magnetic structure of octahedral grains by converting the nonlocal energy terms to sum over exactly as many sub-cubes as required to form an octahedral shape. This turned out to be a complicated algorithm to program and required a high book-keeping overhead. Although using the masking off method is more wasteful in that the masked off sub-cubes still have to be incorporated into the calculations, the FFT technique means it is still faster than the method used by Thomson (1993). It is also a general system that allows the magnetic states of any number of different shaped grains to be calculated. The linear exchange formulation was assumed for irregular grains as the boundary conditions for the 5 point formulation adds considerable complications.

## 4.7 Material parameters for magnetite

The three parameters which need to be determined are the anisotropy constant, $K_1$, the saturation magnetization, $M_s$ and the exchange constant $C_e$. All the values are room temperature values. The value for $K_1 = 1.25 \times 10^4 Jm^{-3}$ was taken from Fletcher and O'Reilly (1974). The value for $M_s = 4.8 \times 10^5 Am^{-1}$ was taken from Heider (1988). The exchange constant $C_e = 2.64 \times 10^{-11} Jm^{-1}$ was taken from Heider and Williams (1988).

## 4.8 Stray fields and simulated Bitter patterns

The experimental Bitter pattern technique permits the observation of domain walls by using a colloid consisting of a suspension of fine superparamagnetic grains which are attracted to the stray field of a domain wall. The density of colloid above a particular point was shown by Kittel (1940), and more thoroughly by Hartmann and Mende (1985) to be proportional to $H^2$ where $H$ is the stray field intensity above the grain. The stray field is defined as the effective field calculated outside the grain and is solely due to the long range magnetostatic force. From equations 4.19 and 3.9,

$$\mathbf{H}_l = -\frac{1}{\mu_0 M_s \Delta^3}\frac{\partial E_d}{\partial \mathbf{m}_l} = -\frac{M_s}{8\pi}\sum_m \mathbf{W}_{l-m}\cdot\mathbf{m}_m \quad . \tag{4.61}$$

For example the $x$ component of the field at the position $l$ in the $3d$ coordinate system, $H_l^x$ is given by

$$H_l^x = -\frac{M_s}{8\pi}\sum_m [W_{l-m}^{\alpha\alpha}\alpha_l + W_{l-m}^{\alpha\beta}\beta_l + W_{l-m}^{\alpha\gamma}\gamma_l] \quad . \tag{4.62}$$

Again this is a convolution which may be expressed as the inverse Fourier transform,

$$\mathbf{H}_l = -\frac{M_s}{8\pi}\sum_m \mathbf{W}_{l-m}\cdot\mathbf{m}_m = -\frac{M_s}{8\pi}(\mathbf{W}*\mathbf{m})_l = -\frac{M_s}{8\pi}\mathcal{F}^{-1}[\tilde{\mathbf{W}}\cdot\tilde{\mathbf{m}}]_l \quad . \tag{4.63}$$

Figure 4.10 compares the stray field from a single-domain cubic grain calculated using equation 4.63 with the stray field for a dipole. The effective field surrounding a $8 \times 8 \times 8$ cube was calculated using a resolution of $n = 16$ and masking off all but a corner of the volume. The magnetization in the remaining cube was then set to a single-domain state in the $z$ direction. The two models agree well at a distance of $x/L = 1$ away from the cube edge, the difference between the FFT calculation and the dipole approximation for the $x$ and $z$ traverses being 0.35% and 0.4% respectively. In addition, figure 4.10 shows how the dipole approximation diverges from the FFT algorithm close to the cube edge.

Figure 4.11 shows how the computational space is divided up in order to simulate experimental Bitter patterns. The lower half of the computation space is allocated to the top half of the grain and the upper half of the computation space is set to non-magnetic sub-cubes. $H^2$ is then calculated for each sub-cube

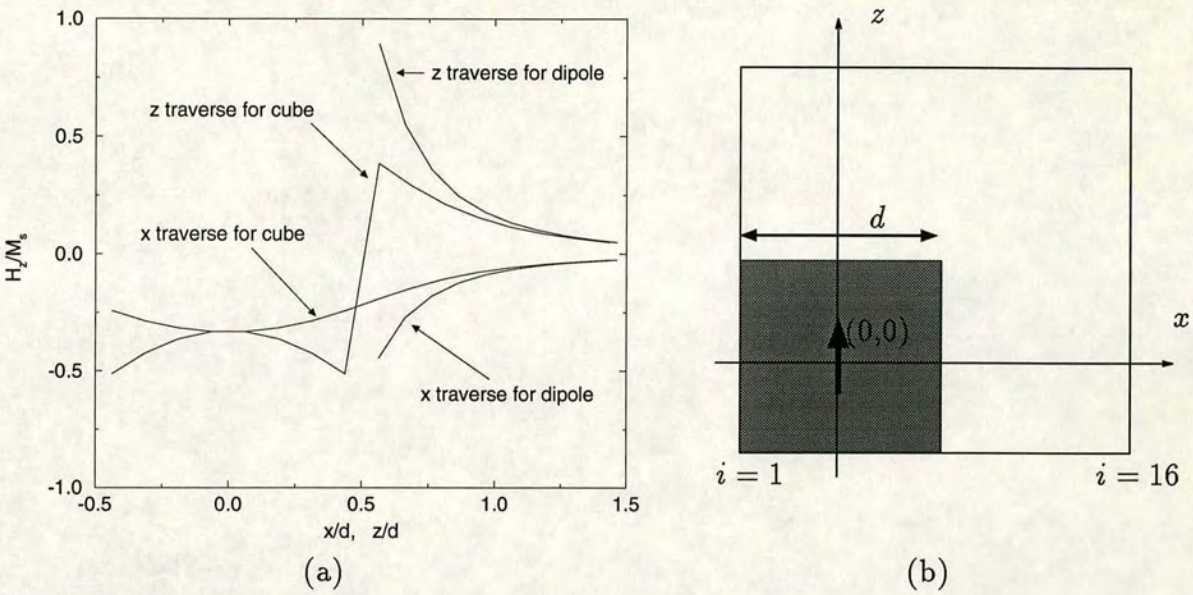


**Figure 4.10.** Comparison of the field due to a dipole and the field due to a uniformly magnetized cube of edge length $d$ calculated using the FFT technique. The coordinate system has been shifted so that the centre of the cube is at the origin.

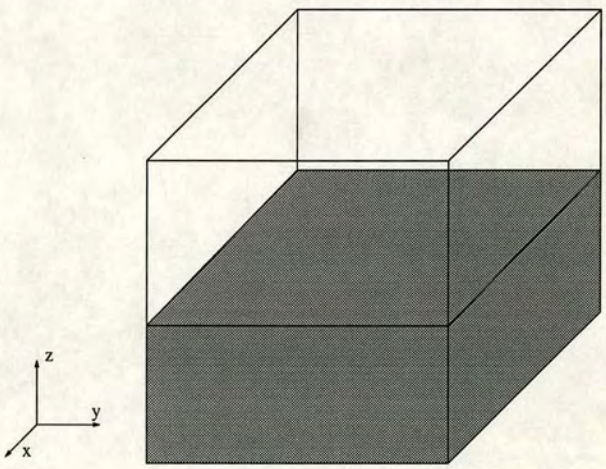


**Figure 4.11.** Sketch of how the computation space is used to simulate Bitter patterns. The shaded region represents the top half of the grain and the upper half of the computation space is set to zero.

in the top half using equation 4.63. The Bitter pattern is then a contour plot of $H^2(i,j)$, which is computed from an integration with $k$ above the grain,

$$H^2(i,j) = \sum_{k=n/2+1}^{n} H_x^2(i,j,k) + H_y^2(i,j,k) + H_z^2(i,j,k) \quad . \tag{4.64}$$

As an example figure 4.12 shows a well defined Bitter pattern from a test structure consisting of two anti-parallel domains and a Bloch wall.

## 4.9 Hysteresis simulation

Hysteresis measurements yield parameters which are related to the stability, i.e coercivity and signal strength, i.e saturation remanence. The reversal mechanism from one domain state to a domain state in the opposite direction is in general a dynamical process described by the Landau-Lifshitz-Gilbert equation,

$$\frac{d\mathbf{M}}{dt} = \gamma_0 \mathbf{M} \times \mathbf{H}_{eff} - \frac{\lambda}{\mathbf{M}_s^2} \times (\mathbf{M} \times \mathbf{H}_{eff}) \tag{4.65}$$

where $\gamma_0$ is the gyromagnetic ratio and $\lambda$ is the damping constant. The first term on the right hand side is the torque exerted on the magnetization by the effective field and the second term is a damping term. The dynamical calculation can be simplified by assuming infinite damping, which sets the second term to zero. Equation 4.65 then reduces to the condition for equilibrium. If the torque on the magnetization, $\mathbf{M} \times \mathbf{H}_{eff}$ is zero then there will be no change with the magnetization with time. The reversal mechanism is then determined by calculating a series of LEM states at intermediate field values from saturation in one direction to saturation in the opposite direction. The magnetization states obtained by Schabes and Bertram (1988) who used this quasi-static approach have been confirmed by Nakatani *et al* (1989) who solved the full dynamic calculation using a backward difference scheme (Press *et al* 1986).

In addition, Nakatani *et al* (1989) calculated that a 0.05$\mu$m SD cubic grain of iron takes 10ns to reverse direction after an external field is applied in the opposite direction to the magnetization. This is many orders of magnitude faster than the time taken for modern magnetometers[2] to measure a full hysteresis curve ($\approx$ 1min.) and standard vibrating sample laboratory magnetometers ($\approx$ 15min.).

[2]Princeton Measurements Corporation, Micromag 2900 Alternating Gradient Magnetometer

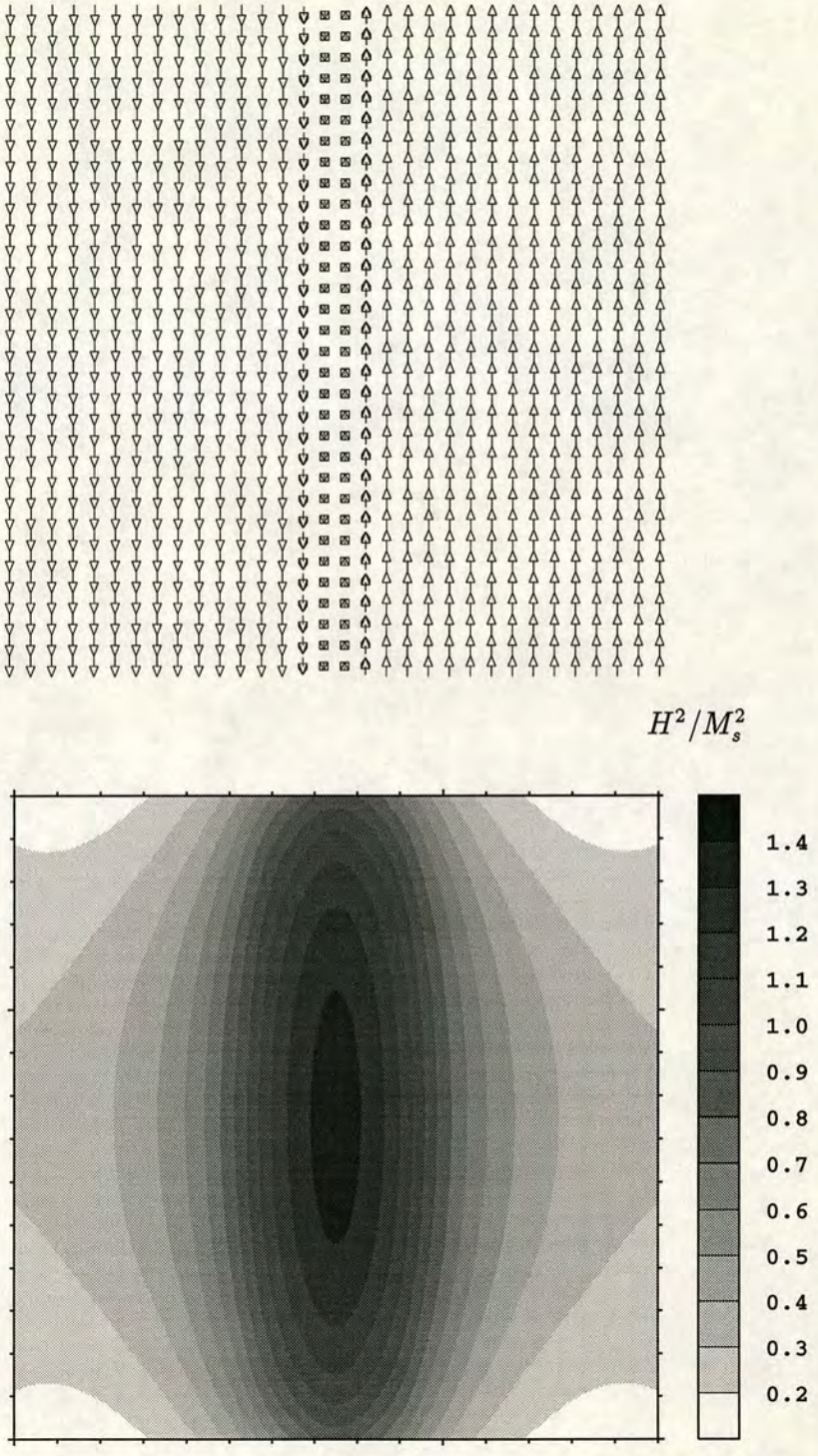


**Figure 4.12.** Magnetization and simulated Bitter pattern for a two-domain state with a Bloch wall. The magnetization plot shows the top slice of a $32 \times 32 \times 32$ resolution cubic grain. The magnetization pattern is repeated through the depth of the grain.

# Chapter 5. Results for cubic grains

## 5.1 Introduction

This chapter presents results which model the room temperature (25°C) magnetization of synthetic cubic grains of magnetite such as those precipitated from solution or grown hydrothermally. The aim is to predict accurately the domain states of PSD grains and then use these domain states to simulate Bitter patterns. The results will be considered in terms of, (a) whether $3d$ models show surface magnetization patterns which are representative of their own internal magnetization and (b) the relationship between simulated Bitter patterns and the magnetization of the grain. Bitter pattern simulations will be compared with experimental domain observations in chapter 8.

The maximum grain size which can be modelled is determined by the resolution of the model which in turn depends on the computing time and the amount of memory available. The maximum resolution on the CM-200 is $64 \times 64 \times 64$ and the maximum grain size using this resolution is $d = 4\mu$m. However using a resolution of $64 \times 64 \times 64$ is extremely time-consuming and so only a few equilibrium states were calculated. Using a smaller resolution of $32 \times 32 \times 32$ allowed equilibrium states to be calculated in a much shorter time, allowing many states to be calculated at a range of grain sizes.

The need to model irregular grains using the linear exchange formulation means that results for cubic grains using both the linear and the 5 point formulation will be compared in this chapter.

## 5.2 Results for grains $0.01\mu m < d < 1\mu m$, $32 \times 32 \times 32$ model

This section predicts the magnetization states of magnetite grains as they crystallize from an aqueous solution. A SD state was first used as an initial state at a small grain size of $d = 0.01\mu$m and an equilibrium solution calculated using the conjugate-gradient (CG) routine. This solution was then used as an initial guess to the CG routine at $0.02\mu$m and this process repeated in steps of $0.01\mu$m until $0.3\mu$m and then in steps of $0.1\mu$m until $1\mu$m. Figure 5.1a shows the energy values for these results as a function of grain size, the results for grains decreasing in size were obtained by a similar process going from $0.4\mu$m to $0.01\mu$m.

Results presented in this section were calculated using the 5 point exchange formulation and a resolution of $32 \times 32 \times 32$ sub-cubes and took 3.5 hours of

computation time for the complete set. All the results were calculated using a zero external field and all energy values have been normalized by the energy of a SD state with the direction of the magnetization parallel to a cube edge.

**State A,** $d = 0.1\mu m$

As the grain size increases from $0.01\mu$m the magnetization changes continuously from a uniform SD state to a state that is mostly single-domain but with deflection at the 8 corners. Figure 5.2 shows the magnetization vectors and the orientation of the $2d$ planes is shown in figure 5.3. This is a flower state similar to that calculated by Schabes and Bertram (1988) and Williams and Dunlop (1989). A plot of the surface magnetization in figure 5.2a shows that there is a gradual variation in vertical deflection from the centre of the grain to the corners. This deflection at the corners decreases the magnetostatic energy by moving like surface charges away from each other and unlike charges together.

Figure 5.1b shows how the [001] component of the magnetization, $M_z/M_s$ varies with increasing grain size. For grains smaller than $d = 0.07\mu$m, $M_z/M_s$ is always greater than 0.95. Although there is no clear distinction between SD grains and flower states, figure 5.1b suggests that for SD grains smaller than $0.07\mu$m, Néel's (1949,1955) theory of TRM and VRM acquisition is still applicable. This is not a conclusive test as a small amount of flowering may affect the energy barrier to domain reversal in a non-linear way. However low resolution $3d$ models by Enkin and Williams (1994) calculated the energy barrier for domain reversal in grains up to $0.07\mu$m in size, and found that any flowering did not significantly increase the energy barrier.

**State B,** $d = 0.2\mu m$

Figure 5.4a shows that at $d = 0.2\mu$m the flowering is no longer uniform throughout the grain and large regions at the corners are now aligned parallel to the $\langle 111 \rangle$ easy directions. This can be seen from the dependence of $E^a$ with grain size as shown in figure 5.5. For grains larger than $0.07\mu$m the anisotropy energy decreases more rapidly with grain size as the direction of the magnetization at the corners aligns with the easy axes. This can also be seen in how the exchange energy, $E^e$ varies between $0.1\mu$m to $0.2\mu$m. As the magnetization in progressively larger regions of the grain becomes aligned parallel to each other, $E^e$ decreases from a maximum at $d = 0.1\mu$m to a minimum at $d = 0.2\mu$m.

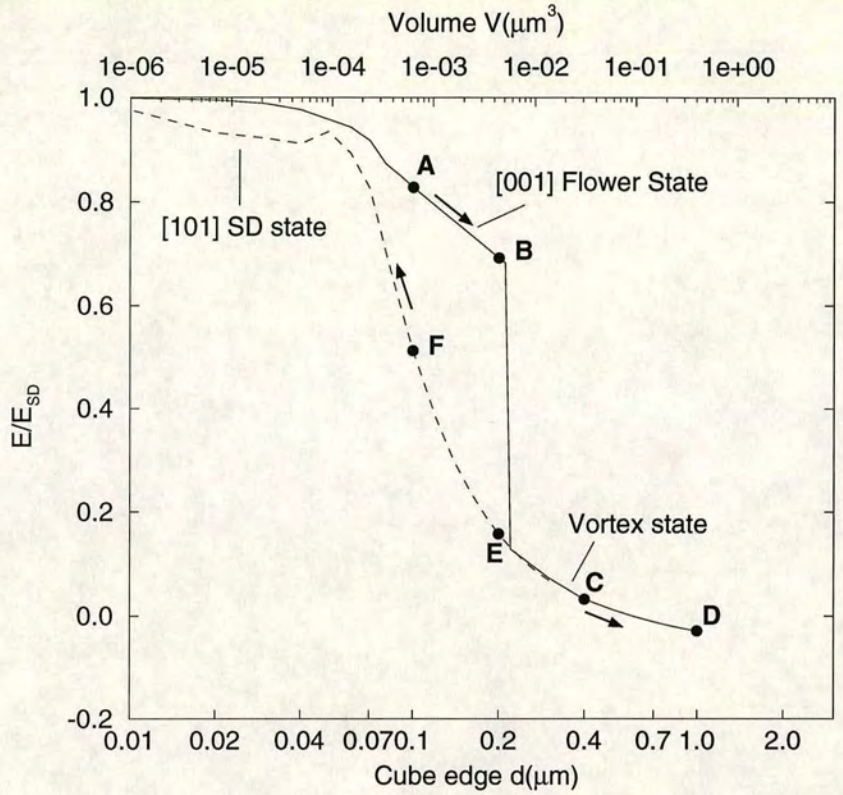


(a) Normalized energy values as a function of grain size

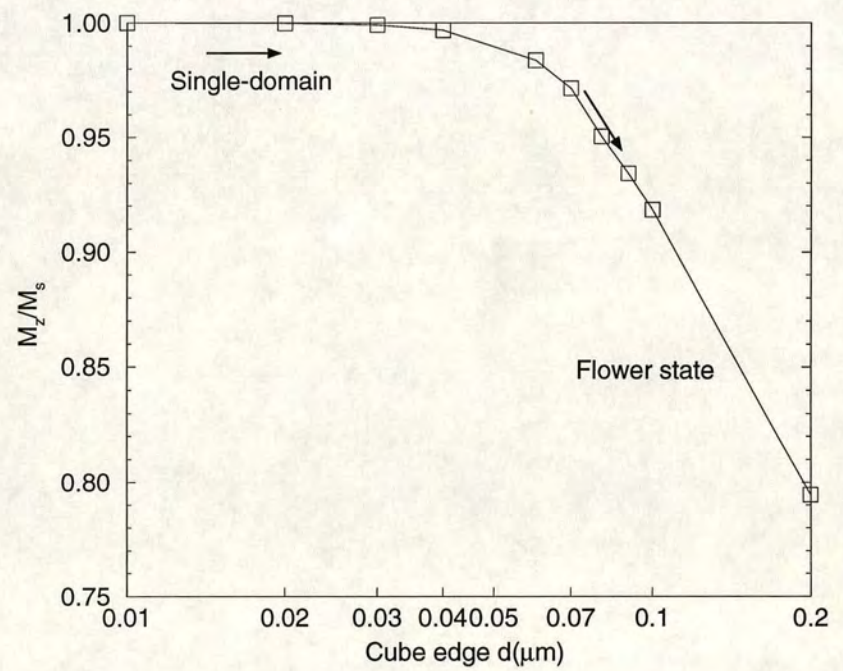


(b) [001] magnetization component

**Figure 5.1.** (a) Normalised free energy results and (b) [001] magnetization component for cubic grains as a function of grain size using the five point exchange formulation. Solid lines represent grains grown from a $0.01\mu$m SD state in the [001] direction and dashed lines are for grains decreasing in size from $0.4\mu$m down to $0.01\mu$m.

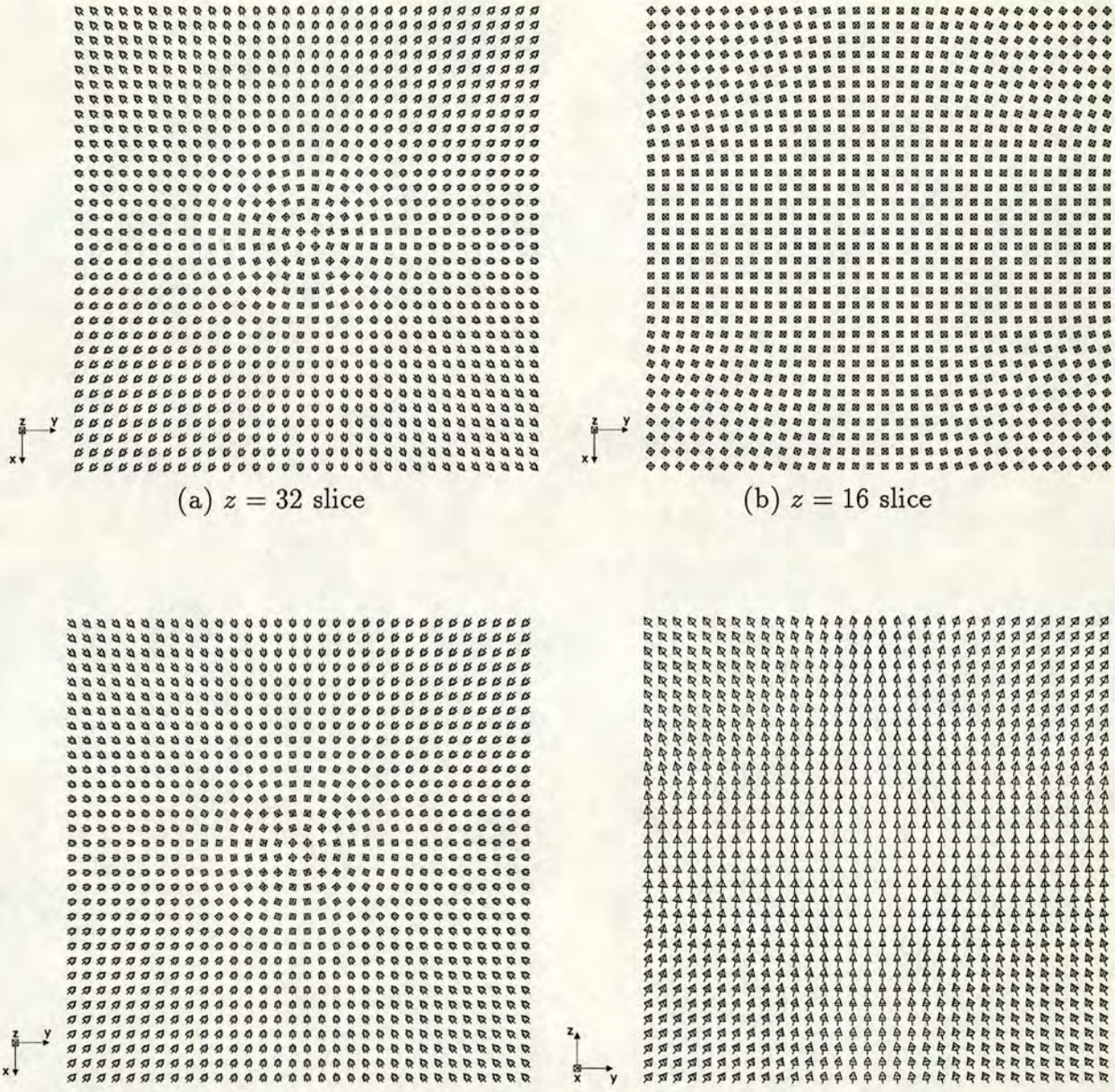

(a) $z = 32$ slice (b) $z = 16$ slice

(c) $z = 1$ slice (d) $x = 32$ slice

**Figure 5.2.** State **A** for a 0.1$\mu$m grain grown from an 0.01$\mu$m SD initial guess, $E/E_{SD} = 0.83$, $M_z/M_s = 0.92$, $H = 0$mT.

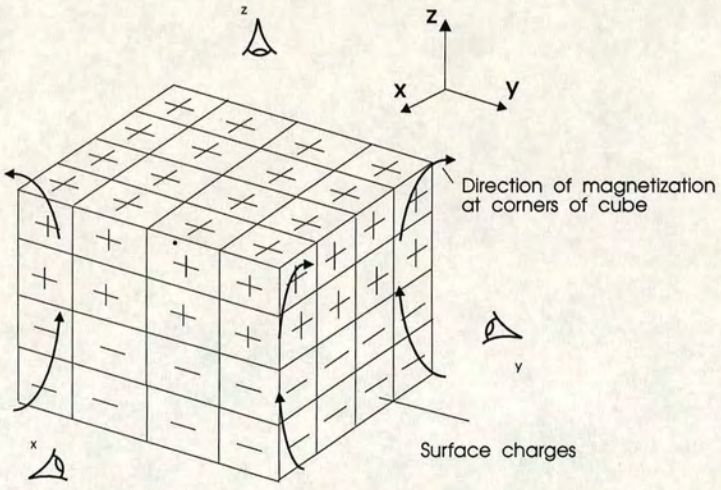


**Figure 5.3.** Sketch of a flower state and the $x$,$y$ and $z$ view directions for results presented in this chapter. The lower rear corner of the cube is positioned at the origin. For a $32 \times 32 \times 32$ model the $z = 32$ plane is defined as the top surface and the $z = 1$ slice is viewed through the grain, in other words the grain is not viewed in the opposite direction for the $z = 1$ slice.

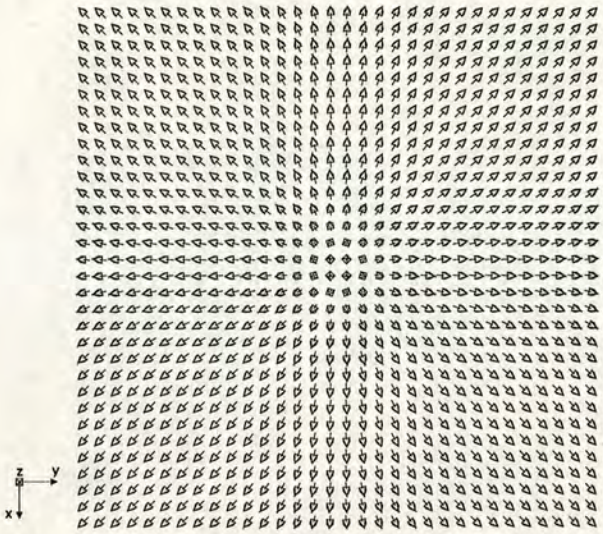

(a) $z = 32$ slice

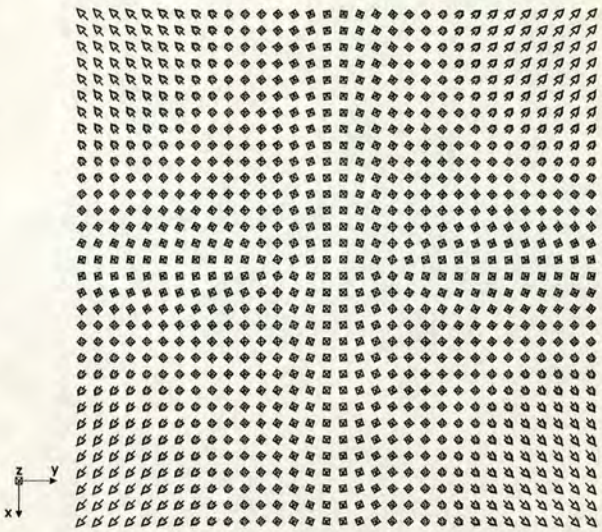

(b) $z = 24$ slice

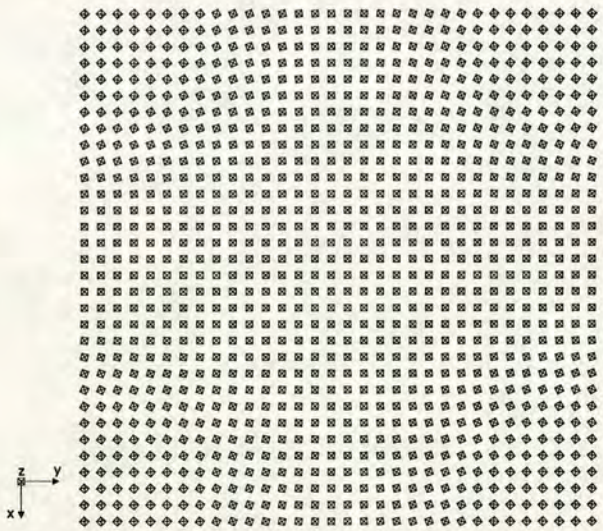

(c) $z = 16$ slice

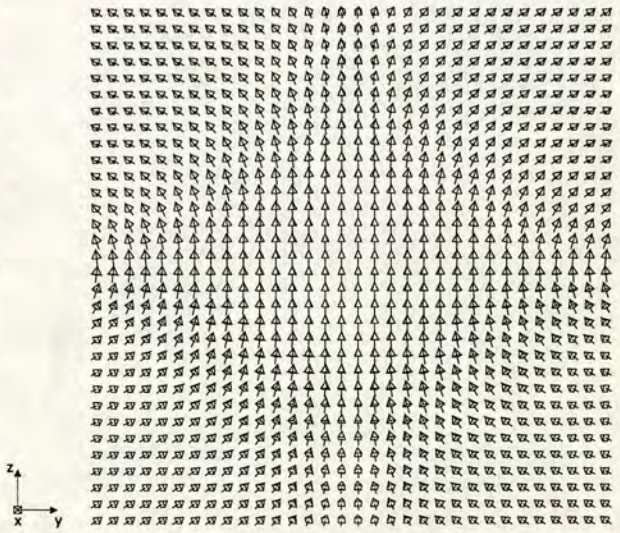

(d) $x = 32$ slice

**Figure 5.4.** State **B**, $d = 0.2\mu$m grain grown from an $0.01\mu$m SD initial guess, $E/E_{SD} = 0.69$, $M_z/M_s = 0.79$, $H = 0$mT.

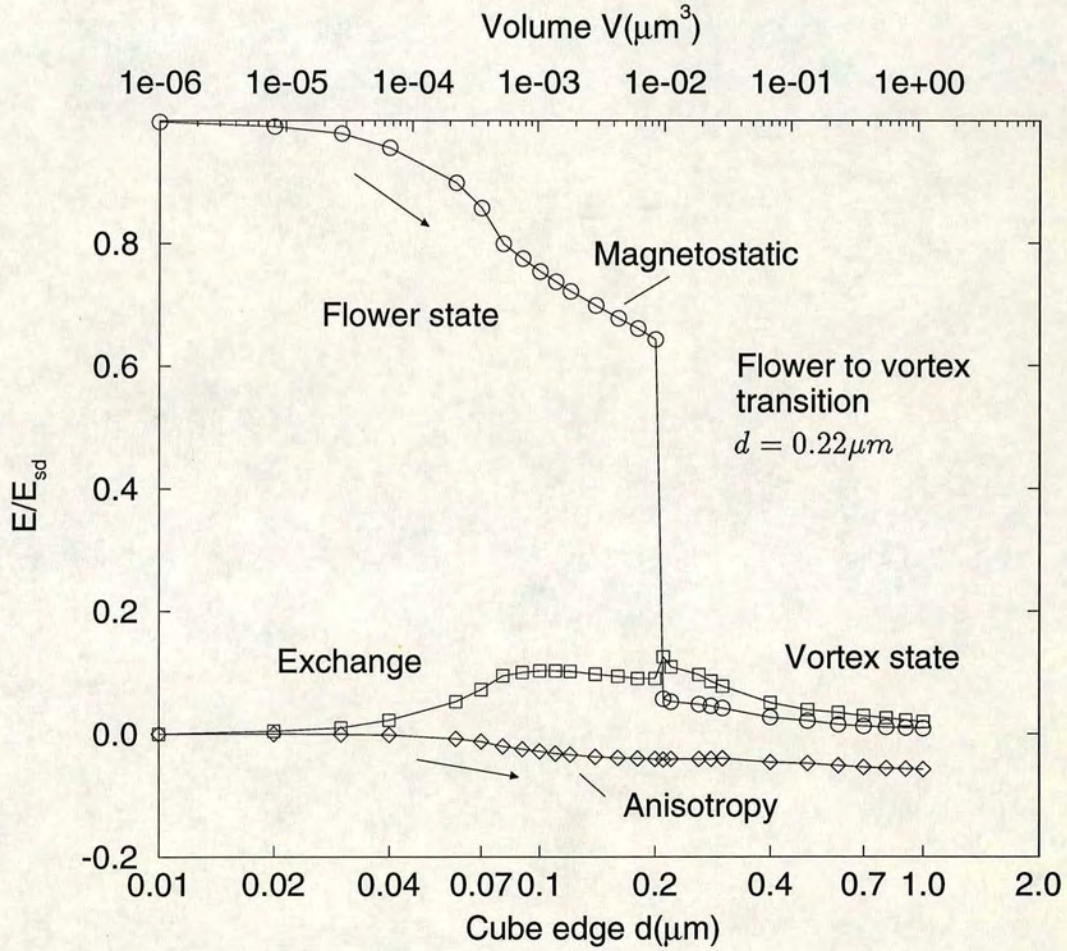


**Figure 5.5.** Dependence of $E^e$, $E^a$ and $E^d$ on grain size $d$.

**State C, $d = 0.4\mu m$**

There is a discontinuous jump at $0.22\mu$m from a flower state in the $z$ direction to a vortex state. The vortex state at $0.4\mu$m is shown as a cutaway in figure 5.6 and as $2d$ planes in figure 5.7. The vortex dominates the grain with the core aligned at an angle of 40° to the $x$ axis in order to reduce the magnetocrystalline anisotropy energy. In addition the surface charges which occur at the edge of the grain in low resolution models do not arise in the high resolution model. This was anticipated by Butler and Banerjee (1975) who suggested that the magnetization may rotate to align along the edges at the expense of the exchange energy. Section 5.3 will show that both these effects become less noticeable as the grain size decreases, so that at $0.1\mu$m the core becomes more aligned in the [001] direction and more surface charges occur at the edges. This state has a total moment given by $M_{tot} = (M_x^2 + M_y^2 + M_z^2)^{1/2}/M_s$=0.033, whereas experimentally measured $M_{rs}/M_s$ values lie between 0.05 and 0.1 at $d = 0.4\mu$m (figure 2.3). Although this is a low moment state it is the magnetization states at saturation remanence, presented in chapter 7 which are required in order to compare with experimental values of $M_{rs}/M_s$.

Figure 5.5 shows that the transition from a flower to a vortex state is dominated by a large decrease in $E^d$. At the surfaces $E^d$ aligns the magnetization parallel to the surfaces, resulting in a reduction in the number of free poles. It is interesting to note that figure 5.5 also shows an increase in $E^e$ at the flower-vortex transition. Furthermore, the vortex state is favourable because the reduction in $E^d$ is much greater than the necessary increase in $E^e$.

Although the magnetization varies uniformly throughout the grain with no well defined domain walls, there is a distinct two-domain component as shown in figure 5.7b. A comparison between figure 5.6 and a schematic sketch of a two-domain grain, shown in figure 5.8, illustrates the limitation of $1d$ Amar models. Each of the models has a similar topology although the high resolution model prohibits the free poles at the surface of the grain which are assumed in the two-domain model. Furthermore, section 5.5 will show that the small grain size and the ⟨111⟩ easy directions in magnetite mean that the vortex state is favoured over a two-domain state with closure domains.

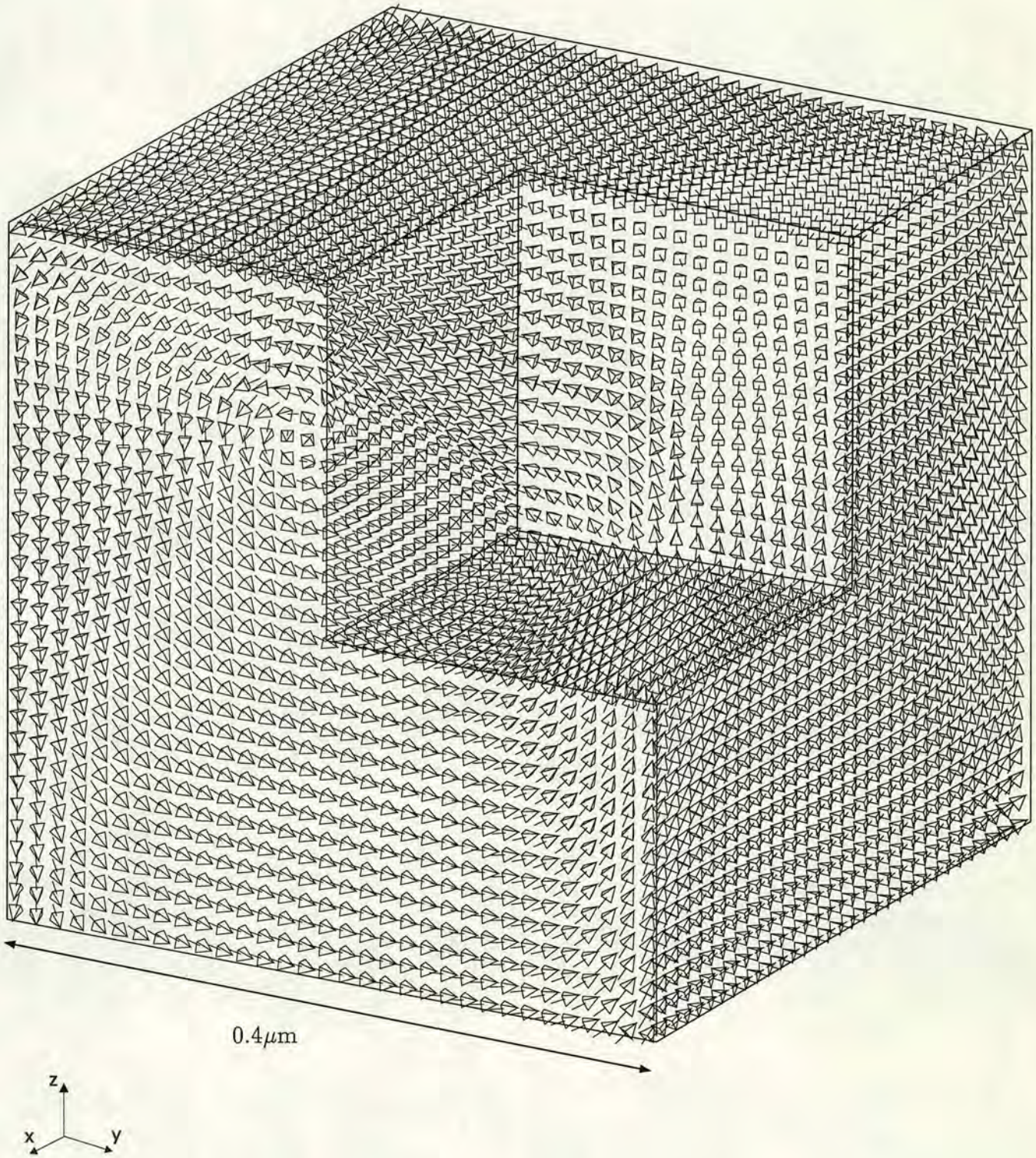


**Figure 5.6.** Cutaway view of the magnetization at $d = 0.4\mu$m (state **C**).

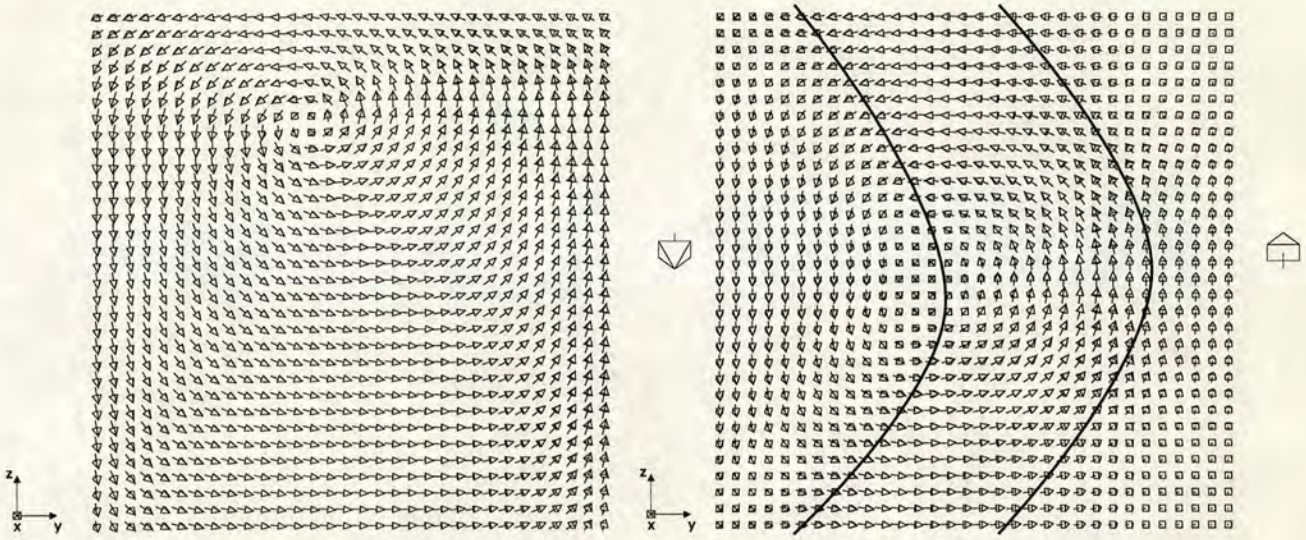

(a) $x = 32$ slice (b) $x = 16$ slice

(c) $x = 1$ slice (d) $z = 32$ slice

**Figure 5.7.** State C for a 0.4$\mu$m grain grown from an 0.01$\mu$m SD initial guess, $E/E_{SD} = 0.032$, $M_z/M_s$=0.0165, $H = 0$mT.

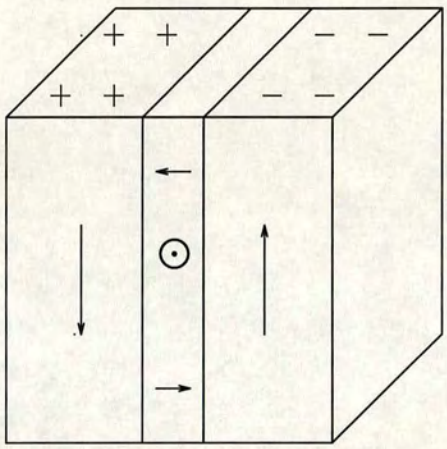


**Figure 5.8.** Schematic diagram of a two-domain grain with a Néel wall which reverses direction. The circle in the centre of the Néel wall represents a Bloch line.

**State D,** $d = 1.0\mu m$

There is a gradual transition from the previous vortex state **C**, to the state **D** shown as a $3d$ view in figure 5.9 and as $2d$ planes in figure 5.10. A comparison between figures 5.7b and 5.10b shows a transition from a vortex state which dominates the grain to a fan type structure in the centre of the grain shielded by two surface domains. The main features of state **D** are listed as;

(a) Figure 5.10b shows that the central region (labeled **I**) consists of a rapidly varying magnetization. Figure 5.11 shows how the vortex state evolves as the grain size increases from $0.1\mu$m up to $1\mu$m by plotting out the diagonal (101) plane. The diagonal plane clearly shows how the state evolves from the vortex state at $0.1\mu$m to a state in which domains form in the $\langle 110 \rangle$ directions at the grain's edges. In addition the sequence shows that at $1.0\mu$m there is no vorticity in the centre of the grain.

(b) Figure 5.9 shows two thin surface domains, **II**a and **II**b in which the vectors are aligned parallel to the surface down to a depth of $0.2\mu$m. The directions of the magnetization in regions **II**a and **II**b are in opposite senses and together they form a shell which encloses and shields the central region (**I**). The domains **II**a and **II**b act as two anti-parallel domains which produce large regions on the surface in which the magnetization aligns parallel to the surface along the $\langle 110 \rangle$ easy directions.

(c) The state has evolved from a vortex state in which the magnetization curls round a central line to a state in which the vorticity is contained within two small regions of the grain. At $0.4\mu$m the vorticity curls around a line whereas at $1.0\mu$m the magnetization curls around two distinct points either side of the grain. These new regions will be referred to as knots which act as nucleation sites for the domain walls shown in figures 5.10 and 5.9. The angle of 109° between the two domain walls nucleated by the knot is similar to that measured experimentally on much larger grains.

(d) Two smaller regions **III**a and **III**b which act as closure domains.

(e) Figure 5.10d shows two well defined domains in the $[\bar{1}\bar{1}0]$ (labelled as **II**a) and $[1\bar{1}0]$ (**III**a) directions, separated by a $0.06\mu$m wide Néel wall. For the first time $3d$ models show domain patterns in which the magnetocrystalline anisotropy controls the magnetization to align along the intermediate $\langle 110 \rangle$

axes at the grain's surface. The left and right edges of figure 5.10d show that the magnetostatic energy controls the magnetization to align along the [100] and [$\bar{1}$00] directions respectively. These ⟨100⟩ directions are only maintained for the first two vectors inside the grain, after which $E^d$ controls the vectors to align parallel to the surface and $E^a$ in the ⟨110⟩ directions.

(f) Other surfaces such as that shown in figure 5.11h show no domain walls. Halgedahl and Fuller (1980) reported that Bitter patterns on much larger grains showed no domain walls and interpreted these grains as being in SD metastable LEM states. The magnetization patterns shown in figure 5.10 suggest that grains which show no surface magnetization patterns can still shield a complicated internal magnetization.

(g) As with state **C**, state **D** is symmetrical about the centre point of the cube; this can be seen in the symmetrical pair of figures 5.10a and 5.10c and figures 5.10b and 5.10f.

The surface patterns from 0.4$\mu$m to 1.0$\mu$m agree with classical domain theory in that at the smaller grain size $E^e$ dominates and causes the magnetization to vary uniformly throughout the surface. As the grain size increases $E^d$ dominates and forms regions in which the magnetization vectors align parallel to each other. In addition the high resolution model shows the magnetocrystalline energy controlling the domain states for the first time in magnetite. This is reflected in the negative energy for state **D** ($E/E_{SD} = -0.03$), and is a result of $E^a$ being negative and larger than the sum of $E^d$ and $E^e$.

The magnetization remains in the same state as the grain size increases from 1$\mu$m to 3$\mu$m but a series of separate LEM states were obtained in this size range by starting from different initial states. For example, figure 5.12 shows a 3$\mu$m grain which was obtained by using a SD initial state in the ⟨111⟩ direction. For grains larger than 3$\mu$m, the $32 \times 32 \times 32$ model breaks up and the magnetization forms a disordered random state.

### Simulated Bitter Pattern for State D

Figure 5.13 shows simulated Bitter patterns for state **D**. The domain wall separating the regions **IIa** and **IIIa** are not imaged due to the shallow depth of the wall. This is a result of the negative anisotropy constant producing ⟨110⟩ domains at the surface and ⟨111⟩ domains in the interior.

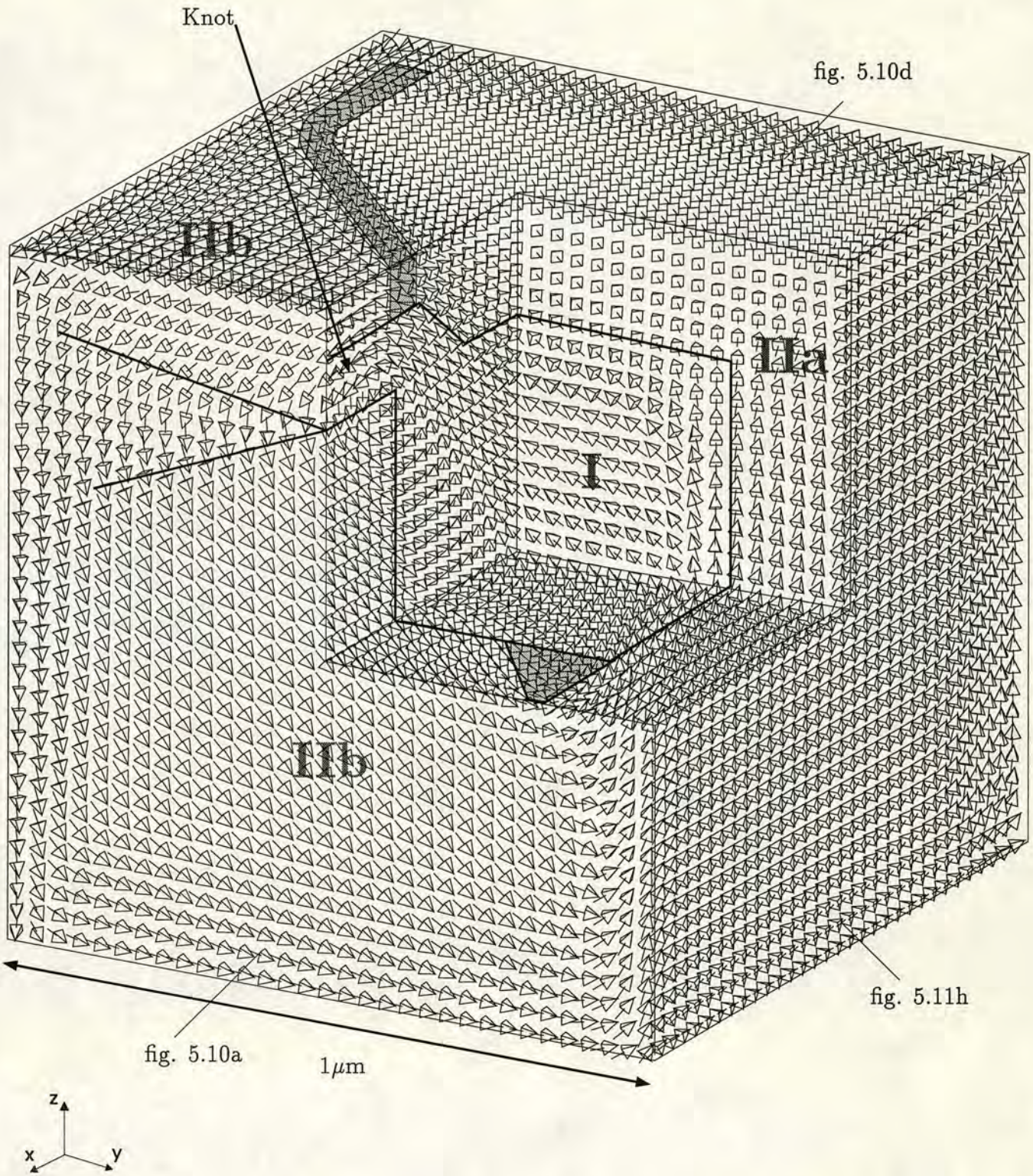


**Figure 5.9.** Cutaway view of the magnetization at 1.0$\mu$m (state **D**). The shaded regions identify domain walls.

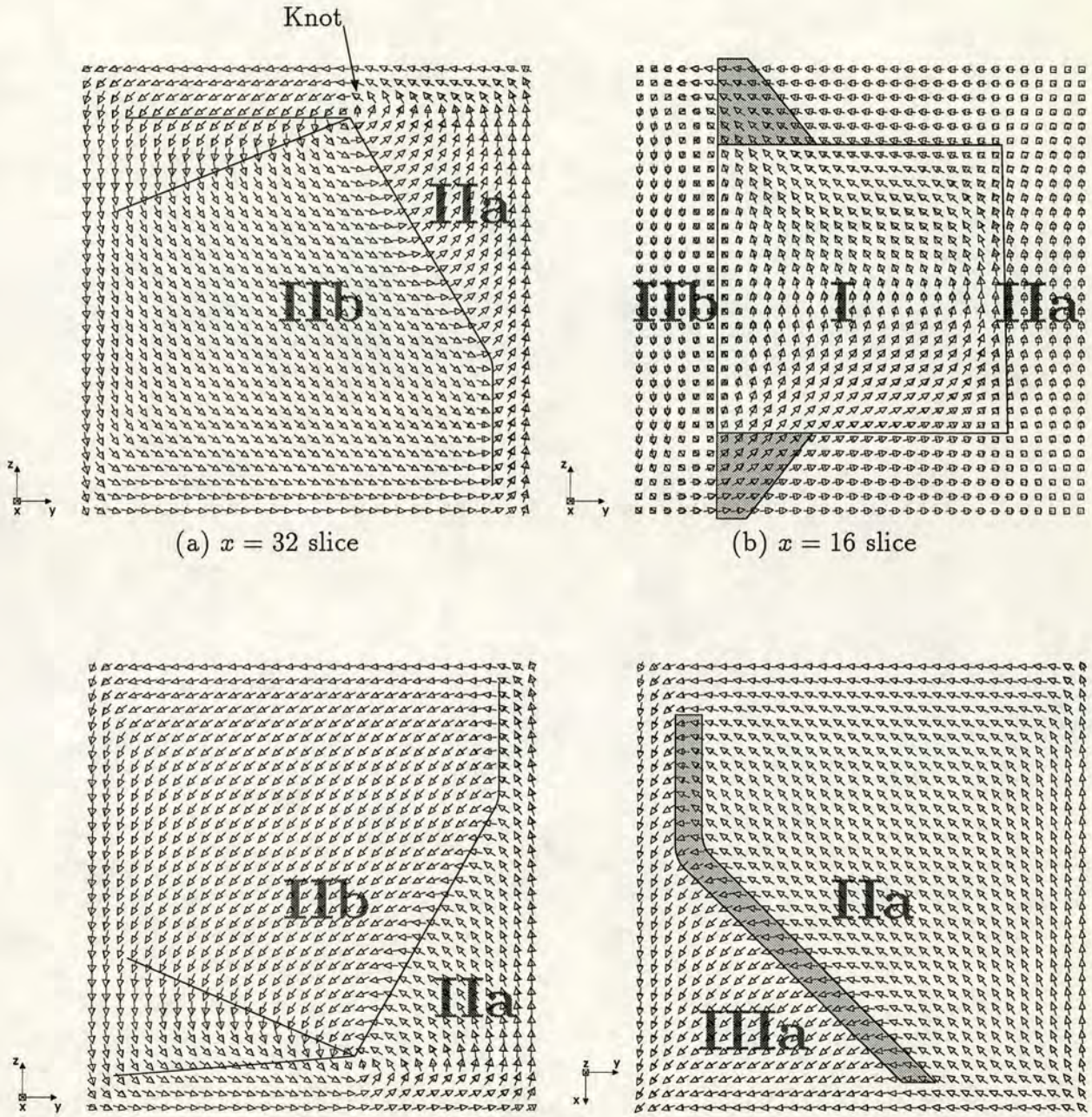


(a) $x = 32$ slice

(b) $x = 16$ slice

(c) $x = 1$ slice

(d) $z = 32$ slice

**Figure 5.10.** Solution **D** for a 1$\mu$m grain grown from an 0.01$\mu$m SD initial guess, the shaded areas represent the domain walls, $E/E_{SD} = -0.029$, $M_{tot}/M_s = 0.010$, $H = 0$mT.

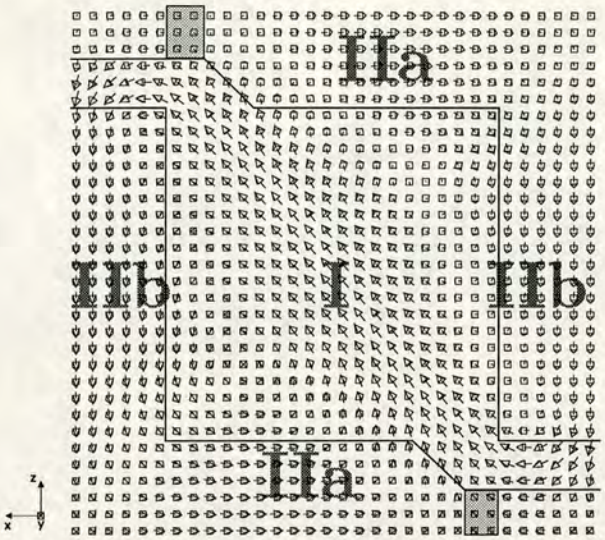


(e) $y = 16$ slice

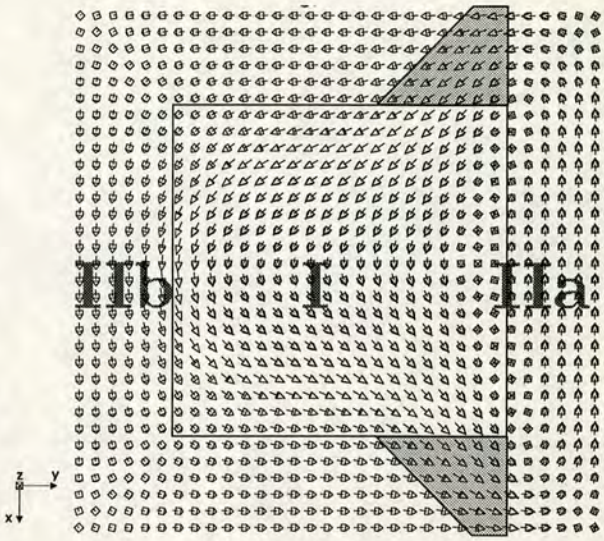


(f) $z = 16$ slice

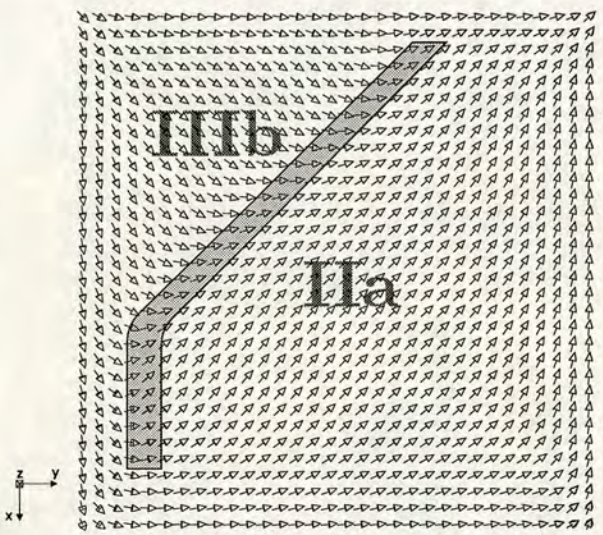


(g) $z = 1$ slice

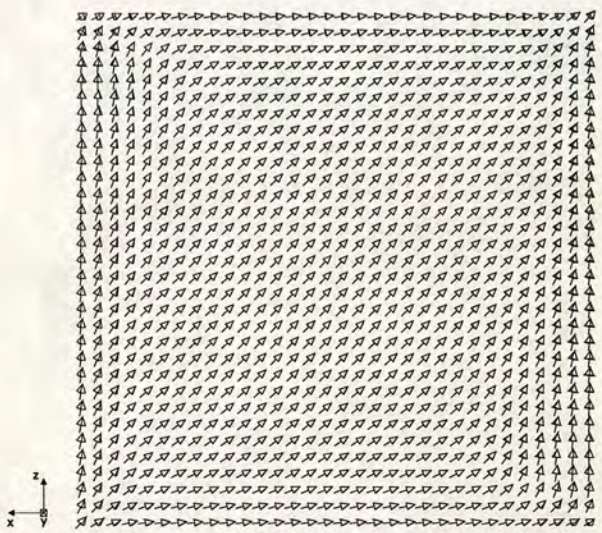


(h) $y = 32$ slice

**Figure 5.10** continued.

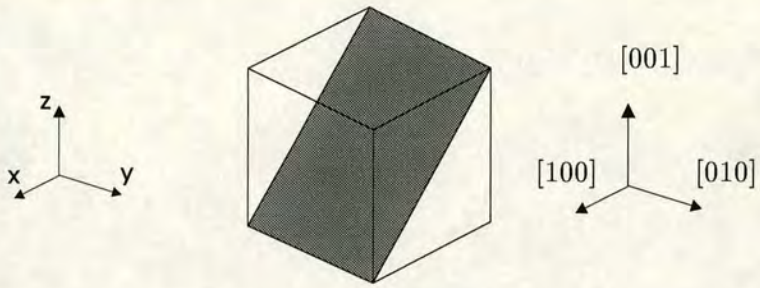


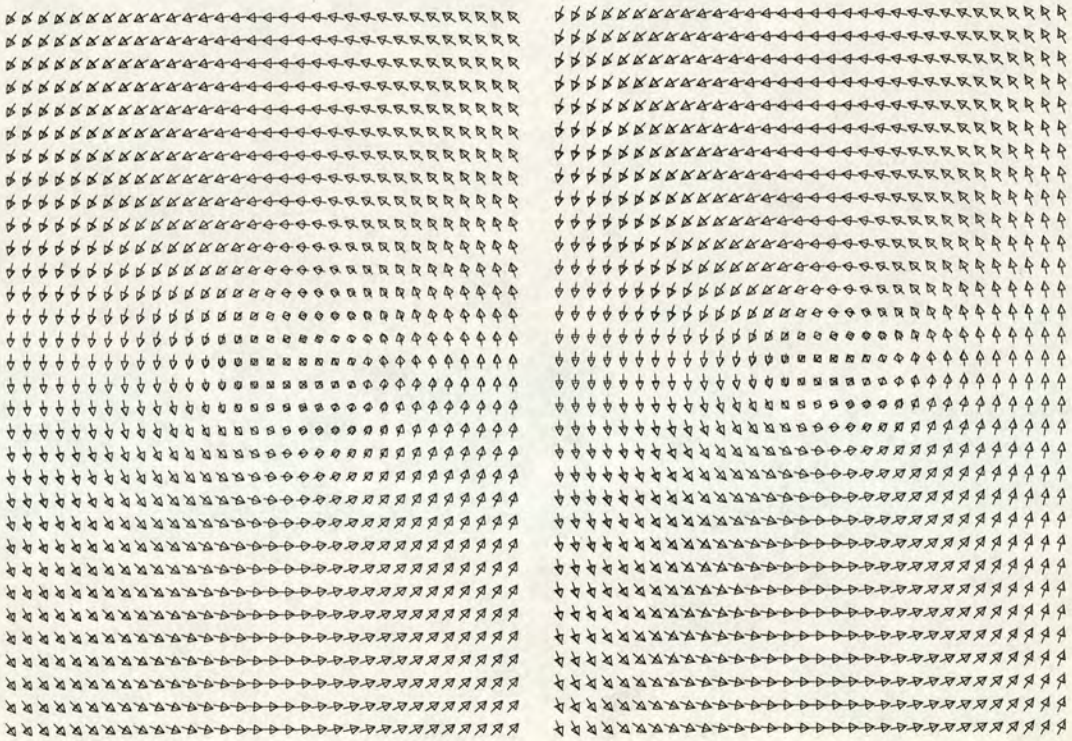

(a) $d = 0.1\mu$m (b) $d = 0.4\mu$m

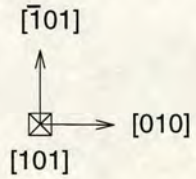


**Figure 5.11.** Evolution from vortex state to domains as the grain size increases. The (101) plane shows the transition from vortex states to domain states more clearly than the (100) plane because the vortex core is offset by 45° to the [100] direction and the domains at $d = 1\mu$m are in the $\langle 110 \rangle$ directions.

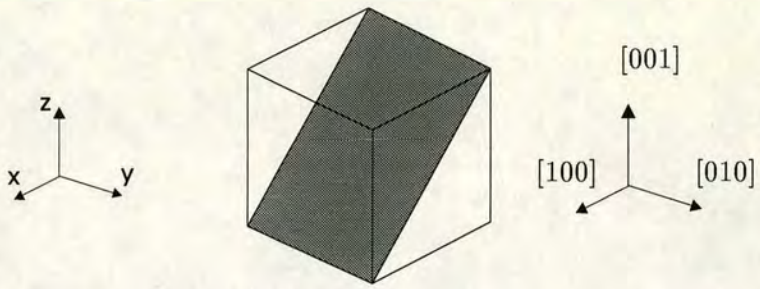


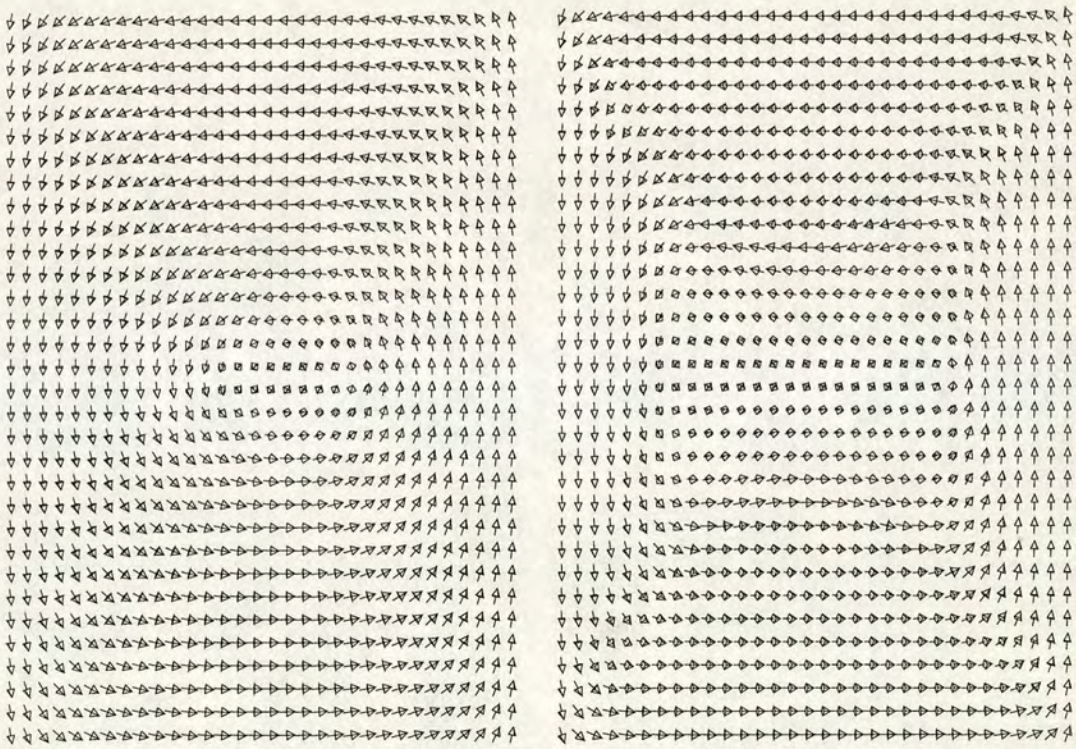

(c) $d = 0.7\mu$m (d) $d = 1.0\mu$m

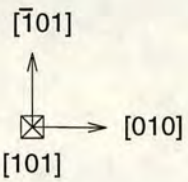


**Figure 5.11** continued

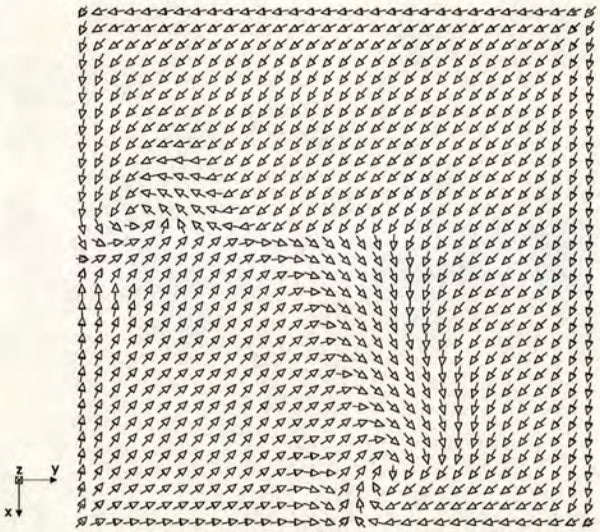

(a) $z = 32$ slice

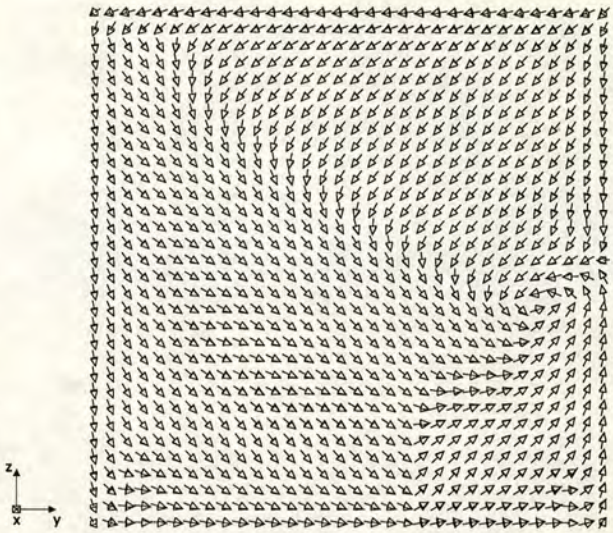

(b) $x = 32$ slice

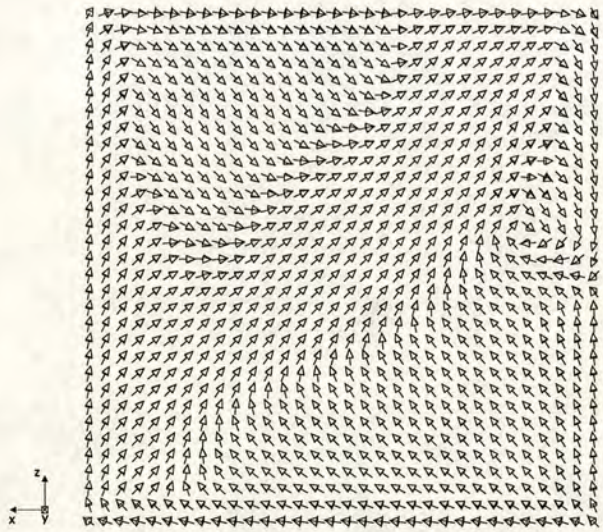

(c) $y = 32$ slice

**Figure 5.12.** Magnetization state for a 3$\mu$m grain using the linear exchange formulation. This solution was obtained by using a SD state in the [111] direction as an initial state for the CG routine.

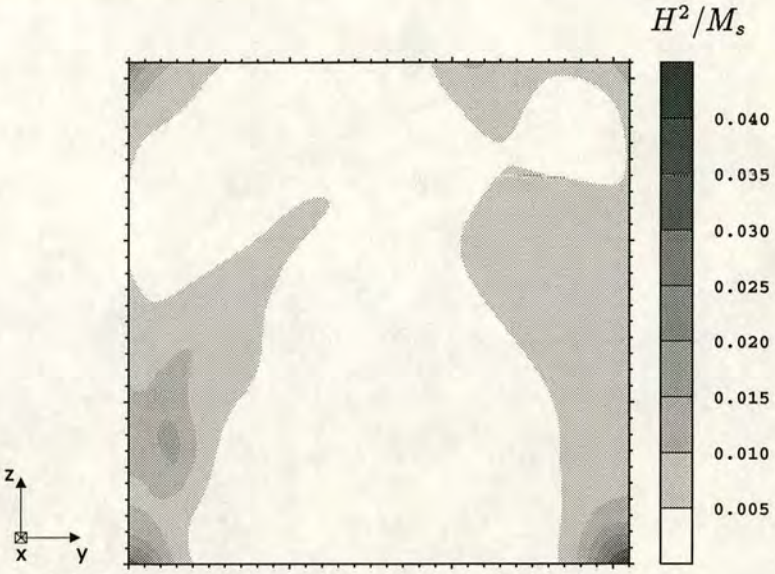


(a) Simulated Bitter pattern for state **D**

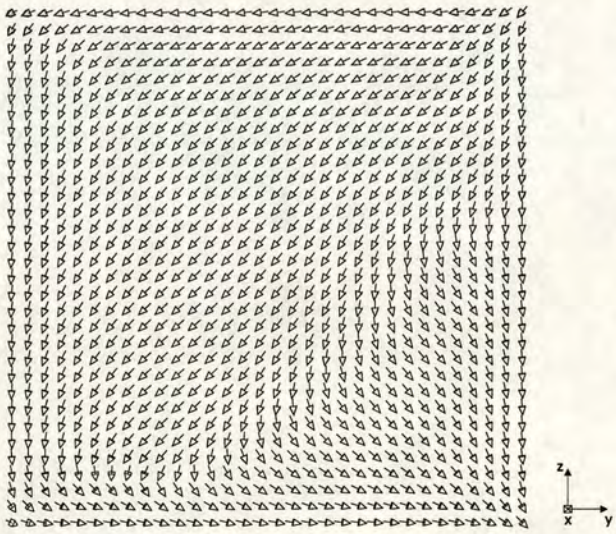


(b) Magnetization vectors, $x = 32$ plane

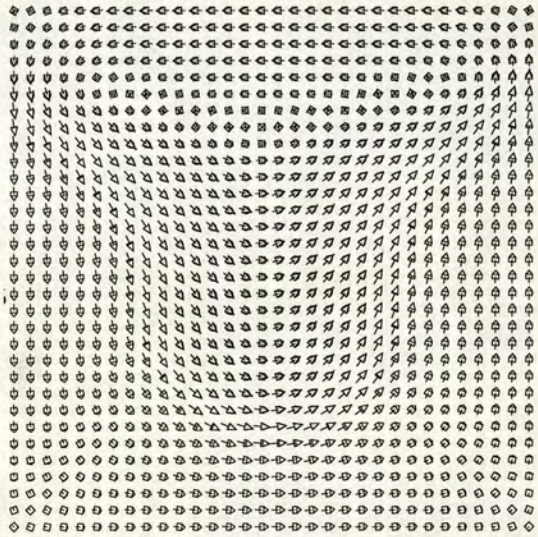

(c) $x = 16$ plane

**Figure 5.13.** Surface magnetization and simulated Bitter pattern for the $1\mu$m state (**D**). The difference between the surface magnetization and the interior magnetization results in a Bitter pattern which is neither representative of the interior nor the surface magnetization.

## 5.3 Critical grain size

Figure 5.14 compares results for increasing and decreasing grain sizes for grains between 0.01$\mu$m and 0.4$\mu$m. The values for grains decreasing in size are shown as a dotted line and were calculated by using state **C** as an initial state at 0.3$\mu$m. An equilibrium state was calculated and this state used as an initial guess at 0.28$\mu$m. This was repeated in steps of 0.02$\mu$m down to 0.1$\mu$m and then in steps of 0.01$\mu$m down to 0.01$\mu$m.

The magnetization remains in a vortex state from $d = 0.4\mu$m to $d = 0.07\mu$m, figures 5.15a and 5.15b show that the vortex state remains well defined but the magnetization becomes progressively aligned in the [100] direction and more surface charges occur at the corners. At $d = 0.06\mu$m and $d = 0.05\mu$m the magnetization changes from a vortex to a flower state aligned along the [101] direction as shown in figure 5.15c. Between $d = 0.04\mu$m and $d = 0.01\mu$m the magnetization occupies a uniform SD state aligned along the [101] direction as shown in figure 5.15d. An important point is that the vortex state changes to a [101] SD state which is a lower energy state than the original [001] SD state. This is a result which occurs in high resolution models but not low resolution models as low resolution models transfer from a vortex state to a [001] SD state.

Figure 5.14a shows that the energy for the vortex state never exceeds that of the flower state. These results predict a definite critical size for magnetite in cubic grains; vortex states exist only in grains larger than 0.07$\mu$m and are more energetically favourable than SD states for all grains larger than 0.07$\mu$m.

One of the important parameters in the CG routine routine is the initial step. `Dfpred` is a scalar factor which determines the angle about which the vectors are first rotated along the direction of steepest descent. There is no guarantee that as the grain size decreases the CG routine remains in an LEM state. The initial step may 'tunnel' through an energy barrier and then find a separate LEM state. Figure 5.16 shows a sketch of two possible situations as the grain size is decreased from $d = 0.07\mu$m to $d = 0.06\mu$m. To test whether the vortex state is unavailable below 0.07$\mu$m the transition from 0.07$\mu$m to 0.06$\mu$m was repeated using several values for `dfpred`. The same transition from a vortex state to a flower to a SD state occurred for a range of values of `dfpred`.

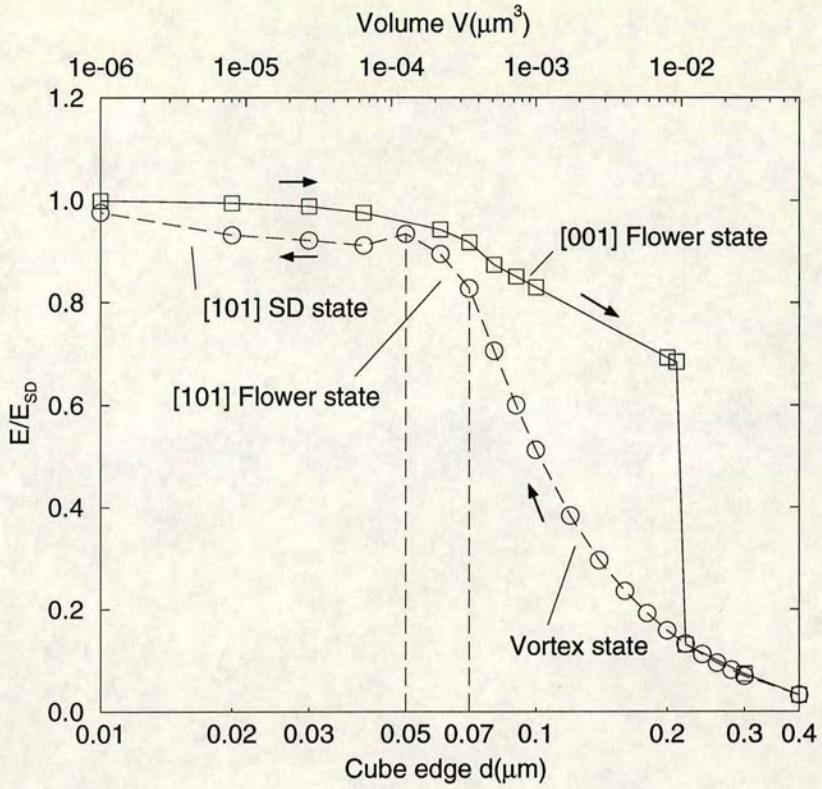


(a)

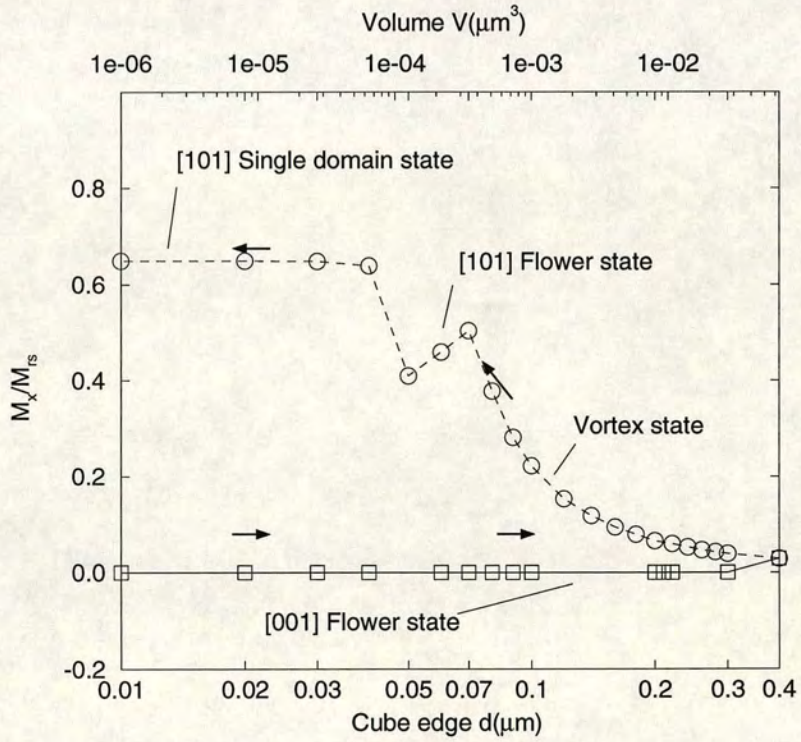


(b)

**Figure 5.14.** (a) Normalised energy and (b) [100] magnetization components as a function of grain size showing a transition from vortex states to SD states as the grain size decreases.

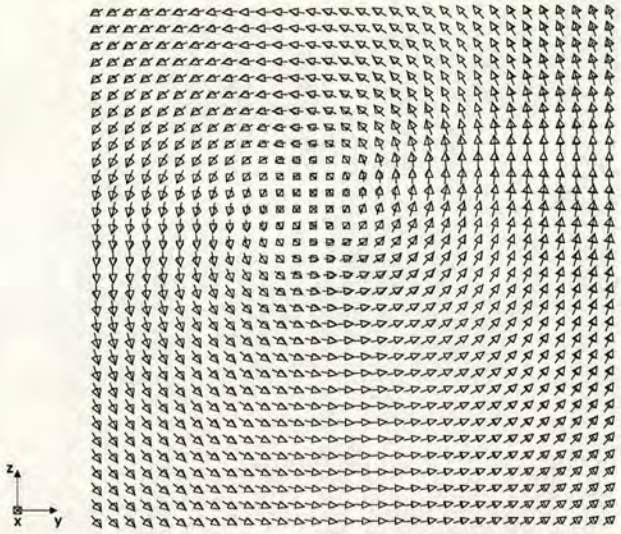

(a) $d = 0.1\mu$m, $x = 32$ slice

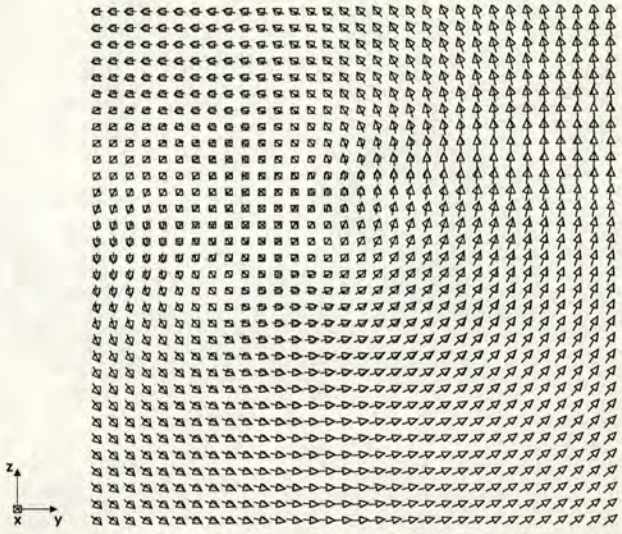

(b) $d = 0.07\mu$m , $x = 32$ slice

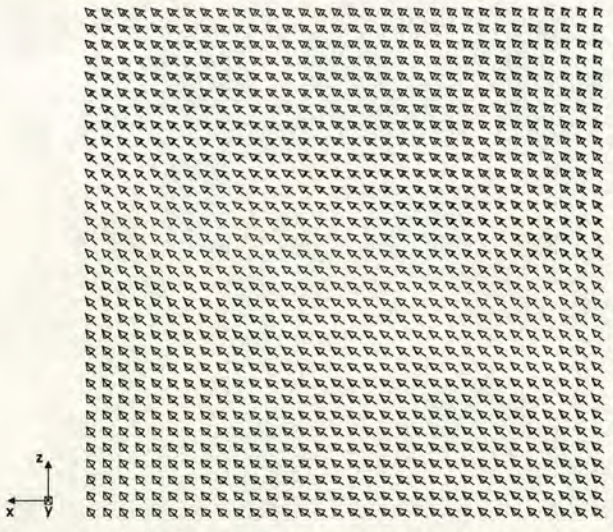

(c) $d = 0.06\mu$m, $y = 1$ slice

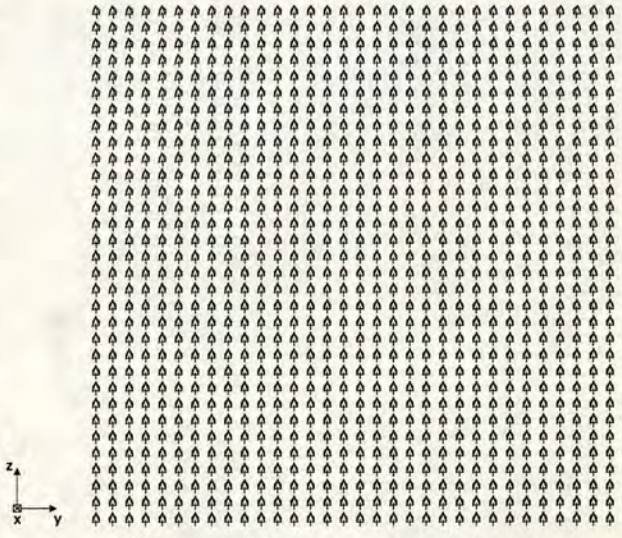

(d) $d = 0.01\mu$m , $x = 32$ slice

**Figure 5.15.** Arrow plots for grains decreasing in size, (a,b) vortex states, (c) [101] flower state with deflection at the corners, (d) [101] single-domain state

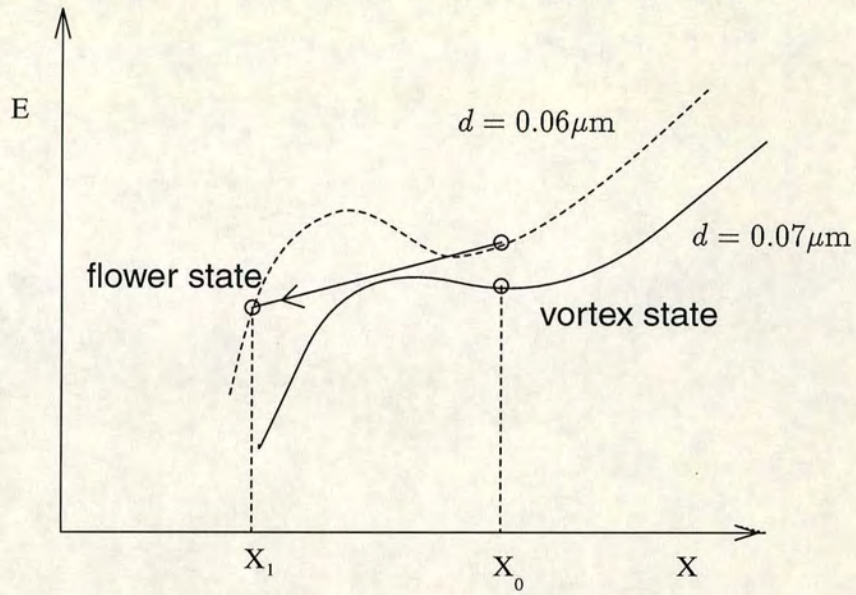


(a) Vortex state exists at $0.06\mu$m

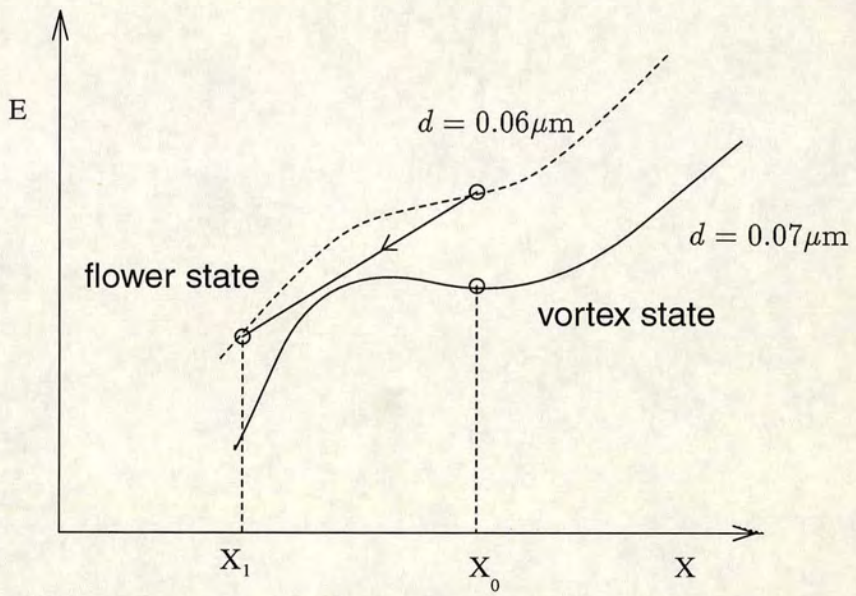


(b) Vortex state doesn't exist at $0.06\mu$m

**Figure 5.16.** Schematic energy surfaces showing two possible situations as the grain size is decreased from $d = 0.07\mu$m to $d = 0.06\mu$m, (a) what may happen if the initial conjugate gradient step is too large and the vortex state exists at $0.06\mu$m. The initial step is too large and the magnetization tunnels through to another LEM state. (b) What actually happens is that the LEM state disappears at the smaller size of $d = 0.06\mu$m.

## 5.4 Solution for a $4\mu m$ grain, $64 \times 64 \times 64$ model

An equilibrium magnetization state at $d = 4\mu$m was obtained by minimizing from a SD initial state using a resolution of $64 \times 64 \times 64$. Figure 5.17a shows that the magnetization at the surface of the grain contains similar features to those seen in experimental domain observations on larger grains. The main feature of the surface plot are three well defined domains which are aligned parallel to the grain surface and along the $[01\bar{1}]$, $[0\bar{1}\bar{1}]$ and $[01\bar{1}]$ intermediate directions. The basic geometry of the domains is similar to the three domain surface state shown in figure 5.12c but with increased detail. For example, figure 5.17a shows 4 small domains at the edge of the grain marked by an asterix. These are features which are similar to the spike domains seen in figure 1.2, although the domains in figure 5.17a are less angular and more rounded. Vortex states which dominated the magnetization in smaller grains have become localized features which nucleate domain walls. These localized vortices are similar to the knots seen in state **D** and figure 5.17a points out one of these knots, the other being on the opposite side of the grain. It is interesting to note that at $4\mu$m it is favourable for some domain walls to extend to the edge of the grain, e.g the domain wall at the top of figure 5.17a. This contrasts with the magnetization in state **D** in which the magnetization along each edge forms an unbroken line.

The three domains in figure 5.17a are surface patterns which only extend $0.6\mu$m into the interior of the grain. Figure 5.17b shows the extent to which the $[0\bar{1}\bar{1}]$ domain in figure 5.17a extends into the grain and also shows that the magnetization in the centre of the grain consists of four lamellar domains. These four lamellar domains in the centre of the grain are aligned along the easy $\langle 111 \rangle$ directions. Figure 5.17b also shows a small closure domain. These are the first results for magnetite which clearly show several well defined lamellar domains.

Figures 5.17b-d show a progression from the centre of the grain through to the surface. Figure 5.17c shows that 1/4 of the way through the grain the magnetization consists mainly of four $\langle 111 \rangle$ domains which rotate around a central line. Figure 5.17d shows that the surface magnetization is composed of $\langle 110 \rangle$ domains separated by curved domain walls.

Figure 5.18 shows that the simulated Bitter patterns are neither representative of either the the interior $\langle 111 \rangle$ domains nor the surface $\langle 110 \rangle$ domains. The only feature which is picked up is the point in the centre of the grain where the 4 domain walls meet (figures 5.17d and 5.18c).

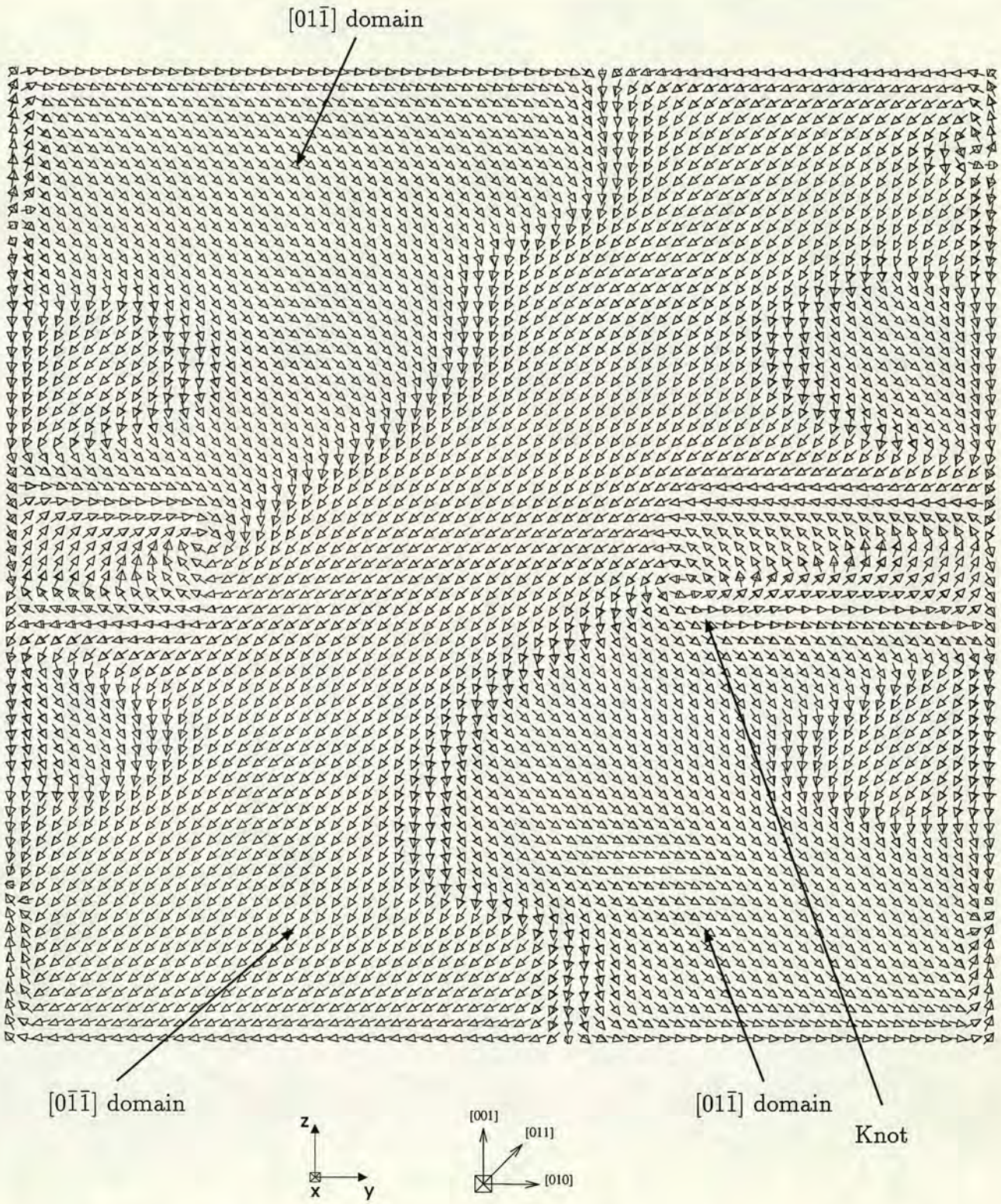


**Figure 5.17.** (a) Surface magnetization state of a 4$\mu$m grain using a $64 \times 64 \times 64$ resolution, $x = 64$ slice.

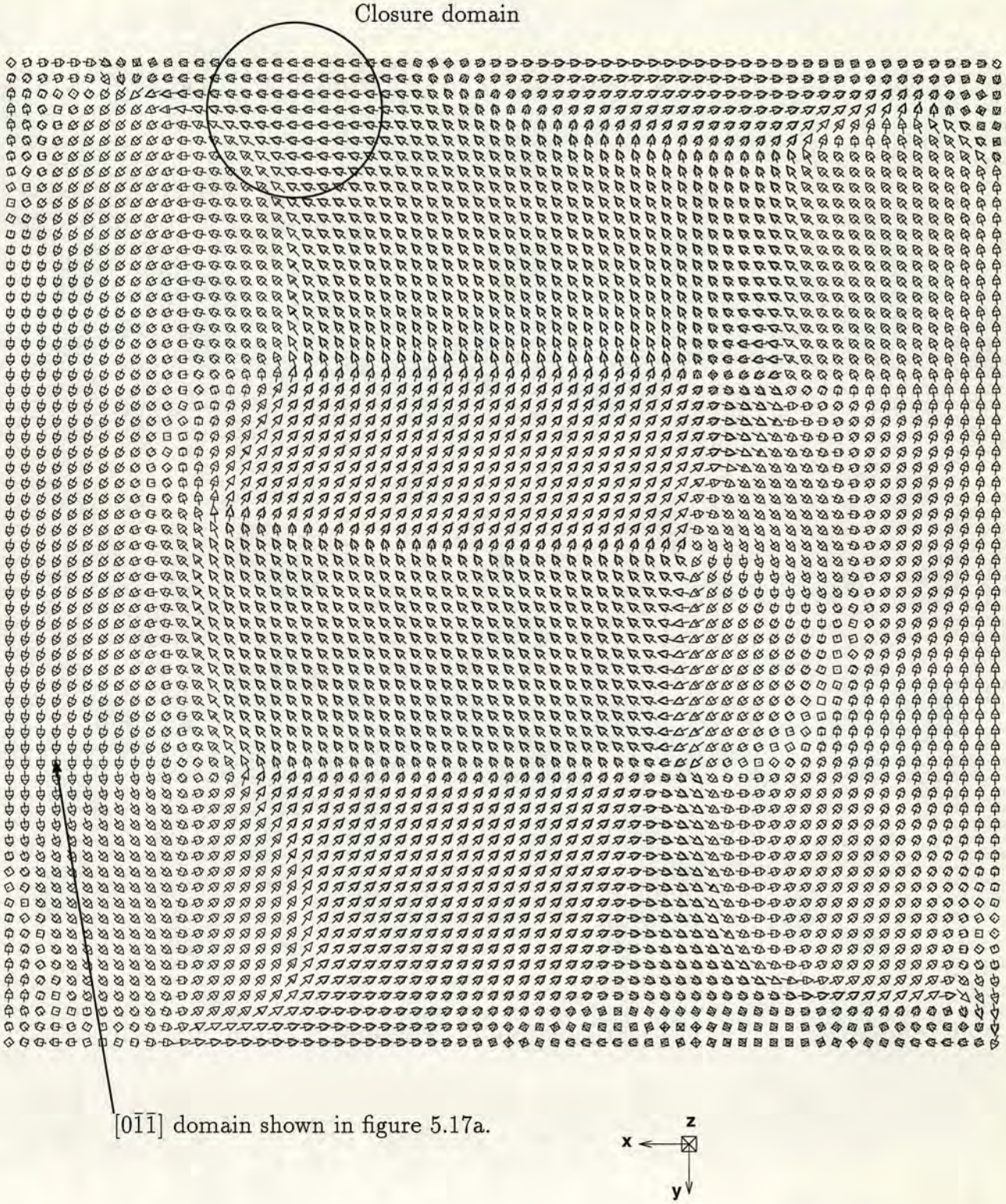


**Figure 5.17** (b) $z = 32$ slice

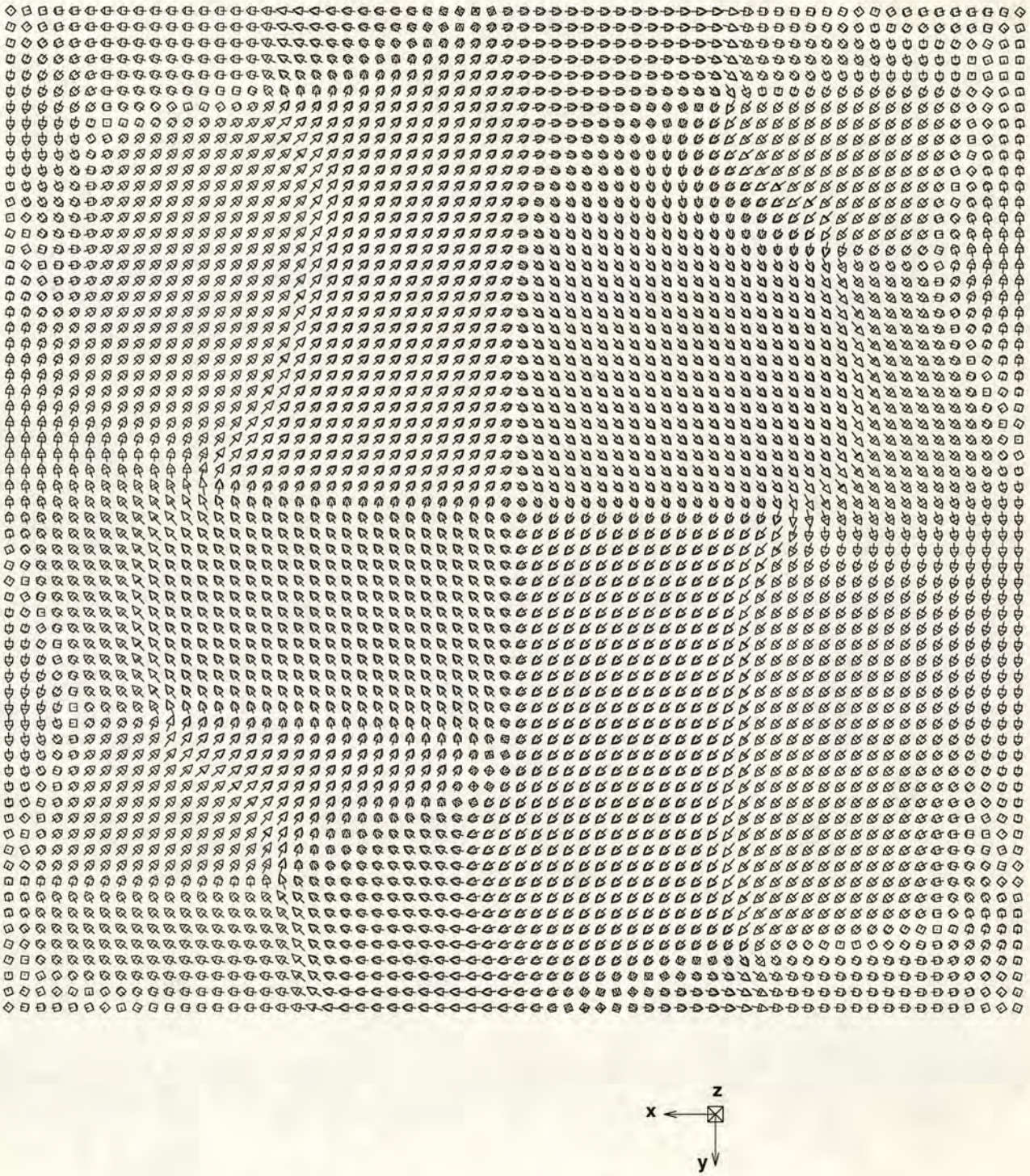


**Figure 5.17** (c) $z = 16$ slice

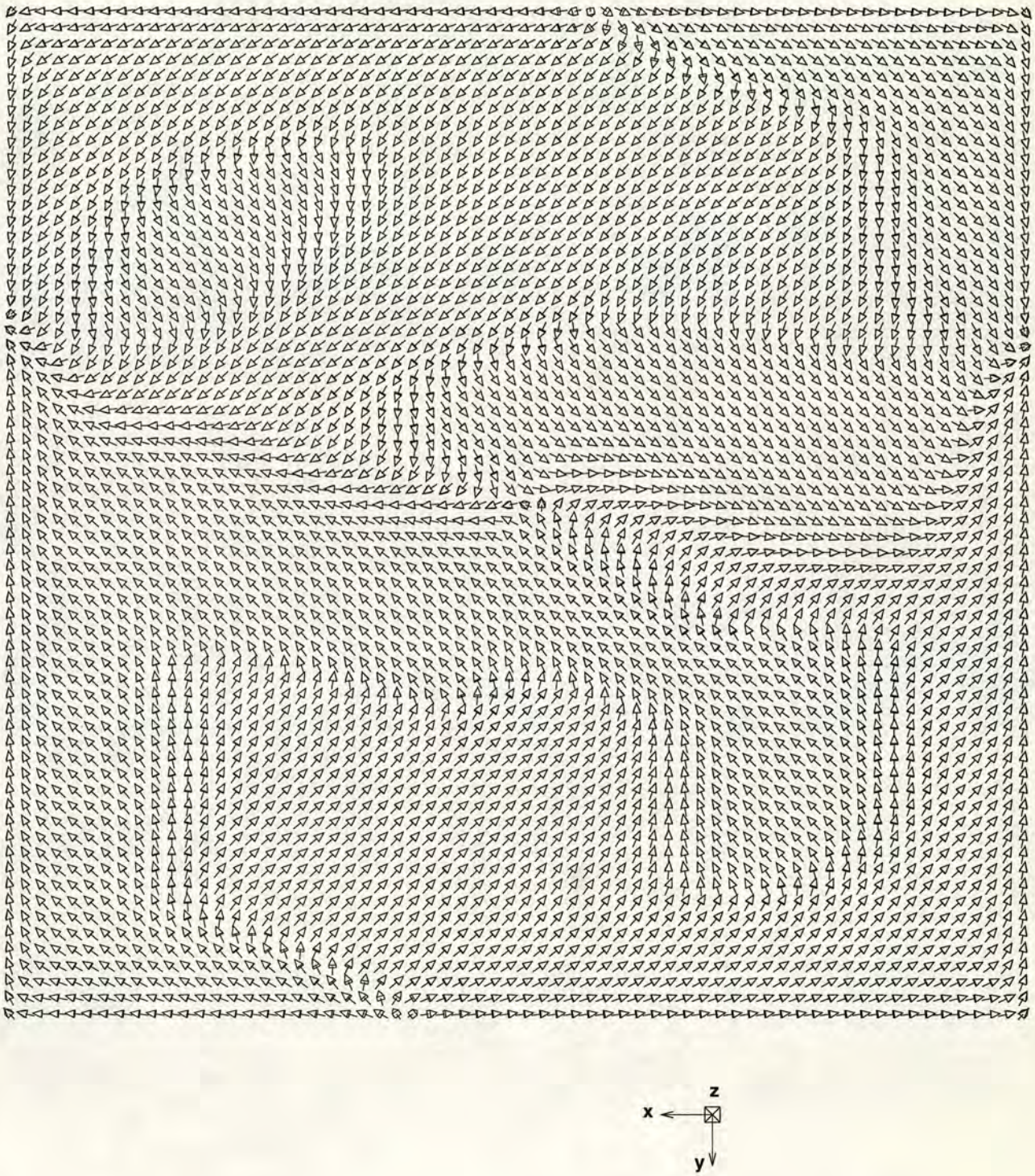


**Figure 5.17** (d) $z = 1$ slice

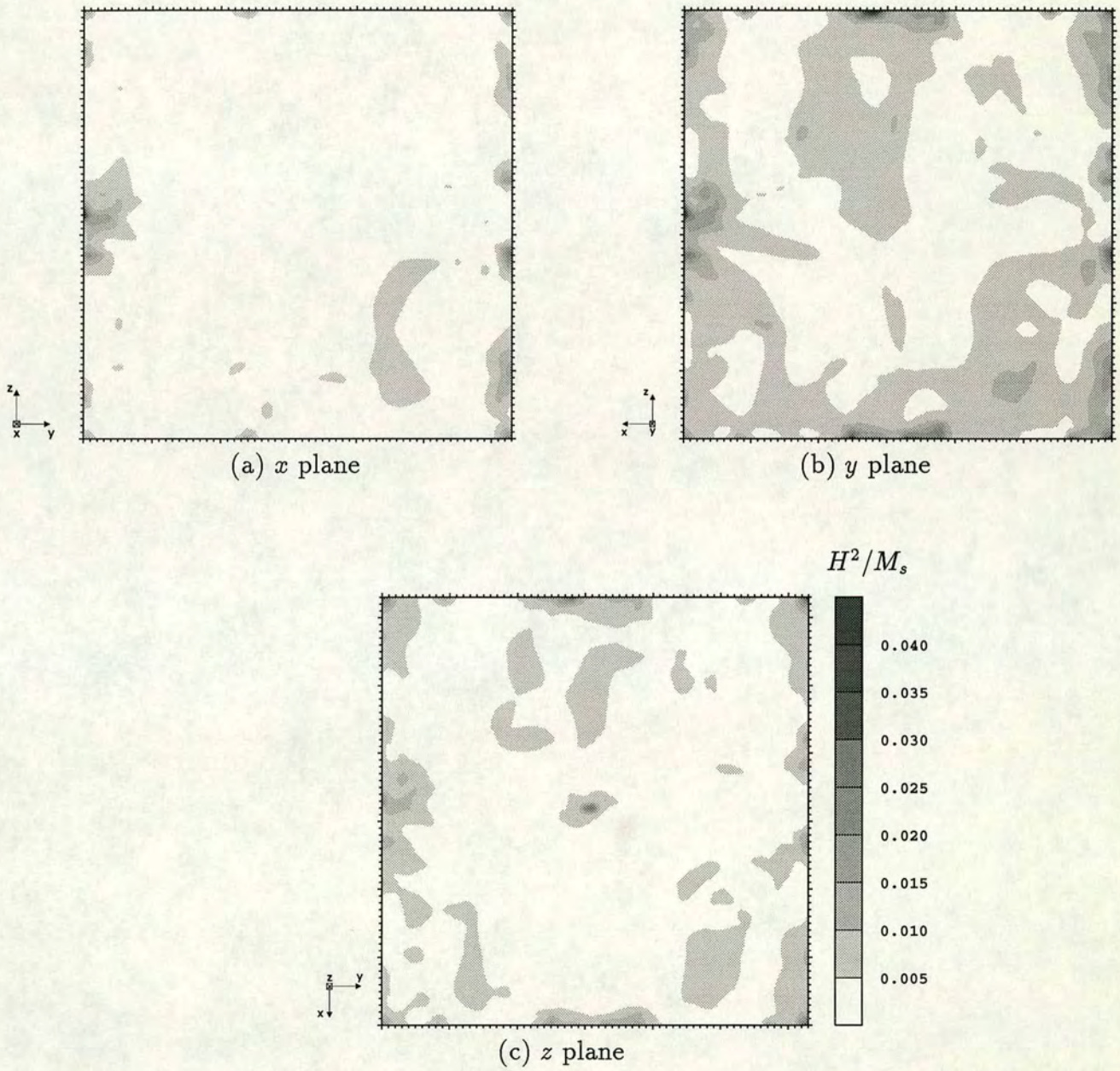


(a) $x$ plane

(b) $y$ plane

(c) $z$ plane

**Figure 5.18.** Bitter pattern predictions for the $4\mu$m structure shown in figure 5.17.

## 5.5 Effect of modifying the anisotropy constant

Results in the previous section showed that magnetization states in larger grains show complicated states as $E^d$ and $E^a$ aligns the magnetization along the $\langle 110 \rangle$ directions at the surface and $E^a$ aligns the magnetization in the $\langle 111 \rangle$ directions in the interior of the grain. The directions of the easy axes can be controlled by varying the anisotropy constant, $K_1$. A negative value for $K_1$ results in easy axes along the $\langle 111 \rangle$ directions and a positive value for $K_1$ results in easy axes along the $\langle 100 \rangle$ directions.

Figure 5.19 shows how the magnetization depends on the value of $K_1$, keeping $M_s$ and $C_e$ constant. As $K_1$ changes from negative to positive there is a corresponding change from the state **D** to the four-closure-domain state shown in figure 5.19d. This four-closure domain state is a $2d$ pattern which extends through the grain in the $x$ direction. In contrast to state E which has different magnetization directions at the surface and in the interior, the positive anisotropy constant controls the magnetization to align along the $\langle 100 \rangle$ directions throughout the grain. Using the state shown in figure 5.19d as an initial state for the CG routine and using $K_1 = -1.25 \times 10^4 \mathrm{Jm}^{-3}$ (the value for magnetite) results in state **D** again; this shows that the classical four-closure-domain state is unstable for magnetite. Furthermore, the four-closure-domain state is identical to that calculated by Xu *et al* (1994) who attempted to model a cubic magnetite grain using the $2d$ scheme shown in figure 3.2c. From the $3d$ results presented, the four-closure-domain state is unavailable to magnetite and attempts to model cubic grains by $2d$ models introduce an artificial anisotropy and thus have to be regarded as fundamentally limited to modelling thin films.

Figures 5.20 and 5.21 show similar results using the material constants for iron with $K_1 = 4.8 \times 10^4 \mathrm{Jm}^{-3}$, $M_s = 17 \times 10^5 \mathrm{Am}^{-1}$ and $C_e = 2.43 \times 10^{-11} \mathrm{Jm}^{-1}$. Both results show well defined Bitter patterns which are similar to those seen experimentally. These two results show that the lack of clear domain walls in the simulated Bitter patterns for magnetite are a result of the inhomogenous magnetization and not of any possible error in the calculation of the stray field. Williams and Dunlop (1990) calculated magnetization states for a $1\mu$m magnetite grain using a $12 \times 12 \times 12$ model and found states which were similar to figure 5.21, suggesting that low resolution $3d$ models also artificially constrain the magnetization states. In low resolution models, the magnetostatic energy aligns the magnetization parallel to the $\langle 100 \rangle$ directions at the surfaces, but in addition, incorrectly extends the $\langle 100 \rangle$ domains to the centre of the grain.

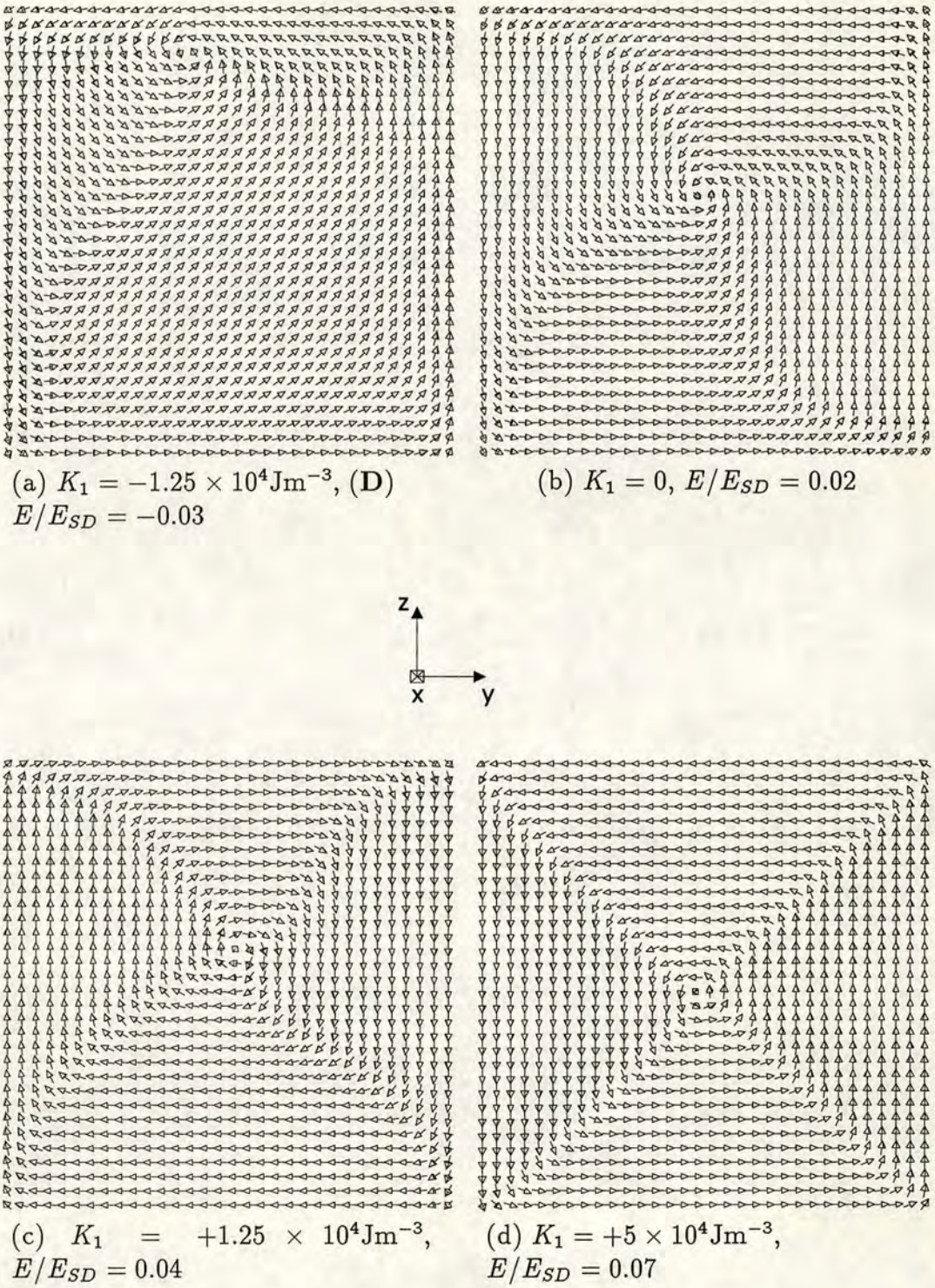


(a) $K_1 = -1.25 \times 10^4 \mathrm{Jm}^{-3}$, (**D**) $E/E_{SD} = -0.03$

(b) $K_1 = 0$, $E/E_{SD} = 0.02$

(c) $K_1 = +1.25 \times 10^4 \mathrm{Jm}^{-3}$, $E/E_{SD} = 0.04$

(d) $K_1 = +5 \times 10^4 \mathrm{Jm}^{-3}$, $E/E_{SD} = 0.07$

**Figure 5.19.** Dependence of the magnetization on the magnetocrystalline anisotropy constant, $K_1$ for a 1$\mu$m grain with $M_s$ and $C_e$ as for magnetite. All slices shown are the $x = 32$ top surface.

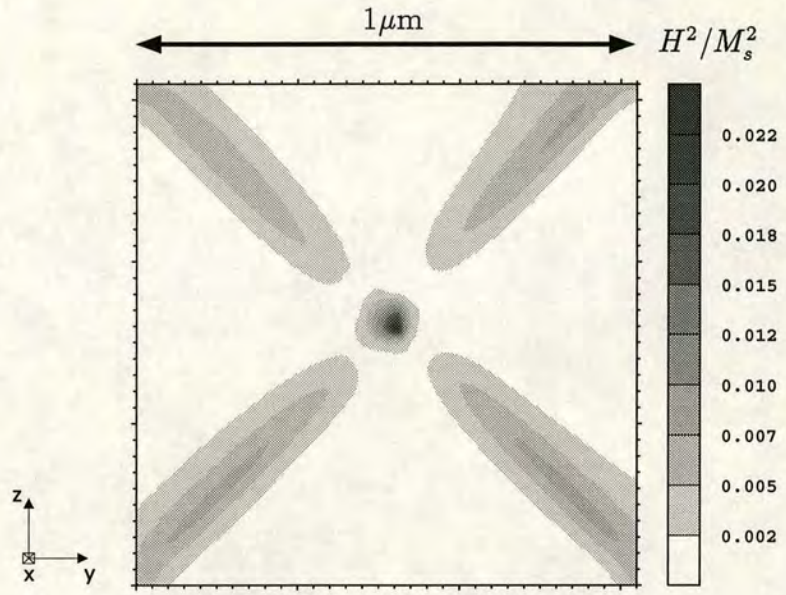


(a) Simulated Bitter pattern.

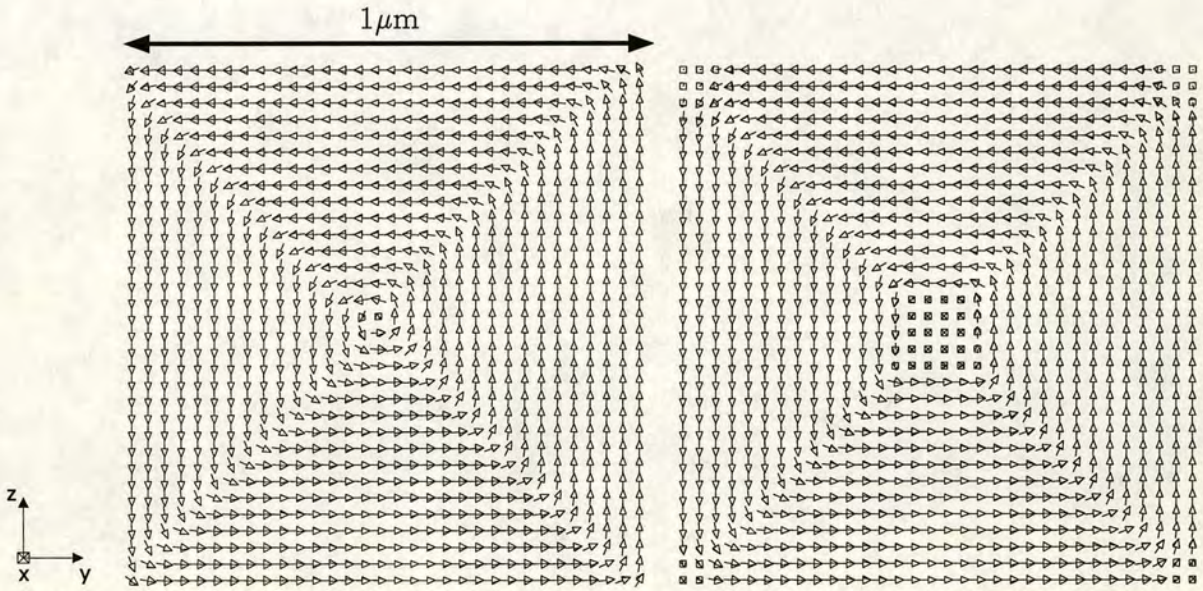


(b) Magnetization vectors, $x = 32$ plane (c) $x = 16$ plane

**Figure 5.20.** Magnetization and simulated Bitter pattern for a 1$\mu$m cubic grain of iron, $E/E_{SD} = 0.072$. This result was obtained by using the vortex state **C** shown in figure 5.7 as an initial state in the CG routine.

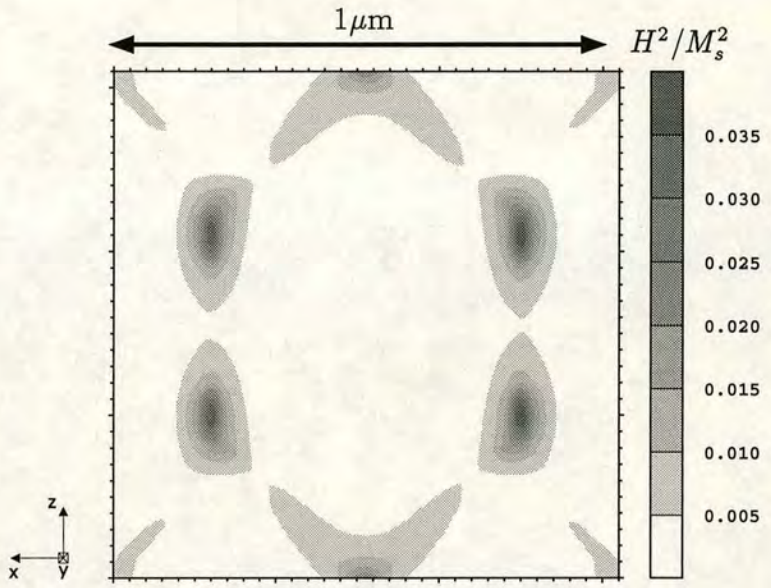


(a) Simulated Bitter pattern.

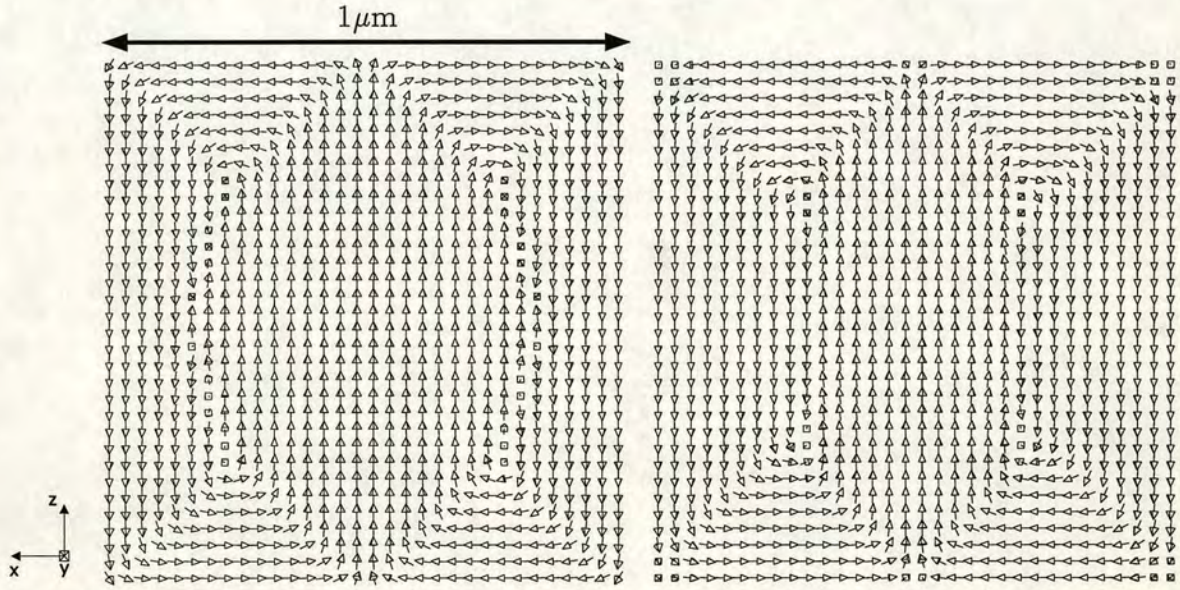


(b) Magnetization vectors, $y = 32$ plane

(c) $y = 16$ plane

**Figure 5.21.** Surface magnetization and simulated Bitter pattern for a $1\mu$m cubic grain of iron, $E/E_{SD} = 0.12$. This state was obtained by minimizing from a [001] SD initial state.

## 5.6 Results using the linear exchange formulation

Figure 5.22 shows the dependence of the energy with grain size using the same method described in section 5.2 except a linear exchange formulation was implemented instead of the 5 point formulation. Figures 5.23a and 5.23d show that as the grain size increases the same transition at $0.2\mu$m from a flower state to a vortex state occurs. The important difference is that as the grain size decreases the magnetization remains in a vortex state down to $0.01\mu$m. Figure 5.23c shows the magnetization becomes progressively aligned in the [001] direction. Although the magnetization is mostly single-domain, each corner rotates in the same sense as the vortex state in figure 5.23d.

Figure 5.22 shows that the flower state is a lower energy state than the two-domain (2D) state for grains smaller than $0.15\mu$m. As the CG routine uses a restricted search space, it may be that the 2D state is still a possible equilibrium state. In order to check this, several minimizations using a 2D state as an initial guess were calculated. Vortex states were consistently obtained at all grain sizes and therefore it is fairly certain that the 2D state is unavailable for magnetite. Furthermore three domain and four domain states were also used as initial states and similar vortex states were obtained for grains smaller than $1.0\mu$m.

Results were also calculated using the linear exchange formulation for a $64 \times 64 \times 64$ model. Instead of the domain structures shown in figure 5.17 the structures consisted of several large vortices. This shows that the micromagnetic model is sensitive to the exchange formulation and that using the stiffer 5 point exchange is important when calculating domain states in cubic grains.

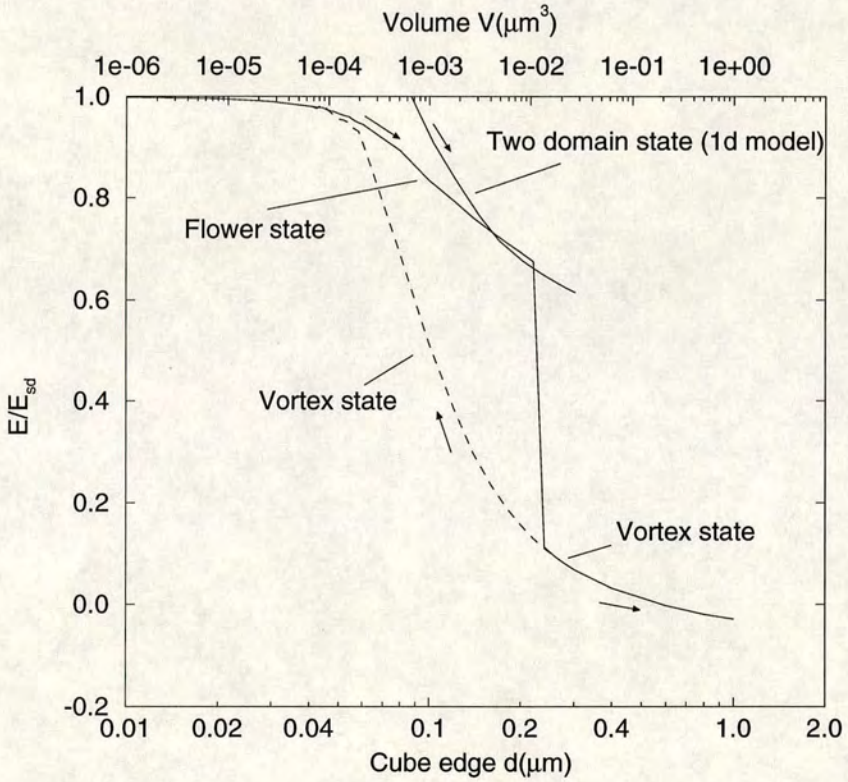


**Figure 5.22.** Normalized free energy results for cubic grains as a function of grain size using the linear exchange formulation. Solid lines represent grains grown from a $0.01\mu$m SD state with the magnetization parallel to the $z$ axis up to $1\mu$m vortex state, dashed lines are for grains decreasing in size from $0.4\mu$m down to $0.01\mu$m . The results for the two-domain state were taken from Enkin and Dunlop (1987) who also used a linear exchange formulation.

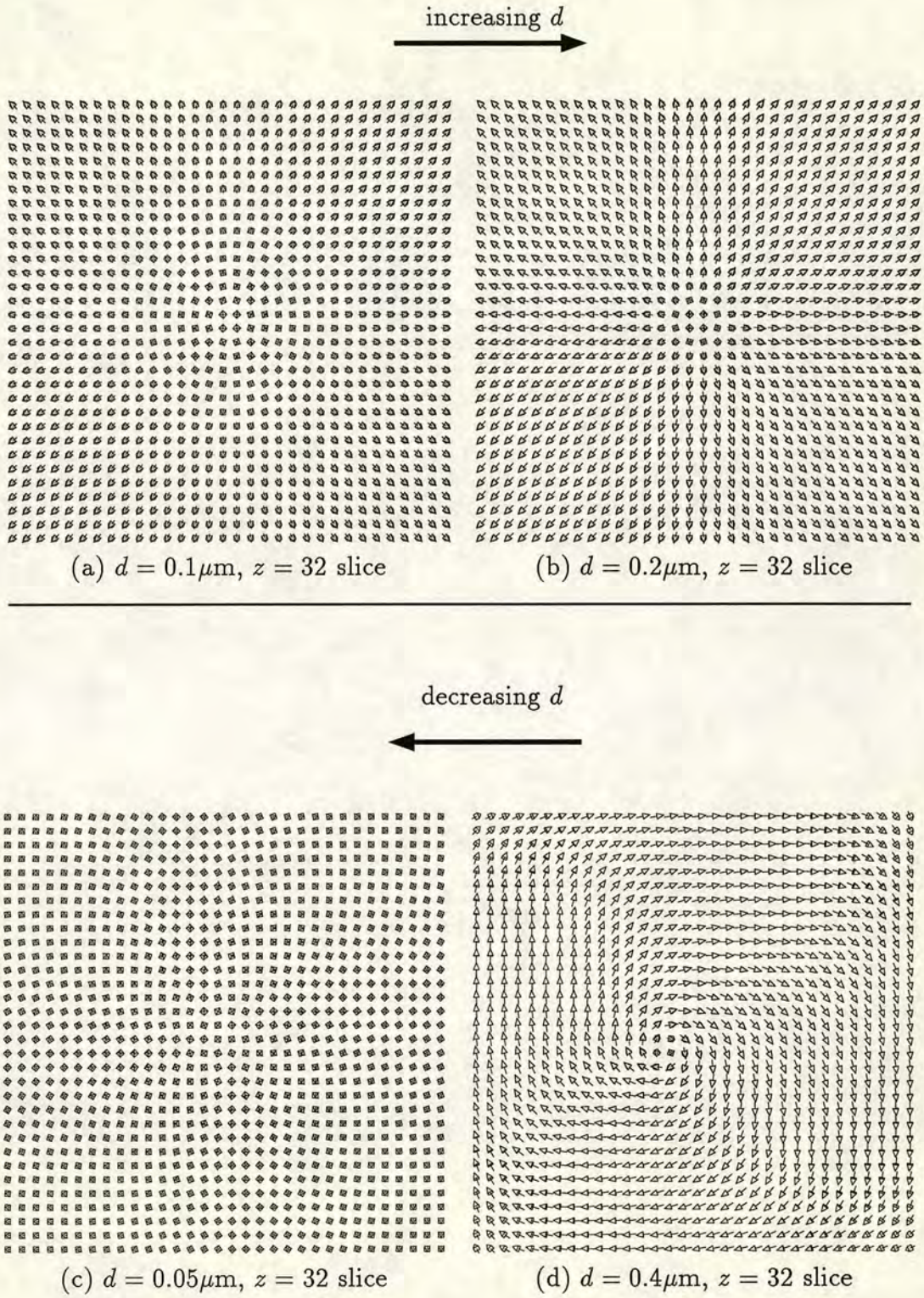


(a) $d = 0.1\mu$m, $z = 32$ slice (b) $d = 0.2\mu$m, $z = 32$ slice

(c) $d = 0.05\mu$m, $z = 32$ slice (d) $d = 0.4\mu$m, $z = 32$ slice

**Figure 5.23.** Solutions for grains of size $d = 0.2\mu$m, $0.4\mu$m and $0.05\mu$m using the linear exchange formulation (from figure 5.22)

## 5.7 Summary

- The lowest energy magnetization states as a function of grain size have been calculated as;

  Single-domain states, $d < 0.07\mu$m

  Vortex states, $0.07\mu\text{m} \lesssim d \lesssim 1\mu$m

  Domain states, $d \gtrsim 1\mu$m.

- A sketch of the progression from domain states is shown in figure 5.24. The transition from vortex states to domain states is characterized by state **D** in which a two-domain outer shell shields an interior magnetization.

- A $4\mu$m grain consists of $\langle 110 \rangle$ surface domains and $\langle 111 \rangle$ interior domains. Any vorticity in the magnetization state is confined to local regions.

- Simulated Bitter patterns do not image the domain walls due to the shallow depth of the surface domains.

- Results from calculations incorporating a positive anisotropy constant show two-dimensional magnetization states and simulated Bitter patterns image the domain walls clearly.

- Two-dimensional micromagnetic models are restricted to modelling thin films.

- The combination of a high resolution and the more accurate 5 point exchange formulation results in vortex states being unavailable in grains smaller than $0.07\mu$m.

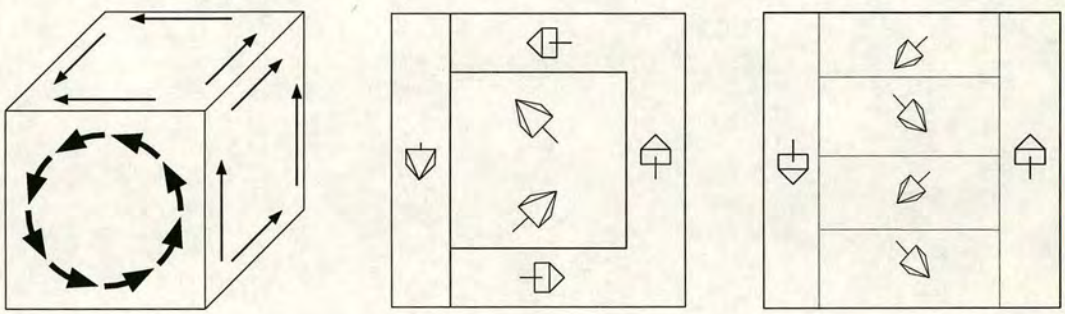

(a) $d = 0.4\mu$m, (b) $d = 1.0\mu$m, centre plane (c) $d = 4.0\mu$m centre plane

**Figure 5.24.** Sketch of how the magnetization varies as the grain size increases.

# Chapter 6. Results for non-cubic grains

## 6.1 Introduction

Magnetite occurs naturally not only in cubic forms but also in octahedral, dodecahedral and quasi-spherical forms. Laboratory grown grains such as the hydrothermal grains grown by Heider (1988) often occur as a mixture of octahedral grains and quasi-spherical grains. This chapter presents results which model the magnetization of some non-cubic magnetite grains. Equilibrium states are presented for elongated, spherical, octahedral and irregularly shaped grains and one aim of this chapter is to determine whether the shape of non-cubic grains affects the flower state to vortex state transition which occurs in cubic grains. High resolution models will also be used to compare the transition to domain states in cubic grains with the transition to domain states in octahedral grains.

This chapter also compares the total moment of octahedral states with the total moment of the cubic vortex states presented in chapter 5. Although the total moment for each of the vortex states presented in chapter 5 are low compared to the experimental values, the moments of the domain states at saturation remanence are required in order to compare with experimental measurements of $M_{rs}/M_s$. This also applies to the states presented in this chapter and simulated hysteresis curves which predict values for $M_{rs}/M_s$ for both cubic and octahedral grain are described in chapter 7.

## 6.2 Elongated grains

Figure 6.1 shows results for rectangular parallelepiped grains. These results were calculated using a rectangular parallelpiped geometry as a base model instead of a cubic geometry. The magnetization was calculated at a range of increasing grain sizes by incrementing in steps of $0.01\mu$m from $0.01\mu$m up to $0.1\mu$m and then in steps of $0.1\mu$m up to $0.4\mu$m. A SD state was used as an initial state at $0.01\mu$m and the solution was then used as an initial state at the next grain size. The same flower state to vortex state transition which is seen in cubic grains occurs at approximately the same grain size of $d = 0.2\mu$m.

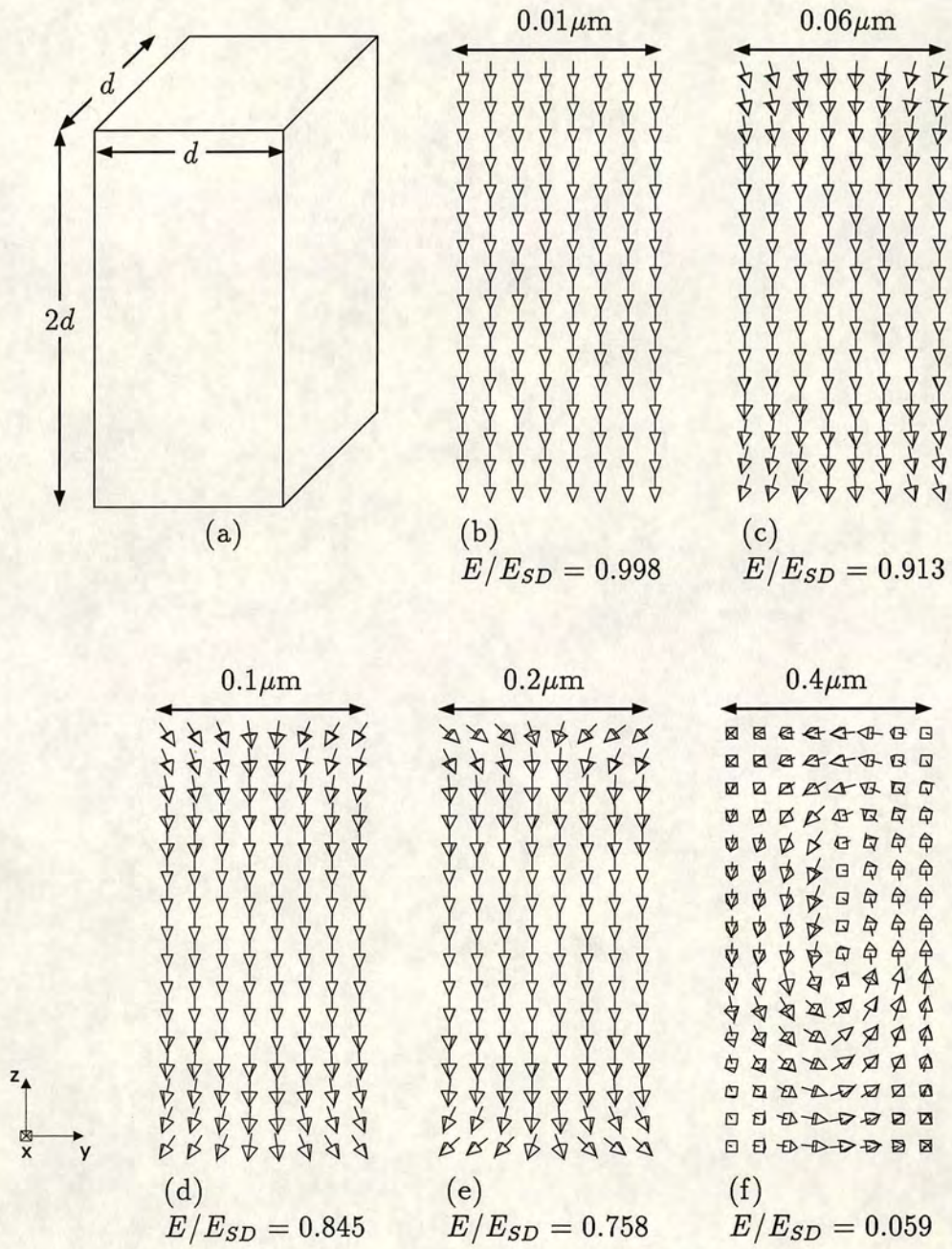


**Figure 6.1.** Magnetization states for an elongated grain using a resolution of $16 \times 8 \times 8$ sub-cubes, all slices are the $x = 4$ midplane.

## 6.3 Spherical grains

Spherical grains were used to to test the masking procedure outlined in section 4.6. It can be shown that because of a uniform demagnetizing field, the magnetization state in a perfect sphere occupies a uniform SD state (Brown 1978). For any computational model with an associated finite resolution only imperfect spheres can be modelled and these will have some flat faces and 'corners' due to the underlying cubic system. If the resolution of the computational model is fine enough then a numerical SD state should have a uniform magnetization. Figure 6.2 shows the result for a 0.1$\mu$m spherical grain and after minimization the grain still occupies a perfect SD state. The flowering which is seen in the 0.1$\mu$m cubic grain (figure 5.2) does not occur in the numerical model showing that the computational model agrees with analytic theory.

Figure 6.3 shows the result for a 0.5$\mu$m spherical grain using a vortex as an initial state. The equilibrium state is a similar vortex state to the initial state showing that vortex states can also exist in spherical grains. Spherical grains have been seen in natural magnetite samples by Saffer and McCabe (1992) and Amin and Matijević (1987).

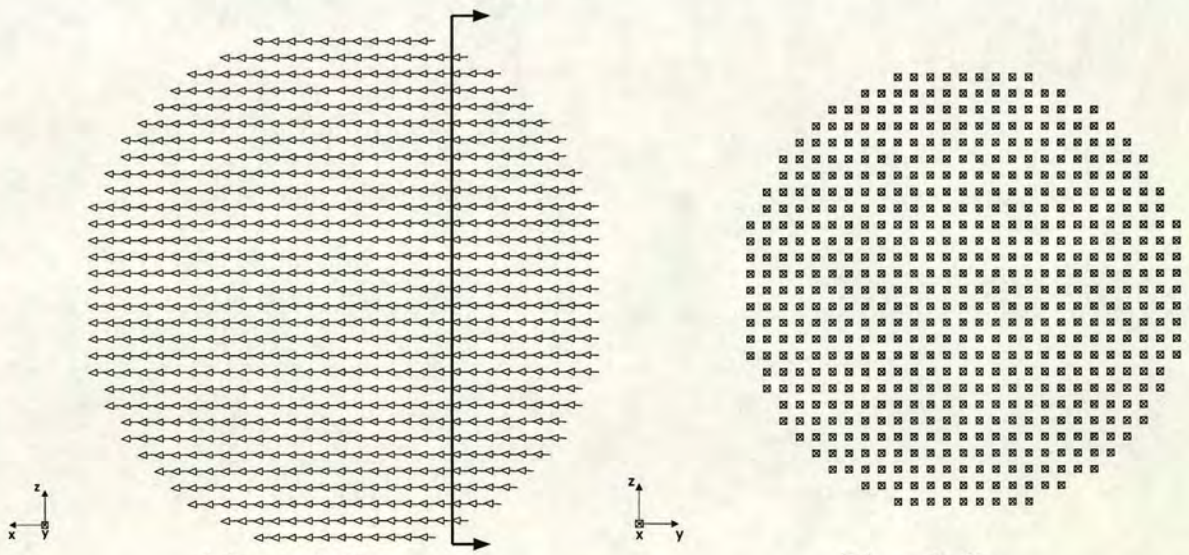

(a) y=16 slice (b) x=8 slice

**Figure 6.2.** Magnetization state for a 0.1$\mu$m spherical grain, The minimization routine is unable to change the initial uniform structure due to the uniform internal demagnetizing field, $M_x = 0.99974$. The arrows in figure (a) show the orientation of the $x = 8$ slice.

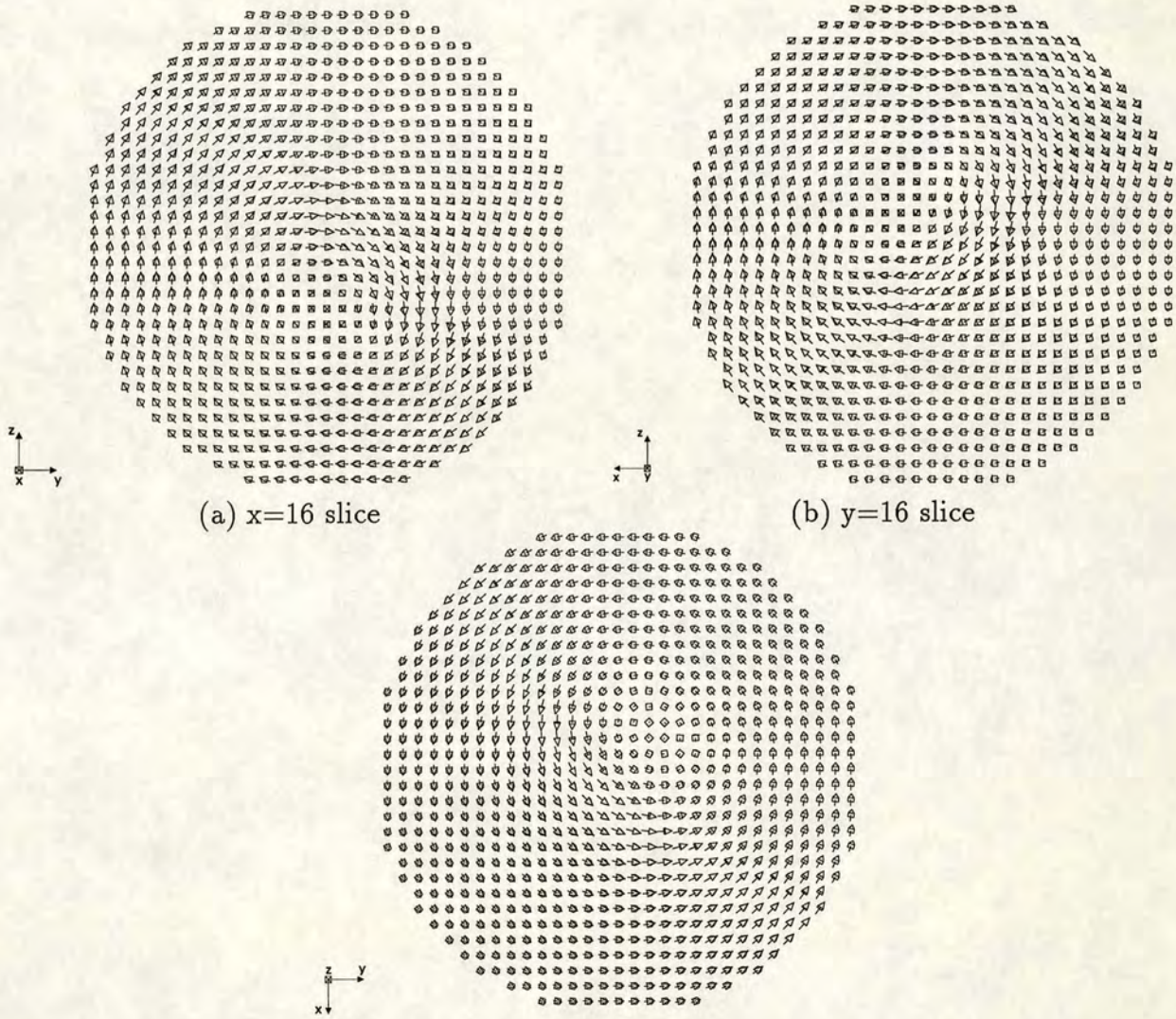

(a) x=16 slice

(b) y=16 slice

(c) z=16 slice

**Figure 6.3.** Magnetization state for a 0.5$\mu$m spherical grain in a vortex state.

## 6.4 Octahedral grains

The efficiency of the masking algorithm is proportional to the ratio of the magnetic to non-magnetic sub-cubes. Therefore one aim in determining a particular masking scheme is to reduce the number of non-magnetic or 'masked out' sub-cubes. Figure 6.4a shows the geometry for regular octahedral magnetite in which each of the {111} crystal faces makes an angle, ($\psi_{oct}$) of 54.74° with the $xy$ plane. Regular octahedral grains have a high aspect ratio, (i.e. the ratio of the height to the width of the square base) and so the ratio of the volume of the octahedral to the surrounding cube ($V_{oct}/V_c$) is only 1/6. Figures 6.4b,c show geometries for the two octahedral models described in this section. These two models are approximations to a regular octahedral and increase the ratio $V_{oct}/V_c$ (and therefore the computational efficiency) at the expense of reducing the aspect ratio.

Figure 6.4b shows a geometry, referred to as a 45° octahedral model, in which the octahedral faces are parallel to the $z = y$, $z = -y$, $z = x$ and $z = -x$ planes. One aim of this section is to compare high resolution results with those by Thomson (1993) who used a similar 45° octahedral model with a resolution of $n = 11$. Another approach suggested by K. Fabian (pers. comm.) is to construct an octahedral from the largest square that will fit into a cube. Figure 6.4c shows the geometry of this octahedral, referred to as a $V_{max}$ octahedral and the orientation of the largest square (shaded gray). This geometry increases $V_{oct}/V_c$ at the expense of moving the faces further away from that of a regular octahedral, as shown by the variation of $\psi_{oct}$ in table 6.1.

| | $\psi_{oct}$ | $V_{oct}/V_c\,(n=\infty)$ | $V_{oct}/V_c\,(n=32)$ | $\theta_a$ | $\phi_a$ |
|---|---|---|---|---|---|
| Regular octahedral | 54.74° | 1/6 | 0.1825 | 0 | 0 |
| 45° octahedral | 45° | 1/3 | 0.365 | 45° | 0 |
| $V_{max}$ octahedral | 39.26° | 0.5625 | 0.563 | 45° | $-\cos^{-1}(1/3)$ |

**Table 6.1.** Summary of octahedral geometries, $\psi_{oct}$ is the angle the crystal faces make with the $xy$ plane, $V_{oct}/V_c$ is given for an infinite resolution and for a resolution of $n = 32$ and $\theta_a$ and $\phi_a$ are the angles used to rotate the coordinate system in order to modify the magnetocrystalline anisotropy. The transformation matrix is given in appendix E.

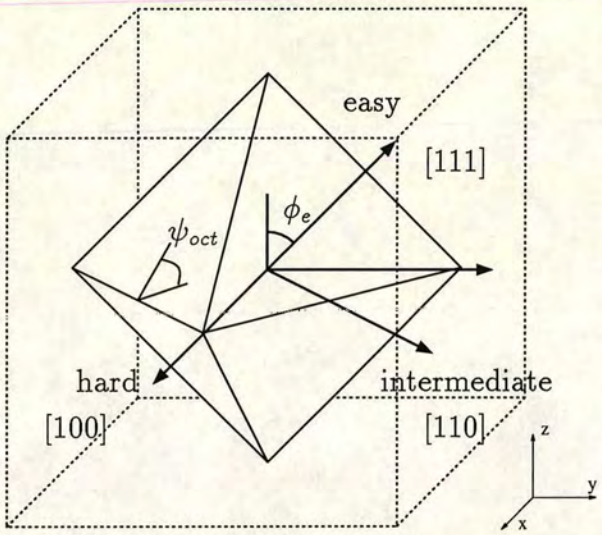


(a) Regular octahedral form for magnetite.

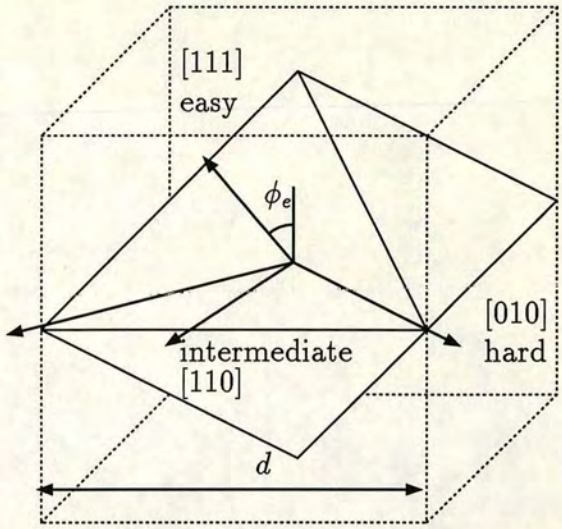


(b) 45° octahedral

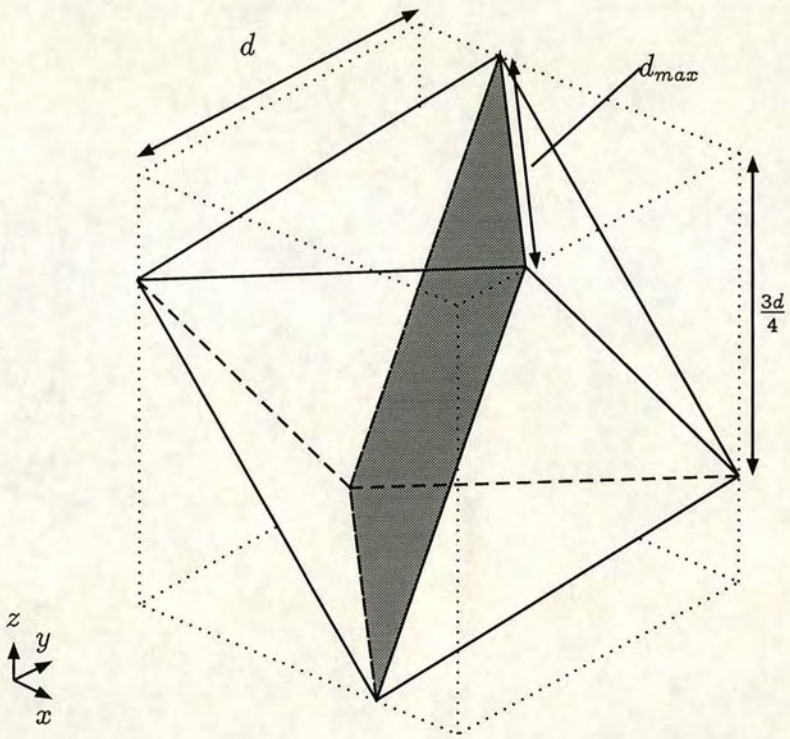


(c) $V_{max}$ octahedral

**Figure 6.4.** (a) True geometry for octahedral magnetite and (b,c) the approximations described in this study. All the vertices of the $V_{max}$ octahedral intersect the cube at a distance $3d/4$ from the corner of the cube. The latitudinal angle for the magnetocrystalline easy axis, $\phi_e = 54.74$ is shown for the regular octahedral and the 45° model. The length of the base for the $V_{max}$ octahedral is labelled as $d_{max}$ and as $d_{max}$ is close to $d$ the two will not be distinguished ($d_{max} = 1.06d$).

### 45° octahedral model

The magnetocrystalline anisotropy for a regular octahedral is a cubic anisotropy with the magnetocrystalline easy ⟨111⟩ axes at 90° to the {111} crystal faces. The cubic anisotropy easy axes are shown in figure 6.4b and were obtained by rotating the anisotropy axes used in the cubic model by 45° in the $xy$ plane. This results in the easy ⟨111⟩ directions making an angle of 99.73° with the crystal faces. It will be shown later in this section that the difference between this and the 90° required for the regular octahedral is insignificant compared to the octahedral shape anisotropy. The $x$ and $y$ directions now become intermediate ⟨110⟩ directions and the diagonals in the $xy$ plane become the hard ⟨100⟩ directions. The same convention for cubic grains will be used so that for a SD state along the hard direction, $E^a = 0$ and along the easy or intermediate axes, $E^a < 0$.

The magnetostatic energy aims to decrease the number of free-poles at the surface of the grain and as there are twice as many free poles for a SD state in the $z$ direction (SD$z$) compared to a SD state in the $x$ direction (SD$x$) the octahedral shape introduces an additional shape anisotropy. By plotting out the magnetostatic energy of a SD state as it rotates from the $z$ direction to the $x$ direction, figure 6.5 shows that a SD$z$ is less energetically favourable than a SD$x$ state. $E^d$ is a maximum for a SD$z$ state and decreases monotonically with $\phi_{SD}$

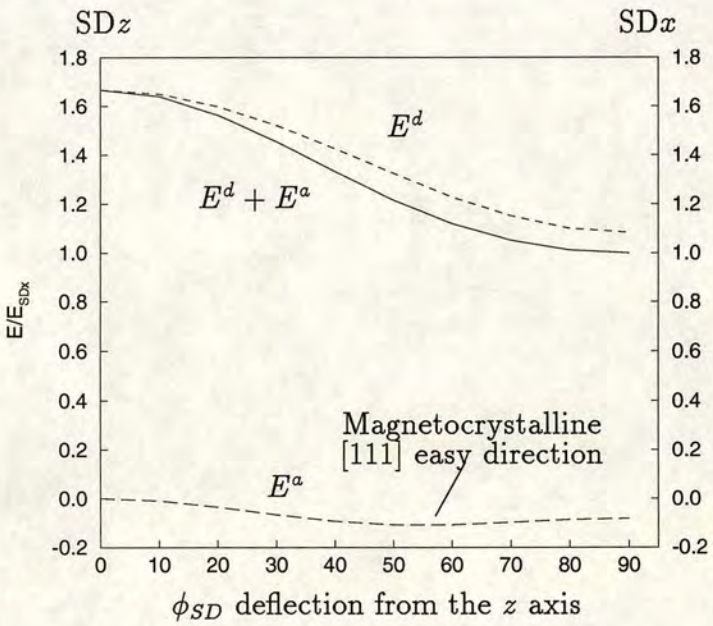


**Figure 6.5.** Dependence of the energy of a SD state on the colatitude for a 45° octahedral grain. $\phi_{SD} = 0$ represents a SD state in the $z$ direction and $\phi_{SD} = 90°$ represents a SD state in the $x$ direction.

and the difference in $E_d$ between the two extremes is an order of magnitude larger than the difference in the magnetocrystalline anisotropy. This effectively creates a hard axis in the $z$ direction and means that the magnetocrystalline easy $\langle 111 \rangle$ directions become insignificant for SD states. Although figure 6.5 does not show this, there is no variation in the magnetostatic energy when a SD state is rotated in the $xy$ plane and so the intermediate magnetocrystalline directions in the $x$ and $y$ directions are maintained.

To summarize, the combination of the shape and magnetocrystalline anisotropy results in easy axes along the $x$ and $y$ directions (equivalent to the $\langle 110 \rangle$ directions) and a hard axis in the $z$ direction.

### Results for grains smaller than $2\mu$m, $32 \times 32 \times 32$ model

Although both $x$ and $y$ directions are global minimum states for a SD state, for grains smaller than $0.1\mu$m the CG method finds a LEM state by flowering out the vectors at the corners. Using a SD state at any arbitrary direction, instead of rotating the SD state towards either the $x$ or $y$ directions the CG routine deflects the magnetization at the corners to form a flower state in the direction of the SD state. This is similar to the configurational anisotropy effect reported by Schabes and Bertram (1988) and Williams and Dunlop (1990) for cubic grains.

Figure 6.6 shows the dependence of the energy with grain size using the same method described in chapter 5. A SD$x$ state was used as an initial guess at $0.01\mu$m and the CG routine used to find a stable configuration. This solution was then used as an initial guess at $0.02\mu$m and repeated in steps of $0.01\mu$m until $0.3\mu$m and then in steps of $0.1\mu$m until $2\mu$m. The magnetization remains in a SD state until $0.05\mu$m and then changes continuously to the flower state shown in figure 6.7a. The flower state is similar to those seen in cubic grains but with the additional feature that the magnetization attempts to align parallel to the faces in order to reduce the number of free poles; this is shown by a (†) in figure 6.7a.

The magnetization changes from a flower state to a vortex state at a slightly larger grain size than in cubic grains, ($d = 0.28\mu$m compared to $0.22\mu$m for the octahedral and cubic grains respectively) but at a slightly smaller volume, ($0.008\mu\text{m}^3$ compared to $0.011\mu\text{m}^3$). Figure 6.7b shows the vortex state at $0.4\mu$m, and these results confirm that the flower state to vortex state transition is a general feature for magnetite. The total moment of the octahedral vortex state is similar to the cubic vortex state, e.g. at $d = 0.4\mu$m, $M_{tot} = 0.032$ and $M_{tot} = 0.033$ for the cubic and octahedral grains respectively. These are both approximately

2.5 times lower than the experimental measured values of $M_{rs}/M_s \approx 0.08$ (figure 2.3). As mentioned in the introduction to this chapter, it is only meaningful to compare results from simulated hysteresis curves with experimental curves and the discrepency noted above does not imply the model is invalid.

The orientation of the outer part of the vortex, shown by a (‡) in figure 6.7b is a result of the strong control that $E^d$ and $E^a$ have in maintaining a complete flux closure in the main plane. This is due to;

- the shape anisotropy prohibiting any deflection from the main $xy$ plane,
- the $\langle 110 \rangle$ directions being easy directions.

The orientation of the inner core is a result of a competition between the magnetostatic energy which favours a core aligned at 45° to the $z$ axis and the exchange energy which favours a core aligned in the $z$ direction. $E^d$ favours a core at 45° due to a combination of the $z$ direction being a hard direction and the strong control $E^d$ has in maintaining the flux closure loop in the main plane. The hard $z$ direction prevents the core aligning in this direction and the flux closure prevents the core aligning in either the $x$ or $y$ directions. Given that $E^d$ strongly favours a vortex in the $xy$ plane, aligning the core in a direction other than the $z$ direction increases the divergence and thus the exchange energy.

At $d = 0.4\mu$m, $E^d$ dominates and the core becomes aligned in the 45° direction, intermediate between the $z$ and $x$ directions. The magnetocrystalline anisotropy is not strong enough to align the core along the 54.74° easy axis as shown in figure 6.8c.

With increasing grain size the vortex core becomes less distinct and lamellar domains form along the [110] easy directions. Figures 6.9a,b and 6.10 also show how the domains arrange themselves to form the beginning of a 180° wall.

### Results for a $64 \times 64 \times 64$ model

It is possible that the step nature of the crystal faces may limit the accuracy or validity of the model. In real grains the step nature at the surface may affect the magnetization to only a few atomic unit cells below the surface, beneath which the magnetization becomes aligned in the $\langle 111 \rangle$ directions. In order to test the validity of the model the calculation for a $0.4\mu$m grain was repeated with an increased resolution of $64 \times 64 \times 64$ sub-cubes and exactly the same vortex state was obtained. At $0.4\mu$m a resolution of $n = 64$ results in a sub-cube length of

$\Delta = 62$Å or 6 lattice unit cells to a side which is a very fine resolution. The states obtained are thus independent of the resolution and the effects of the step nature are not significant at $d = 0.4\mu$m.

Figure 6.11 shows the surface magnetization for a $4\mu$m grain using the result from the $n = 64$ cubic grain shown in figures 5.17a-d as an initial state. An obvious feature is the gently curved 180° domain wall which separates the domains labelled as A and B. This state shows well defined domains which extend deep into the interior of the grain as shown in figure 6.12. At the top and bottom of the grains are small vortices which enable flux closure at the grain apex, and as with the cubic grains the trend is for vortices to become localized features as the grain size increases. Another feature is that the domain wall broadens towards the edge of the grain and this feature could be considered a precursor to closure domains which occur in larger grains.

A small domain which is orientated in the easy [111] direction is shown in figure 6.13. Although the present model cannot model grains larger than $4\mu$m the evolution of the $\langle 111 \rangle$ domains with increasing grain size can be envisaged. For example, as the grain size increases from $4\mu$m the surface effect which produces the $\langle 110 \rangle$ domains would diminish in favour of $\langle 111 \rangle$ body and closure domains.

### Transition from a vortex to a flower state

Figure 6.6 also shows how the energy depends on grain size for octahedral grains decreasing in size from $0.4\mu$m to $0.01\mu$m. Figures 6.14(a-d) show the magnetization states at $d = 0.2\mu$m, $d = 0.1\mu$m, $d = 0.08\mu$m and $d = 0.06\mu$m. As the grain size decreases the exchange energy dominates and the core becomes aligned close to the $z$ direction. Below $0.08\mu$m the shape anisotropy prohibits the vortex state straightening out into a SD$z$ state and instead the magnetization occupies the SD$x$ state shown in figure 6.14d.

Figure 6.6 also shows that for grains smaller than $0.1\mu$m the energy of the vortex state is higher than that of the flower state. The reason that this occurs for octahedral grains and not for cubic grains is that the strong shape anisotropy allows a higher energy LEM vortex state to exist. This effect means that the minimum energy curves for increasing and decreasing sizes shown in figure 6.6 cross over at $d_0 = 0.107\mu$m. This is exactly the same result obtained by Thomson (1993) who used the algorithm described in section 4.6 with a resolution of $n = 11$. This gives further confirmation that the masking off method is appropriate and that the flower-vortex transition is a real transition for magnetite.

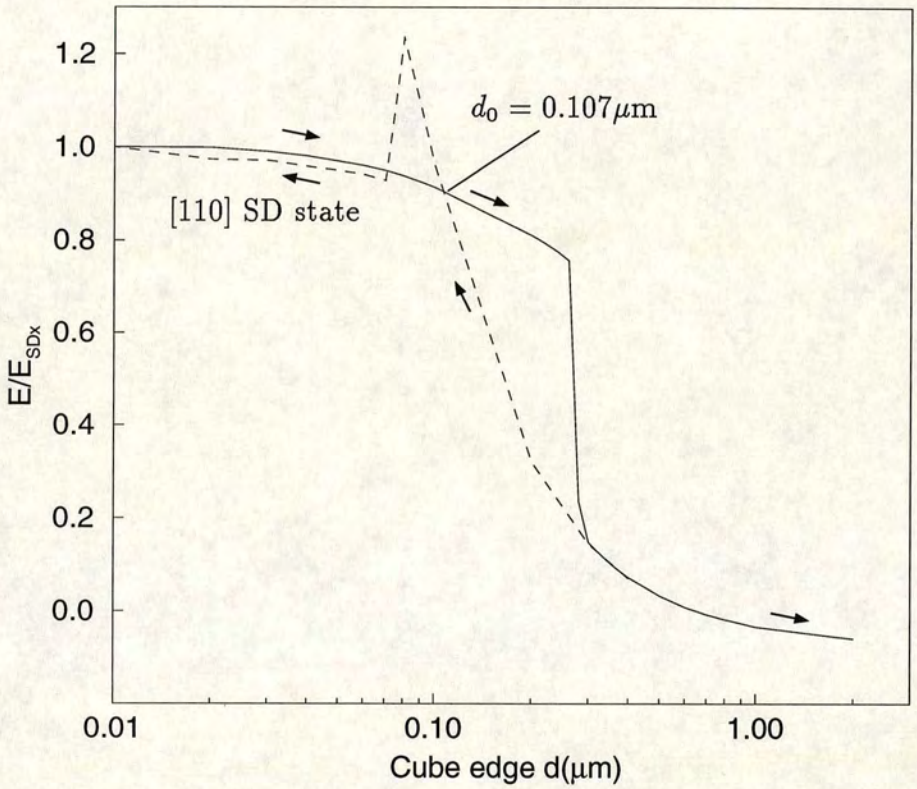


**Figure 6.6.** Dependence of the energy on grain size for a 45° octahedral model. The critical size $d_0$ is shown as the point where it becomes energetically favourable to convert from a flower state to a vortex state.

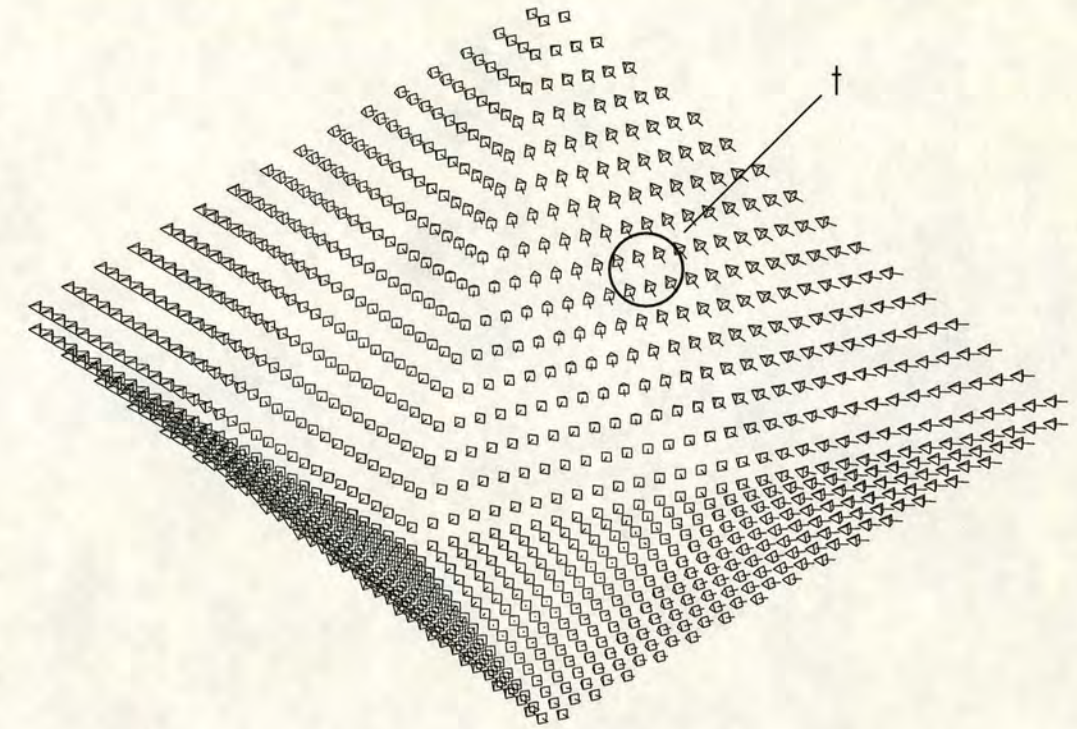


(a) 0.2$\mu$m flower state, $E/E_{SDx} = 0.81$

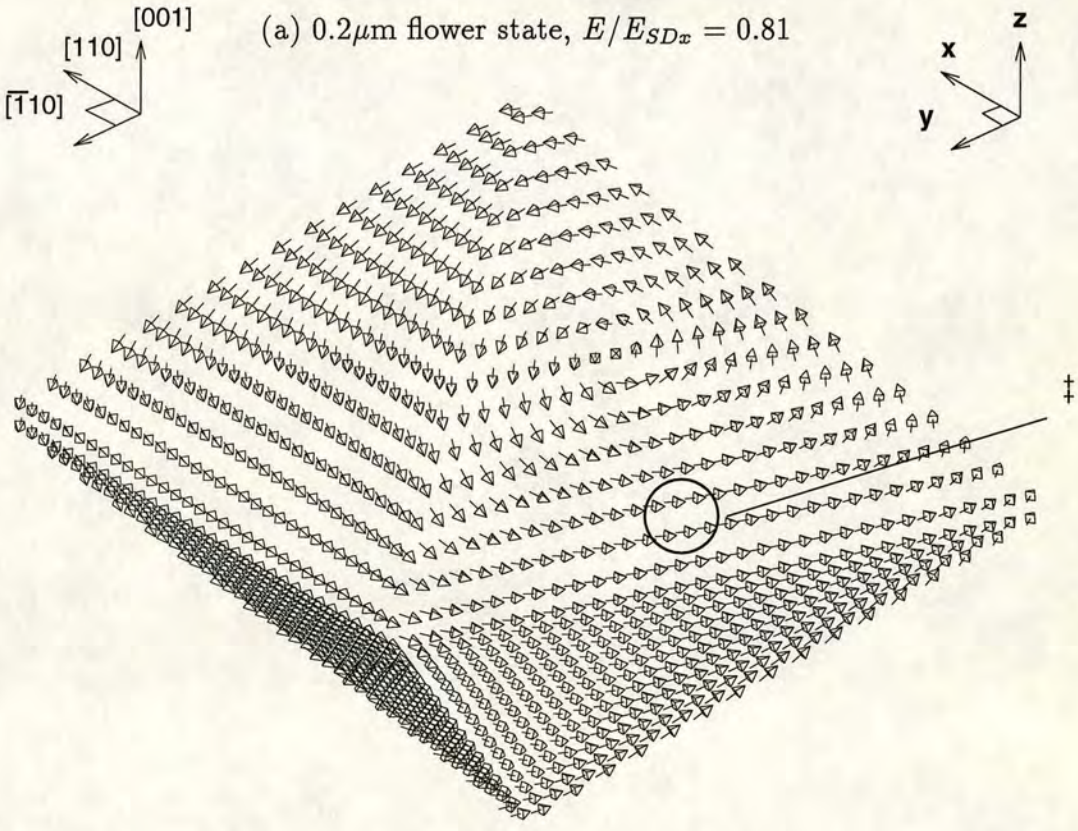


(b) 0.4$\mu$m, vortex state, $E/E_{SDx} = 0.073$

**Figure 6.7.** Magnetization states for the flower and vortex state for the 45° octahedral model. The features marked by † and ‡ are referred to in the text.

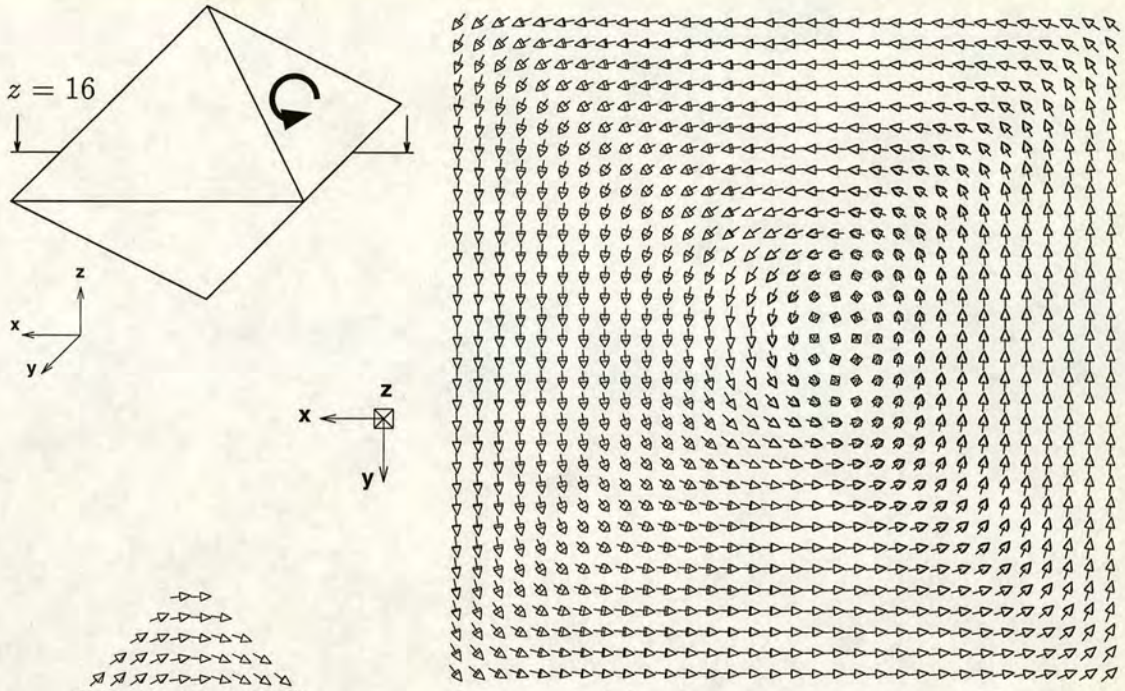


(a) z=16 plane

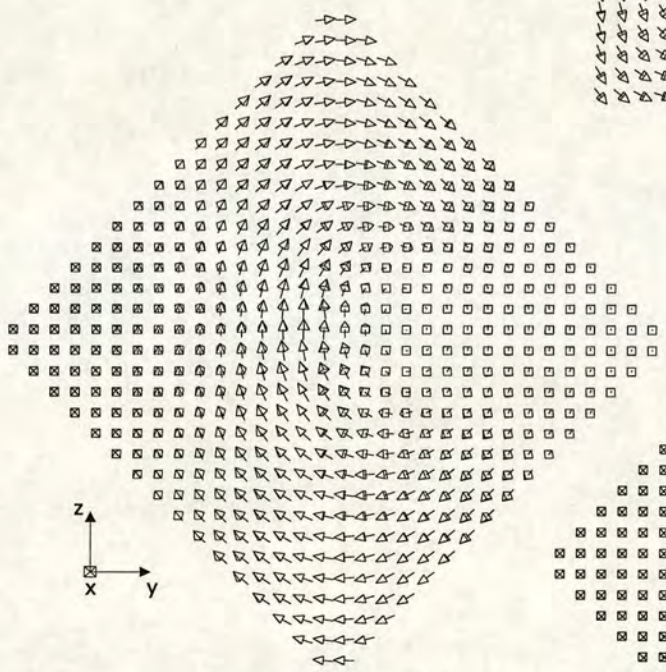


(b) x=16 plane

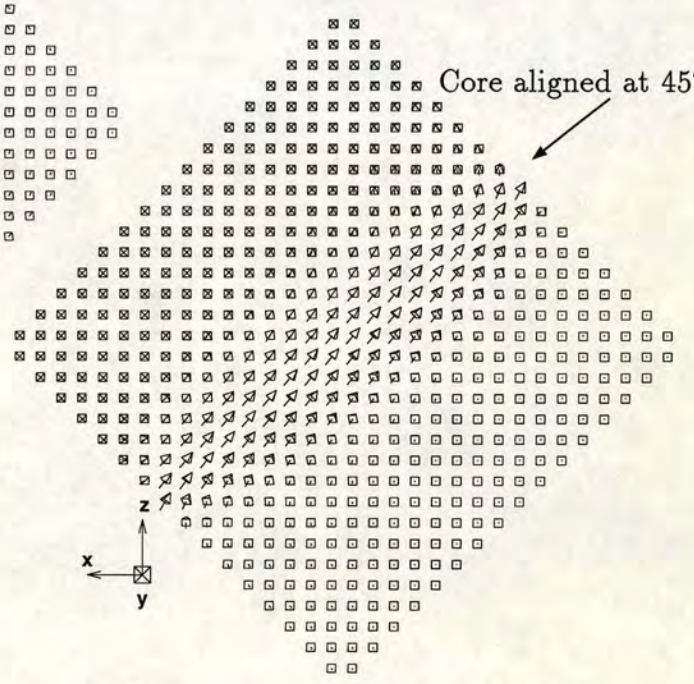


(c) y=16 plane

**Figure 6.8.** Magnetization state at $d = 0.4\mu$m. $E/E_{SDx}$ =0.073, $M_{tot}/M$=0.032.

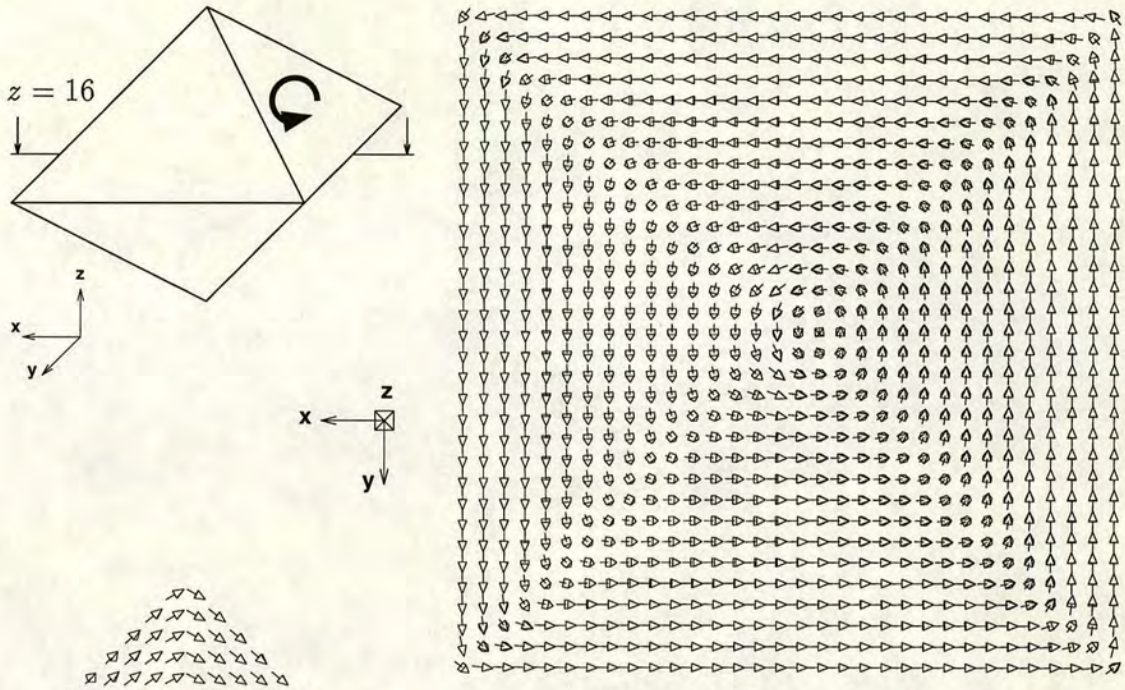


(a) z=16 plane

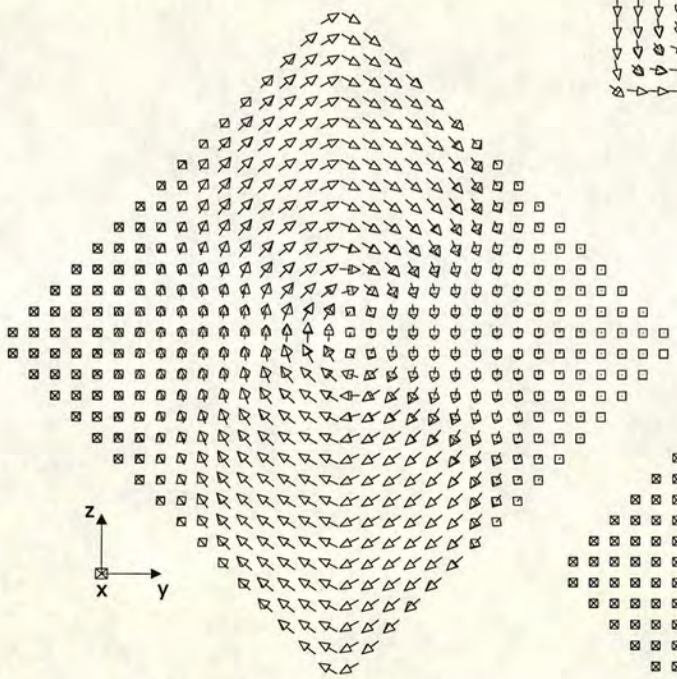


(b) x=16 plane

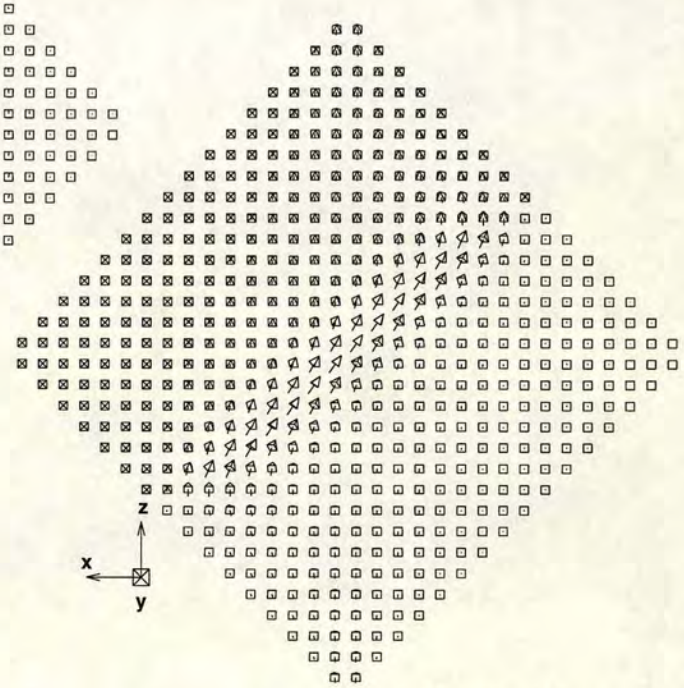


(c) y=16 plane

**Figure 6.10.** 45° octahedral model at 2.0$\mu$m.

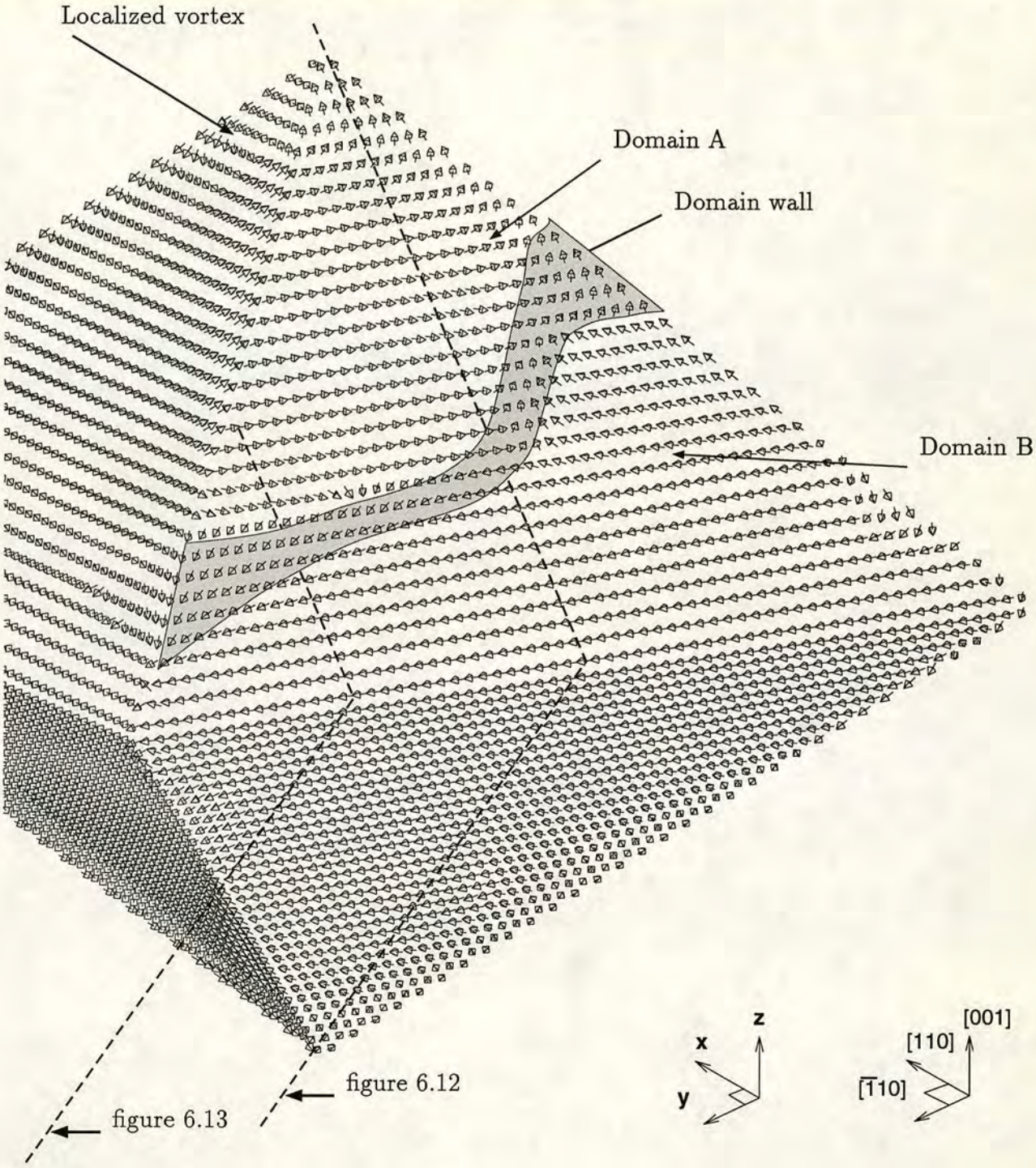


**Figure 6.11.** Surface magnetization for a 4$\mu$m octahedral grain using a resolution of $64 \times 64 \times 64$, $E/E_{sd} = -0.046$, $M_x/M_s = 1.5 \times 10^{-3}$, $M_y/M_s = 3.1 \times 10^{-3}$, $M_z/M_s = 5 \times 10^{-4}$.
The dotted lines show the orientation of the sections in figures 6.12 and 6.13.

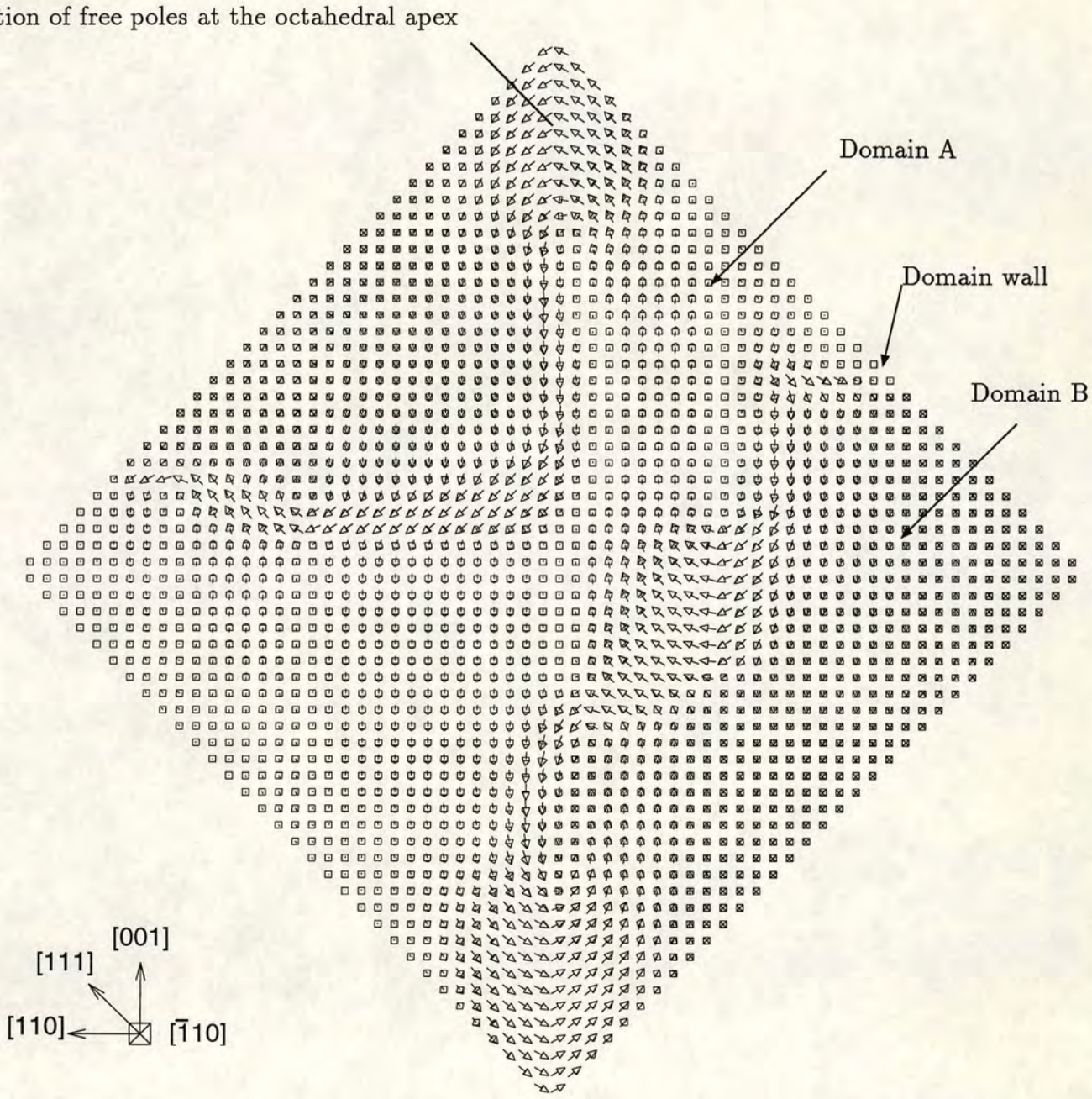


**Figure 6.12.** Cross section through the 4$\mu$m grain shown in figure 6.11.

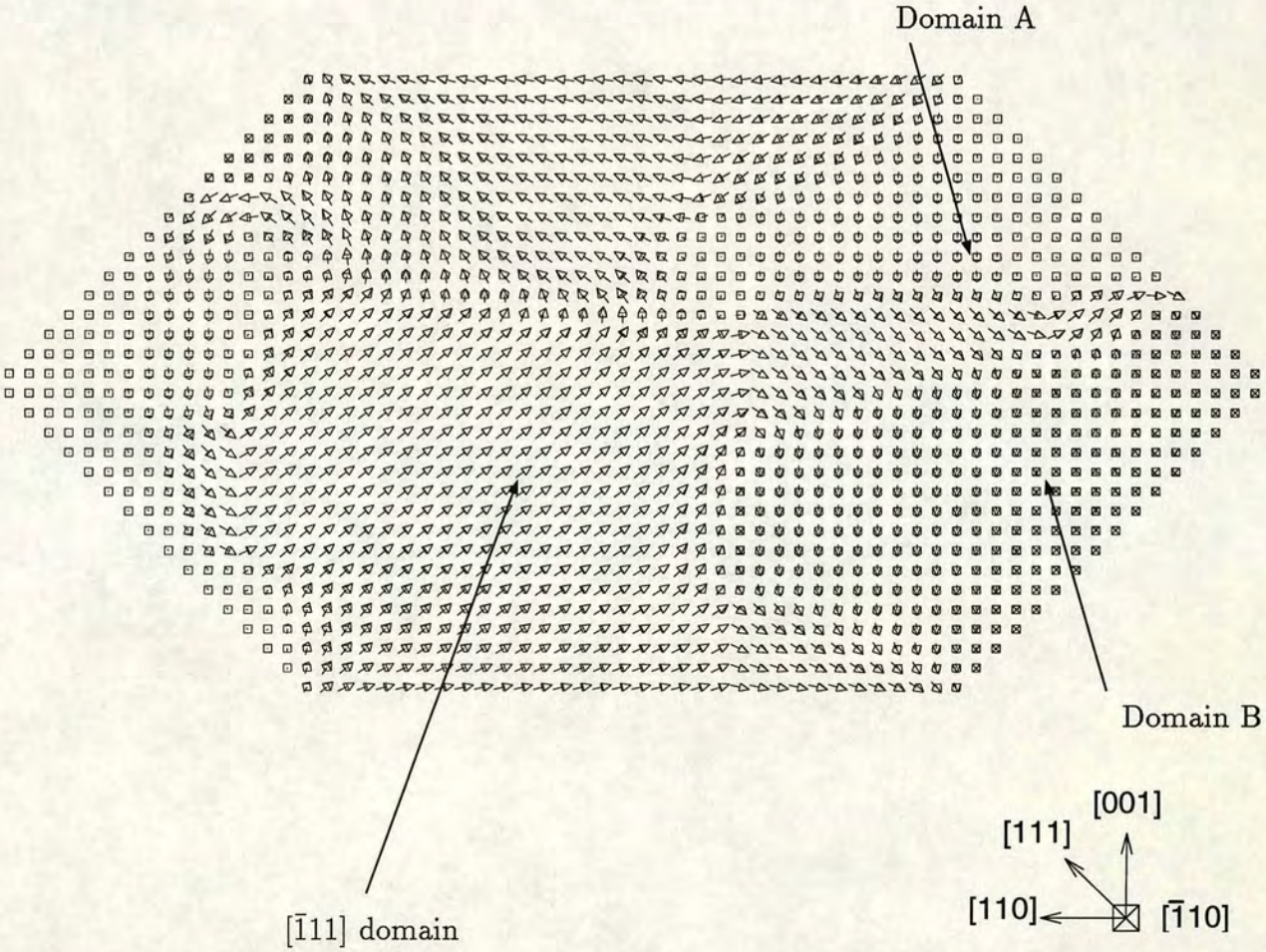


**Figure 6.13.** Section through the 4$\mu$m grain shown in figure 6.11 at $x = 16$.

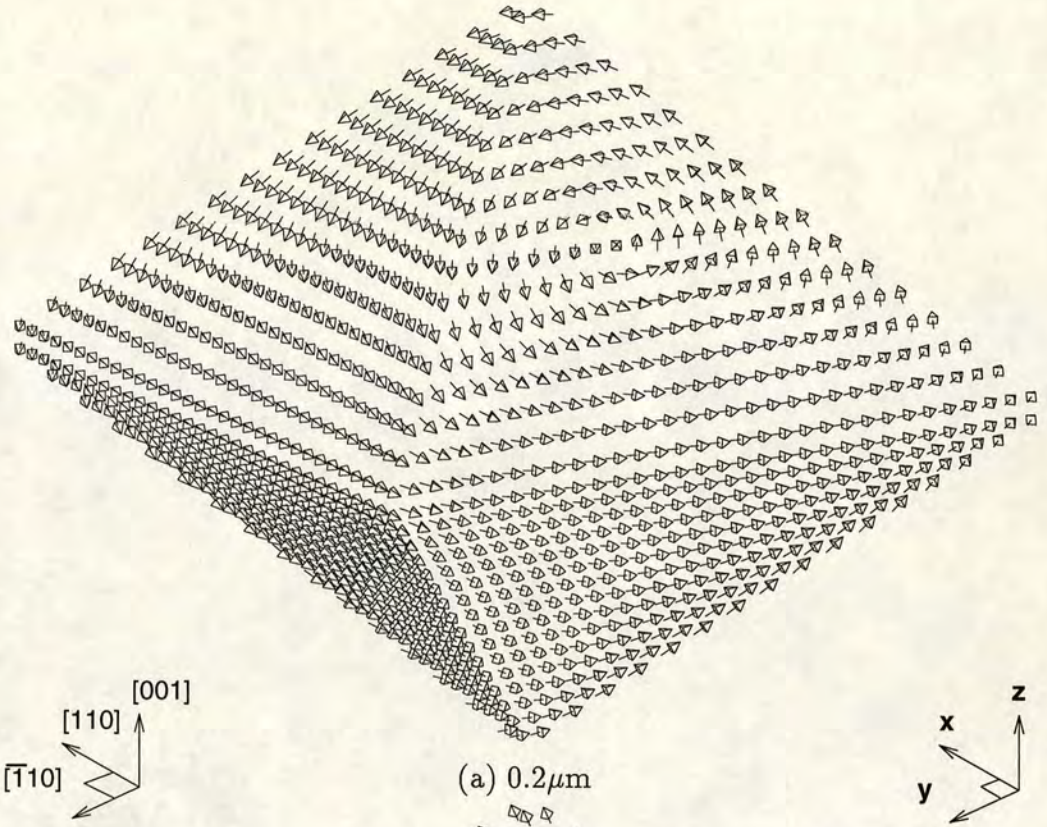


(a) 0.2$\mu$m

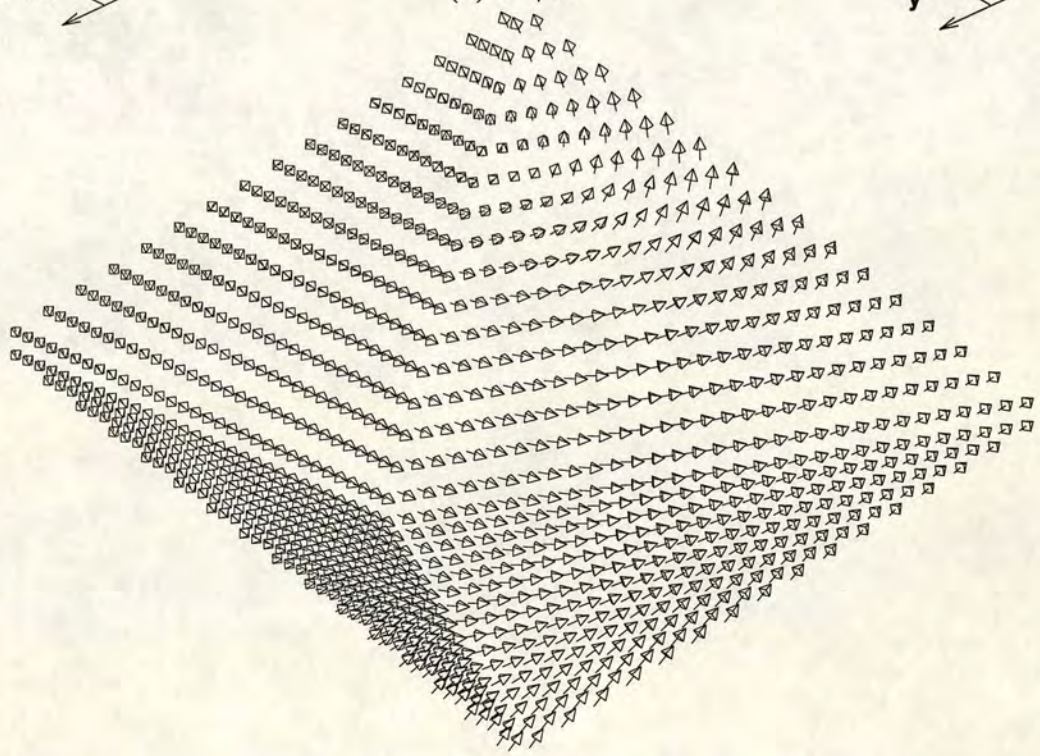

(b) 0.1$\mu$m

**Figure 6.14.** Transition from vortex states shown in (a-c) to a single-domain state shown in (d).

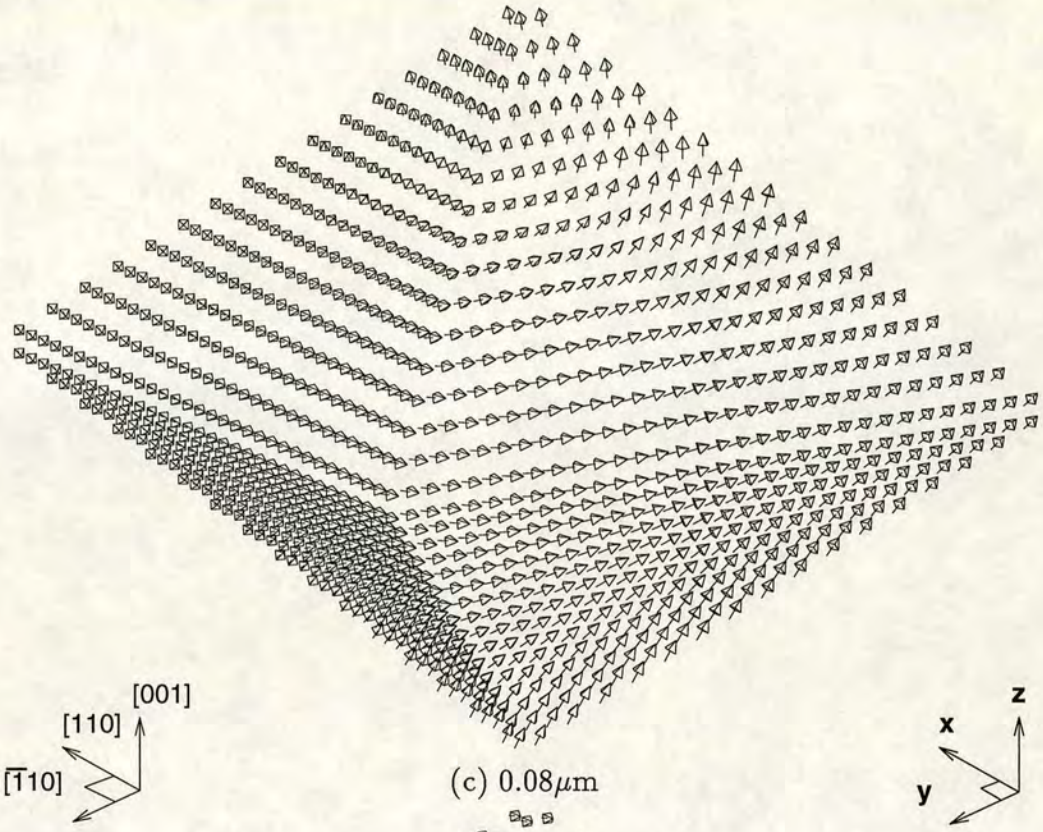


(c) 0.08$\mu$m

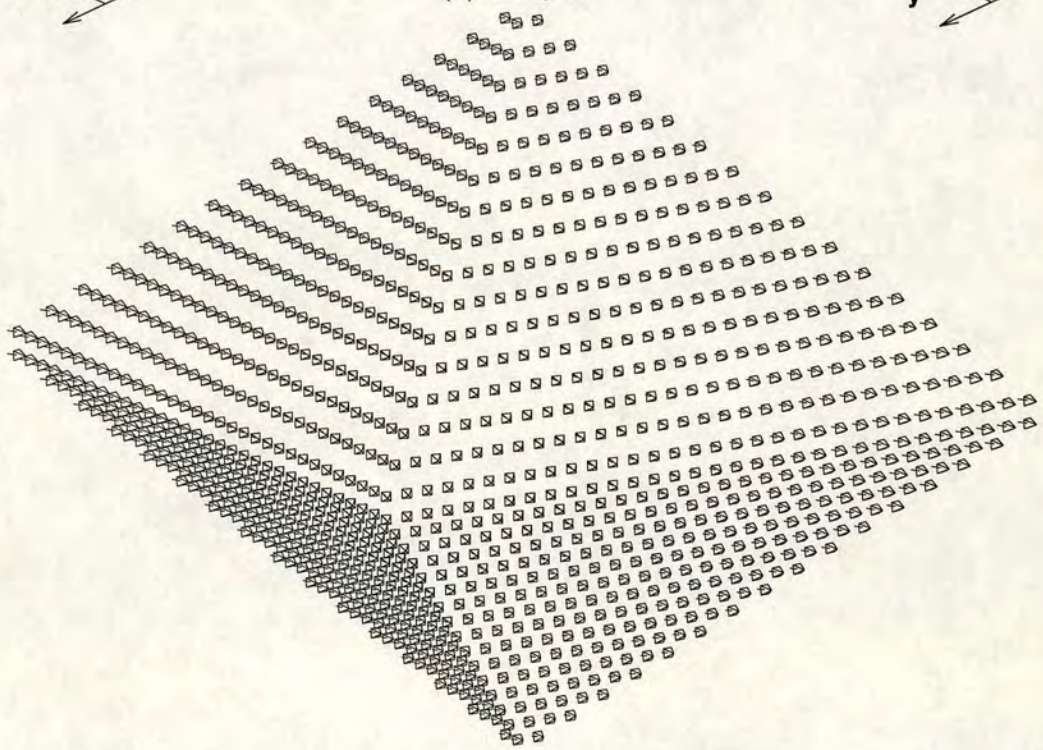

(d) 0.06$\mu$m

**Figure 6.14** continued.

### Results for $V_{max}$ octahedral

Figure 6.15 shows an equilibrium state for the $V_{max}$ octahedral at 0.7$\mu$m. This is a similar single vortex state to the 45° model. Results for the two octahedral models are similar and it is difficult to evaluate whether increasing the volume at the expense of making the model 'squatter' actually makes the model more accurate. The 45° octahedral model was used for high resolution results and the hysteresis simulations, largely because it was easier than the $V_{max}$ octahedral model to implement and visualize.

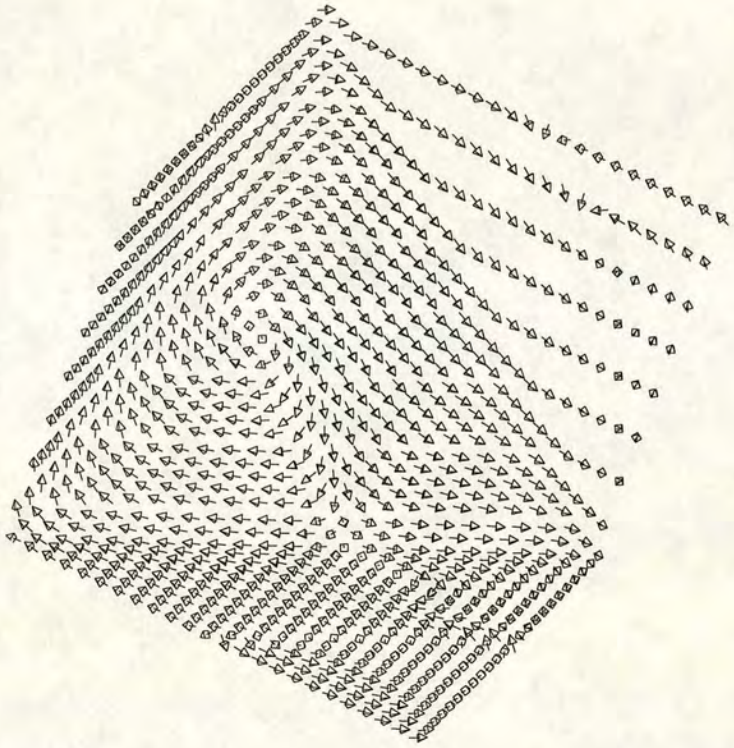

**Figure 6.15.** Single vortex LEM state for a 0.7$\mu$m, $V_{max}$ octahedral grain. Some of the vectors on the right hand side of the grain have been omitted due to the particular step nature of the model.

## 6.5 Other geometries

Figure 6.16 shows two other shapes which were modelled using the masking off method. Figure 6.16a is a combination of a cube and a regular octahedral and figure 6.16b consists of a small $2 \times 2 \times 2$ cube on top of a rectangular parallelpiped. Figure 6.17 shows the dependence of the normalized energy values with the volume of the grain for these two shapes together with the results for cubic and octahedral grains. The combination model switches from a flower state to a vortex state at the same volume as both the cubic and octahedral models but it is interesting to note that the irregular grain transfers to a vortex state at a lower volume. It switches at a lower grain size of $0.1\mu$m due to the asymmetric demagnetizing field produced by the small cube. These results suggest that in real grains with irregular surfaces flower states may be unstable in the size range $0.1\mu$m to $0.2\mu$m. A similar effect could be induced by a clustering effect whereby small grains are attracted and stick to the surface of larger grains. In addition to these results, chapter 5 showed that the amount of flowering in grains smaller than $0.07\mu$m is negligible. These results now suggest that because flower states are unstable in grains larger than $0.1\mu$m flowering only occurs in grains between $0.07\mu$m and $0.1\mu$m.

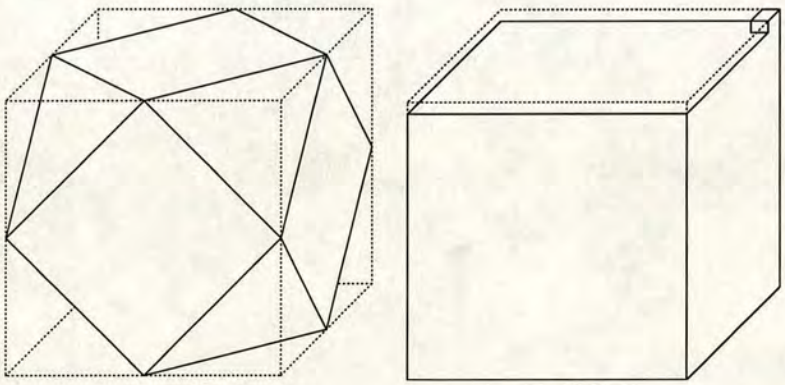


**Figure 6.16.** (a) Combination of a cube and regular octahedral and (b) irregular shaped grain

## 6.6 Permalloy Films

Figure 6.18 shows results for a simulated permalloy film for a range of increasing external field values. The material values for permalloy are $M_s = 8 \times 10^5 \mathrm{Am}^{-1}$, $C_e = 1 \times 10^{11} \mathrm{Jm}^{-1}$, $K = 0 \mathrm{Jm}^{-3}$ and were taken from Nakatani *et al* (1989).

These states are identical in form to those observed experimentally by McVitie *et al* (1988) on a $4\mu m \times 4\mu m \times 0.6\mu m$ thin film, reproduced in figure 6.19. Although the real permalloy films used by McVitie *et al* (1988) are an aglomerate of many fine grains, the strong exchange coupling effect between grains produces an ordered pattern over the whole film. The common feature to both the experimental observations and theoretical predictions is the nucleation of the domain wall shown in figure 6.18b. The slight difference between the results in theoretical predictions is that this additional domain wall labelled in figure 6.18b is straight compared to the curved one seen experimentally. The big difference is that the theoretical models are magnetically harder than the experimental observations. The model saturates at a field 10 times larger than the real grain and this may be due to the fact that the real films are an aglomerate of many fine grains with complex boundary conditions between grains.

## 6.7 The effect of vacancies

A feature commonly seen in experimental domain observations is the pinning of domain walls by non-magnetic impurities on the surface of the grain. These impurities effectively create a vacancy in the magnetization of the grain. This effect was modelled by masking off a rectangular area on the surface of the grain positioned away from the centre of the surface. Figures 6.20a and 6.21a show the effect of masking off vacancies of size 2x2x1 and 3x3x2 sub-cubes respectively. The initial structure used in these calculations was a SD state and at equilibrium the surface domains shield a more complicated internal domain structure. Figures 6.20a and figures 6.21a show that both sizes of vacancies pin the domain wall away from a central line. This occurs in order to reduce the number of free poles at the surface of the vacancy. This can clearly be seen in figure 6.21a where the vectors align parallel to the edge of the vacancy in order to reduce the number of free surface charges.

Figures 6.20b-d show that as an external field is applied the domain wall moves towards a central line away from the vacancy. These results were calculated by using the state for zero field as an initial state, calculating an equilibrium solution at $H = 20\text{mT}$ and then repeating for $H = 40\text{mT}$ and $H = 60\text{mT}$. The larger 3x3x2 vacancy pins the domain wall strongly and the external field is unable to move the domain wall. Instead a second domain wall is nucleated as shown in figure 6.21b.

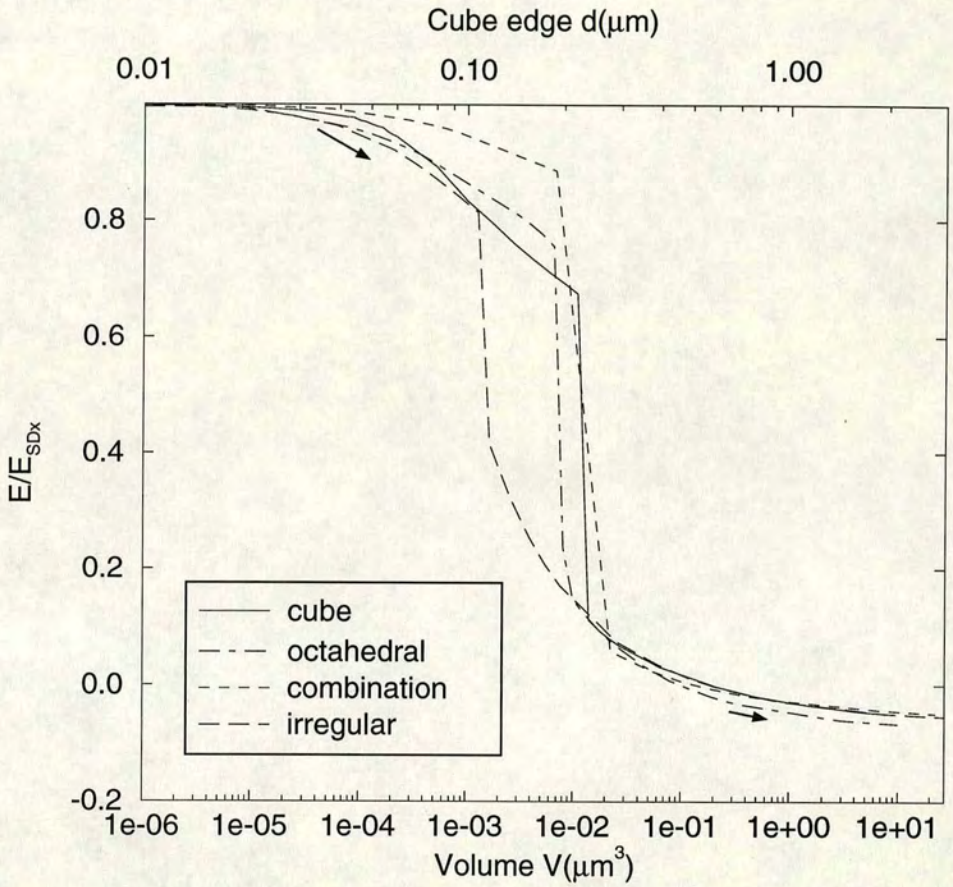


**Figure 6.17.** Total energy as a function of volume for cubic and non-cubic grains. For reference the edge length ($d$) for a cube of volume $V$ is marked on the top edge of the graph. The results for cubic and octahedral grains are the same as those in figures 5.1a and 6.6 respectively.

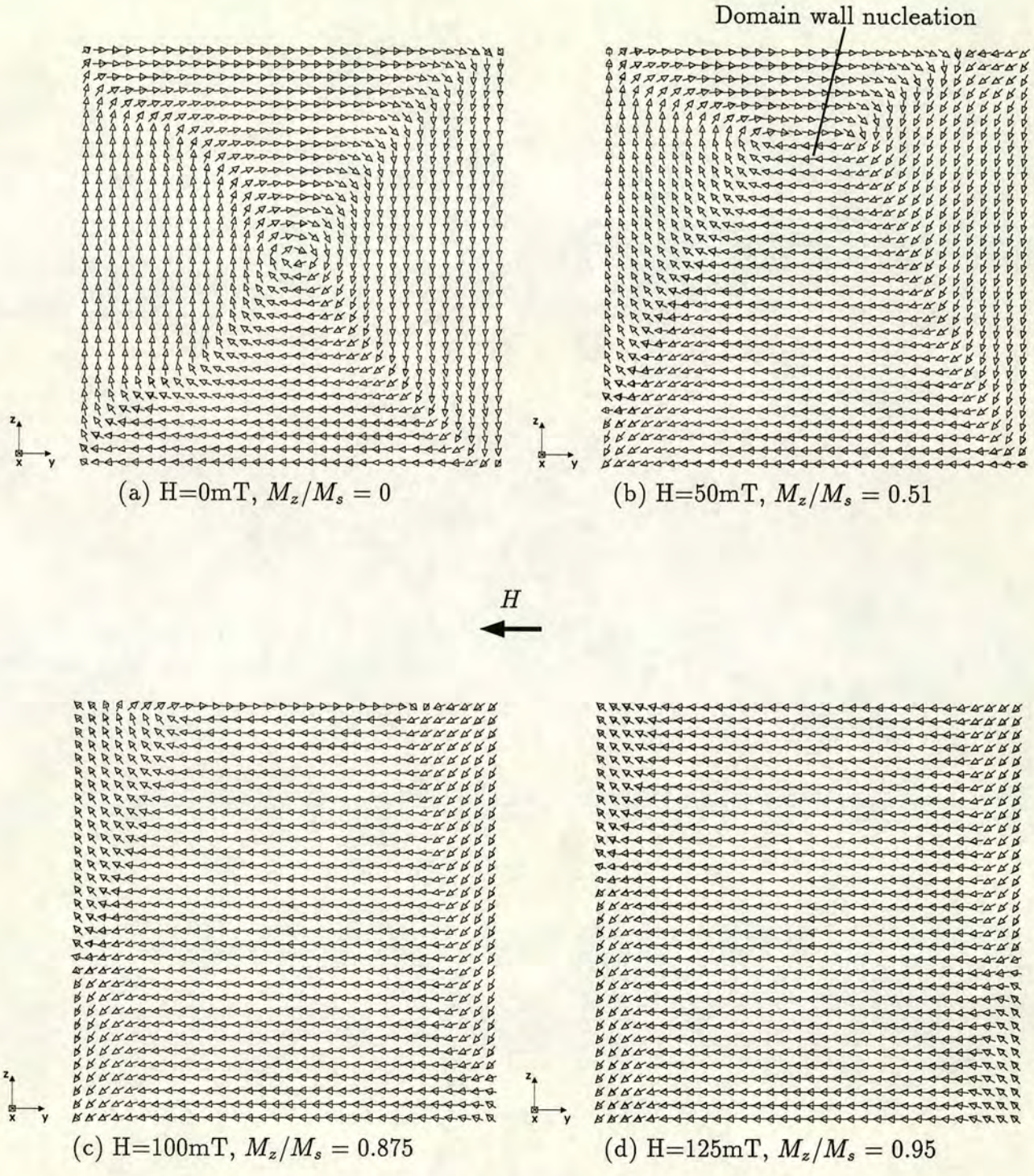


(a) H=0mT, $M_z/M_s = 0$

(b) H=50mT, $M_z/M_s = 0.51$

(c) H=100mT, $M_z/M_s = 0.875$

(d) H=125mT, $M_z/M_s = 0.95$

**Figure 6.18.** $32 \times 32 \times 4$ model of a $1\mu$m$\times 1\mu$m $\times$125nm Permalloy film with an applied field in the $-y$ direction.

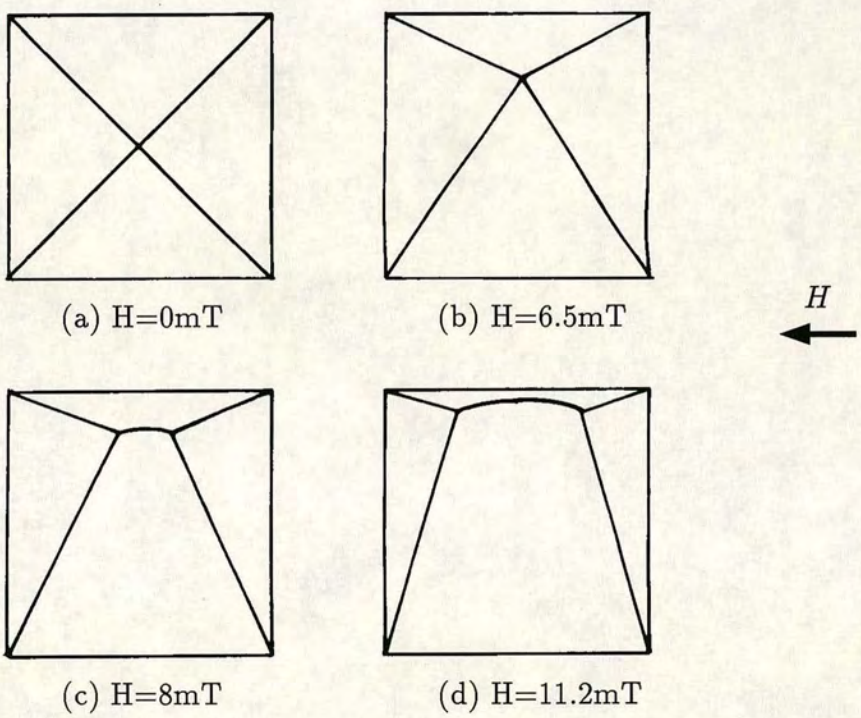


**Figure 6.19.** Sketch of domain states for a 4$\mu$m square permalloy grain of thickness 60nm obtained using the Fresnel mode of Lorentz electron transmission microscopy, from McVitie *et al* (1988).

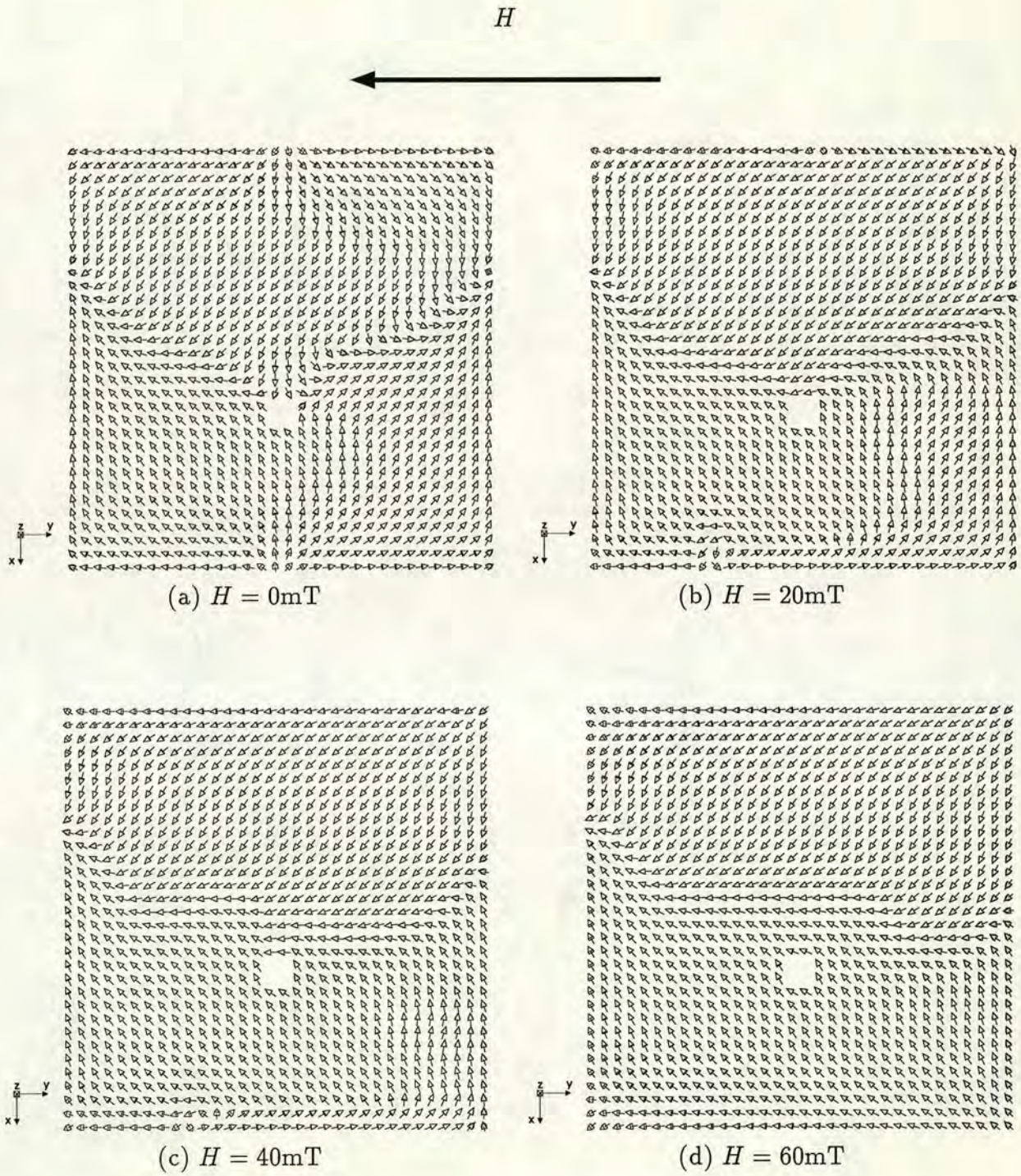


(a) $H = 0\text{mT}$ (b) $H = 20\text{mT}$

(c) $H = 40\text{mT}$ (d) $H = 60\text{mT}$

**Figure 6.20.** Magnetization states for a $2\mu$m cubic grain with a cavity of size $2 \times 2 \times 1$ sub-cubes. Each plane is a $z = 32$ plane.

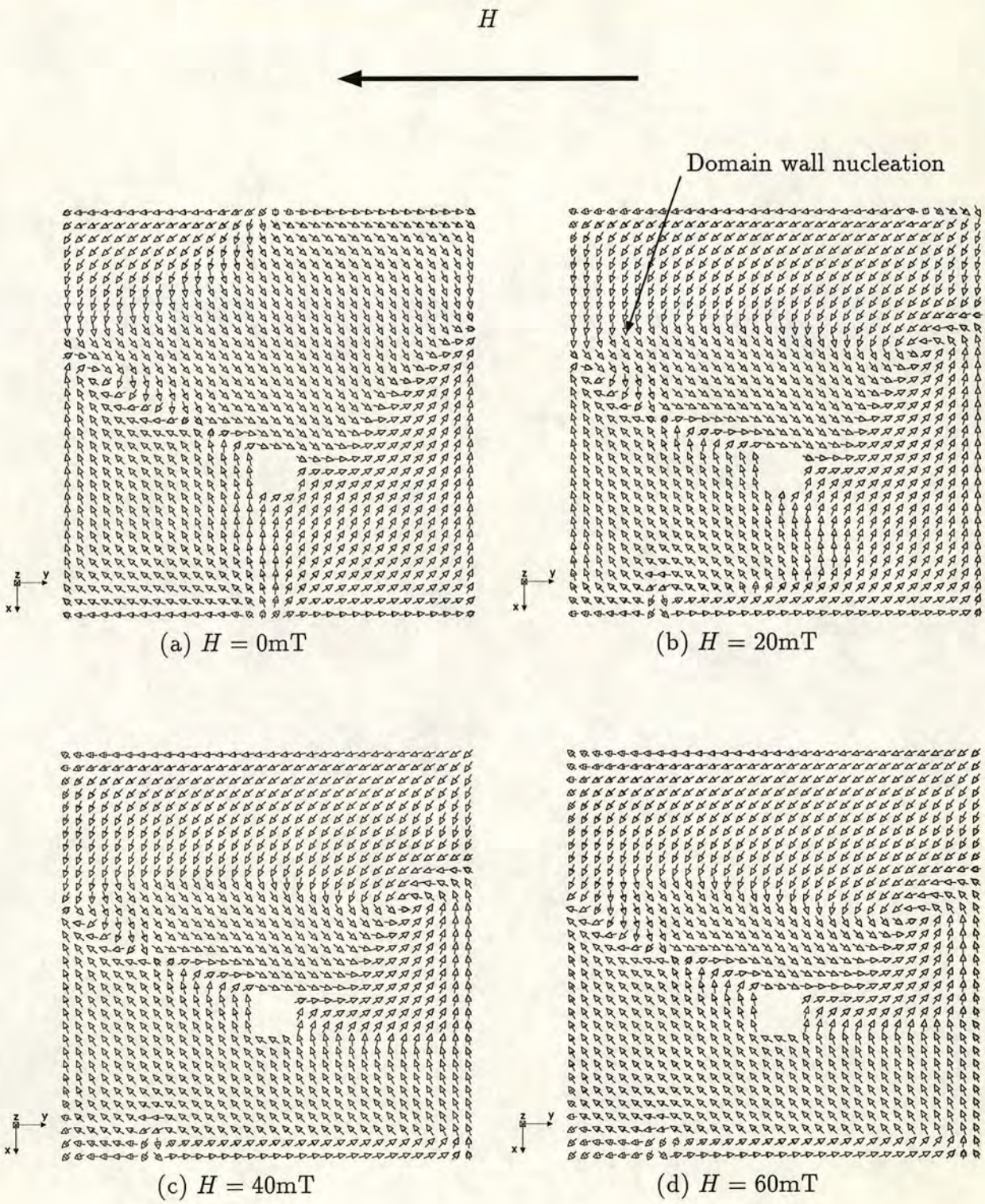


(a) $H = 0\text{mT}$ (b) $H = 20\text{mT}$

(c) $H = 40\text{mT}$ (d) $H = 60\text{mT}$

**Figure 6.21.** Magnetization states for a $2\mu$m cubic grain with a cavity of size $3 \times 3 \times 2$ sub-cubes. Each plane is a $z = 32$ plane.

## 6.8 Summary

Results in this section have shown that a masking method can be used to calculate equilibrium magnetization states for any arbitrary shaped grain. The main results described in this chapter are:

- Octahedral and spherical grains can both occupy similar flower states and vortex states to those seen in cubic grains. In addition the grain size at which the transition occurs is similar for both models ($d = 0.2\mu$m).
- The moments of octahedral vortex states are close to those of the cubic vortex states shown in chapter 5, and are both lower than experimentally measured values of $M_{rs}/M_s$,
- Both octahedral and cubic grains show a similar transition from vortex states to domain states at $d \approx 1\mu$m.
- Grain surface irregularity reduces the stability of flower states.
- Thin film simulations produce magnetization states similar to those observed experimentally.
- Models have shown that vacancies can pin domain walls in order to reduce the amount of surface charge at the surface of the vacancy.

# Chapter 7. Hysteresis simulations

## 7.1 Introduction

By simulating hysteresis loops this chapter aims to determine why experimentally measured values for $M_{rs}$ and $H_c$ in PSD grains are a significant fraction of those predicted by SD theory. Because of the increased computation time required to simulate hysteresis curves, results will be limited to modelling single grains which are smaller than $1\mu$m by using a maximum resolution of $32 \times 32 \times 32$. Experimental hysteresis measurements on single magnetite grains have only been possible on grains larger than $80\mu$m (Heider and Hoffman 1992) and this is an order of magnitude larger than the maximum theoretical grain size of $1\mu$m. Consequently predictions have to compared with experimental hysteresis curves measured on bulk samples.

Bulk samples consist of randomly orientated assemblies of grains. In principle the effect of a large number of randomly orientated grains can be modelled by applying an external field to the model at many different field directions. Ideally the simulated field values should be uniformly distributed over a sphere but in practice the field will be applied in a few chosen directions and the magnetization averaged over these hysteresis curves. The range of grain sizes observed in synthetic bulk samples must also be considered when comparing predictions with experimental results. The synthetically grown bulk samples described in section 2.3 show a relatively narrow grain size distribution compared to crushed and sieved natural samples; however the deviation about the mean grain size is still between 30% and 40% (figure 2.2).

Hysteresis curves are obtained by applying an external field and plotting the component of the magnetization in the direction of the field as a function of the magnitude of the applied field. At a particular grain size hysteresis curves were calculated by using the states (**A**-**F**) described in chapter 5 as initial states and a field of $H = +500$mT applied in steps of 50mT. The initial state at each field value was just the equilibrium solution from the previous field value. The field was then decreased from $H = 500$mT to $H = -500$mT and to make the best use of the computing time, values for $H$ were closely spaced between $H = 20$mT and

$H = -20$mT where detail is important. Values for $H_c$ were calculated using a linear interpolation between the two points either side of the $M/M_s = 0$ axis.

The magnetization states at particular field values will be referred as $\mathbf{A}^x_{50}$ where $\mathbf{A}$ is the initial state, $x$ is the direction of the applied field and 50 is the intensity of the applied field in mT. The state at saturation remanence will be referred to as $\mathbf{A}^x_0$. For fields which are not in the $x$,$y$ or $z$ directions the crystallographic notation will be used, for example, for a 50mT field in the [110] direction the magnetization state will be labelled as $\mathbf{A}^{110}_{50}$. The magnetization states for grains smaller than $0.1\mu$m are as well defined at a resolution of $n = 8$ as at $n = 32$ and so for clarity, hysteresis simulations for these grains are presented at a resolution of $n = 8$.

## 7.2 cubic grain

Figure 7.1 shows results for a $0.05\mu$m cubic grain with a field applied at an angle of 5° to the [001] direction. The field is applied at an angle of 5° because of the nature of the flower state. If a field is applied exactly in the $+z$ direction, the vectors at each corner rotate equally towards the $-z$ direction. This results in an unrealistic reversal mode with an artificially high coercivity ($H_c \approx 300$mT). The hysteresis curve shown in 7.1 is a square loop with a coherent reversal mechanism similar to the quasi-static calculations by Schabes and Bertram (1988) who used a steepest descent method. As the reversal mechanism is also similar to the $3d$ dynamical calculations by Nakatani *et al* (1989), these results show that the quasi-static approach is justified.

The reversal mechanism is a coherent like rotation from a flower state in the [001] direction to a flower state in the [00$\bar{1}$] direction, but during the reversal the states are never truly SD, there is always a certain amount of flowering. However the predicted coercivity of $H_c = 38.2$mT is close to the analytic result of $H_c = 34.7$mT showing that the flowering does not significantly affect the stability of SD grains.

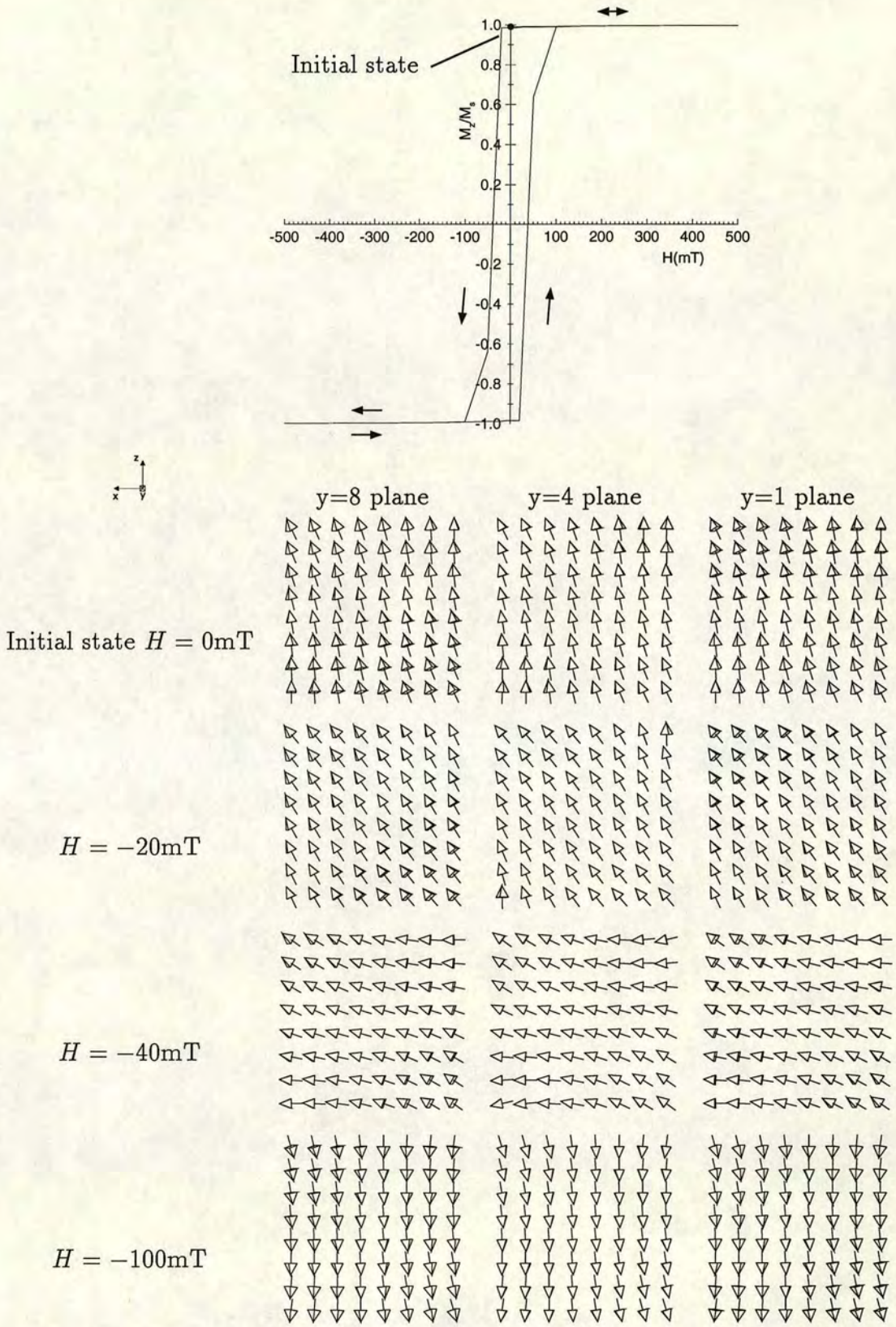


**Figure 7.1.** Hysteresis curves for a 0.05$\mu$m grain using a resolution of $8 \times 8 \times 8$. The field is applied at 5° to the vertical resulting in a slight skew to the magnetization plots, $H_c = 38.2$mT, $M_{rs}/M_s = 0.978$

## 7.3 $0.1\mu m$ cubic grain

Figure 7.2 shows a hysteresis curve using a flower state as an initial state at $d = 0.1\mu$m. The magnetization remains in a flower state as the field is increased to $H = 500$mT and then decreased to zero. The magnetization plots show that as the field decreases from $H = 0$mT to $H = -500$mT the magnetization changes from a a flower state to a vortex state. Between $H = -50$mT and $H = -100$mT the vortex core remains in the $z$ direction whilst the vectors at the edge of the grain rotate towards the $-z$ direction. Between $H = -100$mT and $H = -500$mT the approach to saturation becomes a magnetically softer process as the inner core has 'flipped' over and all the vectors are aligned in the $-z$ direction. The rotation of the vortex core is shown by a 'knee' in the hysteresis curve at $H = -100$mT.

Saturating the vortex state with a finite field, e.g $H = -500$mT means that the vectors still retain a memory of the vortex state, i.e. they all rotate in the same sense by a very small amount. This means that during the next stage of the hysteresis cycle when the magnitude of the field changes from $H = -500$mT to $H = 0$mT the magnetization remains in the vortex state. Only if an infinitely large saturating field is applied to the vortex state would there be a transition back to a flower state. This shows that the transition from a flower state to a vortex state is an irreversible transition.

From $H = -500$mT to $H = 500$mT the reversal process is characterized by the vortex state opening out and then closing up in the opposite direction. This process was referred to as vortex propagation by Enkin and Williams (1994). Chapter 5 showed that for cubic grains, vortex states are always lower energy states than flower states. The limit between coherent rotation and vortex propagation is thus given by the critical size, $d_0 = 0.07\mu$m. The coercivity, $H_c = 21$mT is 2/3 that of coherent rotation and the saturation remanence, $M_{rs}/M_s = 0.26$ is a quarter than that of coherent rotation. These results are important as they show that reversal by vortex propagation can predict high values of $H_c$ and $M_{rs}/M_s$ and vortex states can be considered as good recorders of the geomagnetic field.

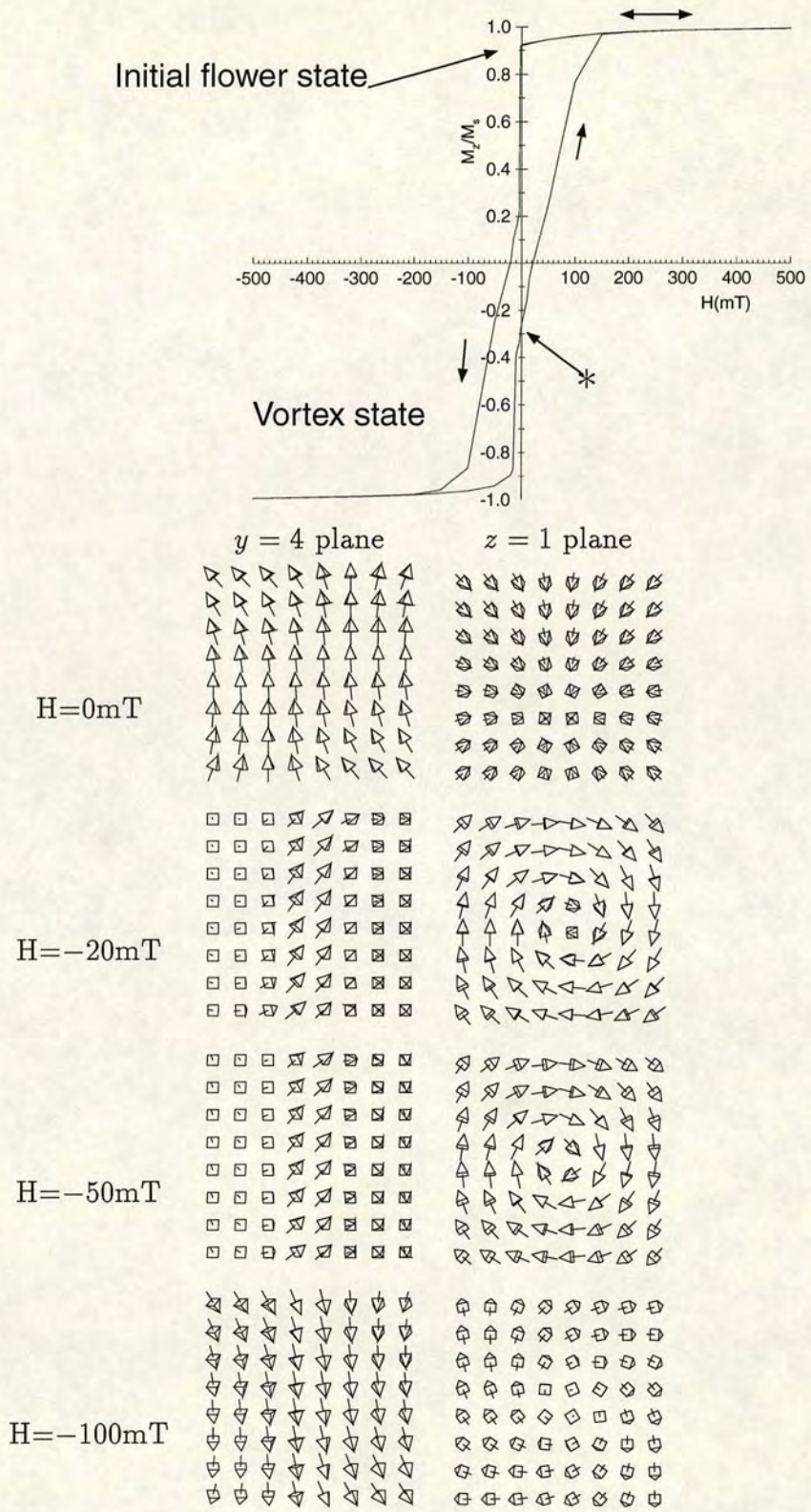


**Figure 7.2.** Hysteresis curves for a $0.1\mu$m grain using a resolution of $8\times8\times8$. The field is applied at 5° to the vertical resulting in a slight skew to the magnetization plots. $H_c = 21.03$mT, the saturation remanence state at $(*)$ is a vortex state with $M_{rs}/M_s = 0.26$.

## 7.4 $0.2\mu m$ cubic grain

This section describes results for fields applied in the $x$ and $z$ directions for a $0.2\mu$m grain using both the flower state (**B**) and the vortex state (**E**) as initial states. Figure 7.3a shows a hysteresis curve for a field applied in the $z$ direction using a flower state as an initial state. As the field increases from $H = 0$mT to $H = 500$mT the magnetization changes from the initial flower state shown in figure 7.4a to a SD state. As the field decreases from $H = 500$mT to $H = 0$mT the magnetization returns to the same flower state shown in figure 7.4b. As the field decreases from $H = 0$mT to $H = -500$mT the vortex states shown in figures 7.4c and 7.4d are nucleated in a similar sequence to that shown in figure 7.2.

The hysteresis curve for a field applied in the $x$ direction is shown in figure 7.3b. The flower state is aligned in the $z$ direction so the moment in the $x$ direction is zero, as shown in the enlarged section of figure 7.3b. In this instance the vortex state is nucleated before the field is reduced to zero and the saturation remanence state is the vortex state $\mathbf{B}_z^0$, shown in figures 7.5a and 7.5b. This vortex state is a separate LEM state to the $0.2\mu$m vortex state (**E**) shown in figure 5.11b. The large central core of the saturation remanence state means that $\mathbf{B}_z^0$ is a higher energy state than the vortex state **E** (the energies for states $\mathbf{B}_z^0$ and **E** are $E/E_{SD} = 0.285$ and $E/E_{SD} = 0.158$ respectively). In addition the large central core also results in a large moment, $M_x/M_s = 0.233$ for $\mathbf{B}_z^0$, compared to $M_x/M_s = 0.065$ for state **E**. Figures 7.5c and 7.5d show that as the field decreases from $H = 0$mT to $H = -500$mT the width of the central core decreases.

Figure 7.6 show hysteresis curves for a $0.2\mu$m grain using the vortex state, **E** as an initial state. The hysteresis curve for a field applied in the $x$ direction is shown in figure 7.6a and the magnetization plots shown in figure 7.7. Figure 7.7a shows that the vortex core for the initial state is offset from the centre of the grain whereas the remanence state, $\mathbf{E}_x^0$ is a separate LEM state with the core aligned parallel to the direction of the applied field. This is also a separate LEM state to $\mathbf{B}_z^0$ and the large central core seen in $\mathbf{B}_z^0$ does not occur in $\mathbf{E}_x^0$. However the core is still aligned in the direction of the field and so the moment increases from $M_x/M_s = 0.065$ for state **E** to $M_x/M_s = 0.103$ for state $\mathbf{E}_x^0$.

A similar sequence is seen for a field applied in the $z$ direction, shown in figures 7.6b and 7.8. In addition to the core being aligned parallel to the external

field the saturation remanence state, $\mathbf{E}_0^z$ has an increased moment as the magnetization at the grain's edges is aligned along the $\langle 111 \rangle$ easy directions. This effect is circled in figure 7.8a. Table 7.1 gives a summary of the different LEM vortex states described in this section. The table shows a trend from left to right of low energy states with low moments to high energy LEM states with high moments

| | Two-domain vtx. $\mathbf{E}$ | Core in $x$ direction $\mathbf{E}_0^x$ | Corners in $\langle 111 \rangle$ direction $\mathbf{E}_0^z$ | Vtx., large core $\mathbf{B}_0^x$ |
|---|---|---|---|---|
| $E/E_{SD}$ | 0.158 | 0.185 | 0.187 | 0.285 |
| $M/M_{rs}$ | 0.065 | 0.103 | 0.119 | 0.244 |
| $H_c$ | | 13.77 | 0.923 | 1.579 |

**Table 7.1.** Total energies and Moments for vortex states for $d = 0.2\mu$m.

Figure 7.9 shows results which compare theoretical hysteresis curves with an experimentally measured hysteresis curve. The predicted curves were saturated using a similar field to the experimental results ($H = 150$mT) and the predicted values are an average over several hysteresis curves in different directions. The magnetization values from saturation to $H = 0$mT agree extremely well with the experimental results and the theoretical results have not been normalized to the experimental results in any way. Values for saturation remanence agree with the experimental results whilst the average coercivity is lower by a factor of 2/3. However, the subsequent magnetization values from $H = 0$ to $H = 150$mT are linear with $H$ and are not as good a fit to the experimental curves. Overall the results fit well and are more accurate than any results which have previously been predicted (chapter 8 will compare these results with low resolution models by Williams (1994)).

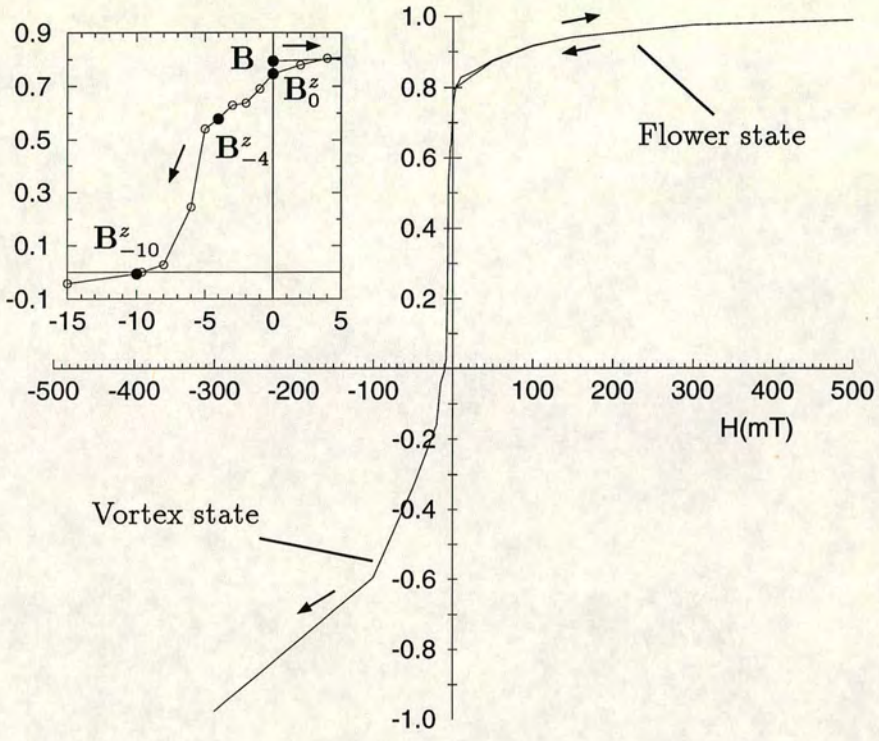


(a) $M_{rs}/M_s = 0.748$, $H_c = 9.590\text{mT}$

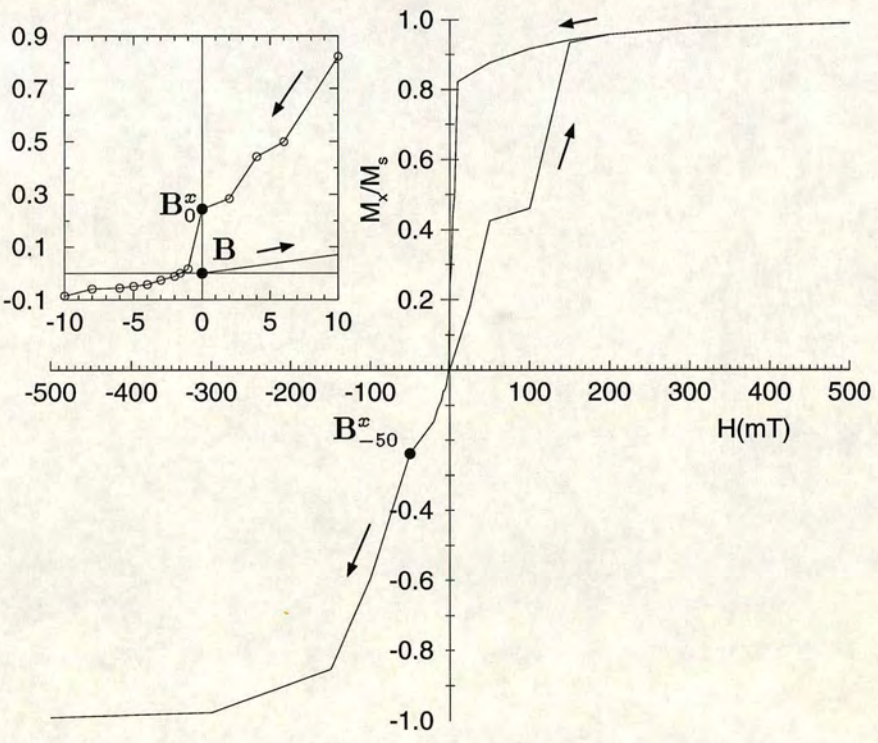


(b) $M_{rs}/M_s = 0.244$, $H_c = 1.579\text{mT}$

**Figure 7.3.** Hysteresis curves for a $0.2\mu$m cubic grain calculated using the flower state **B** as an initial state. External field applied (a) parallel to the $z$ axis and (b) parallel to the $x$ axis. The magnetization states are shown in figures 7.4 and 7.5.

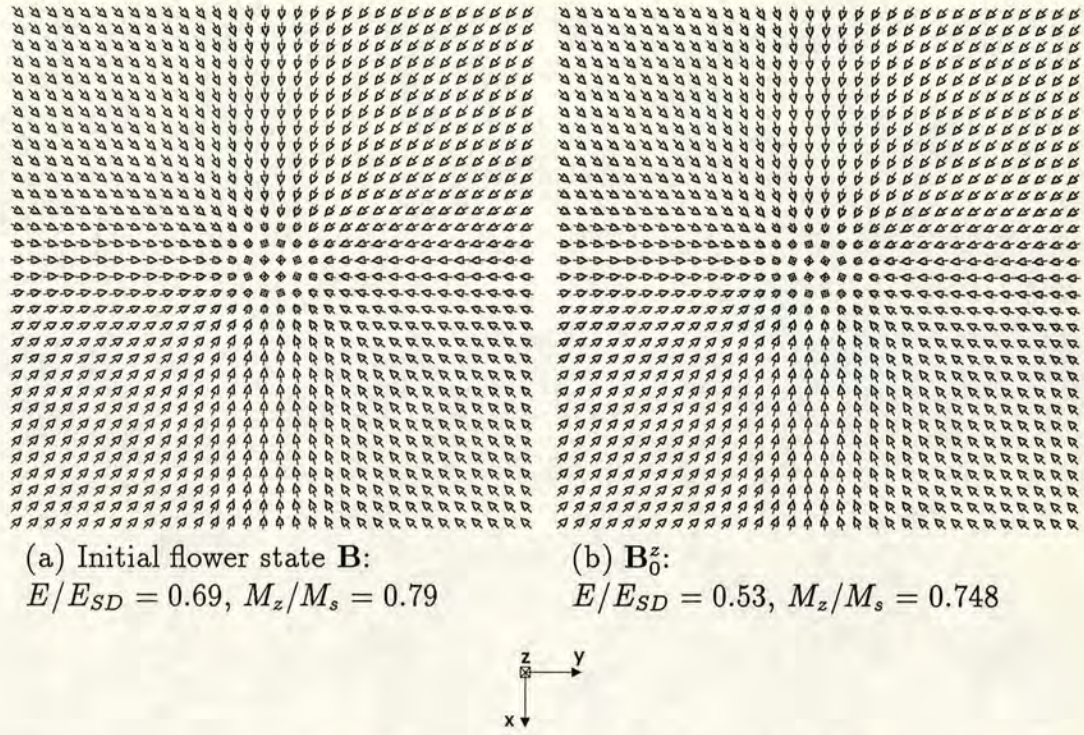


(a) Initial flower state $\mathbf{B}$:
$E/E_{SD} = 0.69$, $M_z/M_s = 0.79$

(b) $\mathbf{B}^z_0$:
$E/E_{SD} = 0.53$, $M_z/M_s = 0.748$

(c) $\mathbf{B}^z_{-4}$: $M_z/M_s = 0.579$

(d) $\mathbf{B}^z_{-10}$: $M_z/M_s = -0.007$

**Figure 7.4.** Magnetization states for a $0.2\mu$m grain with a field applied in the $z$ direction, (a) initial state, (b) remanence state $H$=0mT, (c) $H = -4$mT, (d) $H = -10$mT. Each slice is a $z = 32$ plane.

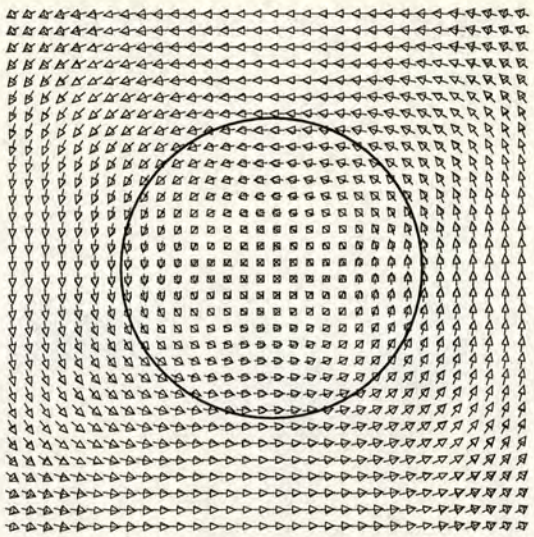

(a) $\mathbf{B}_0^x$: $x = 16$ plane
$E/E_{SD} = 0.29$, $M_x/M_s = 0.244$,

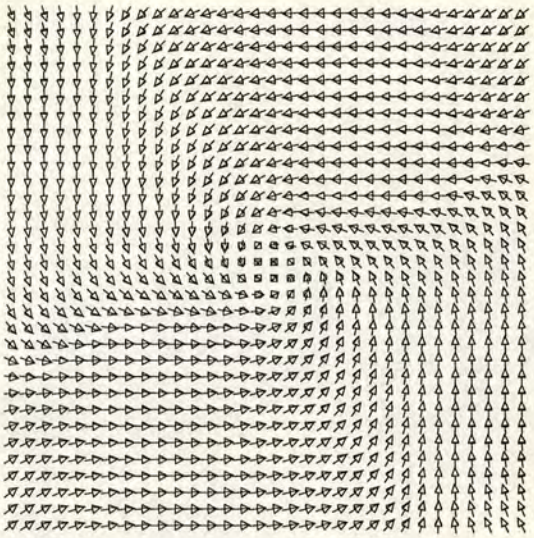

(b) $\mathbf{B}_0^x$: $x = 32$ plane
$E/E_{SD} = 0.29$, $M_x/M_s = 0.244$,

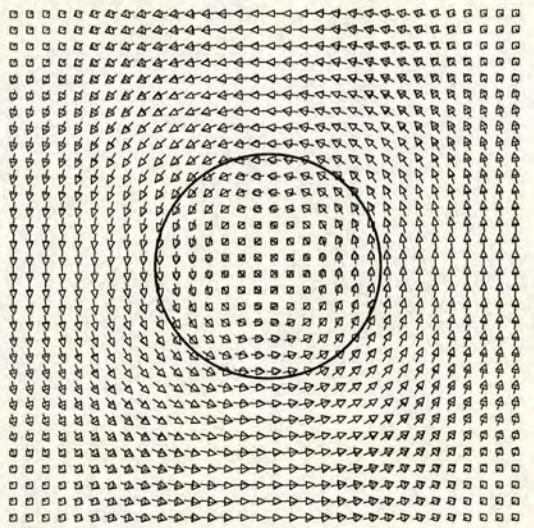

(c) $\mathbf{B}_{-10}^x$: $x$ =16 plane
$M_x/M_s = -0.085$

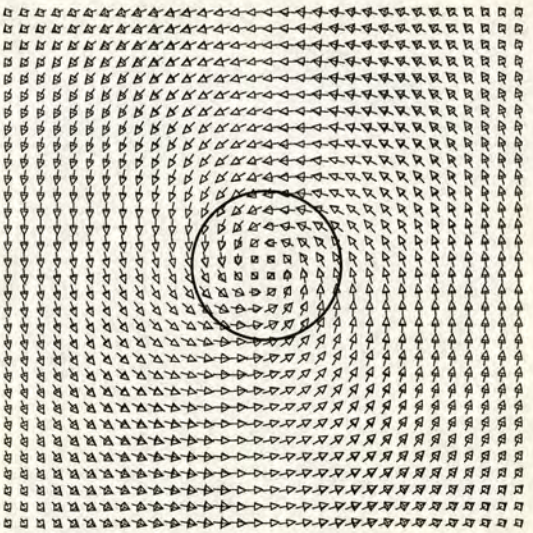

(d) $\mathbf{B}_{-50}^x$: $x = 16$ plane
$M_x/M_s = -0.23$

**Figure 7.5.** Magnetization states for a 0.2$\mu$m grain for a field applied in the $x$ direction, (a,b) saturation remanence state, (c) $H = -10$mT, (d) $H = -50$mT.

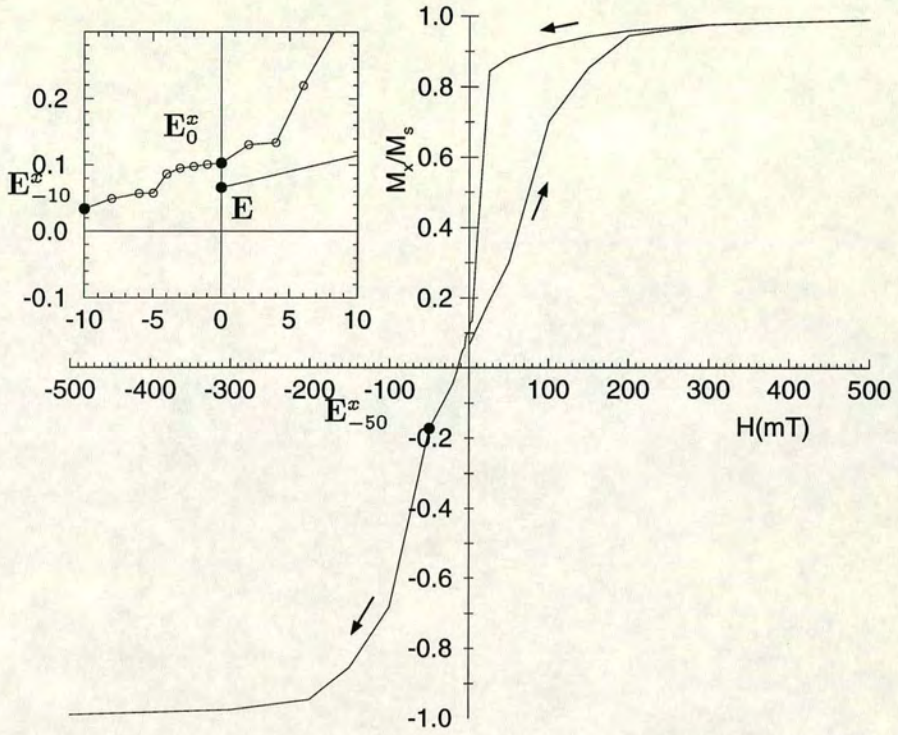


(a) $M_{rs}/M_s = 0.103$, $H_c = 13.768$mT

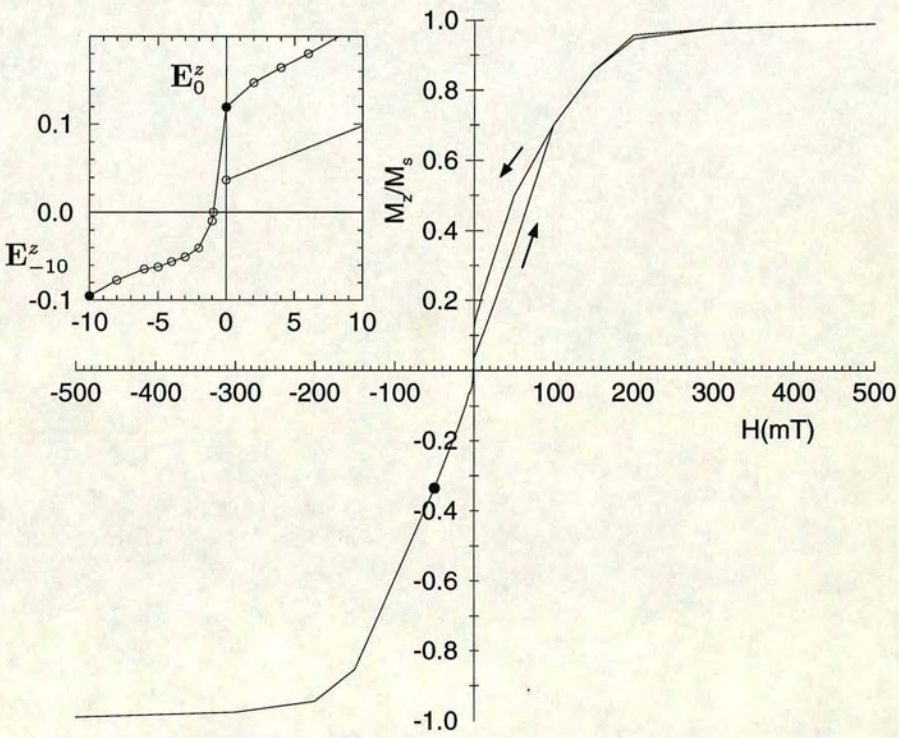


(b) $M_{rs}/M_s = 0.119$, $H_c = 0.923$mT

**Figure 7.6.** Hysteresis results for a 0.2$\mu$m using the vortex state **E** as an initial state. External field applied (a) parallel to the $x$ axis and (b) parallel to the $z$ axis.

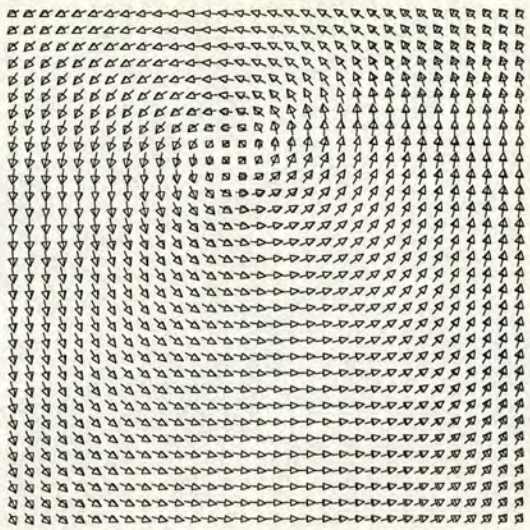

(a) **E**: $E/E_{SD} = 0.158$, $M_x/M_s = 0.065$

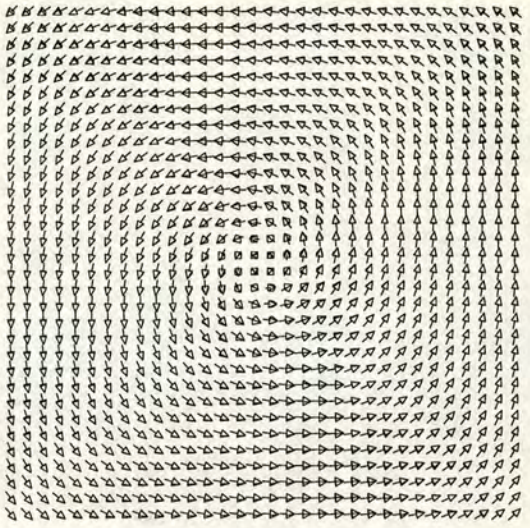

(b) $\mathbf{E}_0^x$: $E/E_{SD} = 0.181$, $M_{rs}/M_s = 0.103$

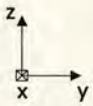


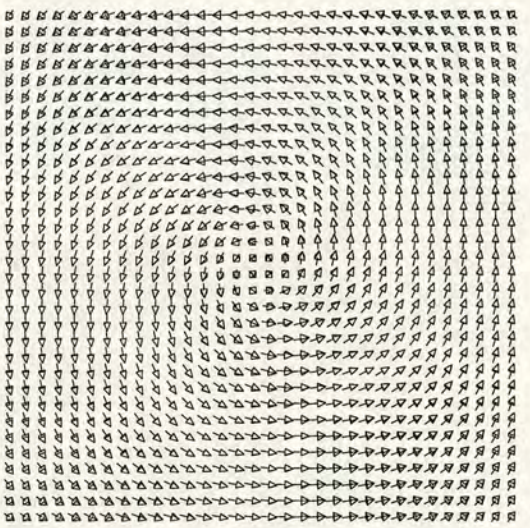

(c) $\mathbf{E}_{-10}^x$: $M_x/M_s = -0.087$

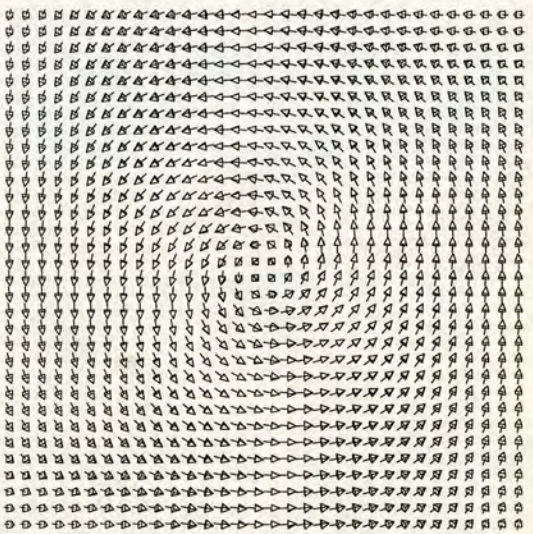

(d) $\mathbf{E}_{-50}^x$: $M_x/M_s = -0.299$

**Figure 7.7.** Magnetization states for a 0.2$\mu$m grain with a field applied in the $+x$ direction using a vortex state as an initial state, (a) initial state **E**, (b) remanence state $H$=0mT, (c) $H = -10$mT (d) $H = -50$mT. Each plane is a $x = 32$ plane.

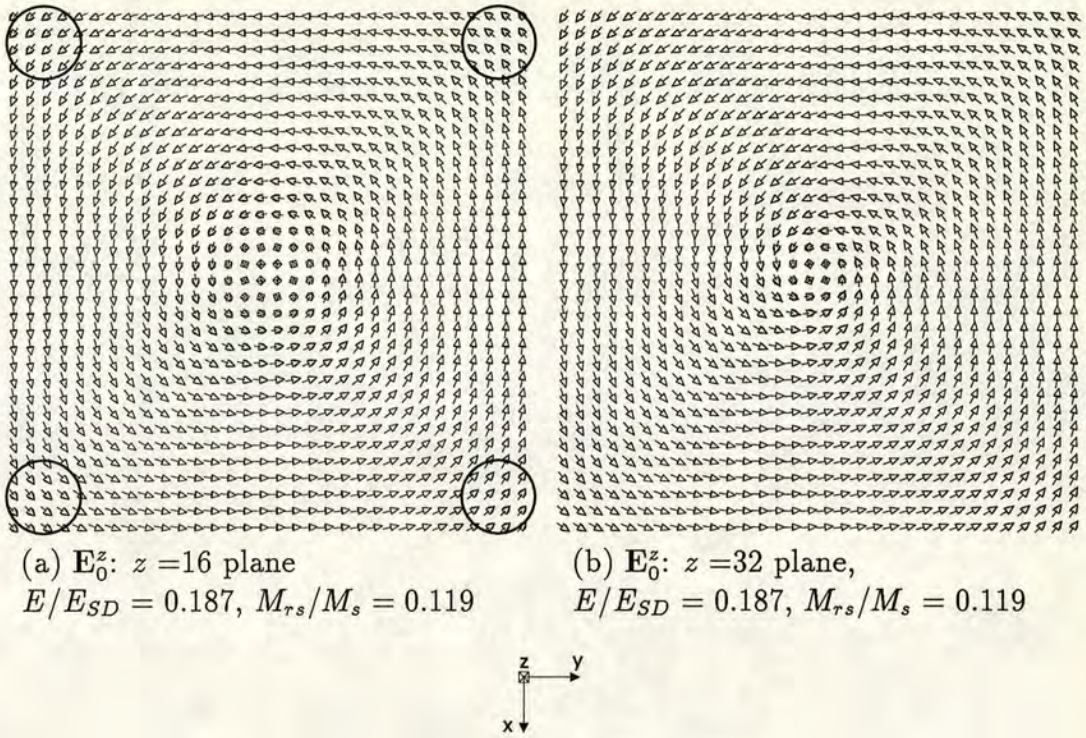


(a) $\mathbf{E}_0^z$: $z$ =16 plane
$E/E_{SD} = 0.187$, $M_{rs}/M_s = 0.119$

(b) $\mathbf{E}_0^z$: $z$ =32 plane,
$E/E_{SD} = 0.187$, $M_{rs}/M_s = 0.119$

(c) $\mathbf{E}_{-10}^z$:$z = 16$ plane
$M_z/M_s = -0.095$

(d) $\mathbf{E}_{-50}^z$: $z = 16$ plane
$M_z/M_s = -0.335$

**Figure 7.8.** Magnetization states for a 0.2$\mu$m grain with a field applied in the $z$ direction using the vortex state $\mathbf{E}$ as an initial state, (a,b) remanence state $H$=0mT, (c) $H = -10$mT, (d) $H = -50$mT. Figure (a) shows the magnetization at the corners aligned along the $\langle 111 \rangle$ easy directions.

| | $d$ ($\mu$m) | $M_{rs}/M_s$ | $H_c$ (mT) | $\chi_0$ (SI) |
|---|---|---|---|---|
| Theoretical | 0.2 | $0.095 \pm 0.031$ | $6.5 \pm 3.9$ | 3.21 |
| Experimental | $0.22 \pm 0.04$ | 0.112 | 10.6 | 3.32 |

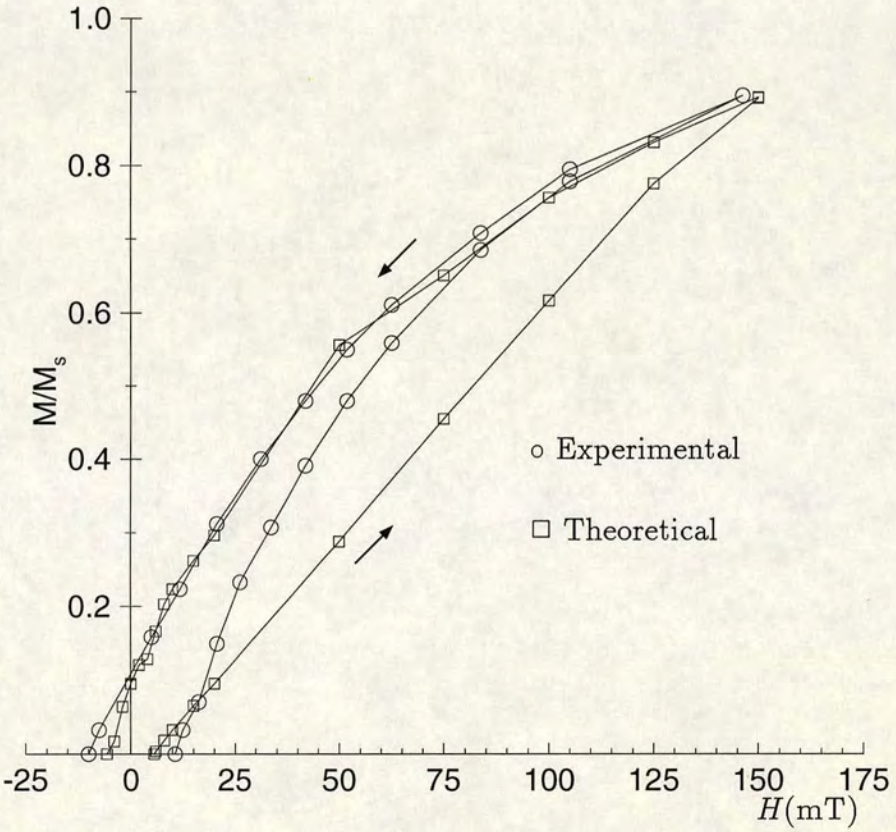


**Figure 7.9.** Predicted hysteresis curve for a single 0.2$\mu$m grain using a $32 \times 32 \times 32$ model (□) compared to experimentally measured curves on a sample of $0.22 \pm 0.04\mu$m sized magnetite grains (o) from Dunlop (1986). The theoretical curve is an average over 5 curves obtained using an external field applied in the [111] direction and at 0°, 22.5°, 45°, 67.5° and 90° to the [001] direction (for clarity the initial curves from state **E** at $H = 0$mT to $H = 150$mT have been omitted).

## 7.5 $1.0\mu m$ cubic grain

Figures 7.10a,b show results from two hysteresis simulations for fields applied in the [001] and [111] directions. The curves for each field direction show different behaviours depending on the orientation of the field, the curve for the [001] field direction shown in figure 7.10a has high values for both $M_{rs}$ and $H_c$ whereas the [111] direction has low values for both $M_{rs}$ and $H_c$. Figures 7.11 and 7.12 show the saturation remanence state, $\mathbf{D}_z^0$. This is a symmetrical state consisting of an internal vortex structure, four closure domains at the top and bottom of the grain and four lamellar domains at the sides of the grain. A consistent feature with this state and state **D** is that the magnetocrystalline anisotropy controls the closure domains and the domains at the sides of the grain to align along the $\langle 110 \rangle$ intermediate directions. Figure 7.11 shows two of these side domains aligned along the $[0\bar{1}\bar{1}]$ and $[10\bar{1}]$ directions. Another feature of the state $\mathbf{D}_z^0$ is the edge domains shown in figure 7.11 which are aligned in the direction of applied field. This state has a relatively high moment of $M_{rs}/M_s = 0.042$ due to the magnetization in the central vortex structure having a significant [001] component. This value of $M_{rs}/M_s = 0.042$ is close to the experimental value of $M_{rs}/M_s = 0.052$ obtained from measurements on the $0.8\mu$m hydrothermal sample by Heider (1988). The hysteresis curve also has a high coercivity, $H_c = 7.13$mT compared to $H_c = 6.1$mT for the same $0.8\mu$m sample. The high coercivity is controlled by the central vortex structure, as the field decreases from $H = 0$mT to $H = -10$mT the edge domains flip over first as shown in figure 7.13d. The central vortex remains in the direction of the applied field but decreases in size as the field decreases from $H = -10$mT.

The hysteresis curve for the [111] field direction, shown in figure 7.10b is characterized by a multi-domain type process with low values for $M_{rs}$ and $H_c$. The low value for $M_{rs}$ and $H_c$ is due to regions in the centre of the grain being aligned in the opposite direction to the field as shown in figure 7.14. This state is a similar low energy state to state **D**, in which a two-domain shell surrounds and shields an interior $\langle 111 \rangle$ magnetization.

Figure 7.15 compares these two predicted hysteresis curves with experimental curves obtained from the $0.8\mu$m sample of hydrothermal grains whose distribution of grain sizes is shown in figure 2.2 . Both of the theoretical curves lie close to the

experimental curve, in particular the 'knee' predicted at $H = 100\text{mT}$ matches up with the experimental curve. Figure 7.15 also compares values for $H_c$ and $M_{rs}/M_s$ with the experimental values and show that $H_c$ is within the upper and lower limits predicted by the [001] and [111] curves although the experimental value for $M_{rs}$ is higher than both the predicted curves. The predicted values for $M_{rs}/M_s$ are lower than the experimental results because the grain sizes are not strictly comparable. The $0.8\mu$m synthetic sample consists of grains between $0.4\mu$m and $0.8\mu$m in width and will have an associated increase in $M_{rs}/M_s$. Including theoretical results for $d = 0.7\mu$m increases $M_{rs}/M_s$, so for example for a field applied in the $z$ direction, $M_{rs}/M_s = 0.065$ at $d = 0.7\mu$m

## 7.6 $0.7\mu$m octahedral grain

Hysteresis curves were predicted for octahedral grains in the size range $0.1\mu$m to $1.0\mu$m using the octahedral vortex states shown in chapter 6 as initial states. For fields applied in the $\langle 100 \rangle$ directions the saturation remanence state is the same single vortex state as the initial vortex state. The variation in the orientation of the vortex core and the deflection of spins at the grain's edges which are seen in cubic grains are not seen in the octahedral remanence states. This is due to the strong octahedral shape anisotropy reducing the number of available LEM states.

For fields applied in $\langle 111 \rangle$ directions the magnetization occupies the double-vortex state shown in figures 7.16 and 7.17. At a particular grain size these double-vortex states are higher energy states than the single vortex states. For example at $d = 0.7\mu$m, $E/E_{sd} = 0.059$ for the double-vortex state compared to $E/E_{sd} = -0.067$ for the single vortex state. This is due to the increased divergence of the magnetization which increases the exchange energy. In addition, because two vortex cores occur at the surface, the number of free charges increases and thus the magnetostatic energy increases. This double-vortex state also has a high moment, for example at $d = 0.4\mu$m, $M_{111}/M_s = 0.16$ where $M_{111}$ represents the moment in the [111] direction. The state shown in figures 7.16 and 7.17 has $M_{111}/M_s = 0.046$ at $d = 0.7\mu$m. This result is important because the single vortex states shown in chapter 6 have low moments compared to these double-vortex states. This shows that both octahedral and cubic grains can occupy high moment states which can contribute to PSD remanences.

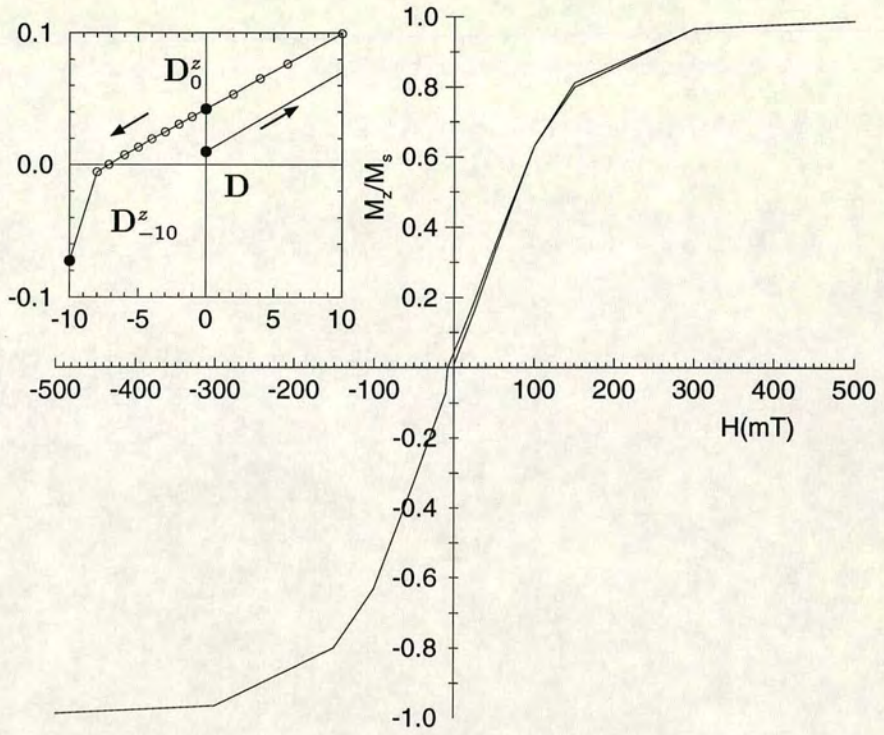


(a) $M_{rs}/M_s = 0.042$, $H_c = 7.133\text{mT}$

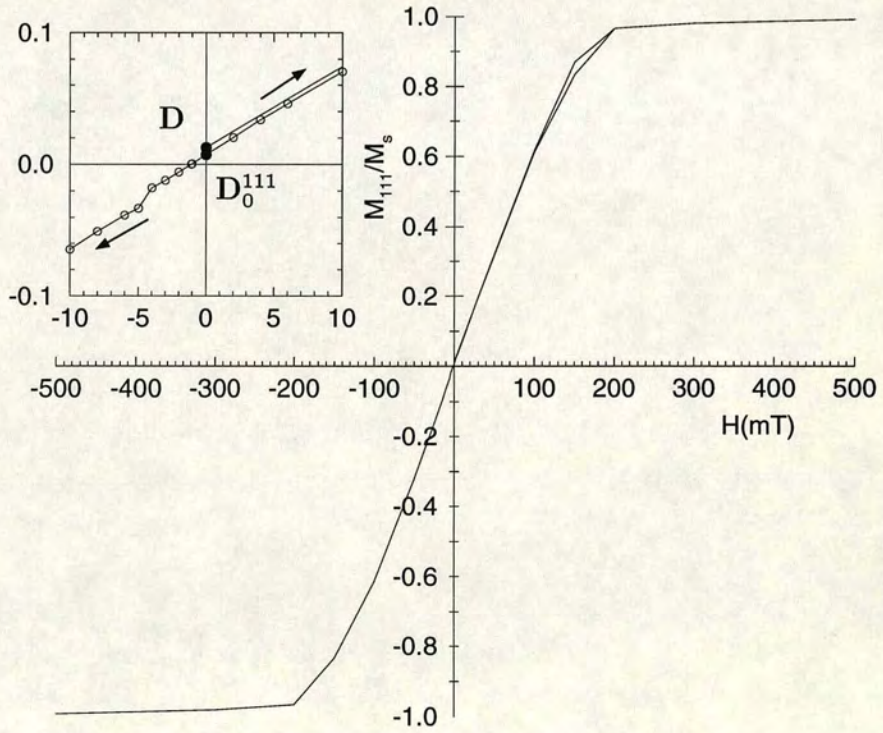


(b) $M_{rs}/M_s = 0.007$, $H_c = 1.089\text{mT}$

**Figure 7.10.** Hysteresis results for a 1$\mu$m grain with a field applied (a) parallel to the $z$ axis and (b) applied parallel to [111] direction. The magnetic structures are shown in figures 7.12 to 7.14

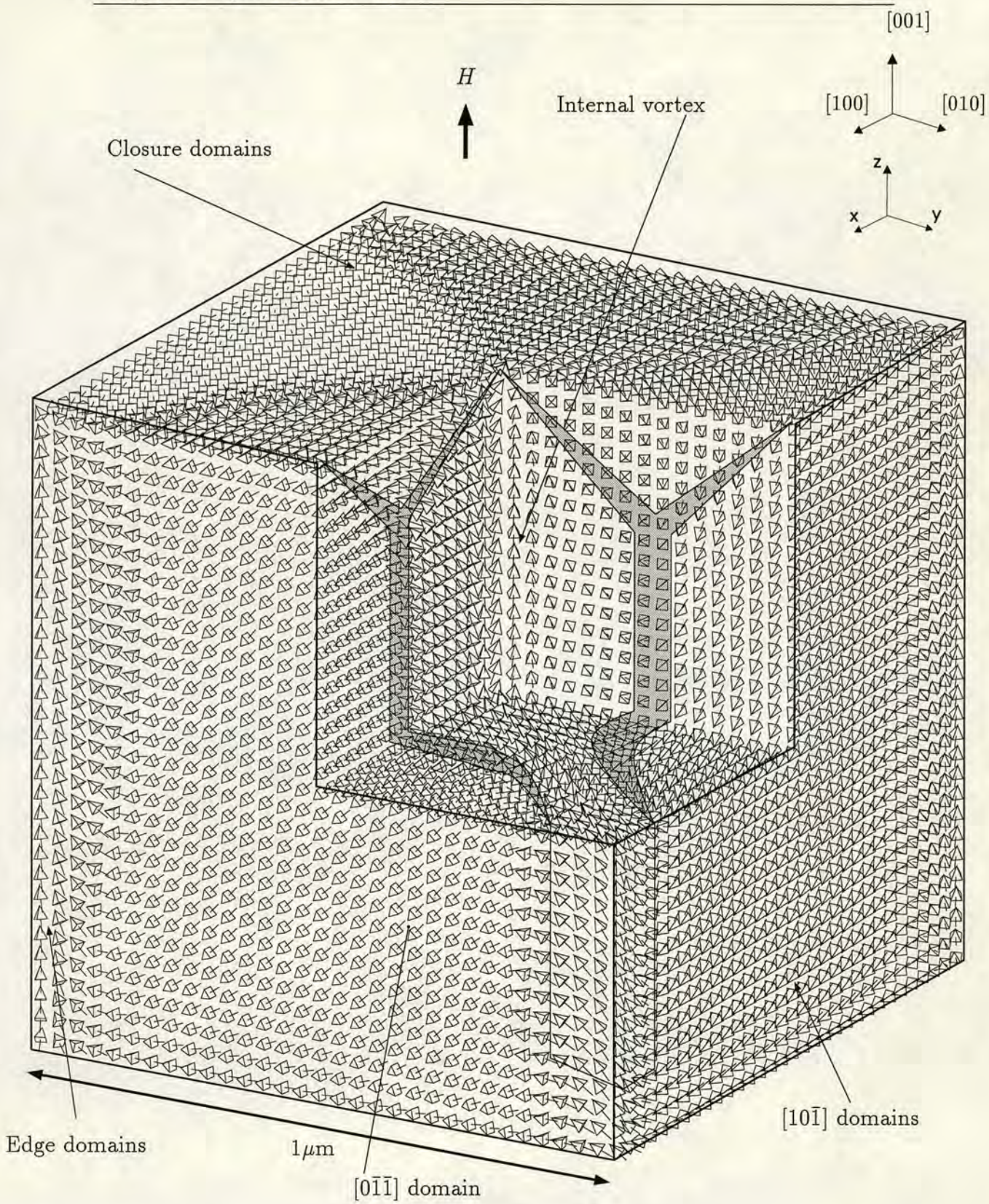


**Figure 7.11.** $\mathbf{D}_0^z$: cutaway view of a 1.0$\mu$m grain at saturation remanence for a field applied in the $z$ direction.

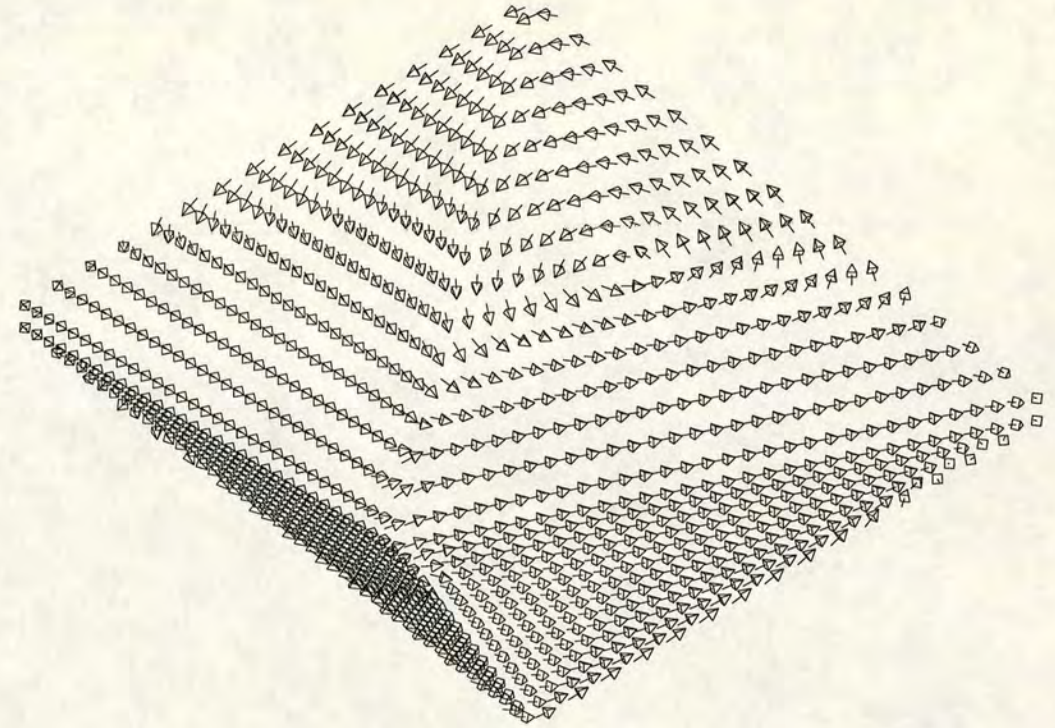

(a) 1.0$\mu$m

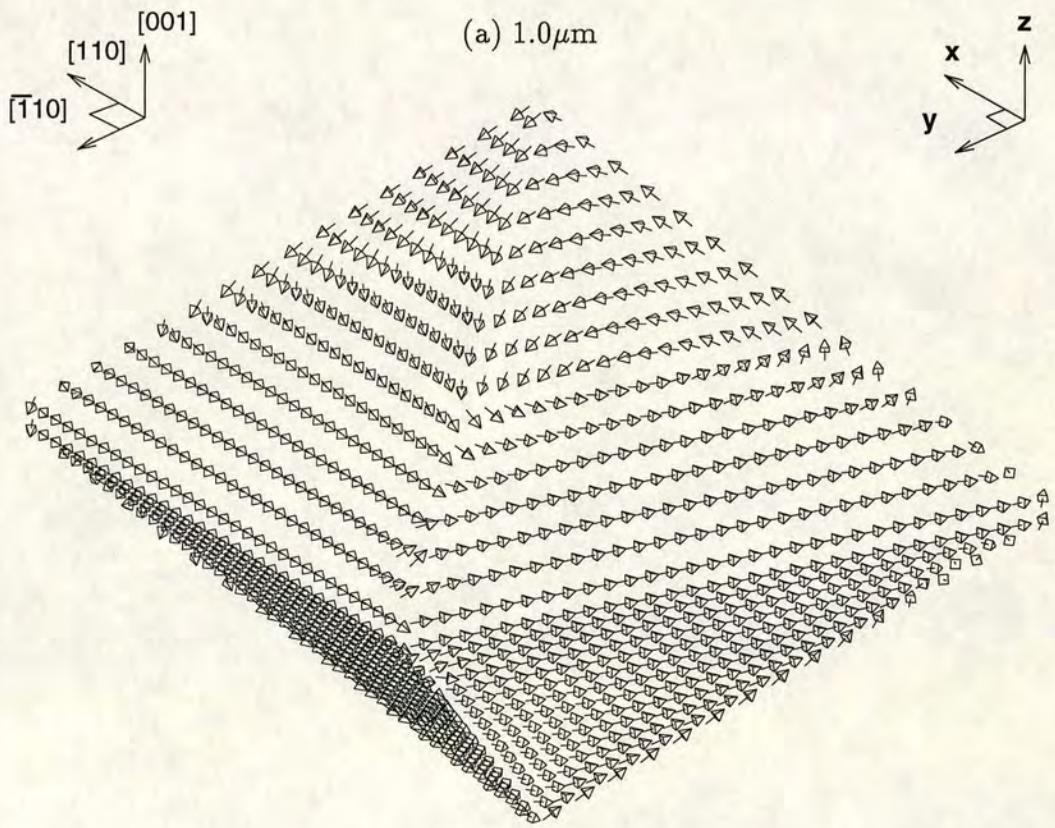


(b) 2.0$\mu$m

**Figure 6.9.** Solutions for the 45° octahedral model for 1$\mu$m and 2$\mu$m grains.

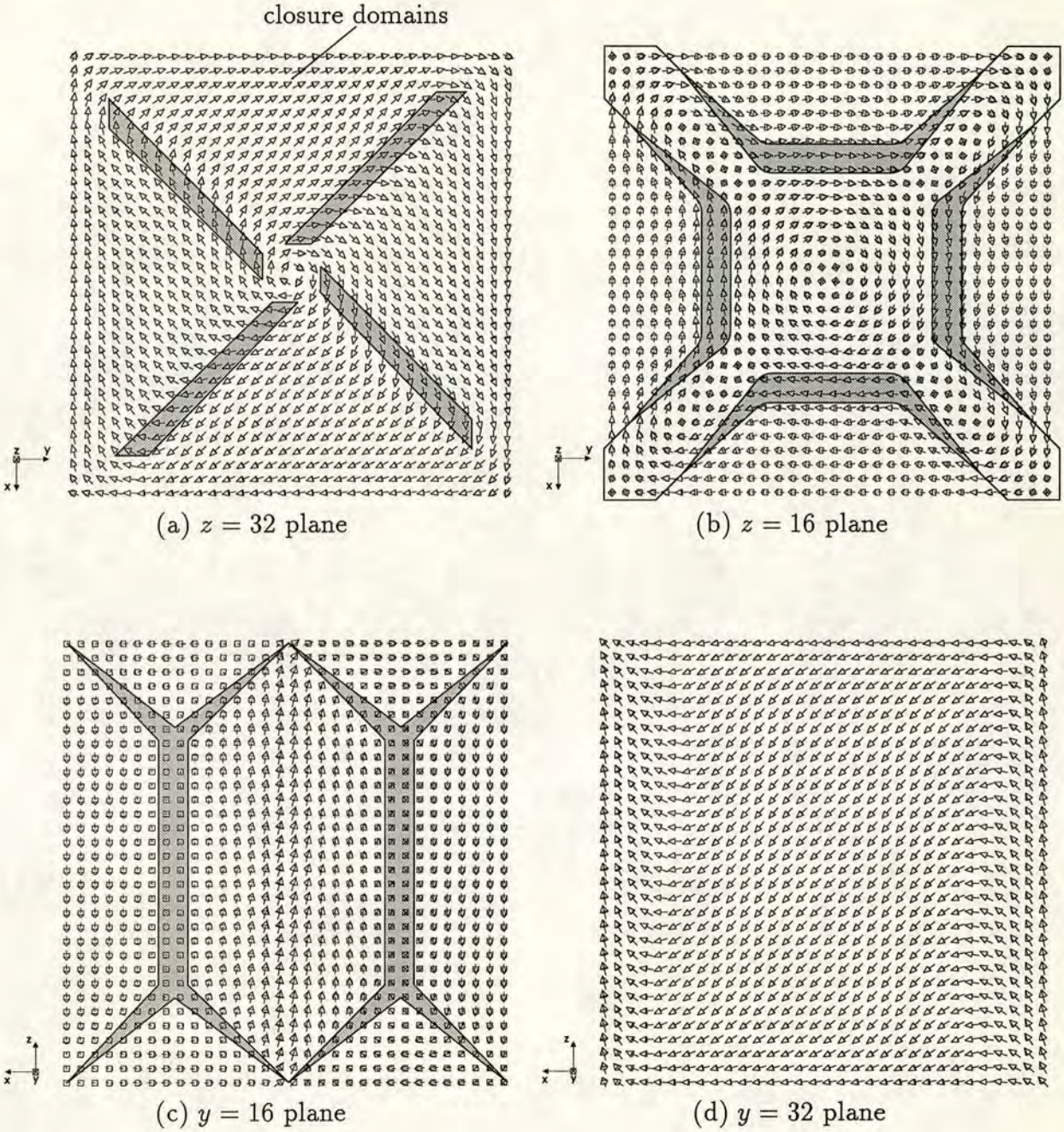


(a) $z = 32$ plane (b) $z = 16$ plane

(c) $y = 16$ plane (d) $y = 32$ plane

**Figure 7.12.** $\mathbf{D}_0^z$: $M_{rs}$ state for a 1$\mu$m grain after being cycled through a field applied in the [001] direction. The gray shaded regions in figure (a) show domain walls and in figures (b,c) how the central vortex structure is separated from the lamellar domains at the sides at the sides of the grain. $E/E_{SD} = -0.013$, $M_{rs}/M_s = 0.042$

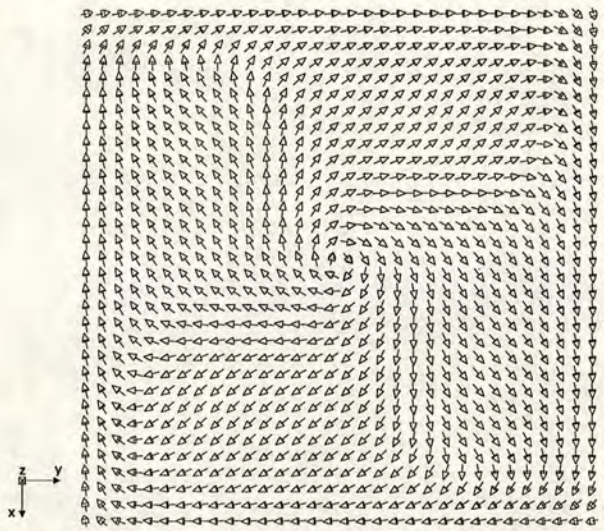

(a) $z = 32$ plane

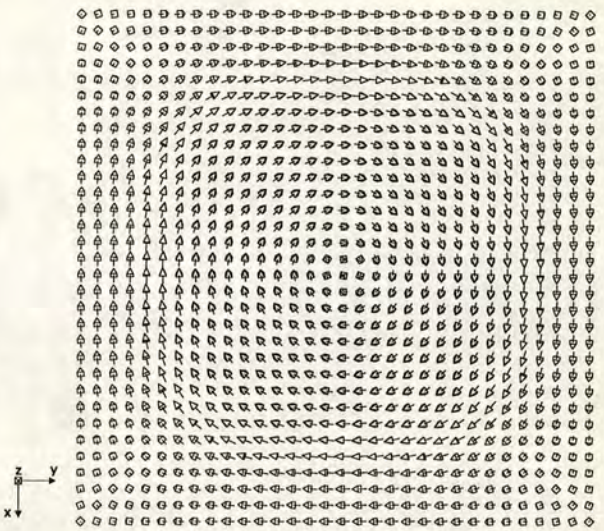

(b) $z = 16$ plane

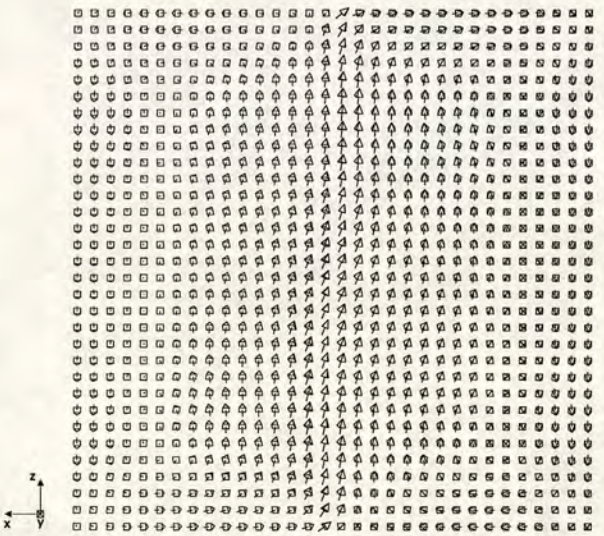

(c) $y = 16$ plane

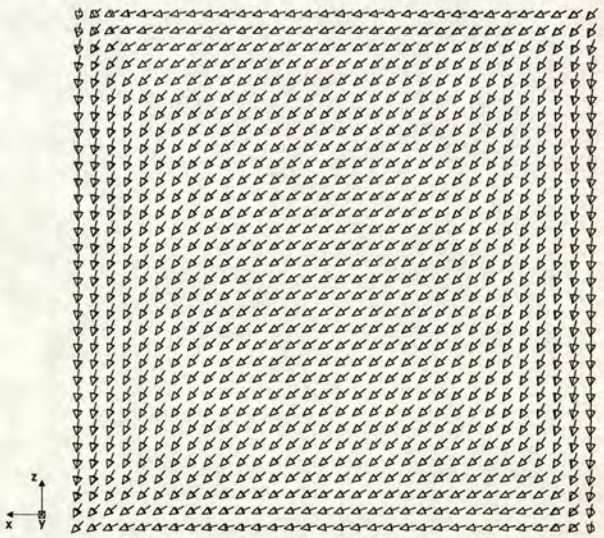

(d) $y = 32$ plane

**Figure 7.13.** $\mathbf{D}^z_{-10}$: Magnetization state at $d = 1.0\mu$m, $H = -10$mT.

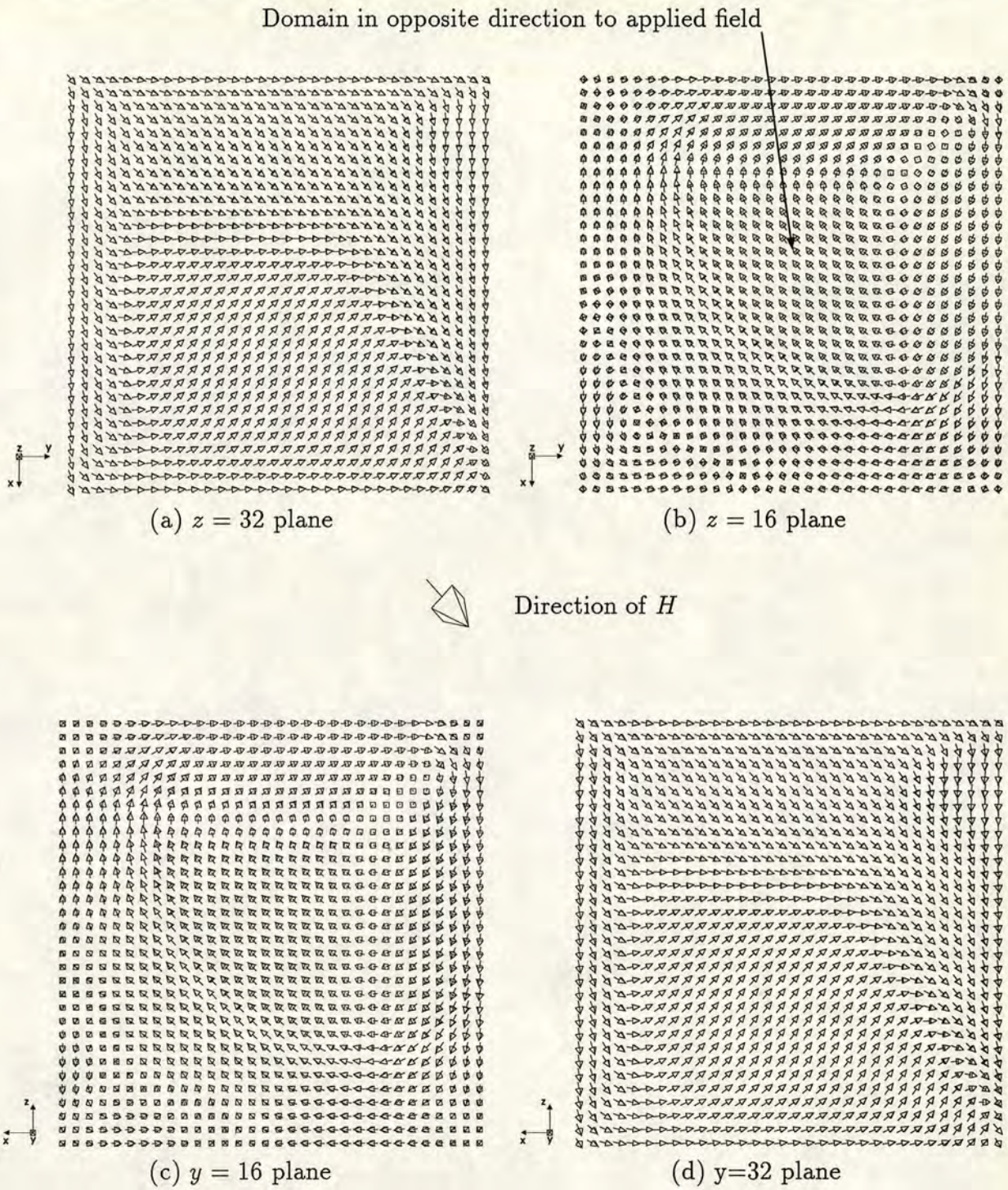


(a) $z = 32$ plane

(b) $z = 16$ plane

(c) $y = 16$ plane

(d) y=32 plane

**Figure 7.14.** $\mathbf{D}_0^{111}$: Saturation remanence state for a 1$\mu$m grain after being cycled through a field applied in the [111] direction. $E/E_{SD} = -0.027$, $M_{rs}/M_s = 0.007$

| | $d$ ($\mu$m) | $M_{rs}/M_s$ | $H_c$ (mT) | $\chi_0$ (SI) |
|---|---|---|---|---|
| Average of [111] and [100] | 1 | 0.024 | 4.1 | 3.65 |
| Experimental | $0.8 \pm 0.31$ | 0.054 | 6.1 | 3.85 |

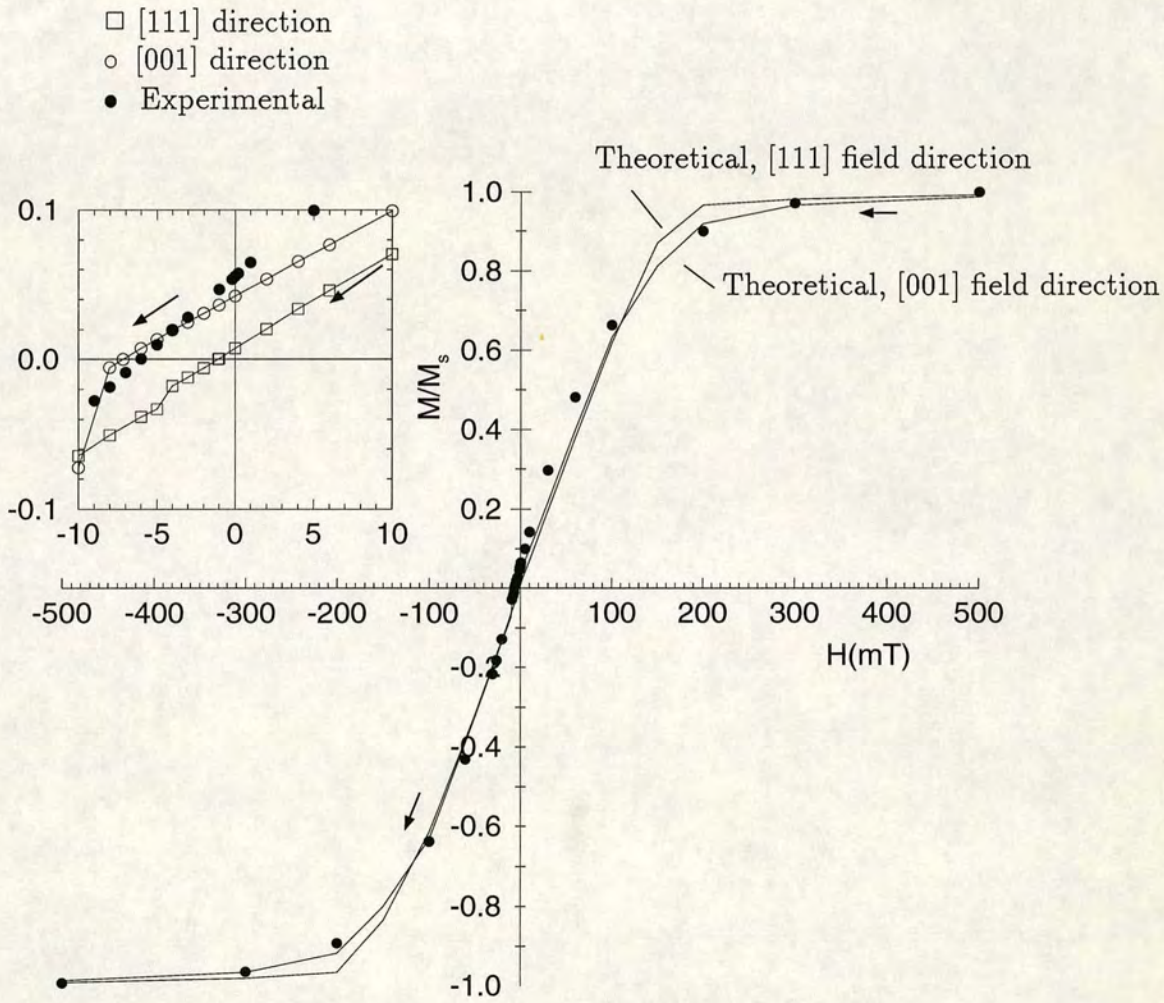


**Figure 7.15.** Predicted hysteresis curves for a single 1.0$\mu$m grain using a $32 \times 32 \times 32$ model (□, ○) compared to experimentally measured curves on a sample of $0.8 \pm 0.31\mu$m sized magnetite grains (•), from Heider and Hoffman (1992). Each hysteresis curve is 'half' a hysteresis curve running from $H = 500$mT to $H = -500$mT. The initial curves from state **D** at $H$=0mT to saturation at $H = +500$mT are omitted for clarity.

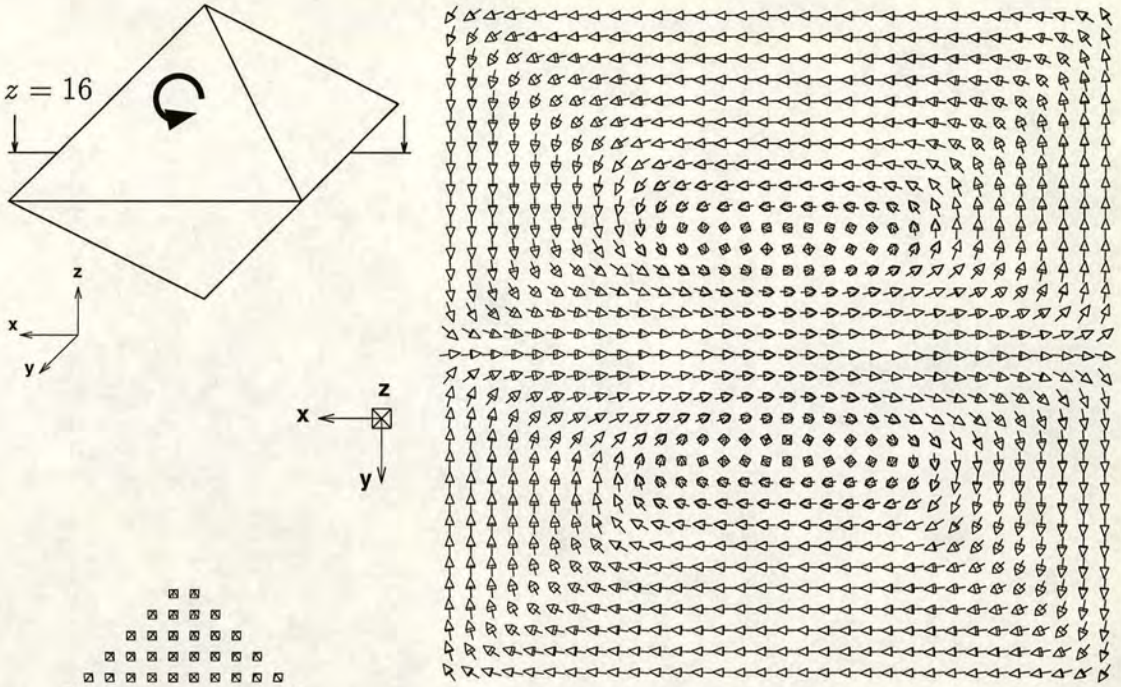


(a) z=16 plane

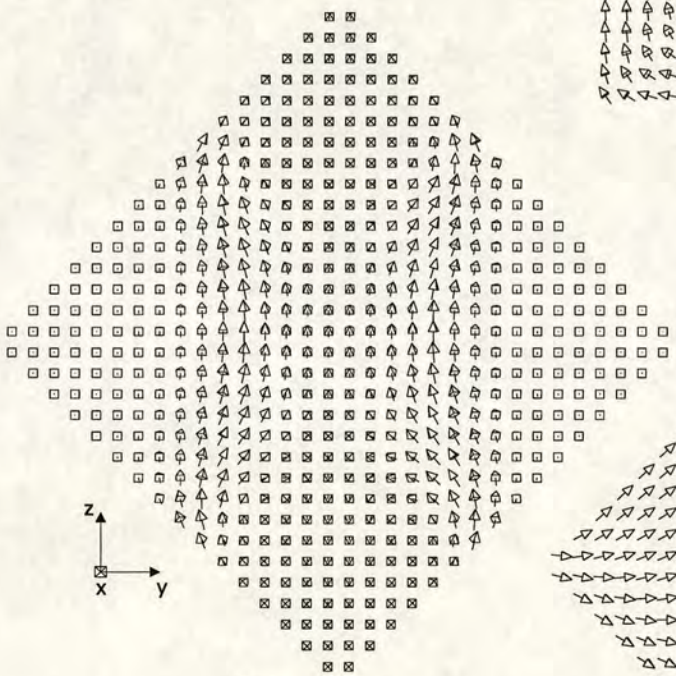


(b) x=16 plane

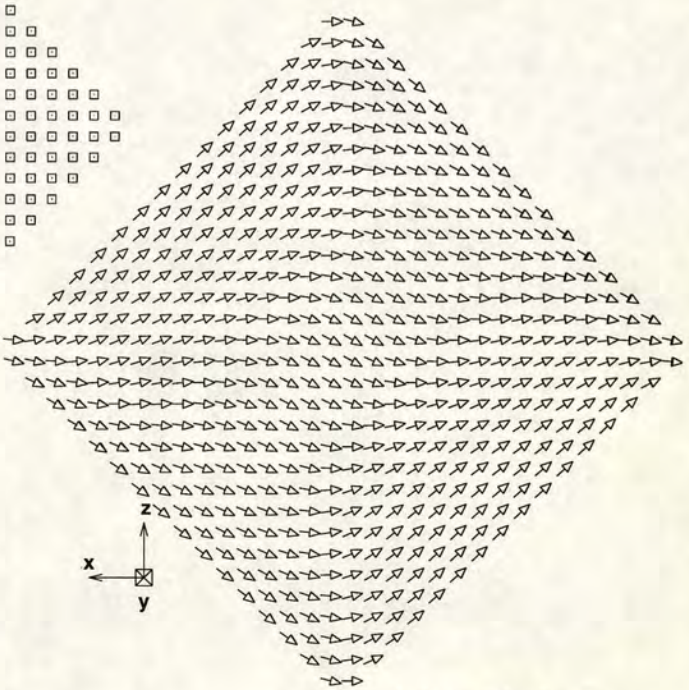


(c) y=16 plane

**Figure 7.16.** 0.7$\mu$m octahedral grain occupying a double-vortex state,
$E/E_{sd} = 0.059$,
$M_{rs}/M_s = 0.046$

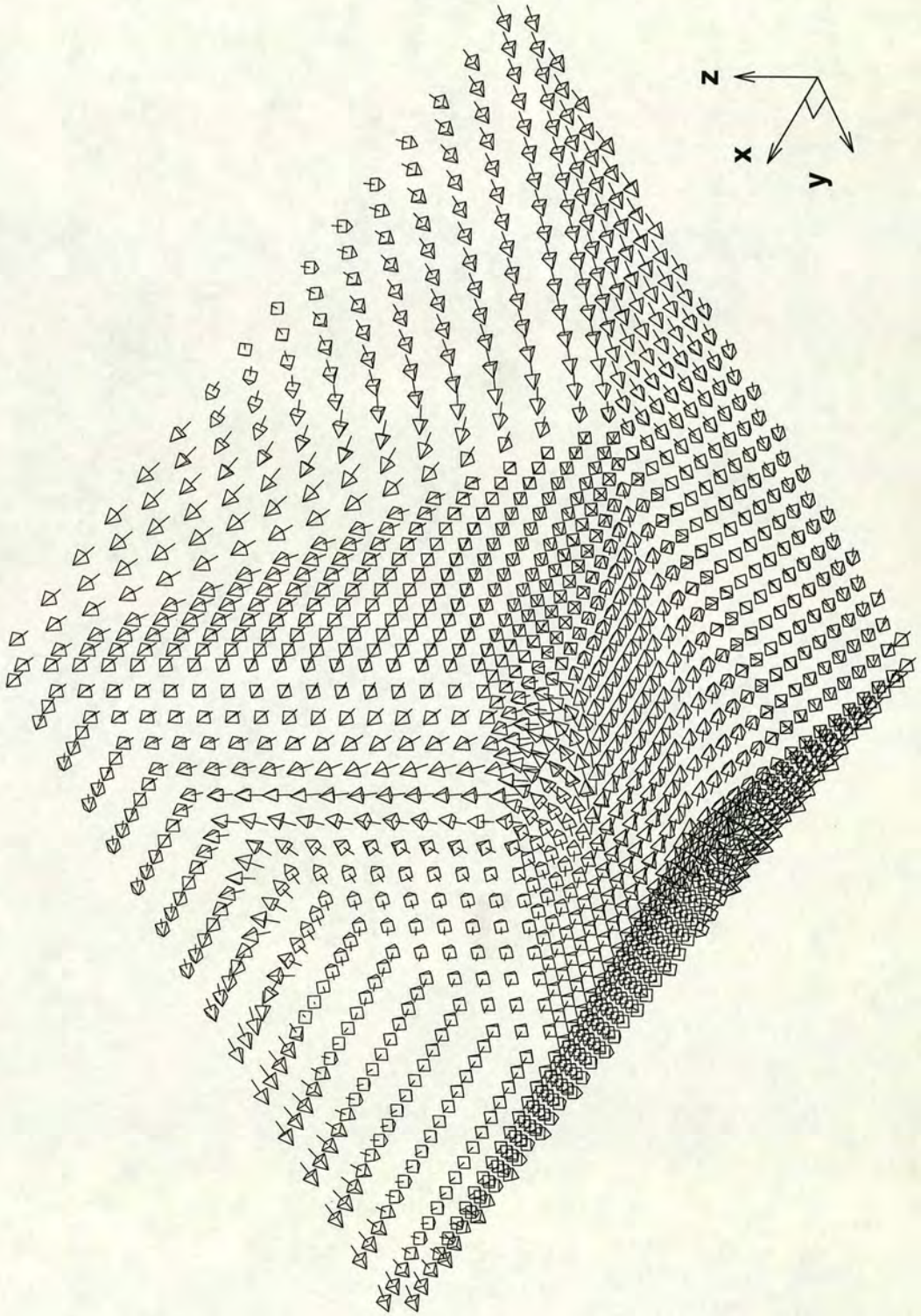


**Figure 7.17.** Cutaway view of the two vortex state at $d = 0.7\mu$m

## 7.7 Hysteresis parameters as a function of grain size

Figure 7.18 compares predictions of $M_{rs}/M_s$ and $H_c$ with experimental measurements on synthetically grown grains. The predicted results at each grain size were obtained by applying a field in an easy and a hard direction. The upper value for the octahedral result is the double-vortex state shown in figures 7.16 and 7.17 and the lower value is the single vortex state shown in 6.8. The predicted results for $M_{rs}/M_s$ are a good fit to the experimental data, whilst the average values for $H_c$ are slightly low. The low values can be explained by fact that experimental samples consist of a range of grain sizes and also by the nature of how $H_c$ and $M_{rs}$ decreases with increasing grain size. Thus, any synthetic grains larger than the average grain size will be included in the grain size count but will not contribute to $H_c$ or $M_{rs}$, whilst grains smaller than the average grain size will raise the experimentally measured values of $H_c$ and $M_{rs}$.

Susceptibility measurements on lake and marine cores have been considered indicators of climate change, for example Maher, Thompson and Zhou (1994) postulated that high susceptibilities measured in Chinese loess deposits are correlated with high concentrations of magnetite and in turn with high precipitation rates. Additionally, studies on North Atlantic deep-sea sediments by Robinson (1986) have correlated inter-glacial cycles with low susceptibilities and glacial cycles with high susceptibilities. Both these studies have relied on the fact that measured susceptibility values are independent of grain size.

In order to test this assumption, theoretical predictions for initial susceptibility as a function of grain size were compared with experimental measurements. The initial susceptibility values were calculated by taking the vortex states shown in chapter 5, applying a field of 20mT and the ratio of $\chi = M\mu_0/H$ calculated ($M$ being the component of the magnetization in the direction of the field). Figure 7.19 shows that most of the the experimental values lie between $\chi = 2$ and $\chi = 4$ for grains up to 1mm in size. Between $0.1\mu$m and $1.0\mu$m the predicted values show little variation in either grain size or direction of applied field and are within the range of experimental measurements. At $d = 0.07\mu$m there is a wide variation in susceptibility values with the direction of the applied field. However the average value of $\chi = 5.3$ at $d = 0.07\mu$m is not much larger than predicted values of $\chi \simeq 4$ for grains larger than $0.1\mu$m. Taking into consideration the fact

cont. on page 149

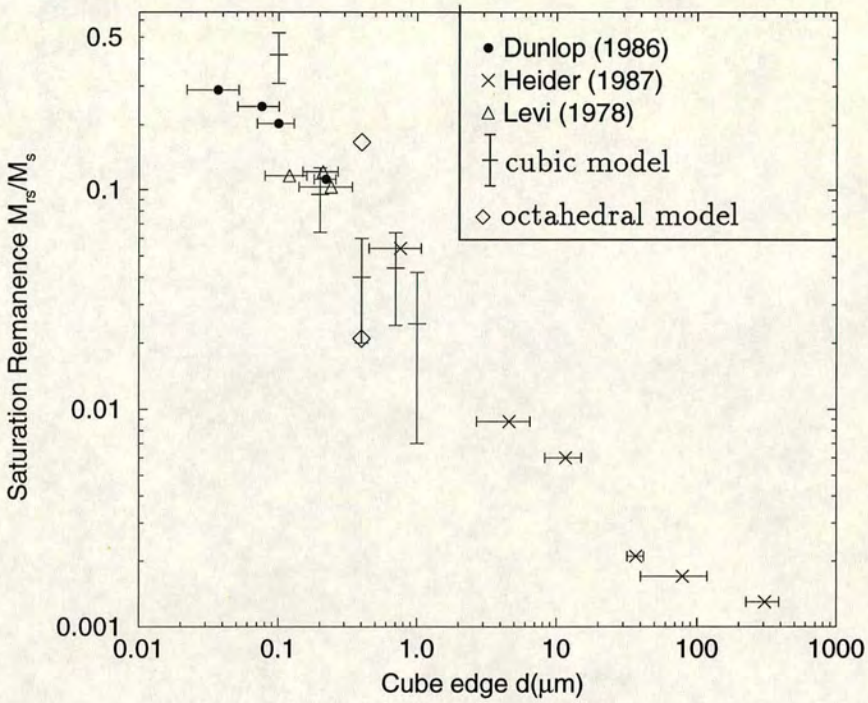


(a) Saturation remanence vs. grain size

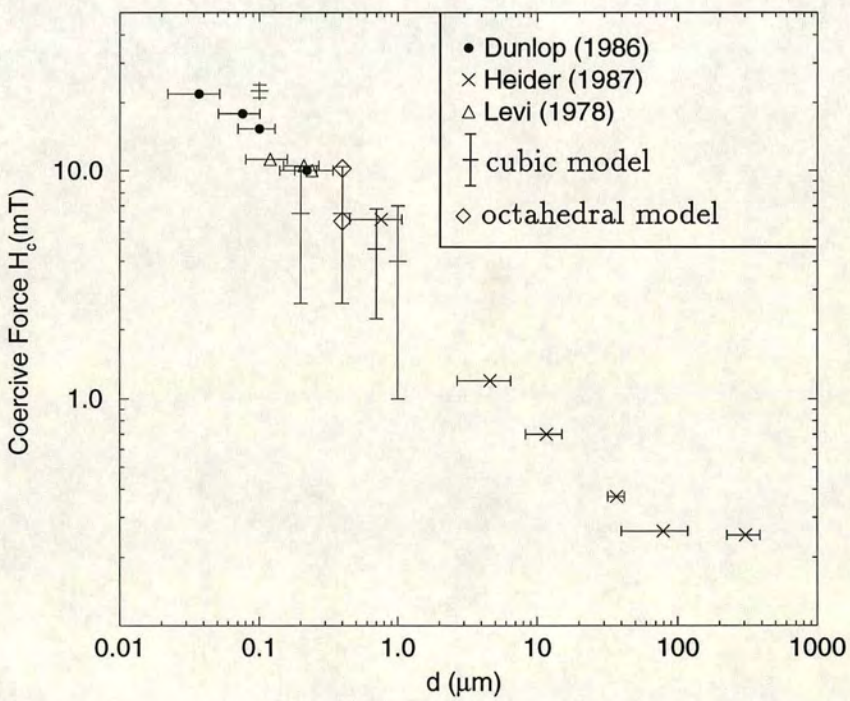


(b) Coercive force vs. grain size

**Figure 7.18.** Dependence of (a) saturation remanences and (b) coercivities as a function of grain size. Experimental data: •,△,×. Theoretical predictions are from a $32 \times 32 \times 32$ model.

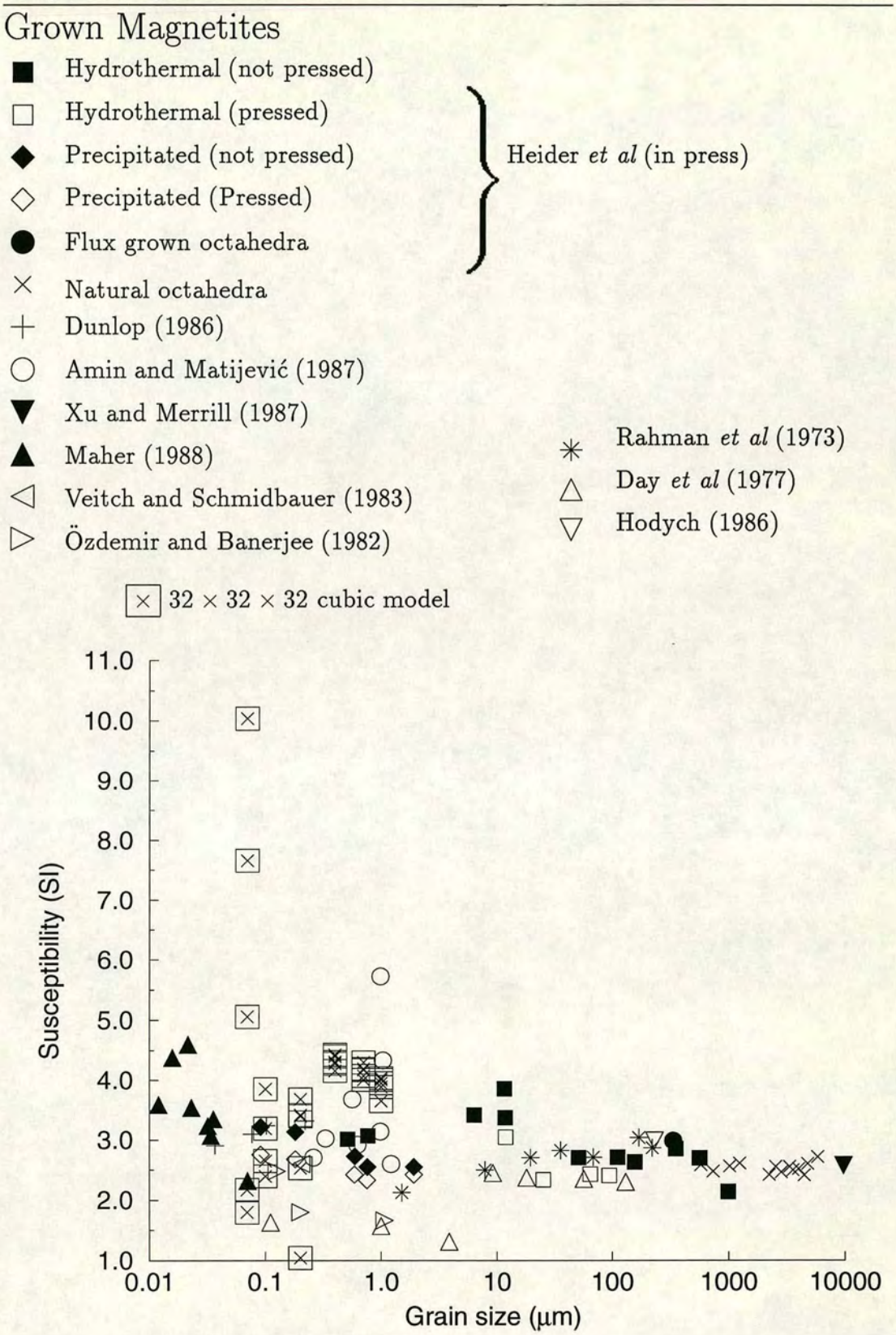


**Figure 7.19.** Comparison of predicted susceptibilities with experimental results. At each grain size susceptibility values are plotted for fields applied at angles of 0°, 22.5°, 45°, 67.5° and 90° to the [001] direction.

that measured susceptibilities values of climate records show variations of between 10 and 100 times the lowest value, these results show that susceptibility values when averaged over a range of field directions do not depend significantly on grain size.

## 7.8 Summary

The reversal mechanism for magnetite can be categorized by the following processes:

- Cubic grains, $d < 0.07\mu$m; SD coherent rotation with a small amount of flowering.
- Cubic grains, $0.07 < d < 1.0\mu$m; Vortex propagation and grains larger than $0.2\mu$m can occupy one of several separate LEM states at saturation remanence.
- Cubic grains, $d = 1.0\mu$m; A combination of domain and vortex processes, For a field applied in the [001] direction the reversal mechanism is controlled by $\langle 110 \rangle$ surface domains and an internal vortex structure, $(\mathbf{D}_0^z)$.

  For a field applied in the [111] direction the reversal mechanism is controlled by $\langle 110 \rangle$ surface domains and internal $\langle 111 \rangle$ domains, $(\mathbf{D}_{111}^z)$.
- Octahedral grains occupy either single-vortex or double-vortex states during hysteresis cycles.
- Peak values for $H_c$ and $M_{rs}$ agree well with experimental measurements; however, mean values are slightly lower. This can be explained by the fact that samples are composed of grains with a range of sizes.
- Susceptibility values when averaged over several field directions do not depend on grain size.

# Chapter 8. Discussion

## 8.1 PSD remanences and stability

The hysteresis results presented in chapter 7 show that vortex states are able to predict the high remanences and coercivities measured experimentally in PSD grains. PSD grains in the size range $0.1\mu$m to $1.0\mu$m are important in palaeomagnetism, firstly, because natural samples have a large percentage of grains in this size range and secondly, they show high coercivities and remanences and thus provide a strong and stable palaeomagnetic signal. At $d = 0.1\mu$m, $M_{rs}/M_s = 0.26$ which is 1/4 that of a SD grain. The coercivity is predicted to be $H_c = 21$mT, 2/3 that of the coercivity predicted by analytic SD theory. These results show that vortex states can show the high values of saturation remanences and coercivities which have been meausured in PSD sized grains, without having to introduce other factors such as the magnetoelastic effect.

An important result from the $3d$ model is that LEM states are as significant as AEM states. Although it is not possible to conclude that the vortex states **C** and **D** are AEM states, they are lower energy states than each of the remanence states shown in chapter 7. The high remanences and coercivity of PSD grains between $0.1\mu$m and $1.0\mu$m are due to grains occupying high moment, high energy vortex states. It is interesting to note that there is a relationship between the energy and the symmetry of the magnetization states. For example, state **D** (figure 5.9) has a lower energy and an increased symmetry than the remanent state $\mathbf{D}_0^z$ (figure 7.11). State **D** is symmetrical about a point in the centre of the grain whereas $\mathbf{D}_0^z$ is symmetrical about a line through centre of a grain in the $z$ direction.

Chapter 7 showed that the anomalously high values for $H_c$ and $M_{rs}$ which are measured experimentally in grains sized between $0.1\mu$m and $1.0\mu$m is a real effect. In addition it predicted that values for $H_c$ and for $M_{rs}/M_s$ at a particular grain size are distributed about a mean value. It is not possible to test this distribution of $H_c$ and $M_{rs}/M_s$ using the synthetically grown bulk samples but James King at Edinburgh University is producing regularly spaced arrays of cubic magnetite grains using electron lithography techniques. This will produce arrays of cubic

grains which are similar to the permalloy grains shown in figure 6.19. These grains will have a well controlled grain size and by spacing the grains sufficiently far apart the effects of intergrain interactions can be reduced to insignificant levels.

The interesting aspect of these arrays will be to see if the high values for $M_{rs}$ and $H_c$ which are predicted by the model are measured for all field directions. The model predicts that at a grain size of $1\mu$m high values for $H_c$ and $M_{rs}$ will be measured in the hard direction and low values in the easy direction. This could easily be tested as there is a direct relationship between the model and a regularly spaced array of cubic grains.

## 8.2 Comparison with previous micromagnetic models.

Figure 8.1 compares predictions of $H_c$ and $M_{rs}$ from the $32 \times 32 \times 32$ model with results from a $12 \times 12 \times 12$ model (Williams 1994) and a $1d$ model (Enkin and Dunlop 1987). Figure 8.1a shows that results from $1d$ unconstrained models predict a transition from a SD to a two-domain state which decreases more rapidly than the experimental results.

Two values are shown at each grain size for the $12 \times 12 \times 12$ model; each value corresponds to a field applied in either an easy or a hard direction. The predicted values for $M_{rs}/M_s$ are significantly lower than the experimental values. For example, at $d = 0.2\mu$m an average of each $M_{rs}/M_s$ value gives 0.038, much less than the experimentally measured value of $M_{rs}/M_s = 0.1$. Table 8.1 shows that the experimentally measured value for $M_{rs}/M_s$ lies between the maximum and minimum values predicted by the $32 \times 32 \times 32$ model.

For the $32 \times 32 \times 32$ model, the mean values for $M_{rs}$ at larger grain sizes (i.e. $\approx 1\mu$m) are still slightly lower than the experimental values. This is probably because the synthetic samples still contain a range of grain sizes.

Comparing predictions of the coercivity of a $0.2\mu$m grain between the $32 \times 32 \times 32$ model and the $12 \times 12 \times 12$ model gives a difference 15% for the lower values and 5% for the higher values. This is an important result as it is the coercivity which is related to the energy barriers to vortex propagation. Predicting these energy barriers is a computationally expensive calculation and these results show that grains smaller than $0.2\mu$m can be modelled using relatively low resolution models and thus saving much computer time.

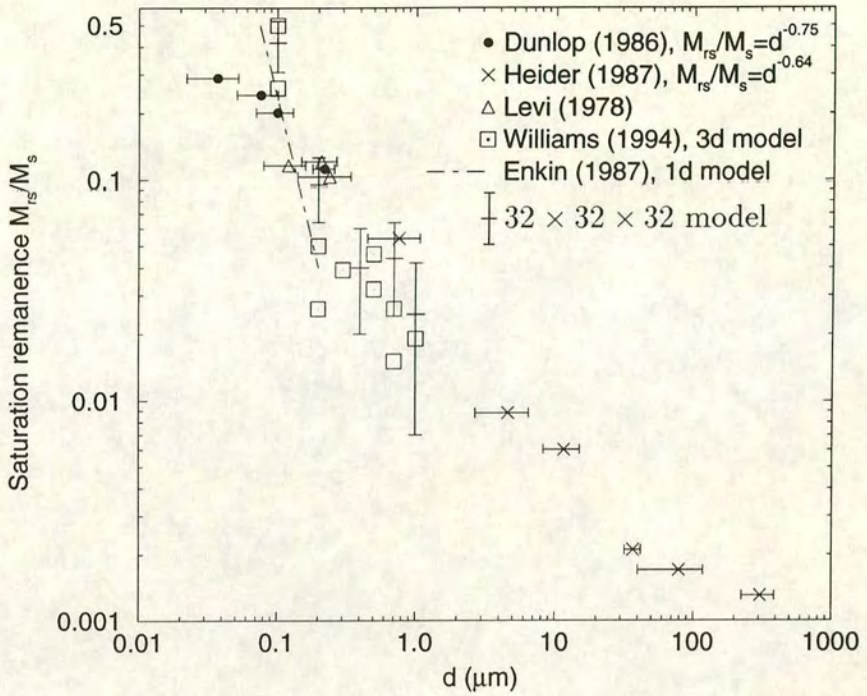


(a) Saturation remanence vs grain size

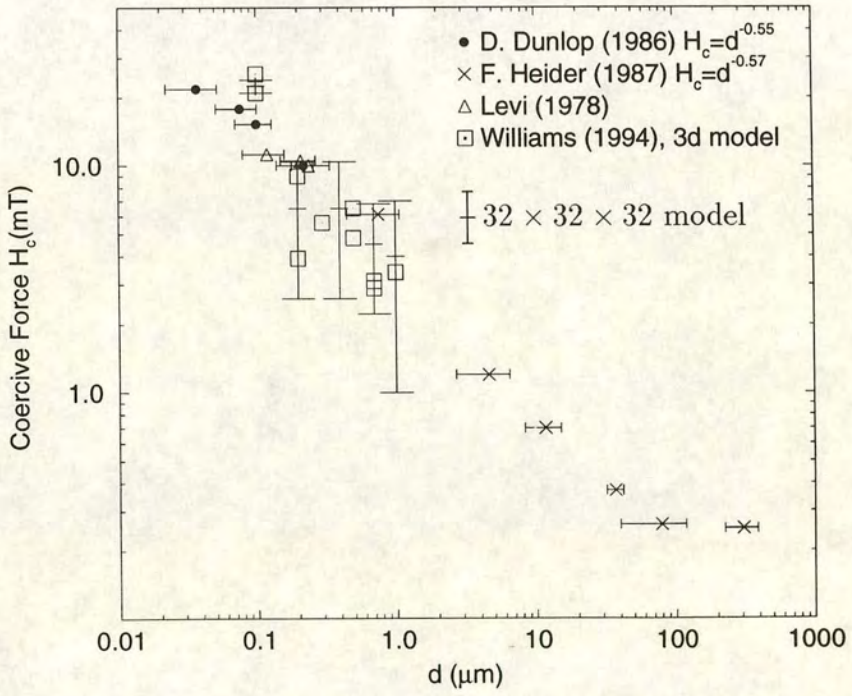


(b) Coercive force vs grain size

**Figure 8.1.** Comparison of $3d$ $12 \times 12 \times 12$ model (Williams 1994) with both results from the present study and with experimental results.

| | $M_{rs}/M_s$ | | $H_c$ (mT) | |
|---|---|---|---|---|
| Field direction | [001] | [111] | [001] | [111] |
| $12 \times 12 \times 12$ | 0.05 | 0.026 | 3.9 | 9 |
| $32 \times 32 \times 32$ | 0.088 | 0.122 | 3.31 | 8.56 |
| Experimental | 0.095 | | 10.6 | |

**Table 8.1.** Comparison between $3d$ micromagnetic results at different resolutions for a cubic grain with $d = 0.2\mu$m. Experimental results are from Dunlop (1986).

## 8.3 Comparison with previous models of PSD states

The micromagnetic model enables previous models of PSD behaviour to be evaluated. Chapter 5 showed that vortex states are occupied in preference to the two-domain states which are assumed in Amar calculations or obtained as a result from $1d$ micromagnetic calculations. This confirms that models for PSD behaviour based on domain wall moments or 'psarks' are inappropriate for magnetite. The two-domain component which is seen in state **C** is a feature for magnetite and state **C** is a lower energy state than the vortex states shown in chapter 7 which do not show this 2D component. However the two-domain component is only a minor feature and does not contribute to PSD stability.

Results have also shown that grains larger than $d = 0.2\mu$m are unable to occupy metastable SD states. Furthermore, the significant amount of flowering which occurs in grains larger than $0.1\mu$m makes the flower state in these grains unstable. One aspect of the metastable SD theory is that Bitter patterns which showed no domain walls were assumed to occupy SD states. Bitter pattern simulations showed that magnetite can show no domain walls because of separate surface and interior domains. This then removes metastable SD states as an explanation for the origin of PSD remanences.

It was shown that vortex states are able to account for the PSD properties of grains smaller than $1\mu$m, and other mechanisms such as those reviewed in chapter 2 need not be incorporated into the models. Hysteresis simulations were not possible using the $64 \times 64 \times 64$ model because of the large amount of computer time required to calculate an equilibrium state at a single field value. However, the domain states seen in the $4\mu$m grain suggest that any increase in $M_{rs}$ and $H_c$

over that predicted by MD theory is likely to be due to one or a combination of the hypotheses reviewed in chapter 2. This is likely to be an insignificant effect but could include transdomain processes, SD inclusions such as closure domains and Barkhausen discreteness.

At $d = 1.0\mu$m state $\mathbf{D}_0^z$ shows features which are common to both vortex states and domain states. State $\mathbf{D}_0^z$ consists of surface $\langle 110 \rangle$ lamellar domains and an internal vortex state. The existence of the surface lamellar domains changes the reversal processes from a simple vortex propagation. State $\mathbf{D}_0^{111}$ consists of surface $\langle 110 \rangle$ domains and an internal $\langle 111 \rangle$ structure. This transition from vortex states to domain states which is predicted by the model is also observed in experimental measurements of the remanent coercivity, $H_{cr}$. Figure 8.2 shows the dependence of $H_{cr}$ with grain size for a series of synthetic magnetites. The graph shows an increase in $H_{cr}$ from $0.01\mu$m to $1.0\mu$m and then a decrease from $1.0\mu$m to $10\mu$m It is clear that different processes must be operating depending on whether grains are smaller or larger than $1\mu$m and this correlates qualitatively with predictions by the micromagnetic model. In general terms it is possible to match up the experimentally measured transition with a change from vortex states in grains smaller than $1\mu$m to domain states in grains larger than $1\mu$m.

## 8.4 Experimental Bitter patterns

Figure 8.3 shows four Bitter patterns of the same hydrothermal grain observed after mechanical polishing with a diamond paste and then fine polishing using a beam of Ar atoms. This is the smallest grain size for which Bitter patterns have been observed and each pattern was obtained after applying and removing an external magnetic field in four different directions. This is a relatively large grain of width $d = 12\mu$m, and each pattern can be interpreted as either one of four LEM states or possibly three LEM states and an AEM state. Multiplicity of domains has also been reported by Soffel (1971) and Halgedahl and Fuller (1983), and occurs with both temperature and field cycling.

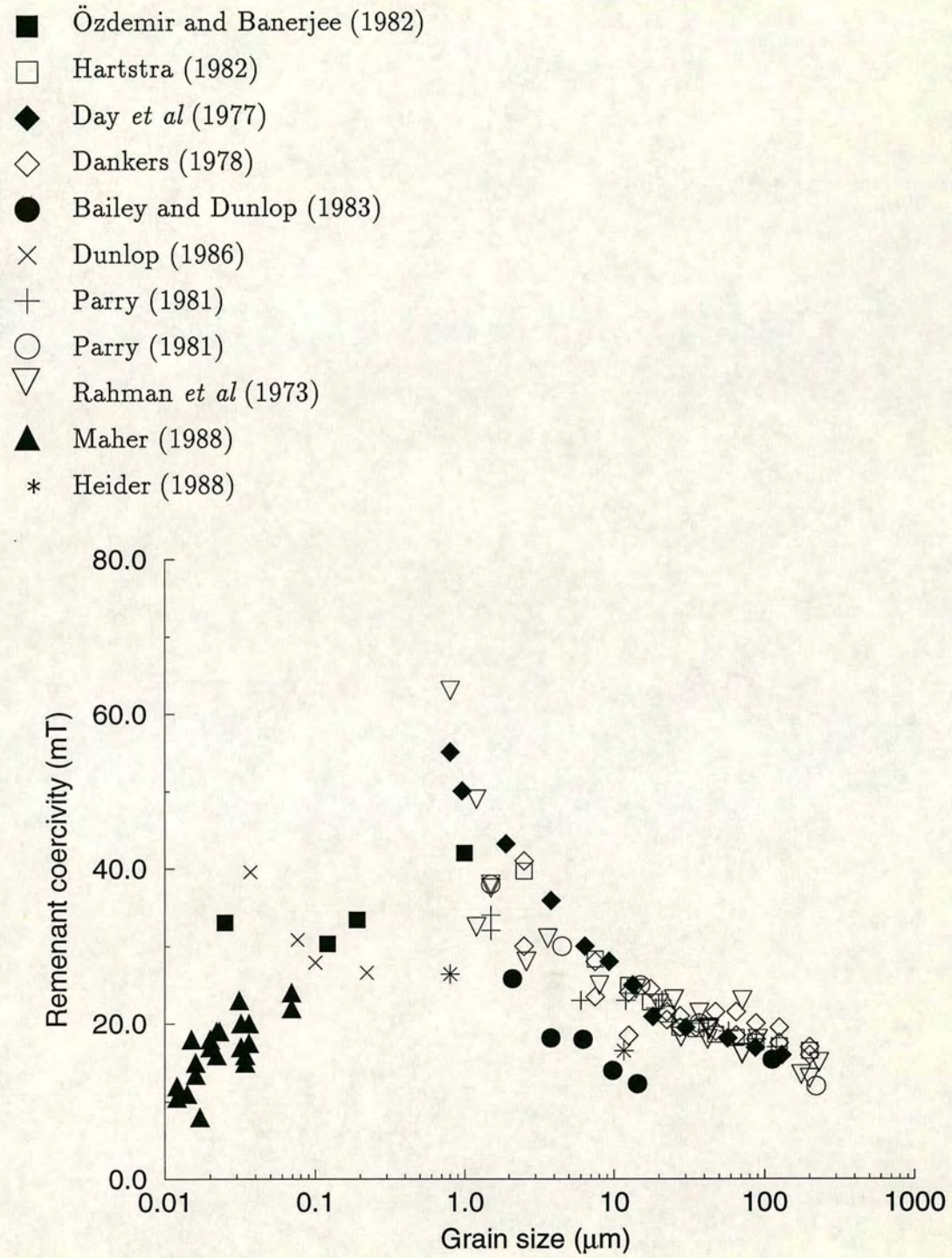


**Figure 8.2.** Experimentally obtained results for the dependence of remanent coercivity with grain size

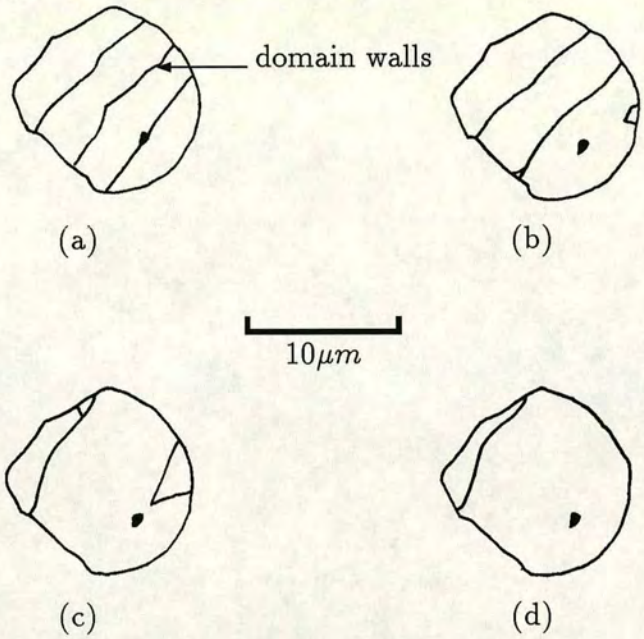


**Figure 8.3.** Four different domain patterns on the same 12$\mu$m crystal at saturation remanence, the different patterns were obtained by applying and removing a 100mT field in 4 different directions (from Heider (1988)).

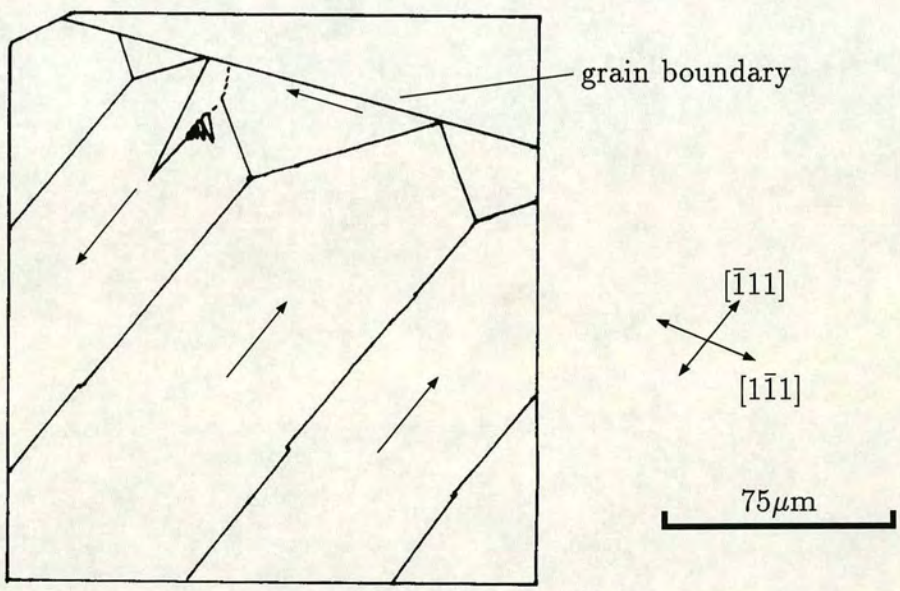


**Figure 8.4.** Closure domains observed on a polished, orientated (110) section through a 3mm octahedral crystal. The section contains two easy directions along which the main domains and closure domains are orientated. Note the difference in scale between this pattern and those shown in figure 8.3 (reproduced from Özdemir (in press)).

Although the maximum grain size which could be modelled using the present algorithm is still four times smaller than the patterns shown in figure 8.3, the model still allows a more meaningful interpretation of experimental Bitter patterns compared to previous models. Results from the $64 \times 64 \times 64$ model predicted that domain states in magnetite grains, of size $d = 4\mu$m, are composed of surface $\langle 110 \rangle$ domains and separate $\langle 111 \rangle$ domains in the interior of the grain. As the surface magnetization predicted by the $64 \times 64 \times 64$, $4\mu$m model shows similar features to the experimental observations it is plausible that the $12\mu$m also consists of separate surface and interior domains. Features which are similar to both the model and the experimental observations include a small number of large domains and domain walls which extend to the edge of the grain (figure 5.17a). In addition, the small domain shown at the edge of figure 8.3b is also seen in figure 5.17a. Although simulated Bitter patterns using the $64 \times 64 \times 64$ model do not image the surface domains, it is possible to envisage that as the grain size increases, the surface domains will become larger and domain walls sufficiently well separated to be imaged by the Bitter pattern method.

In addition, patterns such as those shown in figure 8.3d are unlikely to be imaging a two-domain state which extends through the grain. If the domain state was lamellar then the intense demagnetizing field produced by the domain on the left side of the grain would make the domain state unstable.

By comparing the predicted patterns with the experimental patterns such as the ones shown in figure 8.3 it is possible to put limits on the grain size at which Bitter patterns image the surface domains. As the grain size increases from $4\mu$m there will be a threshold grain size between approximately $5\mu$m and $10\mu$m at which the surface domains become large enough and extend deep enough into the grain to be imaged by the colloid. As the grain size increases to the 3mm grain shown in figure 8.4 domain states change from separate surface and interior domains to true lamellar $2d$ states.

Grains between $10\mu$m and $100\mu$m rarely show closure domains; most of the domain walls shown in figure 8.3 extend to the edge of the grain. If closure domains are present they are the small scale features shown in figures 8.3(b,d). This is consistent with the $4\mu$m modelled results in that domain walls extend to the edge of the grain in both experimental observation and theoretical predictions. Closure domains, such as those shown in figure 5.17b, are seen in results from

the model, however, these are small scale features. Only in large grains such as the 3mm grain shown in figure 8.4 will closure domains become large enough to be imaged by the colloid.

It is interesting that on the basis of the $2d$ micromagnetic results, Özdemir (in press) concluded that the closure domains seen in figure 8.4 are a general feature for magnetite at all grain sizes. Furthermore Özdemir postulated that closure domains would only be observed in $\{110\}$ sections which contain easy $\langle 111 \rangle$ axes and that the lack of closure domains in smaller grains was solely due to the randomly orientated nature of the polished surfaces. However closure domains are only a common feature in very large grains and as orientated slices have not been possible on small $10\mu$m grains it is still not possible to conclude firmly that closure domains are a general property for magnetite grains of all sizes. Results from this study suggest that closure domains are only small scale features in grains smaller than $\approx 10\mu$m. Only in grains larger than $\approx 10\mu$m will closure domains be large enough and distinct enough to be imaged by the Bitter pattern technique.

## 8.5 Kerr effect

The magneto-optical Kerr effect directly discerns between different directions of magnetization at the surface of the grain. Figure 8.5 shows domain states observed by Heider and Hoffman (1992) on a single $80\mu$m grain. The demagnetized state shown in figure 8.5a consists of six parallel domains and domain walls which extend to the edge of the grain. Figure 8.5b shows that as an external field is applied, the central reverse (black) domain decreases in size and the edge domain at the left of the grain disappears. The grain saturates at 100mT as shown in figure 8.5c. With the exception of a a small reversely magnetized domain, figure 8.5d shows that the remanent state appears saturated. This contradicts the usual behaviour expected in grains of this size in which the remanent state should be a similar multi-domain state to the original state. Patterns such as the ones shown in figure 8.5d have been interpreted as being either (a) a metastable mostly SD state, or (b) a surface pattern which shields a multi-domain interior.

Although the grain shown in figure 8.5 is an order of magnitude larger than the grains modelled in this study, similar features can be seen in both the model

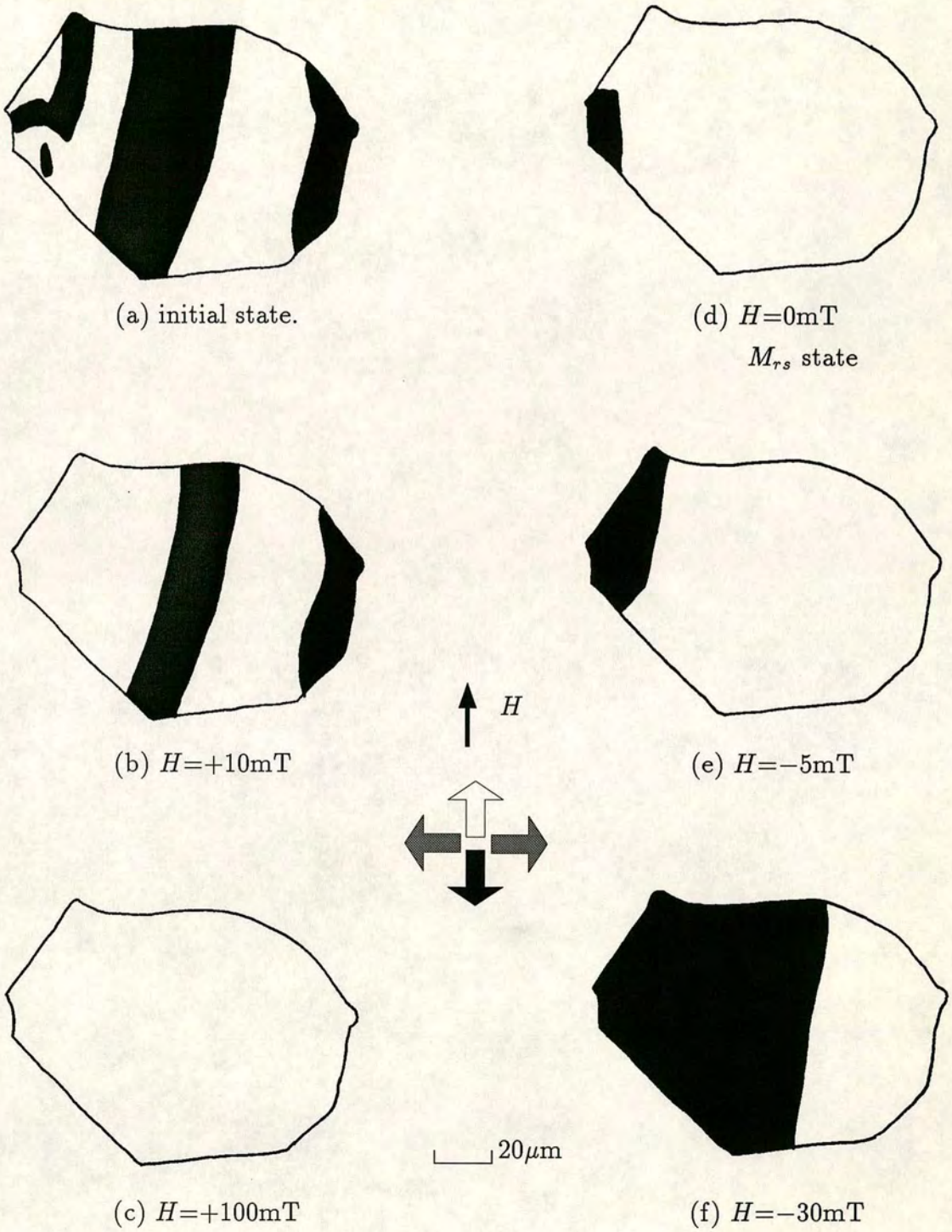


(a) initial state.

(b) $H$=+10mT

(c) $H$=+100mT

(d) $H$=0mT
$M_{rs}$ state

(e) $H$=−5mT

(f) $H$=−30mT

**Figure 8.5.** Dependence of the domain structure with an externally applied field for a 80$\mu$m magnetite grain. Magnetization components parallel to the applied field are shown as white and components anti-parallel as black (from Heider 1992).

and the experimental observations. The remanence state $\mathbf{D}_0^z$, shown in figures 7.11 and 7.12 has a similar surface magnetization to the pattern shown in figure 8.5d. The surface domain pattern in figure 7.12d consists of a large main domain and two smaller anti-parallel domains at the edge of the grain. Although the orientation of the large surface domain is anti-parallel to the field, as opposed to the domain in figure 8.5 which is parallel, Heider and Hoffman (1992) also reported domain observations in which the central domain was in the anti-parallel direction to the applied field. Hysteresis simulations were not possible using the $64 \times 64 \times 64$ resolution model due to the prohibitive computer time. However for grains larger than $1\mu$m, it is likely that the vortex in the centre of $\mathbf{D}_0^z$ transforms to the lamellar domains seen in the centre of figure 5.17b.

Other techniques such as magnetic microforce microscopy (MFM) image the surface magnetization. The technique employs a sharp magnetic tip attached to a flexible cantilever. The tip is placed close to the sample surface (typically within 10-500nm) and interacts with the stray field emanating from the sample. The image is formed by scanning the tip over the sample and measuring the force as a function of position. MFM images of domain walls on large grains have been observed in magnetite (Williams *et al* 1992). The model predicts that for grains of size $1\mu$m in width, curved domains walls such as those shown in figures 5.17d and 7.14a will be observed.

## 8.6 Suggestions for future research

One important aspect of the results from this study is that complex magneto-elastic effects do not have to be assumed to model the magnetization in PSD grains. This is still an interesting effect which could be studied, I studied the effect of screw dislocations on the magnetization by using the linear stress field (equation 3.16) and although most of the results were inconclusive, a few results showed domain walls which were pinned by the dislocation (in a similar manner to the results for vacancies). Even if the complex PDEs which determine the magneto-elastic effect are not solved, the relationship between coercivities and the number and position of dislocations could be modelled using a simple linear stress effect.

The high resolution is the main feature of the model described in this study

and enables several configurations of interacting grains to be modelled. At one extreme the computation space could be used to model arrays of SD grains in which each sub-cube represents a SD grain. Alternatively, configurations such as an array of several $8 \times 8 \times 8$ vortex states could be modelled in order to study how interactions between grains affects non-coherent reversals.

There are two aspects of the model which are important in considering TRM acquisition, either as a primary component or as a secondary viscous component. The first aspect is how the nature of vortex states depend on temperature and whether the number of LEM states is a function of temperature. This first aspect involves calculations similar to the ones presented in this study by which a range of LEM states are predicted between the Curie point (580°) and room temperature. The second aspect is how the energy barriers between different states depend on the temperature This second aspect involves the constrained calculations by Enkin and Williams (1994) and are computationally expensive. It would also be interesting to predict how the stability depends on grain shape and elongation. The energy barriers between different octahedral LEM states would be interesting to model because results show that PSD octahedral grains can only occupy either single or double-vortex states.

The model is also much more efficient that any previous models used to predict the processes operating in magnetic thin films. In particular using the CG method is a good balance between time consuming global search techniques and fast but limited steepest descent methods. The model could easily be extended to modelling thin films consisting of arrays of SD particles. If each sub-cube is a single particle then a $32 \times 32 \times 32$, $3d$ model would be able to predict the behaviour of a $180 \times 180$, $2d$ array of SD particles.

# Chapter 9. Conclusion

The combination of using the FFT algorithm and implementing the full micromagnetic model on a parallel computer results in an efficient model. This has allowed equilibrium states to be calculated using a maximum resolution of $64 \times 64 \times 64$ compared to $12 \times 12 \times 12$ for previous models. In addition the time taken to calculate equilibrium solutions at a resolution of $32 \times 32 \times 32$ was short enough to allow hysteresis curves to be simulated. Although the conjugate gradient technique is restricted to searching for LEM states, its use was justified as the model predicts values of $H_c$ and $M_{rs}$ which are similar to those obtained from experimental measurements on synthetic magnetite grains. This in turn strongly suggests that LEM states are physically realistic.

Results presented in chapter 5 confirmed the transition from SD states to flower states to vortex states predicted by previous $3d$ models. As a magnetite grain crystallizes, the magnetization first changes from a SD state to a flower state. However flower states are unlikely to be dominant in real grains as below $0.1\mu$m the deflection of the magnetization at the corners is insignificant and above $0.1\mu$m flower states become unstable. At $d = 0.22\mu$m there is a discontinuous jump from a flower state to a vortex state. At $d = 0.4\mu$m the magnetization in the vortex state curls around a line which is at an angle of 40° to the cube edge. In grains smaller than $0.1\mu$m the direction of the core is parallel to the $\langle 100 \rangle$ axis.

The increased resolution enables the the transition from vortex states to domain states to be predicted, and shows that the transition is a gradual one. State **D** at $d = 1.0\mu$m is an intermediate state in which a two-domain shell surrounds an inner fan type structure. The magnetization in grains larger than $1.0\mu$m form multi-domain states in which vortices become localized features confined to small regions in the grain. The domain states in cubic grains larger than $1\mu$m develop relatively complicated domain states with separate surface and interior domains. The magnetocrystalline A comparison anisotropy causes domains in the interior of the grain to align along the $\langle 111 \rangle$ directions. The magnetostatic energy causes the surface domains to align parallel to the surface in order to reduce the number of magnetic surface charges. The magnetocrystalline anisotropy then aligns these surface domains in the $\langle 110 \rangle$ directions.

The difference in direction between the internal domains and the surface domains mean that simulated Bitter patterns image neither the surface magnetization patterns or the interior bulk magnetization. These results suggest that any experimentally observed Bitter patterns on grains smaller than $4\mu$m should not be taken to be representative of either the surface magnetization nor the internal bulk magnetization. The model predicts that techniques such as the MFM method which image the surface magnetization will image curved domain walls in grains smaller than $4\mu$m. Comparisons with experimentally observed domain patterns in larger grains suggest that there is a threshold grain size at which surface domains become large enough to be imaged by Bitter patterns.

Chapter 5 also showed that by varying the sign of the magnetocrystalline anisotropy constant from negative to positive, two-dimensional lamellar domain states become occupied. Because of this Bitter patterns for cubic grains of iron predict domain patterns similar to those observed experimentally.

Chapter 6 presented results for non-cubic grains which included spherical, elongated, and octahedral grains. These results predicted that the transition from SD states to flower states to vortex states is a general transition for magnetite regardless of grain shape. High resolution results for octahedral grains also predict a similar gradual transition from vortex states to domain states to that seen in cubic grains. In addition the transition between states occurs at similar sizes for both octahedral grains and cubic grains. These are; from SD states to flower states ($0.1\mu$m), from flower states to vortex states ($0.2\mu$m) and from vortex states to domain states ($\approx 1\mu$m). Octahedral grains introduce an additional shape anisotropy which makes the line running between the two octahedral apexes a hard direction. This hard direction causes the domains states in grains smaller than $4\mu$m to align along the $\langle 110 \rangle$ directions in preference to the $\langle 111 \rangle$ magnetocrystalline easy directions.

Chapter 7 predicted the coercivity for SD rotation to be $H_c = 38.2$mT, only slightly larger than the analytic result of $H_c = 34.7$mT. Therefore Néel's SD theory is still applicable for grains smaller than $0.07\mu$m despite their non-uniform magnetization. At $0.2\mu$m, predicted values for $M_{rs}/M_s$ are 15% lower than experimental values; $M_{rs}/M_s = 0.112$ and $M_{rs}/M_s = 0.095 \pm 0.031$ for experimental and predicted values respectively. The predicted coercivity is 39% lower than the experimental value, $H_c = 10.6$mT and $H_c = 6.5 \pm 3.9$mT for experimental and

predicted results respectively. The discrepancy in the coercivity can be explained by the range of grain sizes which occurs in the experimental sample.

Simulated hysteresis curves for grains between $0.1 < d < 1.0\mu$m showed that the reversal mechanism is by vortex propagation. However cubic grains can occupy one of several separate vortex states at saturation remanence. These states are distinguished by three features; the angle which the vortex core makes with the crystalline axes, the size of the core and variations in the direction of the magnetization at the edge of the grain. At a particular grain size each of these states is a lower energy LEM state than the vortex states described in chapter 5. In addition there is a general relationship between the energy and the moment of the vortex states, high energy vortex states have high moments and low energy vortex states low moments. These results show that PSD moments in grains between $0.1\mu$m and $1.0\mu$m can be attributed to high energy vortex states with high moments.

The shape of octahedral grains restricts the number of LEM states available to a grain. At saturation remanence the magnetization can occupy either a single-vortex state or a double-vortex state depending on the direction of the applied field. The variation in the magnetization which occurs in cubic vortex states does not occur in the single-vortex octahedral state. Although the single vortex-state is a low moment state, the double-vortex state is a high energy, high moment LEM state. This shows that both cubic and octahedral grains can contribute to PSD remanences.

A transition occurs at $d = 1.0\mu$m between reversal by simple vortex propagation and more complicated reversals by domain processes. If a field is applied in the hard direction for a $1.0\mu$m cubic grain then the saturation remanence state consists of a vortex structure confined to the centre of the grain, and lamellar domains at the sides. This state has a high moment and a high coercivity. If a field is applied in the easy direction then multi-domain processes operate with associated low values for $M_{rs}$ and $H_c$.

Simplified models for PSD stability can be considered in terms of the resolution of the model. For cubic grains smaller than $0.2\mu$m the coercivities for a $12 \times 12 \times 12$ model agree with results from the $32 \times 32 \times 32$ model. The increased resolution of the model increases the predicted values of $M_{rs}/M_s$ and brings them close to experimental values. Also the strong shape anisotropy of the octahedral

grains means that the vortex states are as well defined at a resolution of $n = 12$ as at $n = 64$. Therefore calculations which aim to determine the energy barrier between LEM states for grains smaller than $0.2\mu$m can be done using low resolution models. Grains of size $1\mu$m involve domain process and require resolutions of size $32 \times 32 \times 32$.

# Appendix A. Superparamagnetic threshold

The upper limit to the size of superparamagnetic grains may be calculated using Néel's (1955) relaxation expression,

$$\tau = f_0^{-1} \exp(E_B/k_bT) \tag{A.1}$$

where $E_B$ is the energy barrier to domain reversal. For cubic grains the energy barrier is solely a magnetocrystalline energy barrier. For cubic anisotropy the energy barrier is given by the [110] direction and the [111] direction,

$$E_B = E^k[110] - E^k[111] \tag{A.2}$$

where $E_k[110]$ and $E_k[111]$ are the magnetocrystalline anisotropy energies for the [110] and [111] directions of magnetization. $E_k[110] = -K_1v/3$ and $E_k[111] = -K_1v/4$ where $K_1$ is the first order magnetocrystalline constant and $v$ is the volume of the grain. Thus $E_B = K_1v/12$ and equation A.1 becomes,

$$\tau = f_0^{-1} \exp(K_1v/12k_bT) \quad . \tag{A.3}$$

The threshold size for superparamagnetic behaviour can be determined by rearranging A.3 for $d_s$,

$$d_s = [12k_bT \ln(f_o\tau_s)/K_1]^{1/3} \quad . \tag{A.4}$$

The frequency factor, $f_0 = 10^9 \mathrm{s}^{-1}$ is the frequency at which the grain attempts to reverse direction. The frequency factor is difficult to determine exactly, Aharoni (1973) describes how to calculate $f_0$ for cubic anisotropy. However the value of $d_s$ is is insensitive to the exact value of $f_0$. Equation A.4 gives a lower limit of $d_s = 0.044\mu$m for $\tau_s = 1$s and $f_0 = 10^9 \mathrm{s}^{-1}$ and an upper limit of $d_s = 0.048\mu$m for $\tau_s = 100$s and $f_0 = 10^{10} \mathrm{s}^{-1}$.

# Appendix B. Implementation on the CM-200

The model was coded in CM-Fortran which is similar to Fortran 90 and I implemented the CG routine to run on the CM-200 without any external library calls. I found that not only did the FFT speed up the magnetostatic energy calculation but it was the only algorithm which I could implement on a parallel machine such as the CM-200. Other algorithms for calculating the magnetostatic energy, such as a dipole approximation did not improve the performance sufficiently.

The model was also coded in F77 and table B.1 compares computation times obtained from a Stardent serial computer with the CM-200. The combination of the FFT algorithm and the parallel computer results in very fast run times, taking into account the fact that the GS1000 is a four processor vector machine and the CM-200 a $N_p$ =16000 processor parallel machine the computation time for the CM-200 model is faster by approximately $1/(4N_p)$.

The CG routine requires only a few matrix multiplications and $E^e$, $E^a$ and $E^h$ are local terms. The computationally time consuming calculation is the FFT routine. The code is portable except that a proprietary FFT routine optimized for the CM-200 was implemented.

| | Stardent GS 1000 | | CM-200 |
|---|---|---|---|
| | Serial alg. | FFT alg. | |
| One energy + gradient calculation | 65536 s | 1053 s | 1.352 s |
| Total time for hysteresis curve | $\approx$ 10334 days | $\approx$ 166 days | 307 min. |

**Table B.1.** Comparison of run times for the hysteresis curve shown in figure 7.10a using a $32 \times 32 \times 32$ resolution. The times for the GS1000 have been extrapolated by multiplying the time for one energy and gradient calculation by 13625, the number of calculations used by the CM-200.

### CM-Fortran

To increment each value of a two-dimensional array A by 1 in Fortran 77 the familiar loop construct is used.

```
      do 30 i=1,4
         do 40 j=1,4
            A(i,j)=A(i,j)+1
40       continue
30    continue
```

CM-Fortran is functionally similar to Fortran-90 in that it dispenses with the array subscripts and the above operation is simply expressed as

```
A=A+1
```

Parts of arrays can be specified, for example to copy the first row of A into B would require writing:

```
B(1,:)=A(1,:)
```

### Examples of energy calculations

An array of magnetization directions $\theta_1, \phi_1, \ldots \theta_N, \phi_N$ denoted by x is allocated and the cartesian components $\alpha, \beta, \gamma$ calculated and stored in the arrays alpha,beta and gamma (of dimension 3).

### Local energy terms

For an applied field with cartesian components Hx, Hy and Hz and magnitude Hmag the code for calculating $E^h$ would look like,

```
Eh = Hmag*(delta**3)*sum( Hx*alpha + Hy*beta+ Hz*gamma)
```

where l is the width of the subcube and sum(A) returns the sum of all the elements in array A. A similar expression is used for the anisotropy energy,

```
Ea = K1*(delta**3)*sum( alpha**4 + beta**4+ gamma**4)
```

### Exchange energy

The exchange energy can be calculated using the operator `eoshift(A,dim,shift)` a feature which shifts the array `A` by an amount `shift` in the direction `dim`. For a two-dimensional array $A$ where $A$ is either $\alpha$, $\beta$ or $\gamma$,

$$A = \begin{pmatrix} 1 & 2 & 3 & 4 \\ 1 & 2 & 3 & 4 \\ 1 & 2 & 3 & 4 \end{pmatrix} \quad \texttt{A=eoshift(A,1,1)} \Rightarrow A = \begin{pmatrix} 0 & 1 & 2 & 3 \\ 0 & 1 & 2 & 3 \\ 0 & 1 & 2 & 3 \end{pmatrix}. \quad \text{(B.1)}$$

To calculate the exchange using the linear approximation requires:

```
Ee=sum(alpha*eoshift(alpha,1,1)+beta*eoshift(beta,2,1)
+gamma*eoshift(gamma,3,1)
```

with similar expression for the other 2 components, `beta` and `gamma`.

The boundary conditions for the 5 point formulation can be satisfied by setting `shift=2`,

$$A = \begin{pmatrix} 1 & 2 & 3 & 4 \\ 1 & 2 & 3 & 4 \\ 1 & 2 & 3 & 4 \end{pmatrix} \quad \texttt{eoshift(A,1,2)} \Rightarrow A = \begin{pmatrix} 0 & 0 & 1 & 2 \\ 0 & 0 & 1 & 2 \\ 0 & 0 & 1 & 2 \end{pmatrix} \quad \text{(B.2)}$$

So

```
fplus2=eoshift(A,1,2)
fplus2(1,:)=A(2,:)
fplus2(2,:)=A(1,:)
```

would give

$$\texttt{fplus2} = \begin{pmatrix} 2 & 1 & 1 & 2 \\ 2 & 1 & 1 & 2 \\ 2 & 1 & 1 & 2 \end{pmatrix} \quad \text{(B.3)}$$

where `fplus2` represents $f_{i+2}$ in equation 4.7. The code for the total energy energy then looks like,

```
Ee=alpha(-fplus2+16.*fplus1-30*alpha+16*fminus1-fminus2)
Ee=-Ce*delta*sum(ee)/24
```

with similar expressions for `beta` and `gamma`. These calculations also have to be repeated by shifting `fplus1`, `fminus1`... in each of the other two dimensions.

### Magnetostatic energy

The six arrays $\tilde{W}^{\beta\alpha}$, $\tilde{W}^{\gamma\alpha}$, $\tilde{W}^{\gamma\beta}$, $\tilde{W}^{\alpha\alpha}$, $\tilde{W}^{\beta\beta}$ and $\tilde{W}^{\gamma\gamma}$ need to be calculated and transformed only once at the beginning of the calculation. Each energy calculation requires calculating the Fourier transform of $\alpha$, $\beta$ and $\gamma$ and calculating

```
ed=conjg(alphafft)*betafft*Wxyfft
ed=ed+0.5*conjg(alphafft)*alphafft*Wxxfft

ed=ed+conjg(betafft)*gammafft*Wyzfft
ed=ed+0.5*conjg(betafft)*betafft*Wyyfft

ed=ed+conjg(alphafft)*gammafft*Wxzfft
ed=ed+0.5*conjg(gammafft)*gammafft*Wzzfft

edtotal=sum(ed)*(delta**3)*u0*(Ms**2)/real(n*n*n*8)
```

where ed is a three-dimensional array of the same size as `alphafft` ($2n \times 2n \times 2n$).

Table B.2 compares the accuracy of both serial and FFT demagnetizing energy calculations using a $8 \times 8 \times 8$ resolution for various structures. The analytical value for the 2D state is calculated using

$$E/E_{SD} = \frac{3}{2\pi}\{F(1,1) - F(1,0) + 2[F(0.5,0) - F(0.5,1)]\}, \qquad \text{(B.4)}$$

where the function $F$ is derived by Rhodes and Rhowlands (1954) and is similar to that given in appendix C.

| State | Stardent GS 1000 | | CM-200 | Analytic |
|---|---|---|---|---|
| | serial | FFT | | |
| vortex | 0.09755558 | 0.09755134 | 0.09755600 | N/A |
| flower | 0.68288064 | 0.68287811 | 0.68288102 | N/A |
| two-domain | 0.51223388 | 0.51223441 | 0.51223427 | 0.512233875 |

**Table B.2.** Comparison of accuracy of magnetostatic energy calculations for different machines (All energy values were calculated in double precision.)

# Appendix C. Interaction co-efficients

The demagnetizing energy arises from the Coulomb dipole-dipole interactions between the elemental sub-cubes of the model. The magnetostatic energy between two dipoles is given by,

$$E_{dipole} = -\frac{3{M_s}^2}{4\pi\mu_0 r^3}(\cos^2\theta - \frac{1}{3}) \tag{C.1}$$

where $r$ is the distance between the dipole centres, $\theta$ is their angular separation and $M_s$ is the dipole magnetic strength.

Much computer time can be saved by resolving each dipole into its equivalent magnetostatic surface charges and evaluating the interaction between these charged sheets in the manner of Rhodes and Rowlands (1954). In this way the angular and spatial components of the interactions can be separated and the invariant spatial components evaluated once and stored in a look-up table. The angular component simply represents the varying magnetostatic charges on the surface as the direction of each elementary vector changes.

If we represent the magnetostatic charges on a pair of interacting sheets in the $xy$ plane as $\sigma_1$ and $\sigma_2$, then the interaction energy $E_m$ is given by

$$E_m = \sigma_2 \int_0^{\Delta}\int_0^{\Delta} V(x_2, y_2, z_2)dx_2dy_2 \tag{C.2}$$

where $V(x_2, y_2, z_2)$ is the magnetic potential at the point $(x_2, y_2, z_2)$ on the second sheet, due to the magnetic charge of the first. Thus

$$V(x_2, y_2, z_2) = \sigma_1 \int_0^{\Delta} dx_1 \int_0^{\Delta} ((x_2 - x_1)^2 + (y_2 - y_1)^2 + {z_2}^2)^{-1/2} dy_1 \tag{C.3}$$

where $a$ and $b$ are the dimensions of the sheets in the $x$ and $y$ directions respectively.

For one-dimensional models only interactions between parallel sheets need be evaluated, however for three-dimensional models both parallel and orthogonal interactions must be calculated. Care must be taken when evaluating the integral to ensure that the limits are of the same sign. The case of interacting parallel sheets has been described by Rhodes and Rowlands (1954), and can be described

in terms of a function $\mathcal{F}(x,y,z)$.

$$\begin{aligned}
2\mathcal{F}(x,y,z) &= z^2x\,\sinh^{-1}(\frac{x}{y^2+z^2}) + x^2z\,\sinh^{-1}(\frac{z}{x^2+y^2}) + y^2z\,\sinh(z/y) \\
&\quad + y^2x\,\sinh^{-1}(x/y) + xyz\,\tan^{-1}\Big(\frac{(x^2+y^2+z^2)^{1/2}y}{xz}\Big) \\
&\quad + \frac{2}{3}y^2(x^2+y^2+z^2)^{-1/2} + \frac{1}{3}x^2(x^2+y^2)^{-1/2} + \frac{1}{3}z^2(y^2+z^2)^{-1/2} \\
&\quad + \frac{2}{3}y^3 - y^2x\,\sinh^{-1}(\frac{x}{y^2+z^2}) - y^2z\,\sinh^{-1}(\frac{z}{x^2+y^2}) - \pi xyz \\
&\quad - \frac{1}{3}(x^2+z^2)(x^2+y^2+z^2)^{-1/2} - \frac{2}{3}y^2(x^2+y^2)^{1/2} \\
&\quad - \frac{2}{3}y^2(y^2+z^2)^{1/2} \qquad \text{(C.4)}
\end{aligned}$$

for interaction between pairs of $x-y$ planes. For interacting orthogonal planes the integral to be evaluated is similar to equation (B.3) except that for an $xy$ plane interacting with an $xz$ plane the integration in equation (B.2) is now over $x$ and $z$. The result can be represented in terms of a function $\mathcal{G}(x,y,z)$:

$$\begin{aligned}
\mathcal{G}(x,y,z) &= xyz + \ln(p+x) + \frac{1}{2}x^2y\,\ln(p+z) + \frac{1}{2}x^2z\,\ln(p+y) \\
&\quad + \frac{1}{12}y^3\,\ln(x^2+y^2) + \frac{1}{12}z^3\,\ln(x^2+z^2) \\
&\quad + \frac{1}{6}z^3\,\ln((z^2+y^2)^{1/2}+y) + \frac{1}{6}y^3\,\ln((z^2+y^2)^{1/2}+z) \\
&\quad + \frac{1}{6}x^3\,\tan^{-1}(\frac{px}{yz}) + \frac{1}{2}y^2x\,\tan^{-1}(\frac{py}{xz}) \\
&\quad + \frac{1}{2}z^2x\,\tan^{-1}(\frac{pz}{xy}) + \frac{1}{3}zy(y^2+z^2)^{1/2} \\
&\quad - \frac{1}{2}xyz\,\ln(y^2+z^2) - \frac{1}{6}y^3\,\ln(p+z)beta - \frac{1}{6}z^3\,\ln(p+y) \\
&\quad - \frac{1}{4}x^2y\,\ln(x^2+y^2) - \frac{1}{4}x^2z\,\ln(x^2+z^2) - \frac{1}{6}y^3\,\ln(y) \\
&\quad - \frac{1}{6}z^3\,\ln(z) - \frac{1}{1}\pi x(x^2+3y^2+3z^2) - \frac{1}{3}pzy \qquad \text{(C.5)}
\end{aligned}$$

where $p=(x^2+y^2+z^2)^{1/2}$. The functions needed for interactions between other pairs of orthogonal sheets can be obtained by symmetry.

The convolution theorem requires the interaction between the sub-cube at

position $i = 1$, $j = 1$, $k = 1$ each of the other sub-cubes. The interaction coefficients in terms of the functions $\mathcal{G}$ between this sub-cube at position (1,1,1) and a sub-cube at co-ordinates $i = a$, $j = b$, $k = c$ is given by,

$$\begin{aligned}
W^{\beta\gamma} = \; & 2[\mathcal{G}(\Delta+a,b,2\Delta+c)+\mathcal{G}(\Delta+a,b,c)+\mathcal{G}(a,b,\Delta+c)+ \\
& \mathcal{G}(2\Delta+a,b,\Delta+c)+4\mathcal{G}(\Delta+a,\Delta+b,\Delta+c)+\mathcal{G}(a,\Delta+b,2\Delta+c)+ \\
& \mathcal{G}(a,\Delta+b,c)+\mathcal{G}(2\Delta+a,\Delta+b,2\Delta+c)+\mathcal{G}(2\Delta+a,\Delta+b,c)+ \\
& \mathcal{G}(\Delta+a,2\Delta+b,2\Delta+c)+\mathcal{G}(\Delta+a,2\Delta+b,c)+\mathcal{G}(a,2\Delta+b,\Delta+c)+ \\
& \mathcal{G}(2\Delta+a,2\Delta+b,\Delta+c)]- \\
& 4\mathcal{G}(\Delta+a,b,\Delta+c)+\mathcal{G}(a,b,2\Delta+c)+\mathcal{G}(a,b,c)+ \\
& \mathcal{G}(2\Delta+a,b,2\Delta+c)+\mathcal{G}(2\Delta+a,b,c)+4[\mathcal{G}(\Delta+a,\Delta+b,2\Delta+c)+ \\
& \mathcal{G}(\Delta+a,\Delta+b,c)+\mathcal{G}(a,\Delta+b,\Delta+c)+\mathcal{G}(2\Delta+a,\Delta+b,\Delta+c)+ \\
& \mathcal{G}(\Delta+a,2\Delta+b,\Delta+c)]+\mathcal{G}(a,2\Delta+b,2\Delta+c)+\mathcal{G}(a,2\Delta+b,c)+ \\
& \mathcal{G}(2\Delta+a,2\Delta+b,2\Delta+c)+\mathcal{G}(2\Delta+a,2\Delta+b,c)
\end{aligned}$$

and from symmetry

$$W^{\alpha\gamma}(\alpha,\beta,\gamma) = W^{\beta\gamma}(\beta,\alpha,\gamma) \tag{C.6}$$

$$W^{\alpha\beta}(\alpha,\beta,\gamma) = W^{\beta\gamma}(\gamma,\beta,\alpha) \tag{C.7}$$

The coefficient $W^{\beta\beta}$ is given by:

$$\begin{aligned}
W^{\beta\beta} = \; & 2[(\mathcal{F}(2\Delta+a,\Delta+b,2\Delta+c)+\mathcal{F}(2\Delta+a,\Delta+b,c)+ \\
& 4\mathcal{F}(\Delta+a,\Delta+b,\Delta+c)+\mathcal{F}(a,\Delta+b,2\Delta+c)+\mathcal{F}(a,\Delta+b,c)+ \\
& \mathcal{F}(2\Delta+a,b,\Delta+c)+ \\
& \mathcal{F}(\Delta+a,b,2\Delta+c)+\mathcal{F}(\Delta+a,b,c)+\mathcal{F}(a,b,\Delta+c)+ \\
& \mathcal{F}(2\Delta+a,2\Delta+b,\Delta+c)+\mathcal{F}(\Delta+a,2\Delta+b,2\Delta+c)+ \\
& \mathcal{F}(\Delta+a,2\Delta+b,c)+\mathcal{F}(a,2\Delta+b,\Delta+c)]- \\
& 4[\mathcal{F}(2\Delta+a,\Delta+b,\Delta+c)+\mathcal{F}(\Delta+a,\Delta+b,2\Delta+c)+ \\
& \mathcal{F}(\Delta+a,\Delta+b,c)+\mathcal{F}(a,\Delta+b,\Delta+c)]- \\
& \mathcal{F}(2\Delta+a,b,2\Delta+c)-\mathcal{F}(2\Delta+a,b,c)-4\mathcal{F}(\Delta+a,b,\Delta+c)+ \\
& \mathcal{F}(a,b,2\Delta+c)-\mathcal{F}(a,b,c)-\mathcal{F}(2\Delta+a,2\Delta+b,2\Delta+c)+ \\
& \mathcal{F}(2\Delta+a,2\Delta+b,c)-4\mathcal{F}(\Delta+a,2\Delta+b,\Delta+c)+
\end{aligned}$$

$$\mathcal{F}(a, 2\Delta + b, 2\Delta + c) + \mathcal{F}(a, 2\Delta + b, c)$$

Because the limits of integration of equations C.2 and C.3 have to be split differently depending on the relative positions of the interacting sheets the following conditions have to be taken into consideration;

(1) When $i' \neq 1, j' \neq 1, k' = 1$
$W^{\alpha\beta} = W^{\beta\gamma} = 0$, $W^{\alpha\gamma} = W^{*\alpha\gamma}$ and $W^{\alpha\alpha} = W_3^{\alpha\alpha}$, $W^{\beta\beta} = W_{5a}^{\beta\beta}$, $W^{\gamma\gamma} = W_{5a}^{\gamma\gamma}$

(2) When $i' = 1, j' \neq 1, k' \neq 1$
$W^{\alpha\beta} = W^{*\alpha\beta}$, $W^{\beta\gamma} = W^{\alpha\gamma} = 0$ and $W^{\alpha\alpha} = W_{5b}^{\alpha\alpha}$, $W^{\beta\beta} = W_{5b}^{\beta\beta}$, $W^{\gamma\gamma} = W_3^{\gamma\gamma}$

(3) When $i' \neq 1, j = 1, k \neq 1$
$W^{\alpha\beta} = W^{\alpha}\gamma = 0$ , $W^{\beta\gamma} = W^{*\beta\gamma}$ and $W^{\alpha\alpha} = W_{5c}^{\alpha\alpha}$, $W^{\beta\beta} = W_3^{\beta\beta}$, $W^{\gamma\gamma} = W_{5c}^{\gamma\gamma}$

(4) When $i' \neq 1, j' = 1, k' = 1$
$W^{\alpha\beta} = W^{\beta\gamma} = W^{\alpha\gamma} = 0$ and $W^{\alpha\alpha} = W_{2a}^{\alpha\alpha}$, $W^{\beta\beta} = W_{2a}^{\beta\beta}$, $W^{\gamma\gamma} = W_1^{\gamma\gamma}$

(5) When $i' = 1, j' = 1, k' \neq 1$
$W^{\alpha\beta} = W^{\beta\gamma} = W^{\alpha\gamma} = 0$ and $W^{\alpha\alpha} = W_1^{\alpha\alpha}$, $W^{\beta\beta} = W_{2b}^{\beta\beta}$, $W^{\gamma\gamma} = W_{2b}^{\gamma\gamma}$

(6) When $i' = 1, j' \neq 1, k' = 1$
$W^{\alpha\beta} = W^{\beta\gamma} = W^{\alpha\gamma} = 0$ and $W^{\alpha\alpha} = W_{2c}^{\alpha\alpha}$, $W^{\beta\beta} = W_1^{\beta\beta}$, $W^{\gamma\gamma} = W_{2c}^{\gamma\gamma}$

$$\begin{aligned} W^{*\beta\gamma} \;=\; & 4[\mathcal{G}(\Delta, 2\Delta + b, \Delta + c) + \mathcal{G}(\Delta, \beta, \Delta + c) + \\ & \mathcal{G}(\Delta, \Delta + b, \gamma) + \mathcal{G}(\Delta, \Delta + b, 2\Delta + c)] - \\ & 2[4\mathcal{G}(\Delta, \Delta + b, \Delta + c) + \mathcal{G}(\Delta, 2\Delta + b, \gamma) + \mathcal{G}(\Delta, \beta, \gamma) + \\ & \mathcal{G}(\Delta, 2\Delta + b, 2\Delta + c) + \mathcal{G}(\Delta, \beta, 2\Delta + c)] \end{aligned}$$

And from symmetry

$$W^{*\alpha\gamma}(\alpha, \beta, \gamma) = W^{*\beta\gamma}(\beta, \gamma, \alpha)$$

$$W^{*\alpha\beta}(\alpha, \beta, \gamma) = W^{*\beta\gamma}(\gamma, \beta, \alpha) \quad .$$

The coefficient ${W_1}^{\beta\beta}$ is given by,

$${W_1}^{\beta\beta} = 4(2\mathcal{F}(\Delta, \Delta + b, \Delta) - \mathcal{F}(\Delta, b, \Delta) - \mathcal{F}(\Delta, 2\Delta + b, \Delta))$$

and from symmetry

$${W_1}^{\gamma\gamma}(\alpha, \beta, \gamma) = {W_1}^{\beta\beta}(\beta, \gamma, \alpha)$$

$$W_1{}^{\alpha\alpha}(\alpha,\beta,\gamma) = W_1{}^{\beta\beta}(\beta,\alpha,\gamma)$$

The coefficient $W_{2a}^{\beta\beta}$ is given by:

$$\begin{aligned} W_{2a}^{\beta\beta} &= 4[\mathcal{F}(2\Delta+a,0,\Delta) - 2\mathcal{F}(\Delta+a,0,\Delta) + \mathcal{F}(a,0,\Delta) \\ &\quad -\mathcal{F}(2\Delta+a,\Delta,\Delta) + 2\mathcal{F}(\Delta+a,\Delta,\Delta) - \mathcal{F}(a,\Delta,\Delta)] \end{aligned}$$

And from symmetry

$$W_{2b}^{\beta\beta}(\alpha,\beta,\gamma) = W_{2a}^{\beta\beta}(\gamma,\beta,\alpha)$$

$$W_{2c}^{\alpha\alpha}(\alpha,\beta,\gamma) = W_{2a}^{\beta\beta}(\beta,\alpha,\gamma)$$

$$W_{2a}^{\gamma\gamma} = W_{2a}{}^{\beta\beta} \quad W_{2b}^{\alpha\alpha} = W_{2b}{}^{\beta\beta} \quad W_{2c}^{\gamma\gamma} = W_{2a}{}^{\alpha\beta}$$

The coefficient $W_3{}^{\beta\beta}$ is given by

$$\begin{aligned} W_3^{\beta\beta} &= 2(\mathcal{F}(2\Delta+a,0,2\Delta+c) - 2\mathcal{F}(2\Delta+a,0,\Delta+c) + 2\mathcal{F}(\Delta+a,0,c) - \\ &\quad 2\mathcal{F}(\Delta+a,0,2\Delta+c) + 4\mathcal{F}(\Delta+a,0,\Delta+c) - 2\mathcal{F}(\Delta+a,0,c) + \\ &\quad \mathcal{F}(a,0,2\Delta+c) - 2\mathcal{F}(a,0,\Delta+c) + \mathcal{F}(a,0,c)) - \\ &\quad 2(\mathcal{F}(2\Delta+a,\Delta,2\Delta+c) - 2\mathcal{F}(2\Delta+a,\Delta,\Delta+c) + \\ &\quad \mathcal{F}(2\Delta+a,\Delta,c) - 2\mathcal{F}(\Delta+a,\Delta,2\Delta+c) + 4\mathcal{F}(\Delta+a,\Delta,\Delta+c) - \\ &\quad 2\mathcal{F}(\Delta+a,\Delta,c) + \mathcal{F}(a,\Delta,2\Delta+c) - 2\mathcal{F}(a,\Delta,\Delta+c) + \\ &\quad \mathcal{F}(a,\Delta,c)) \end{aligned}$$

And from symmetry

$$W_3^{\gamma\gamma}(\alpha,\beta,\gamma) = W_3{}^{\beta\beta}(\alpha,\gamma,\beta)$$

$$W_3{}^{\alpha\alpha}(\alpha,\beta,\gamma) = W_3{}^{\alpha\alpha}(\beta,\alpha,\gamma)$$

$$\begin{aligned} W^{\beta\beta} &= 2[(\mathcal{F}(2\Delta+a,\Delta+b,2\Delta+c) + \mathcal{F}(2\Delta+a,\Delta+b,\gamma) + \\ &\quad 4\mathcal{F}(\Delta+a,\Delta+b,\Delta+c) + \mathcal{F}(\alpha,\Delta+b,2\Delta+c) + \mathcal{F}(\alpha,\Delta+b,\gamma) + \end{aligned}$$

$$
\begin{aligned}
&\mathcal{F}(2\Delta+a,\beta,\Delta+c)+\\
&\mathcal{F}(\Delta+a,\beta,2\Delta+c)+\mathcal{F}(\Delta+a,\beta,\gamma)+\mathcal{F}(\alpha,\beta,\Delta+c)+\\
&\mathcal{F}(2\Delta+a,2\Delta+b,\Delta+c)+\mathcal{F}(\Delta+a,2\Delta+b,2\Delta+c)+\\
&\mathcal{F}(\Delta+a,2\Delta+b,\gamma)+\mathcal{F}(\alpha,2\Delta+b,\Delta+c)]-\\
&4[\mathcal{F}(2\Delta+a,\Delta+b,\Delta+c)+\mathcal{F}(\Delta+a,\Delta+b,2\Delta+c)+\\
&\mathcal{F}(\Delta+a,\Delta+b,\gamma)+\mathcal{F}(\alpha,\Delta+b,\Delta+c)]-\\
&\mathcal{F}(2\Delta+a,\beta,2\Delta+c)-\mathcal{F}(2\Delta+a,\beta,\gamma)-4\mathcal{F}(\Delta+a,\beta,\Delta+c)+\\
&\mathcal{F}(\alpha,\beta,2\Delta+c)-\mathcal{F}(\alpha,\beta,\gamma)-\mathcal{F}(2\Delta+a,2\Delta+b,2\Delta+c)+\\
&\mathcal{F}(2\Delta+a,2\Delta+b,\gamma)-4\mathcal{F}(\Delta+a,2\Delta+b,\Delta+c)+\\
&\mathcal{F}(\alpha,2\Delta+b,2\Delta+c)+\mathcal{F}(\alpha,2\Delta+b,\gamma)
\end{aligned}
$$

And from symmetry

$$W_4{}^{\gamma\gamma}(\alpha,\beta,\gamma)=W_4{}^{\beta\beta}(\alpha,\gamma,\beta)$$

$$W_4{}^{\alpha\alpha}(\alpha,\beta,\gamma)=W_4{}^{\beta\beta}(\gamma,\alpha,\beta)$$

The coefficient $W_{5a}^{\beta\beta}$ is given by,

$$
\begin{aligned}
W_{5a}^{\beta\beta} \;=\;& 2(\mathcal{F}(2\Delta+a,\Delta+b,\Delta)-4\mathcal{F}(\Delta+a,\Delta+b,\Delta)+2\mathcal{F}(a,\Delta+b,\Delta)\\
&-\mathcal{F}(2\Delta+a,b,\Delta)+2\mathcal{F}(\Delta+a,b,\Delta)-\mathcal{F}(a,b,c)\\
&-\mathcal{F}(2\Delta+a,2\Delta+b,\Delta)+2\mathcal{F}(\Delta+a,2\Delta+b,\Delta)-\mathcal{F}(a,2\Delta+b,c))
\end{aligned}
$$

And from symmetry

$$\mathbf{C}_{\mathbf{5a}_{yz}}(\alpha,\beta,\gamma)=\mathbf{C}_{\mathbf{5a}_{xz}}(\beta,\alpha,\gamma)$$

$$\mathbf{C}_{\mathbf{5b}_{xz}}(\alpha,\beta,\gamma)=\mathbf{C}_{\mathbf{5a}_{xz}}(\gamma,\beta,\alpha)$$

$$\mathbf{C}_{\mathbf{5b}_{xy}}(\alpha,\beta,\gamma)=\mathbf{C}_{\mathbf{5a}_{xz}}(\beta,\gamma,\alpha)$$

$$\mathbf{C}_{\mathbf{5c}_{xy}}(\alpha,\beta,\gamma)=\mathbf{C}_{\mathbf{5a}_{xz}}(\alpha,\gamma,\beta)$$

$$\mathbf{C}_{\mathbf{5c}_{yz}}(\alpha,\beta,\gamma)=\mathbf{C}_{\mathbf{5a}_{xz}}(\gamma,\alpha,\beta)$$

# Appendix D. The FFT algorithm

This appendix shows how the magnetostatic energy can be calculated in frequency space without calculating an inverse FFT. Using $\tilde{\sigma}$ to represent the discrete Fourier transform coefficients of $\sigma$,$\sigma \Longleftrightarrow \tilde{\sigma}$,

$$\sigma_l = \frac{1}{N}\sum_k \tilde{\sigma}_k \exp[-2\pi i k l/N] \tag{D.1}$$

$$\sigma_m = \frac{1}{N}\sum_{k'} \tilde{\sigma}_{k'} \exp[-2\pi i k' m/N] \tag{D.2}$$

$$W_{l-m} = \frac{1}{N}\sum_{k''} \tilde{W}_{k''} \exp[-2\pi i k''(l-m)/N] \quad . \tag{D.3}$$

Equation 4.21 now becomes,

$$E^d = \frac{\mu_0}{8\pi N^3}\sum_l\sum_m\sum_k\sum_{k'}\sum_{k''}\tilde{\sigma}_k\tilde{\sigma}_{k'}\tilde{W}_{k''} \exp[-2\pi i[l(k+k'')+m(k'-k'')]/N] \tag{D.4}$$

and using the definition of a delta function,

$$\delta(k+k'') = N\sum_{l=1}^{N} e^{-2\pi i(k+k'')l/N} = \begin{vmatrix} 1 & k+k''=0 \\ 0 & k+k''\neq 0 \end{vmatrix} \tag{D.5}$$

$$E^d = \frac{\mu_0}{8\pi N}\sum_k\sum_{k'}\sum_{k''}\tilde{\sigma}_k\tilde{\sigma}_{k'}\tilde{W}_{k''}\delta(k+k'')\delta(k'-k'') \quad . \tag{D.6}$$

The first delta function has a value of 1 only when $k'' = -k$ and the second when $k' = k'' = -k$,

$$E^d = \frac{\mu_0}{4\pi N}\sum_k \tilde{\sigma}_k\tilde{\sigma}_{-k}\tilde{W}_{-k} \quad , \tag{D.7}$$

and as the array $W$ is an even function then $\tilde{W}$ is real and it follows that $W_k$=$W_{-k}$ giving,

$$E^d = \frac{\mu_0}{8\pi N}\sum_k \tilde{\sigma}_k\tilde{\sigma}_{-k}\tilde{W}_k. \tag{D.8}$$

### Comparison between different FFT schemes

One fundamental basis of the FFT method is that the interaction coefficient between two fundamental units (either charged sheets or sub-cubes) must be only a function of the relative positions between them, Figure D.1 shows how splitting the system into individual charged plates contradicts this tenet and increases the complexity of the algorithm. This does not prohibit the use of the FFT algorithm, however it does introduce some extra bookkeeping.

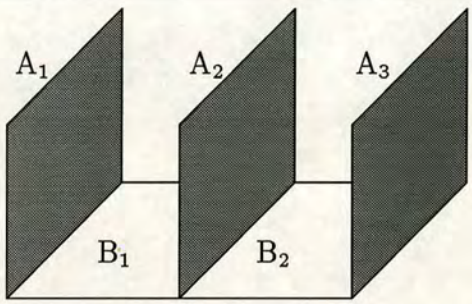


**Figure D.1.** Discretization scheme as used by Berkov *et al* (1993), the system is split into charged plates without considering individual sub-cubes. Even though the interaction co-efficient between the pair $A_1$,$B_1$ and $A_2$,$B_1$ should be the same, in terms of the index notation the relative distance between them are different, the distance between $A_1$ and $B_1$ is 0 whilst the distance between $A_2$,$B_1$ is 1.

### On the orientation of the sub-cubes

The arrays $W$ are either even or odd in each dimension depending on the orientation of the plates. Figure D.2a shows three cubes A,B,C in the same plane with cube A being equidistant from B and C. The plates $A_-$ and $B_-$ are equidistant from $A_+$ and $C_-$ so the magnitude of $W$ should be identical for both. However in order to satisfy this the sign of $W$ needs to be modified for the combination $A_+$ and $C_-$ due to the different charges on the plates ($- \times - \Rightarrow +, + \times - \Rightarrow -$). Similarly for the other three interactions,

$$A_-B_+ \equiv -A_+C_+, \quad A_+B_+ \equiv -A_-C_+, \quad A_+B_- \equiv -A_-C_- \tag{D.9}$$

This results in $W$ being real and odd in the two $i, j$ directions and even in the third and the corresponding FFT ($\tilde{W}$) is real and odd in two directions and even

in the third.

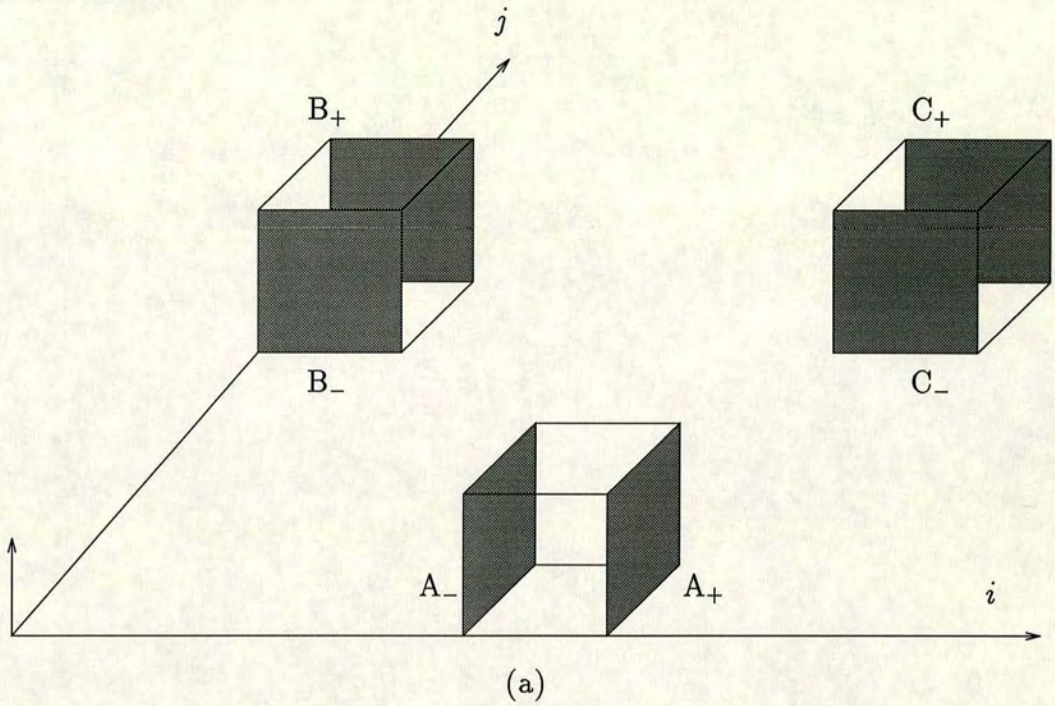


**Figure D.2.** Arrangement of the surface charges for three sub-cubes in the same plane.

# Appendix E. Rotation of the co-ordinate system

The two rotation matrices are given by,

$$\begin{pmatrix} x' \\ y' \\ z' \end{pmatrix} = \begin{pmatrix} \cos\theta_a & \sin\theta_a & 0 \\ -\sin\theta_a & \cos\theta_a & 0 \\ 0 & 0 & 1 \end{pmatrix} \begin{pmatrix} x \\ y \\ z \end{pmatrix} \tag{E.1}$$

$$\begin{pmatrix} x' \\ y' \\ z' \end{pmatrix} = \begin{pmatrix} \cos\phi_a & 0 & -\sin\phi_a \\ 0 & 1 & 0 \\ \sin\phi_a & 0 & \cos\phi_a \end{pmatrix} \begin{pmatrix} x \\ y \\ z \end{pmatrix} \tag{E.2}$$

Multiplying E.1 andE.2 gives the full transformation matrix,

$$\begin{pmatrix} x' \\ y' \\ z' \end{pmatrix} = \begin{pmatrix} \cos\theta_a\cos\phi_a & \sin\theta_a & -\cos\theta_a\sin\phi_a \\ -\sin\theta_a\cos\phi_a & \cos\theta_a & \sin\theta_a\sin\phi_a \\ \sin\phi_a & 0 & \cos\phi_a \end{pmatrix} \begin{pmatrix} x \\ y \\ z \end{pmatrix} . \tag{E.3}$$

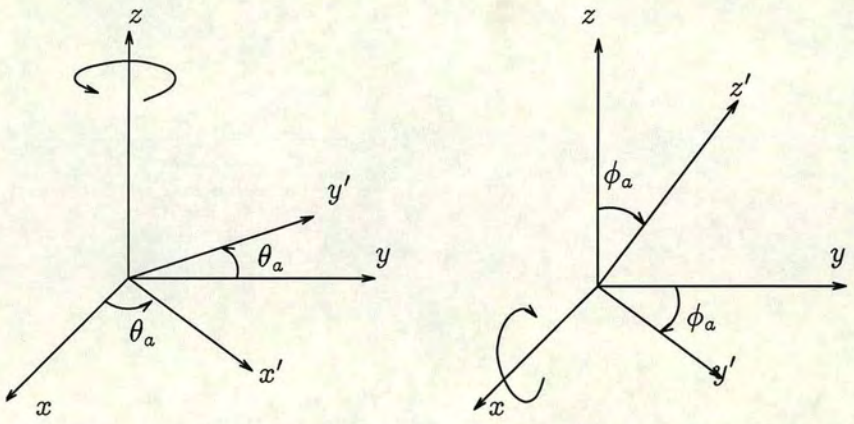


**Figure E.1.** Rotation of the co-ordinate system about the $x$ axis and the $z$ axis

# Bibliography


Aharoni, A. (1973), Relaxation time of superparamagnetic particles with cubic anisotropy, *Phys. Rev. B* **7**(3), 1103–1107.

Amar, H. (1957), On the width and energy of domain walls in small multi-domain particles, *J. Appl. Phys.* **28**, 732–733.

Amar, H. (1958*a*), Magnetization and domain structures of multidomain particles, *Phys. Rev.* **111**, 149–53.

Amar., H. (1958*b*), Size dependence of the wall characteristics in a two-domain iron particle, *J. Appl. Phys.* **29**, 542–543. moon 1991.

Amin, N. A. and Matijević, E. (1987), Magnetic properties of uniform spherical magnetite particles prepared from ferrous hydroxide gels, *Physica status solidi A* **101**, 233–238.

Argyle, K. S. and Dunlop, D. J. (1984), Theoretical domain-structure in multidomain magnetite particles, *Geophysical Research Letters* **11**, 185–188.

Bailey, M. E. and Dunlop, D. J. (1983), Alternating field characteristics of pseudo-single-domain ($2-14\mu m$) and multidomain magnetite, *Earth and Planetary Science Letters.* **63**, 335–352.

Berkov, D. V., Ramstock, K. and Hubert, A. (1993), Solving micromagnetic problems - towards an optimal numerical method, *Physica Status Solidi A* **137**(1), 207–225.

Boissin, N. and Lutton, J. L. (1993), A parallel simulated annealing algorithm, *Parallel Computing* **19**(8), 859–872.

Brown, W. F. and LaBonte, A. E. (1965), Structure and energy of one-dimensional domain walls in ferromagnetic thin films, *J. Appl. Phys.* **36**, 1380–1386.

Brown, W. H. (1978), *Micromagnetics*, Robert E. Krieger.

Butler, R. F. and Banerjee, S. K. (1975), Theoretical single-domain grain size range in magnetite and titanomagnetite, *Journal of Geophysical Research* **80**, 4049–4058.

Chikazumi, S. and Charap, S. H. (1964), *Physics of magnetism*, Wiley and Sons. pp. 188.

Clark, A. (1990), *Seeing beneath the soil*, Batsford London.

Dankers, P. H. M. (1978), Magnetic properties of dispersed natural iron-oxides of known grain-size, PhD thesis, University of Utrecht.

Day, R., Fuller, M. and Schmidt, V. A. (1977), Hysteresis properties of titanomagnetites: grain size and compositional dependence, *Physics of the Earth and Planetary Interiors* **13**, 260–267.

Dietz, R. S. (1961), Continent and ocean basin evolution by spreading of the sea floor, *Nature* **190**, 854–857.

Dunlop, D. J. (1973), Superparamagnetic and single-domain threshold sizes in magnetite, *Journal of Geophysical Research* **78**(11), 1780–1793.

Dunlop, D. J. (1977), The hunting of the 'psark', *J. Geomagn. Geoelectr.* **29**, 293–318.

Dunlop, D. J. (1986), Hysteresis properties of magnetite and their dependence on particle size – a test of pseudo-single-domain remanence models, *Journal of Geophysical Research-Solid Earth And Planets* **91**(NB9), 9569–9584.

Dunlop, D. J. (1990), Developments in rock magnetism, *Reports On Progress in Physics* **53**(6), 707–792.

Elmore, R. D. and McCabe, C. (1991), The occurrence and origin of remagnetization in the sedimentary rocks of North America, *Reviews of Geophysis* **29 supp.**, 377–383.

Enkin, R. J. and Dunlop, D. J. (1987), A micromagnetic study of pseudo single-domain remanence in magnetite, *Journal of Geophysical Research-Solid Earth And Planets* **92**(NB12), 12726–12740.

Enkin, R. J. and Williams, W. (1994), Three dimensional micromagnetic analysis of stability in fine magnetic grains, *Journal of Geophysical Research* **99**(B1), 611–618.

Fletcher, E. J. and O'Reilly, W. (1974), Contribution of $Fe^{2+}$ ions to the magnetocrystalline anisotropy constant $K_1$ of $Fe_{3-x}Ti_xO_4$ ($0 < x < 0.1$)., *J. Phys. C* pp. 171–178.

Fredkin, D. R. and Koehler, T. R. (1987), Numerical micromagnetics by the finite element method, *IEEE Trans. Magnetics.* **23**, 3385–3387.

Giles, R. C., Kotiuga, P. R. and Humphrey, F. B. (1990), 3 dimensional micromagnetic simulations on the Connection machine, *J. Appl. Phys.* **67**(9), 5821–5823.

Gill, P. E., Murray, W. and Wright, M. H. (1981), *Practical Optimization*, Academic Orlando Fla.

Glen, W. (1982), *The road to Jamarillo*, Stanford University Press.

Gordon, R. G., Cox, A. and O'Hare, S. (1984), Paleomagnetic Euler poles and the apparent polar wander and absolute motion of North America since the Carboniferous, *Tectonics* **3**(5), 499–537.

Halgedahl, S. L. and Fuller, M. (1980), Magnetic domain observations of nucleation processes in fine particles of intermediate titanomagnetite, *Nature* **288**, 70–72.

Halgedahl, S. L. and Fuller, M. (1983), The dependence of magnetic domain structure upon magnetization state with emphasis upon nucleation as a mechanism for pseudo-single-domain behaviour, *Journal of Geophysical Research* **88**, 6505–6522.

Hartmann, U. and Mende, H. H. (1985), Ferrohydrodynamical fundamentals of Bitter-pattern evolution, *Z. Phys.* **B61**, 29–21.

Hartstra, R. L. (1982), Some Rockmagnetic parameters for natural iron-titanium oxides, PhD thesis, University of Utrecht.

Heider, F. (1988), Magnetic properties of hydrothermally grown $Fe_3O_4$ crystals, PhD thesis, University of Toronto.

Heider, F. and Hoffman, V. (1992), Magneto-optical Kerr effect on magnetite crystals with externally applied magnetic fields., *Earth and Planetary Science Letters* **108**, 131–138.

Heider, F. and Williams, W. (1988), Note on temperature-dependence of exchange constant in magnetite, *Geophysical Research Letters* **15**(2), 184–187.

Heider, F., Dunlop, D. J. and Sugiura, N. (1987), Magnetic-properties of hydrothermally recrystallized magnetite crystals, *Science* **236**(4806), 1287–1290.

Heider, F., Halgedahl, S. L. and Dunlop, D. J. (1988), Temperature-dependence of magnetic domains in magnetite crystals, *Geophysical Research Letters* **15**(5), 499–502.

Heider, F., Zitzelsberger, A. and Fabian, K. (in press), Magnetic susceptibility and remanent coercive force in grown magnetite crystals from 0.1$\mu$m to 6mm, *Journal of Geophysical Research.*

Hillis, W. D. (1985), *The Conection Machine*, MIT Press Cambridge MA.

Hodych, J. P. (1986), Evidence for magnetostrictive control of intrinsic susceptibility and coercive force of multidomain magnetite in rocks., *Physics of the Earth and Planetary Interiors* **42**, 184–194.

Holland, J. H. (1992), Genetic algorithms, *Scientific Americam* pp. 44–50.

Holmes, A. (1928), Continental drift, *Nature* **122**, 431–433.

Hubert, A. (1968), Stray-field-free magnetization configuration, *Phys. Status. Solidi* **32**, 519–534.

Ingber, L. and Rosen, B. (1992), Genetic algorithms and very fast simulated reannealing: A comparison, *Mathl. Comput. Modelling* **11**(16), 87–100.

Irving, E., Robertson, W. A. and Scott, P. M. (1963), The paleomagnetism of some Mesozoic rocks in eastern Australia, *Journal of Geophysical Research* **68**(8), 2281–2282.

Jackson, J. D. (1975), *Classical Electrodynamics*, John Wiley and Sons, New York. p 194.

Kent, D. V. (1985), Thermoviscous remagnetization in some Appalachian limestones, *Geophysical Research Letters* **12**(12), 805–808.

Kent, D. V. and Miller, J. D. (1987), Redbeds and thermoviscous magnetization theory, *Geophysical Research Letters* **14**, 327–330.

Kirkpatrick, S., Gelatt, C. D. and Vecci, M. P. (1983), Optimisation by simulated annealing, *Science* pp. 671–680.

Kittel, C. (1940), Theory of the formation of powder patterns on ferro-magnetic crystals, *Phys. Rev.* **57**, 528–531.

Kittel, C. (1949), Physical theory of ferromagnetic domains, *Rev. Mod. Phys.* pp. 541–583.

Kneller, E. F. and Luborsky, F. E. (1963), Particle size dependence and remanence of single domain particles, *J. Appl. Phys* **34**, 656–658.

Kukla, G., Heller, F., Ming, L. X., Chun, X. T., Sheng, L. T. and Sheng, A. Z. (1988), Pleistocene climates in China dated by magnetic susceptibility, *Geology* **16**, 811–814.

La Bonte, A. E. (1969), Two-dimensional Bloch-type domain walls in ferromagnetic films, *J. Appl. Phys.* **40**, 2450–2458.

Landau, L. and Lifshitz, E. (1935), On the theory of the dispersion of magnetic permeability in ferromagnetic bodies., *Phys. Z. Sowjet.* **8**, 153.

Levi, S. L. and Merrill, R. T. (1978), Properties of single-domain, pseudo-single-domain, and multidomain magnetite, *Journal of Geophysical Research* **83**(B1), 309–323.

Maher, B. A. (1988), Magnetic properties of some synthetic sub-micron magnetites, *Geophys. J.* **94**, 83–96.

Maher, B. A., Thompson, R. and Zhou, L. P. (1994), Spatial and temporal reconstructions of changes in the asian palaeomomsoon: A new mineral magnetic approach, *Earth and Planetary Science Letters* **125**, 461–467.

Maxwell, A. E., von Herzen, R. P., Hsü, K. J., Andrews, J. E., Saito, T., Percival, S. F. J., Milow, E. D. and Boyce, R. E. (1970), Deep sea drilling in the south Atlantic, *Science* **168**, 1047–59.

McCabe, C. R., Van der Voo, R., Peacor, D. R., Scotese, C. R. and Freeman, R. (1983), Diagenetic magnetite carries ancient yet secondary remanence in some Paleozoic sedimentary carbonates, *Geology* **11**, 221–223.

McVitie, S., Chapman, J. N., Hefferman, S. J. and Nicholson, W. A. P. (1988), Effect of application of fields on the domain structure in small regularly shaped magnetic particles, *Journal de Physique* **12**, 1817–1818.

Moon, T. and Merrill, R. T. (1988), Single-domain theory of remanent magnetization, *Journal of Geophysical Research-Solid Earth And Planets* **93**(NB8), 9202–9210.

Moon, T. S. and Merrill, R. T. (1984), The magnetic-moments of non-uniformly magnetized grains, *Physics of the Earth And Planetary Interiors* **34**(3), 186–194.

Moon, T. S. and Merrill, R. T. (1985), Nucleation theory and domain states in multidomain magnetic material, *Physics of the Earth And Planetary Interiors* **37**(2-3), 214–222.

Moskowitz, B. M. and Banerjee, S. K. (1979), Grain size limits for pseudo-single domain behaviour in magnetite: Implications for paleomagnetism, *IEEE Trans.* **MAG15**, 1241–1246.

Moskowitz, B. M. and Halgedahl, S. L. (1987), Theoretical temperature and grain-size dependence of domain state in $x = 0.6$ titanomagnetite, *Journal of Geophysical Research-Solid Earth And Planets* **92**(NB10), 10667–10682.

Nagata, T., Akimoto, S. and Uyeda, S. (1951), Reverse thermo-remanent magnetism., *Proc. Jap. Acad.* **27**, 643–645.

Nakatani, Y., Uesaka, Y. and Hayashi, N. (1989), Direct solution of the Landau-Lifshitz-Gilbert equation for micromagnetics, *Japanese Journal of applied physics* **28**(12), 2485–2507.

Néel, L. (1949), Théorie due trainage magnétique des ferromagnétiques en grains fins avec applications au terres cuites., *Ann. Géophys* **5**, 99–136.

Néel, L. (1955), *Adv. Phys.* **4**, 191–242.

Özdemir, O. (in press), Closure domains in magnetite, *Journal of Geophysical Research.*

Özdemir, O. and Banerjee, S. K. (1982), A preliminary magnetic study of soil samples from west-central Minnesota, *Earth Planet Sci. Lett.* **59**, 393–403.

Parry, L. G. (1965), Magnetic properties of dispersed magnetite powders, *Philos. Mag.* **11**, 303–312.

Parry, L. G. (1981), The influence of fine structures on the remanence of multidomain particles of magnetite and titaomagnetitenetgoma, *Phys. Earth Planet. Interiors* **26**, 63–71.

Powell, M. J. D. (1977), Restart procedures for the conjugate gradient method, *Mathematical Programming* **12**, 241–254.

Press, W. H., Flannery, B. P., Teukolsky, S. A. and Vetterling, W. T. (1986), *Numerical Recipes*, Cambridge University Press.

Pullaiah, G., Irving, E., Buchan, K. L. and Dunlop, D. J. (1975), Magnetization changes caused by burial and uplift, *Earth Planet. Sci. Lett.* **28**, 133–143.

Rahman, A. A., Duncan, A. D. and Parry, L. G. (1973), Magnetization of multidomain magnetite particles, *Riv. Ital. Geofis.* pp. 259–266.

Rhodes, P. and Rowland, G. (1954), Demagnetizing energies of uniformly magnetized rectangular blocks, *Proc. Leeds Philos. Lit. Soc. Sci. Sect.* **6**, 191–210.

Robertson, W. A. (1979), Paleomagnetism of some Mesozoic intrusives and tuffs from eastern Australia, *J. Proc. R. Soc. N. S. W.* **112**, 31–35.

Robinson, S. G. (1986), The late Pleistocene palaeoclimatic record of North Atlantic deep-sea sediments revealed by mineral-magnetic measurements, *Phys. Earth Planet. Interiors* **42**, 22–47.

Saffer, B. and McCabe, C. (1992), Further studies of carbonate remagnetization in the northern appalachian basin, *Journal of Geophysical Research* **97**(B14), 4331–4348.

Sambridge, M. and Drijkoningen, G. (1992), Genetic algorithms in seismic waveform inversion, *Geophys. J. Int.* **109**, 323–342.

Schabes, M. E. and Bertram, H. N. (1988), Magnetization processes in ferromagnetic cubes, *Journal of Applied Physics* **64**(3), 1347–1357.

Schmidt, P. W. and Embleton, B. J. J. (1981), Magnetic overprinting in southeastern Australia and the thermal history of its rifted margin, *Journal of Geophysical Research* **86**(B5), 3998–4008.

Shcherbakov, V. P. (1978), *Earth Phys.* **14**, 356–362.

Soffel, H. (1971), The single domain–multidomain transition in natural intermediate titanomagnetites, *Z Geophys* **37**, 451–470.

Stacey, F. D. (1963), The physical principles of rock magnetism, *Adv. Phys.* **12**, 45–133.

Stacey, F. D. and Banerjee, S. K. (1974), *The physical principles of rock magnetism*, Elsevier.

Stender, J., Hillebrand, E. and Kingdon, J., eds (1994), *Genetic Algorithms in optimization, simulation and Modelling*, IOS Press, Amsterdam.

Thompson, R. and Oldfield, F. (1986), *Environmental Magnetism*, London: Allen and Unwin.

Thomson, L. C. (1993), A three-dimensional investigation of the magnetic properties and structures of magnetite, PhD thesis, University of Edinburgh.

Thomson, L. C., Enkin, R. J. and Williams, W. (1994), Simulated annealing of three-dimensional micromagnetic structures and simulated thermoremanent magnetization., *Journal of Geophysical Research* **99**(B1), 603–609.

Van der Voo, R. (1989), Paleomagnetism of North America: The craton, its margins and the Appalachian belt, *Geol. Soc. Am. Mem* **172**, 447–470.

Veitch, R. and Schmidbauer, E. (1983), Anhysteretic and hysteretic magnetic properties of small $Fe_3O_4$ particles, *J. Magn. Magn. Mat.* pp. 63–68.

Verhoogen, J. (1959), The origin of thermoremanent magnetization, *Journal of Geophysical Research* **1959**, 2441–2449.

Vine, F. J. (1966), Spreading of the ocean floor: new evidence, *Science* **154**, 1405–15.

Vine, F. J. and Mathews, D. H. (1963), Magnetic anomalies over oceanic ridges, *Nature* **199**, 947–9.

Wegener, A. (1922), *Discovery* **3**, 114.

Williams, T. (1994), Paleomagnetic and magnetic records for the last 300,000 years from Lac du Bouchet France, applications to geomagnetism and the environmnet, PhD thesis, University of Edinburgh.

Williams, W. and Dunlop, D. J. (1989), 3-dimensional micromagnetic modeling of ferromagnetic domain-structure, *Nature* **337**(6208), 634–637.

Williams, W. and Dunlop, D. J. (1990), Some effects of grain shape and varying external magnetic-fields on the magnetic-structure of small grains of magnetite, *Physics of the Earth And Planetary Interiors* **65**(1-2), 1–14.

Williams, W. and Dunlop, D. J. (1995), Simulation of magnetic hysteresis in pseudo-single domain grains of magnetite, *Journal of Geophysical Research* **100**(B3), 3859–3871. (in press).

Williams, W., Enkin, R. J. and Milne, G. (1992), Magnetic domain-wall visibility in bitter pattern imaging, *Journal of Geophysical Research-Solid Earth* **97**(B12), 17433–17438.

Xu, S. and Merrill, R. T. (1987), The demagnetizing factors in multidomain grains, *Journal of Geophysical Research-Solid Earth And Planets* **92**(NB10), 10657–10665.

Xu, S. and Merrill, R. T. (1992), Stress, grain-size, and magnetic stability of magnetite, *Journal of Geophysical Research-Solid Earth* **97**(NB4), 4321–4329.

Xu, S., Dunlop, D. J. and Newell, A. (1994), Micromagnetic modelling of two-dimensional domain structures in magnetite, *Journal of Geophysical Research* **99**, 9035–9044.

Yu, S. P. and Morrish, A. H. (1955), Dependence of the coercive force on density of some iron oxide powders., *J. Appl. Phys.* **26**, 1049–1055.

Yuan, S. W. and Bertram, H. N. (1992), Fast adaptive algorithms for micromagnetics, *IEEE Trans. Mag.* **28**(5), 2031–2036.

Zijderveld, J. D. (1967), *Methods in Paleomagnetism*, Elsevier, New York, pp. 254–286.